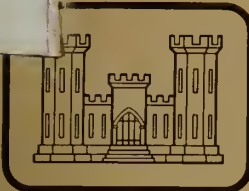


551.22  
St29  
v.11



MISCELLANEOUS PAPER S-73-I

# STATE-OF-THE-ART FOR ASSESSING EARTHQUAKE HAZARDS IN THE UNITED STATES

Report II

## IMAGERY IN EARTHQUAKE ANALYSIS

by

Charles E. Glass

Department of Mining and Geological Engineering

University of Arizona, Tucson, Arizona

and

David B. Slemmons

Department of Geological Sciences

MacKay School of Mines

University of Nevada, Reno, Nevada

December 1978

Report II of a Series

Approved For Public Release; Distribution Unlimited



Prepared for Office, Chief of Engineers, U. S. Army  
Washington, D. C. 20314

Under Purchase Order No. CW-77-M-1371

Monitored by Geotechnical Laboratory

U. S. Army Engineer Waterways Experiment Station  
P. O. Box 631, Vicksburg, Miss. 39180

~~E~~  
ENGINEERING LIBRARY  
UNIVERSITY OF ILLINOIS  
URBANA, ILLINOIS

551.22

St 29

v 11

Destroy this report when no longer needed. Do not return  
it to the originator.

551.22  
L729  
v.11

Unclassified

SECURITY CLASSIFICATION OF THIS PAGE (When Data Entered)

REPORT DOCUMENTATION PAGE		READ INSTRUCTIONS BEFORE COMPLETING FORM
1. REPORT NUMBER Miscellaneous Paper S-73-1	2. GOVT ACCESSION NO.	3. RECIPIENT'S CATALOG NUMBER
4. TITLE (and Subtitle)  STATE-OF-THE-ART FOR ASSESSING EARTHQUAKE HAZARDS IN THE UNITED STATES; Report 11, IMAGERY IN EARTHQUAKE ANALYSIS		5. TYPE OF REPORT & PERIOD COVERED  Report 11 of a series
7. AUTHOR(s)  Charles E. Glass David B. Slemonns		6. PERFORMING ORG. REPORT NUMBER  Purchase Order No. CW-77-M-1371
9. PERFORMING ORGANIZATION NAME AND ADDRESS  Department of Mining and Geological Engineering University of Arizona Tucson, Ariz. 85721		10. PROGRAM ELEMENT, PROJECT, TASK AREA & WORK UNIT NUMBERS  Department of Geological Sciences Mackay School of Mines University of Nevada Reno, Nevada 89507
11. CONTROLLING OFFICE NAME AND ADDRESS  Office, Chief of Engineers, U. S. Army Washington, D. C. 20314		12. REPORT DATE  December 1978
14. MONITORING AGENCY NAME & ADDRESS (if different from Controlling Office)  U. S. Army Engineer Waterways Experiment Station Geotechnical Laboratory P. O. Box 631, Vicksburg, Miss. 39180		13. NUMBER OF PAGES  233
16. DISTRIBUTION STATEMENT (of this Report)		15. SECURITY CLASS. (of this report)  Unclassified
17. DISTRIBUTION STATEMENT (of the abstract entered in Block 20, if different from Report)		15a. DECLASSIFICATION/DOWNGRADING SCHEDULE
18. SUPPLEMENTARY NOTES		
19. KEY WORDS (Continue on reverse side if necessary and identify by block number)  Earthquake engineering Earthquake hazards Earthquakes Remote sensing Seismic risks State-of-the-art studies		
20. ABSTRACT (Continue on reverse side if necessary and identify by block number)  Recent advances in the fields of remote sensing, engineering geology, seismology, and earthquake engineering have developed a need for a systematic comprehensive review of the basic principles and methods of applying remote sensing for evaluation of earthquake hazards and seismic risk.  This paper responds to this need by reviewing basic concepts, summarizing essential, state-of-the-art knowledge of theory and instrumental methods, establishing procedures evaluations, and discussing representative case histories that illustrate earthquake hazard evaluations that are based on remote sensing analysis.  The approach that is recommended is based on a "multi" approach that uses an integrated and systematic study of a region or a fault with a variety of imagery varying from small-scale (synoptic) to large-scale		
(Continued)		

20. ABSTRACT (Continued).

(detailed). The imagery analysis should be followed by a ground verification program of study that should include both ground and aerial reconnaissance examination of the major geologic structures of concern.

The character of the earthquake hazards is discussed in the context of the lithologic, structural, vegetational, and topographic variations that are associated with different types of active geologic structures. The response of earth materials, landforms, and geologic structures is summarized for the several main types of passive and active electromagnetic radiation used in current remote-sensing practice. Limitations of the different spectral regions used in remote sensing are reviewed to assist in the selection of ideal methods or sequences of methods of study for effective evaluation of active or capable faults and for assessing the earthquake potential of geologic structures that may affect a given engineering site.

The case histories provide examples of representative problems, approaches, sequences of study, and methods of estimating the activity or nonactivity of faults. These studies were based on lineament analysis, estimating earthquake magnitudes that could be associated with future faulting along active faults, or determining fault lengths, zone widths, and maximum expected surface displacement or separations.

THE CONTENTS OF THIS REPORT ARE NOT TO BE  
USED FOR ADVERTISING, PUBLICATION, OR  
PROMOTIONAL PURPOSES. CITATION OF TRADE  
NAMES DOES NOT CONSTITUTE AN OFFICIAL EN-  
DORSEMENT OR APPROVAL OF THE USE OF SUCH  
COMMERCIAL PRODUCTS.

## PREFACE

This report was prepared by Professor C. E. Glass, Department of Mining and Geological Engineering, University of Arizona in Tucson, and Professor D. B. Slemmons of the Mackay School of Mines, University of Nevada in Reno, under Purchase Order No. CW-77-M-1371. It is part of the ongoing work at the U. S. Army Engineer Waterways Experiment Station (WES) in Civil Works Investigation Studies, "Methodologies for Selecting Design Earthquakes," sponsored by the Office, Chief of Engineers, U. S. Army. This is Report No. 11 of the series of state-of-the-art reports for assessing the severity of bedrock motion during earthquakes.

Preparation of the report was under the direction of Dr. E. L. Krinitzsky, Engineering Geology and Rock Mechanics Division (EG&RDM), Geotechnical Laboratory, (GL), WES. General direction was by Mr. J. P. Sale, Chief, GL, and Dr. D. C. Banks, Chief, EG&RMD. The authors wish to express their appreciation for many helpful editorial and technical suggestions from Mrs. E. Bell and Mr. D. R. Slemmons. The report was reviewed by Mr. R. Baker of the General Electric Corporation, Space Division. His many constructive suggestions are appreciated and have been incorporated in the report.

COL G. H. Hilt, CE, and COL J. L. Cannon, CE, were Directors of WES during the period of this study. Mr. F. R. Brown was Technical Director.

## CONTENTS

	<u>Page</u>
PREFACE . . . . .	2
CONVERSION FACTORS, U. S. CUSTOMARY TO METRIC (SI)	
UNITS OF MEASUREMENT . . . . .	5
PART I: INTRODUCTION . . . . .	6
Scope of Paper . . . . .	6
General Comments . . . . .	7
Terminology . . . . .	9
PART II: IDENTIFYING EARTHQUAKE HAZARDS . . . . .	11
Active Faults . . . . .	11
Crustal Tilting or Distortion . . . . .	69
Ground Failure . . . . .	69
Tsunamis . . . . .	79
PART III: RESPONSE OF EARTH MATERIALS TO ELECTROMAGNETIC RADIATION . . . . .	82
Process of Response . . . . .	83
Response of Earthquake Materials to Ultraviolet Radiation . . . . .	92
Response of Earth Materials to Radiation in the Visible Region . . . . .	99
Response of Earth Materials to Radiation in the Near Infrared Region . . . . .	108
Response of Earth Materials to Radiation in the Thermal Infrared Region . . . . .	113
Response of Earth Materials to Radiation in the Microwave Region . . . . .	120
PART IV: USES AND LIMITATIONS OF MULTISPECTRAL IMAGE ANALYSIS . . . . .	137
Image Enhancement Techniques . . . . .	137
Image Quality . . . . .	170
PART V: MULTISPECTRAL IMAGERY PLATFORMS . . . . .	174
Airborne Multispectral Imagery . . . . .	174
Spacecraft Multispectral Imagery . . . . .	175
PART VI: EVALUATION AND SELECTION OF MOST APPROPRIATE TYPES OF IMAGERY FOR SPECIFIC TYPES OF STUDY AREAS . . . . .	179
Determination of Specific Information Desired . . . . .	179
Formulating a Decision Analysis . . . . .	183
PART VII: CASE HISTORIES OF REMOTE SENSING USED IN EARTHQUAKE HAZARD ASSESSMENT . . . . .	197
General Comments . . . . .	197

	<u>Page</u>
Case History One: Wasatch Fault Zone, Utah . . . . .	197
Case History Two: Search for Active Faults In Eastern Alaska . . . . .	205
Case History Three: Evaluation of the Pipe Creek Fault Zone at the Libby Reregulating Dam, Northwestern Montana . . . . .	208
Case History Four: The 1872 Pacific Northwest Earthquake Fault Study . . . . .	210
REFERENCES . . . . .	217
TABLES 1-1 <sup>4</sup>	
APPENDIX A: GLOSSARY OF TERMS . . . . .	A1
APPENDIX B: GUIDE FOR ORDERING AIRBORNE AND LANDSAT IMAGERY . . . . .	B1

CONVERSION FACTORS, U. S. CUSTOMARY TO METRIC (SI)  
UNITS OF MEASUREMENT

U. S. customary units of measurement used in this report can be converted to metric (SI) units as follows:

Multiply	By	To Obtain
degrees (angular)	0.01745329	radians
Fahrenheit degrees	5/9	Celsius degrees or Kelvins*
feet	0.3048	metres
inches	25.4	millimetres
miles (U. S. nautical)	1.852	kilometres
miles (U. S. statute)	1.609344	metres

---

\* To obtain Celsius (C) temperature readings from Fahrenheit (F) readings, use the following formula:  $C = (5/9)(F - 32)$ . To obtain Kelvin (K) readings, use:  $K = (5/9)(F - 32) + 273.15$ .

STATE-OF-THE-ART FOR ASSESSING EARTHQUAKE  
HAZARDS IN THE UNITED STATES  
IMAGERY IN EARTHQUAKE ANALYSIS

PART I: INTRODUCTION

Scope of Paper

1. The rapid expansion of knowledge, improvement in equipment, and development of new methods of analysis in remote sensing, combined with increased concern about public exposure to seismic risks, have led to this comprehensive review of state-of-the-art methods for assessing earthquake hazards by means of remote sensing. Rapid urbanization and other facets of human development give emphasis to the need to avoid construction of homes and buildings astride active faults or in areas subject to other earthquake hazards. Several papers discuss the application of remote sensing to evaluation of earthquake hazards and active faults,<sup>1-3</sup> although no complete review has been attempted. Accordingly, the U. S. Army Engineer Waterways Experiment Station (WES), is supporting this comprehensive synthesis of methods and criteria needed to conduct adequate studies of earthquake hazards. This report provides an introduction to the subject of remote sensing, a brief outline of the kinds of features associated with earthquake hazards, a review of the response of earth materials to electromagnetic radiation, an outline of the uses and limitations of multispectral imagery, an outline of the methods of selecting imagery and conducting image analysis projects, and, finally, a presentation of several case histories.

2. This analysis is based on a "multi" approach, using a variety of imagery varying from synoptic to detailed, and using a combination of laboratory and field examinations. The field examination should include both aerial and ground review.

### General Comments

3. A little over a century ago, the earth scientist was mainly confined to on-the-ground observation for measuring and interpreting earth processes. Aerial photography was introduced into the field of geology in the 1920's. Since then the view afforded from aircraft and, more recently, from spacecraft has revolutionized the earth scientist's search for needed information. This process of examining the earth's surface from a distance to study its physical properties is referred to as remote sensing. Recent advances in remote sensing include improvement of film emulsions, cameras, scanners, platforms, and image data processing, enhancement, and display. The past few years have seen a steady increase in the use of interactive computer analysis methods for remote sensing projects undertaken by governments, private industry, and universities. Such analysis methods are also used by underdeveloped countries for evaluation of natural resources.

Increasingly, digital techniques of data processing are demonstrating their advantages over less reliable and less flexible imagery techniques....the trend is unmistakably in the direction of the more versatile computerized methods of handling and utilizing the flow of data from the satellite sensors.<sup>4</sup>

This opinion not only emphasizes the rapid changes taking place in both the number and variety of techniques being developed in remote sensing, but also reinforces the need to design remote sensing projects to meet specific project goals with available resources.

4. Until recently, individual remote sensing projects were commonly conducted on a single date and with a single set of specifications in terms of film, filter, and scale. However, the primary objective of a remote sensing project cannot always be achieved under these constraints. A "multi" approach usually provides a more effective program for achieving project goals. This multiple approach commonly includes a combination of the following, which are expanded from Colwell:<sup>5</sup>

- a. Multistation imagery--successive overlapping photographs are taken along a flight line to produce stereoscopic parallax.
- b. Multiband imagery--reflectance or radiance of an object is sensed in several bands of the electromagnetic spectrum.
- c. Multidate imagery--an area is imaged at different times during the year.
- d. Multistage or multilevel imagery--progressively larger scale imagery is obtained of progressively smaller subsamples of an area.
- e. Multipolarization imagery--the polarization characteristics of various surfaces are used as identification keys.
- f. Multienhancement techniques--several digital or optical techniques are applied to imagery to aid interpretation.
- g. Multiple observers--provide a more complete and less subjective evaluation.

5. This multiple or "multi" approach to imagery analysis has greatly aided the earth scientist in his understanding of "ground truth" and promises to further improve his predictive capabilities in the future. A well-planned remote sensing project, then, should involve a systematic approach and should not necessarily rely solely on conventional panchromatic photography. Neither should it rely on luck by indiscriminate use of a large number of imaging systems and spectral regions in the hope of stumbling upon the proper combination.

6. The major goal of remote sensing in earthquake engineering should be to acquire images possessing the maximum possible contrast between a fault, or other earthquake associated hazard, and its background. This contrast may occur as the result of varying rock properties, vegetation properties, moisture content, or topography. The recording of each property may require a different sensor or combination of sensors. Thus, a thorough literature, aerial reconnaissance, and ground study conducted before imagery is produced provides the best insurance for project success. Previously, such studies were limited to selecting a convenient image scale, selecting a desired spectral range and image format (usually 9- by 9-in.\* panchromatic prints) and, finally,

---

\* A table of factors for converting U. S. customary units of measurement to metric (SI) units is presented on page 5.



DEPARTMENT OF THE ARMY  
WATERWAYS EXPERIMENT STATION, CORPS OF ENGINEERS  
P. O. BOX 631  
VICKSBURG, MISSISSIPPI 39180

IN REPLY REFER TO: WESGV

2 March 1979

Errata Sheet

No. 1

STATE-OF-THE-ART FOR ASSESSING  
EARTHQUAKE HAZARDS IN THE  
UNITED STATES

Report 11

IMAGERY IN EARTHQUAKE ANALYSIS

Miscellaneous Paper S-73-1

December 1978

1. Page 8, paragraph 4b:  
First word should read "Multispectral".
2. Page 16, Figure 6:  
Rotate the photograph 180°.
3. Page 16, paragraph 15:  
First word of eighth line should read "within".
4. Page 29, Figure 17:  
Rotate the photograph 180°.
5. Pages 33 and 34, Figures 20 and 21:  
Reverse the two figure titles.
6. Page 53, Figure 39:  
Fourth word of seventh line of title should read "quiescence".
7. Page 70, Figure 48:  
Rotate the photograph 90° clockwise.
8. Page 75, Figure 54:  
Seventh word of second line of title should read "Corfu".
9. Page 86, paragraph 67:  
Second word of fourth line should read "Raman".
10. Page 92, paragraph 82:  
Ninth word of second line should read "L-band".

(Continued)

11. Page 95, title of Figure 64 should read:  
Spectral reflectance curves:33 (a) granite, (b) obsidian,  
(c) basalt, and (d) calcite (sheet 1 of 2)
12. Page 103, paragraph 96:  
Tenth word of second line should read "more".
13. Page 123, paragraph 129:  
Third word of third and fifth lines should read "dielectric  
constant".
14. Page 135, Figure 87:  
Rotate the photograph 180°.
15. Page 140, paragraph 153:  
In line 4 change ( $0 \geq S(i,j) \dots$ ) to ( $0 \leq S(i,j) \dots$ ).
16. Page 149, Figure 97b:  
Rotate the figure 90° counterclockwise.
17. Page 159, Figure 106:  
Reverse the figure titles for 106a and 106b.
18. Page 172, paragraph 179:  
Third word of ninth line should read "can".
19. Page 213, paragraph 254:  
Last two words of last line should read "a gravity slide."
20. Page A2, asterisk footnote:  
Seventh word of third line should read "photos".

extracting the available information. The revolutionary advances in remote sensing and the wide range of systems available today, however, require that the above procedure be applied essentially in reverse by asking specific questions (Figure 1).

WHAT EARTHQUAKE HAZARDS ARE WE LOOKING FOR?	WHAT ARE THE BEST IMAGING METHODS FOR SENSING THESE HAZARDS?	HOW MAY THE IMAGES BE ENHANCED TO IMPROVE INTERPRETATION?
a. Active faults	a. Spectral band,	a. Computer enhance-
b. Landslide hazards	b. Scale,	ment,
c. Liquefaction hazard	c. Format, and	b. Optical enhance-
d. Tsunami hazard	d. Required resolution.	c. Stereoscopic viewing, and
e. Crustal tilting hazard.		d. Seasonal.

Figure 1. Design algorithm for remote sensing project

7. The first step involves realistically determining the specific information needed to successfully accomplish project goals. This specific information will generally include an assessment of the type of contrast, or contrasts, that specific earthquake-related hazards are likely to produce within the project area. If the probable ground contrasts can be defined, the imaging system (in terms of spectral sensitivity, signal resolution, spatial resolution, and image format) which possesses the highest probability of accurately recording the ground contrasts may be chosen. It is possible that no single system will provide the image contrasts required to arrive at a unique interpretation, and multiple systems and/or enhancement techniques may be required. The economic limitations of a specific project may require that cost-benefit be considered for the ultimate imaging program.

#### Terminology

8. The field of remote sensing uses terminology that is unfamiliar to many geologists and engineers. The remote sensing terms used in this report are defined in Appendix A. Faults, landslides, liquefiable sediments, tilted or deformed terraces, alluvial areas, or other surficial deposits are the principal geomorphic features

which can be detected, delineated, and evaluated on remotely sensed images. They can thus be used in assessing earthquake hazards. Classification of fault activity, slip types and distortion, and methods of fault evaluation for determining earthquake magnitude and design values are given by Krinitzsky,<sup>6</sup> Krinitzsky and Chang,<sup>7</sup> and Slemmons.<sup>3</sup>

## PART II: IDENTIFYING EARTHQUAKE HAZARDS

9. The first step in assessing earthquake hazards is to inventory the potential for damage from: active faulting, crustal tilting or distortion, ground failure, and tsunamis. Each of these four hazards has its own set of diagnostic physical characteristics which form the information elements necessary for proper imagery analysis. The following paragraphs outline those diagnostic physical characteristics for each earthquake hazard.

### Active Faults

10. Since the presence of active faults provides the most positive evidence of earthquake hazard, their detection is of primary importance to hazard assessment. Active or capable faults are variously defined, with over thirty different definitions proposed.<sup>8</sup> The methods for determining fault activity or nonactivity is discussed in Slemmons.<sup>3</sup> There have been probably between 100 and 200 documented surface fault breaks throughout the world over the last 150 years.<sup>9</sup> Though recent experience has shown that surface faulting can be associated with relatively small shocks and aseismic creep, most of the documented surface fault displacements have been associated with large earthquakes. Thus, active fault studies are useful in determining potential future sources of large earthquake ground motion. Such studies should take place in three phases: (a) location of faults, (b) assessment of fault activity, and (c) assessment of fault length and fault type for active faults. Since imagery is useful in all three of these phases, recognition of faults on imagery should constitute the first step of a project, and the successful delineation of faults (most of which will prove to be inactive) is instrumental to insuring the success of later phases. There are several factors which an image interpreter may use to delineate faults, but all generally reduce to locating discontinuities or changes across the surface expression of a fault or identifying an alignment of features along its strike.

11. A discontinuity across the surface expression of a fault provides one of the most common recognition keys for fault detection. Displacements along faults commonly bring features of different rock types into juxtaposition. If these features possess measurable differences in their physical or botanical properties, there is a good chance that these differences may be sensed on appropriate types of imagery and the fault contact between them identified.

#### Lithologic variations

12. Faults commonly bring different rock types into contact. Rock units having measurable differences in reflectance (color) may be readily distinguished on imagery even though it is generally not possible to identify precise mineralogy (Figures 2 and 3). Occasionally a fault will be detectable as a color change even within a single rock type due to differences in weathering along fresh fault surfaces as opposed to the rock on either side of the fault which has been exposed to weathering agents for a longer period of time (Figure 4).

13. Though color is often useful in detecting lithologic variations across a fault, the texture and overall pattern of rock masses are usually more useful in distinguishing rock types and boundary faults. The dominant textural component of rock masses from an imagery standpoint is the texture associated with stream (or drainage) pattern. Rock mass structure and hardness are both reflected in the pattern and density of the drainage system (Figures 5 and 6). In addition to stream patterns, variations in rock strength, hardness, and stress history result in fracture patterns having widely varying orientations and spatial frequencies. Changes in the pattern, density, or texture of stream patterns and fracture systems often denote a fault contact though ancillary data should always be used as verification.

14. The thermal properties of rocks may provide useful contrasts when imagery equipment is sensitive to radiation in the appropriate thermal range even though the reflectance of the two rock units are equal. For example, thermal inertia (ease with which rocks heat or cool) may vary among different rocks to the degree that a thermal scan made at night may show one unit as warmer than another even though the



Figure 2. Fault in Prima Canyon, Arizona, marks the contact between a buff colored gneiss on the right and a red gneiss on the left. The color change is obvious on color imagery but is too subtle to be seen on panchromatic imagery without contrast stretching



Figure 3. Vertical areal photograph of fault in Utah marked by an abrupt discontinuity between the dark shale units on one side and lighter siltstone units on the other. The fault, which extends from the upper left to the lower right, is more difficult to detect within the light-toned unit at the lower right in the photograph. (U. S. Geological Survey (USGS) photograph)



Figure 4. Bear Valley fault, Utah. This photograph shows the difference in color due to weathering along a fault. At the upper left-hand corner the fault plane is a dark gray. The latest displacement has presented fresh rock to the elements, and weathering has turned the rock an orange color. Fresh rock (white stripe) has been exposed by excavation at the base of the scarp. These color contrasts are easily detectable from the air



Figure 5. San Andreas Fault, Imperial Valley, California. The San Andreas fault is dramatically marked in this high oblique photograph by the change in texture across the fault. The stream patterns and fracture patterns in the foreground are more dense and deeply incised than the patterns across the fault. Note the fault at the lower center of the photograph which brings a light-toned rock into juxtaposition with the dark-toned, deeply incised rock



Figure 6. Vertical aerial photograph of fault on Colorado Plateau, Arizona. Drainage pattern in the basalt plateau (upper right) differs markedly from the pattern on the lower left in density (stream channels per unit area) making identification of the fault easy even though the photographic tones are nearly identical on both sides

two have the same color and brightness during the day. At present, however, major problems exist with instrumental methods of spatial and radiometric resolution of ambient temperature variations of earth materials.\*

15. Faults occurring within a single rock unit are usually indistinguishable using rock reflectance or texture alone and other diagnostic interpretation keys must be used. The difficulty in locating faults within continuous rock units may profoundly affect a project. For example, a fault may be easily traced for tens of kilometres and appear to abruptly stop at an igneous intrusion only to resume on the other side. Since the color, fracture pattern, and stream pattern without the intrusion are usually the same on both sides of the fault, the faulting may not be apparent on conventional imagery and literature sources may indicate that the fault is "pinned" or that

---

\* R. Baker, General Electric Corporation, personal communication.

fault activity ceased before intrusion. The authors are aware of two cases in which active faults were classified as inactive based on the radiometric age of an "unfaulted" pluton. Careful interpretation of large scale, low-sun angle photography to enhance fault features, coupled with fractured density mapping and ground studies, indicated in both cases that the fracture density increased near the projection of the fault through the pluton and that the faults displaced the pluton along a wide zone of minor fractures. Conclusions regarding the temporal frequency and activity of faults in such cases should not be made by relying on published literature or conventional imagery alone but should be made only after a thorough aerial and ground analysis.

16. If a fault produces a variation in lithology, the parameters most likely to be useful for detecting these variations are:

- a. Differences in reflectance (e.g., changes in hue in color photography or tone in panchromatic photography).
- b. Differences in texture or pattern (e.g., changes in texture due to joints, stream patterns, etc.).
- c. Temperature differences (e.g., changes in tone on thermal imagery; however, this is difficult to detect in most cases).

#### Vegetation variations

17. Different rock or soil types may support different plant assemblages or may support the same plant assemblage but with varying growth characteristics. Thus, even though the actual rock surface may be partially or totally obscured, differences in the type, age, vigor, density, or pattern of vegetation may provide clues to fault location.

18. Vegetation variations may occur as a tone contrast across a fault in which case the contrast is generally due to differences in the type of vegetation on one side as opposed to the other (Figures 7, 8, and 9). Vegetation contrasts may also occur as texture contrasts across a fault due to changes in vegetation type or more typically in vegetation density. Moisture dammed by a fault may promote a more dense vegetal growth on one side than another (Figure 10). Faults may also serve as a conduit for fluid flow promoting vegetal growth along the fault and associated fractures. In this case alignments of vegetation



Figure 7. Low oblique photograph of Cache Valley, Utah. This normal fault along the western edge of the Bear Mountain range has been active during historical time through not in this location. Note the predominance of conifer vegetation on the upthrown fault block and grasses and deciduous vegetation on the downthrown block. Two branches of the fault can be seen with disturbances of stream courses across them. The abruptness of the contrasts as well as topographic relief suggests activity even though no historical surface displacements have taken place



Figure 8. Vertical aerial photograph of Owens Valley, California. The Owens Valley fault extending nearly horizontally across the photograph causes a vegetation contrast through the town of Lone Pine, California. Though the fault scarp, which broke in 1872, has been modified by agriculture activity, it is discernable on aerial photography due to the vegetation contrast



Figure 9. Low oblique photograph of Columbia River Terrace, Kennewick, Washington. This old terrace of the Columbia River produces a striking contrast in vegetation which could easily be mistaken for a fault without careful ground studies. The terrace bench is the light area on the right two-thirds of the photograph. The dimensions of the field at the top of the photograph are approximately 300 by 400 m



Figure 10. High oblique photograph of Chino Valley fault, Arizona. This fault graben has probably not been active during Holocene time but is still easily distinguishable due to more dense vegetation on the upthrown sides. The sparse vegetation within the graben may be due in part to the accumulation of wind-blown sand

are formed which may extend for tens of kilometres (Figures 11, 12, and 13a and b). Vegetation along fault scarps may be of a younger age than vegetation on either side yielding a relative age relationship.

19. Imagery in the near infrared region is optimum for sensing variations in vegetation since plant reflectance in this region is a function of plant health and leaf structure. Thus, plants under stress will exhibit a lower reflectance in the infrared than healthy plants even though the reflectance in the green region due to chlorophylls may be the same for both (Figures 14, 15, and 16). The reason for plant stress may be due to lack of moisture or to toxic fluids flowing along a fault or fracture.

20. The parameters most likely to be useful for detecting a variation in vegetation are:

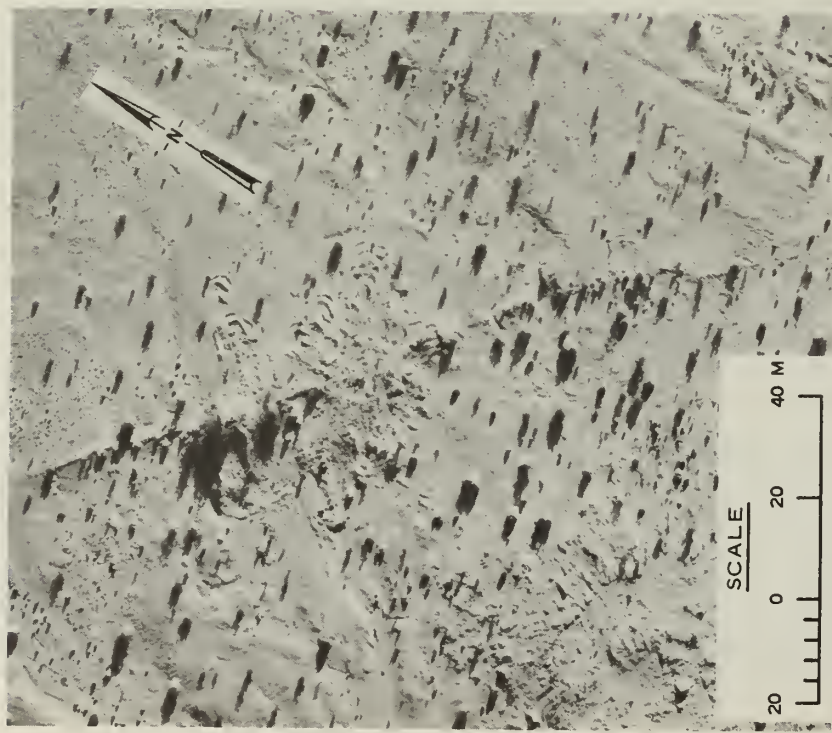
- a. Differences in reflectance of plants due to stunting or abnormal growth (particularly in the visible, near infrared and thermal infrared).



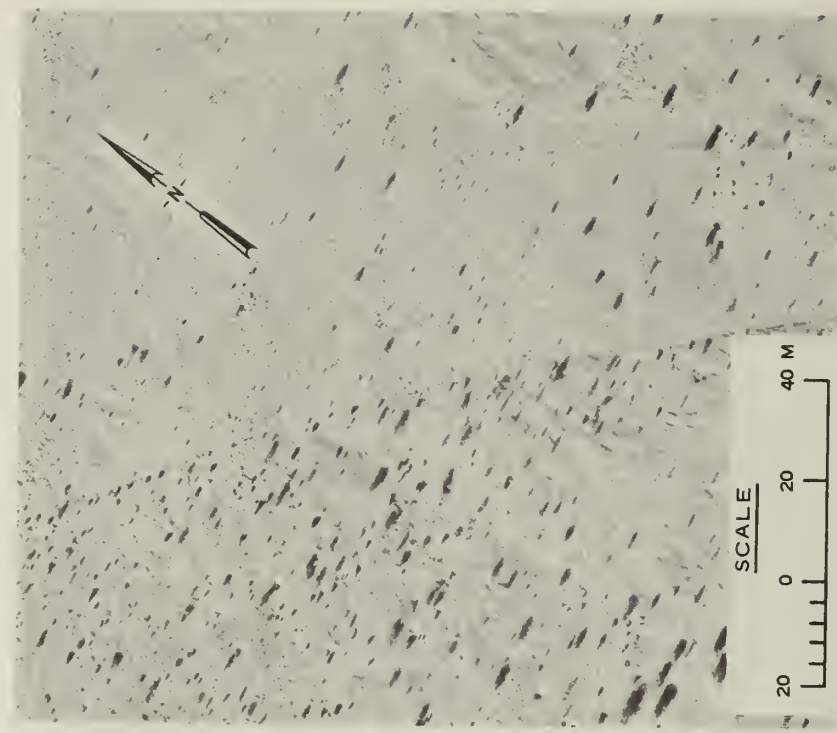
Figure 11. Vertical aerial photograph of Owens Valley, California. The Owens Valley fault north of Lone Pine consists of a very straight alignment of vegetation and sag ponds. The fault may be seen on the photograph extending left to right. The Owens River is at the top of the image.



Figure 12. Vertical aerial photograph showing complex swarm of branching fault scarps near Reno, Nevada. The northerly trending scarps are generally marked by alignments and clusters of larger shrubs. The low morning sunlight from N78°E (right of photograph) highlights the east-facing scarps and shades the steeper parts of the west-facing scarps. The angle of sun incidence is at an inclination of 23°. The steeper west-facing scarps are in full shadow and the more gentle older, and more deeply weathered scarps with slopes from 5° to 23° have various lighter gray tones, with the tone related to scarp angle



a. Alignment of large shrubs and elongate sand mounds



b. Alignment of smaller plants

Figure 13. Vertical aerial photograph of the San Andreas fault near Ocotillo Wells, California. The scarp which was formed during the Borrego Mountain earthquake of April 8, 1968, can be seen as an alignment of large shrubs and elongate sand mounds. The vertical photograph was taken on May 6, 1969, indicating that the plants had grown along an older scarp which was reactivated in 1968. Alignment of smaller plants is seen further along the scarp as well as a marked change in density of plant growth across the fault.



Figure 14. Landsat color composite print of central Washington. Lake Chelan is at the top of the image and Mt. Ranier at the lower left. The red and orange signify cultivated areas. The Yakima anticlines in the lower right corner are distinguishable by texture produced by streams.

Several lineaments can be crossing the anticlines\*

---

\* Image enhancement processed at Battelle Northwest Laboratory and provided through the courtesy of Mr. David D. Tillson, Washington Public Power Supply System.

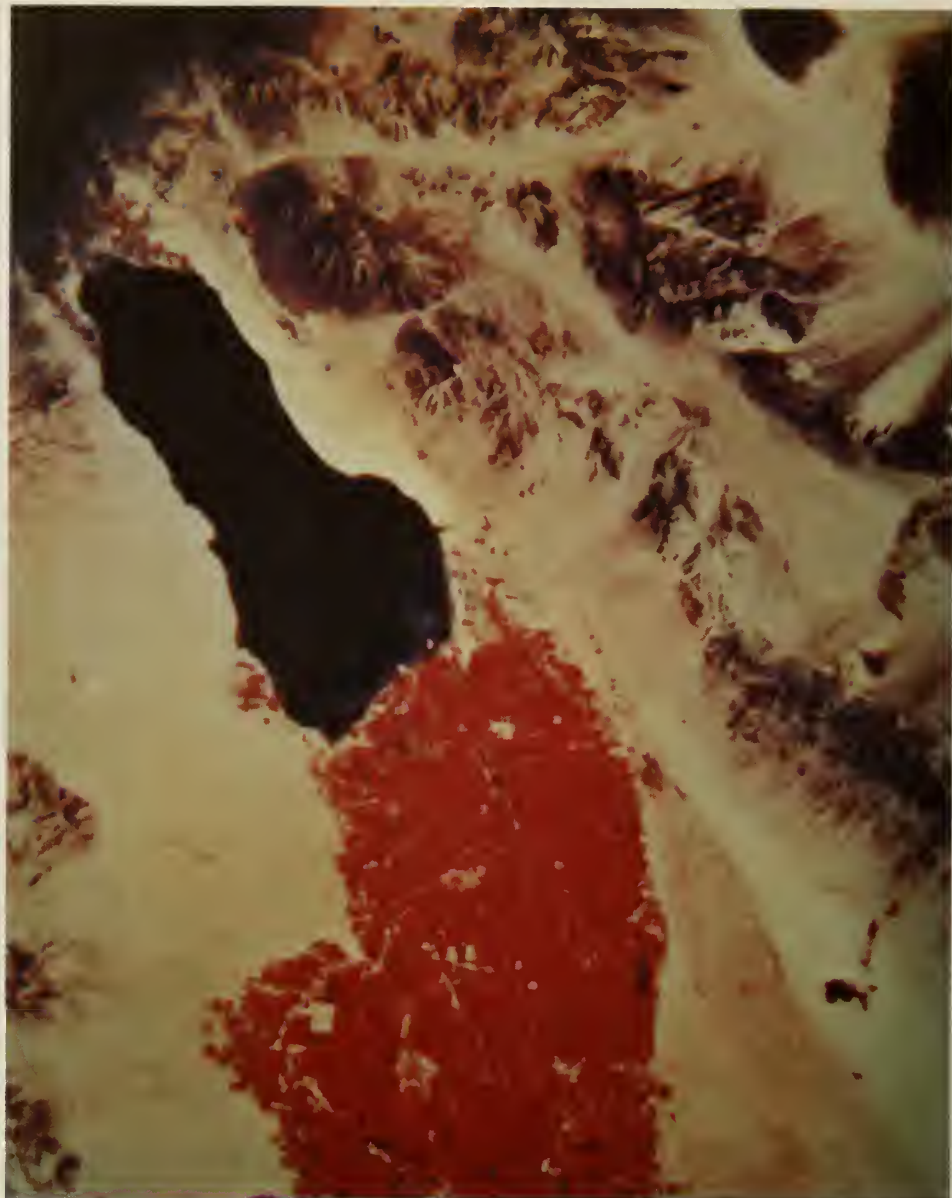


Figure 15. Landsat color composite of Imperial Valley, California. Vegetation appears red in this color composite image due to the strong reflectance in the infrared. Notice the strong difference between returns from fields in the United States and those in Mexico due to irrigation differences across the border. Also, the agricultural area contrasts markedly from the pinkish natural vegetation immediately to the east. This area in turn is separated by the San Andreas fault from the structurally controlled dune field (white) near the base of the mountains. Topographic zonation of vegetation can be seen in the ranges as well as faulting at their bases

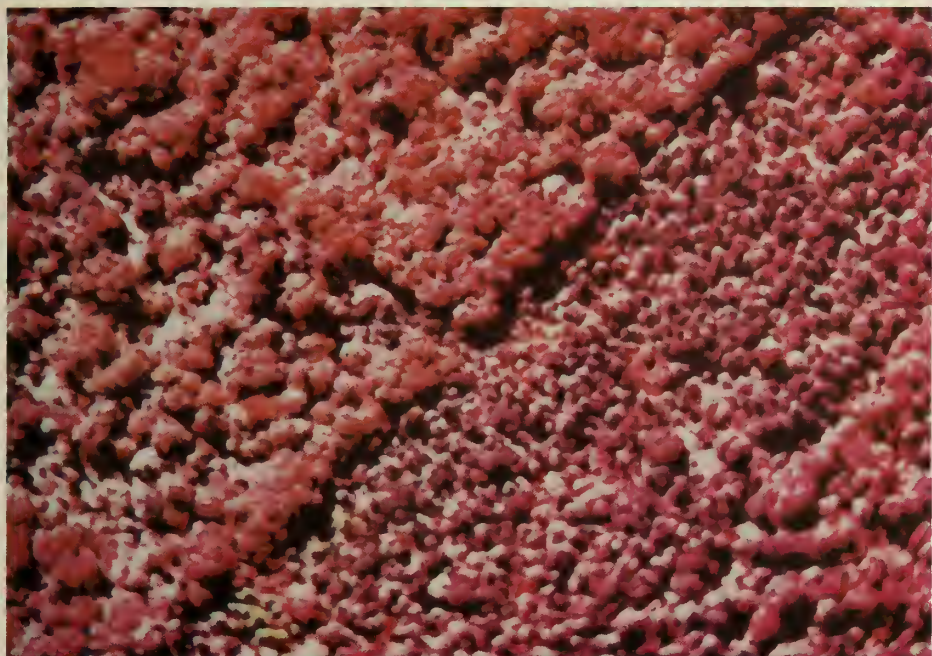


Figure 16. Low oblique view of younger trees on the lower right show up markedly different from trees to the upper left in this color infrared photograph. Yellow trees in the lower left of the image indicate trees under stress from the Southern Pine Beetle. Similar stress could be caused by a lack of moisture or by toxic fluids within a fault or fracture. (Photo by W. M. Ciesla, United States Forestry Service, Southeastern Area Division of Forest Pest Control; from "Applied Infrared Photography" Kodak Technical Publication M-28, 1968)

- b. Differences in general reflectance of ground surface.
- c. Vegetation distribution patterns.

#### Ground moisture variations

21. Active faults often form a barrier to the free flow of water through near-surface materials or provide a conduit for flow. This variation in moisture across, or along, a fault may be large enough to be sensed remotely. The most striking effect of moisture accumulation is the increased plant growth causing changes in the type, pattern, and/or density of vegetation. In areas with sparse vegetation, the moisture discontinuity may result in measurable changes in ground temperature due to evaporation. Moisture may also change the reflectance of the soils on opposite sides of a fault (Figure 17). Ponding may also occur along the trace of a fault forming a string of "sag" ponds characteristic of active faults (Figure 11).

22. The parameters most likely to be useful in detecting a discontinuity in ground moisture are:

- a. Differences in reflectance and reflectivity.
- b. Temperature differences (e.g., tone changes on thermal infrared imagery).
- c. Differences in vegetation pattern.

#### Topographic variations

23. The most definitive indicator of active faulting is oversteepened land surfaces (fault scarps). Fault scarps may often be detected in materials of uniform mineralogy, surface texture, or moisture conditions simply because one side of the fault, or portions within the fault zone, is closer to the sensor. Since the ability to distinguish these topographic discontinuities is a powerful aid in fault detection, stereoscopic parallax is one of the more important factors to be considered when selecting a remote sensing system (Figure 18). This effect of sensing topographic relief is most conspicuous with large differences in elevation on either side of the scarp and also with increased steepness of slope angle of the scarp (Figure 19).

24. The following parameters are especially important for detecting topographic variations:



Figure 17. Vertical aerial photograph of Owens Valley, California. The Owens Valley fault crosses the highway at the upper left edge of the photograph and continues across old shorelines forming a contrast in moisture toward the center right edge of the photograph. Note the detailed structures shown on this wet playa floor. These are not present on photographs taken when the playa is dry. Most of this pattern disappears during the summer months

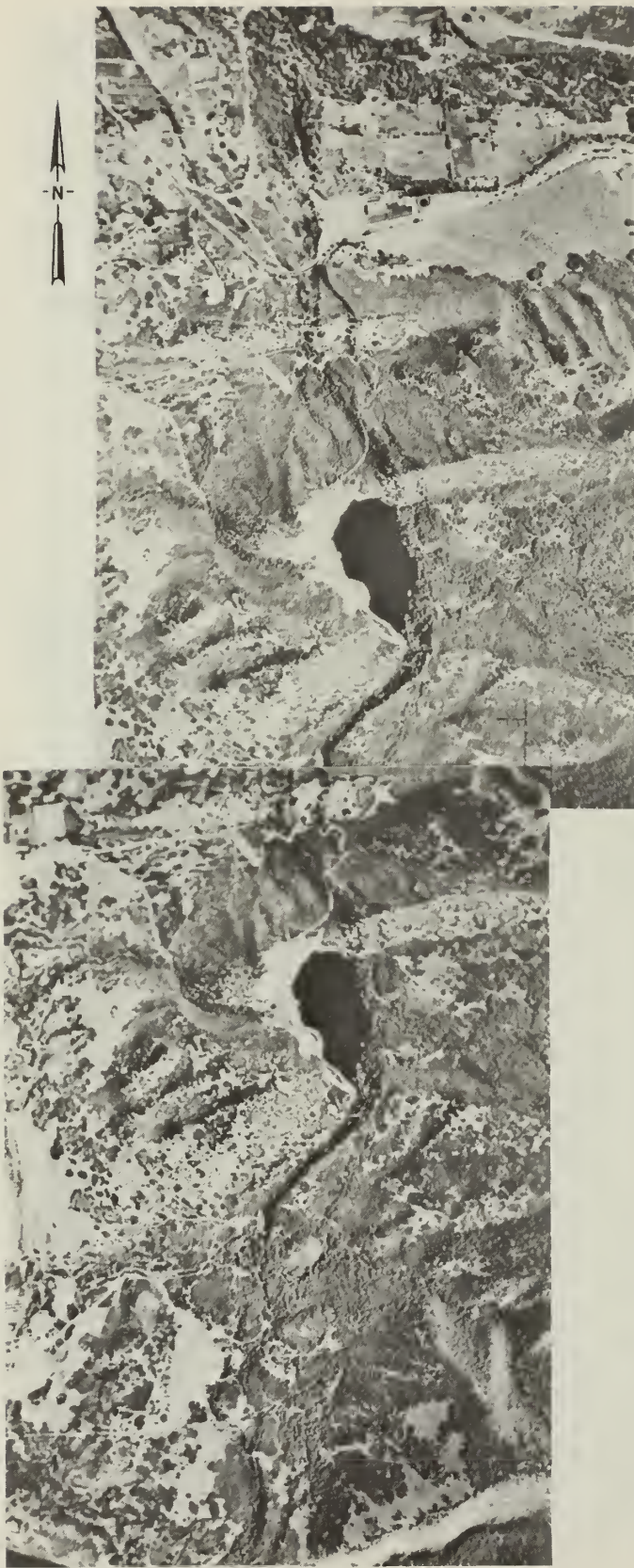


Figure 18. Stereopair photographs of Bells Canyon, Utah. The active Wasatch fault can be seen displacing the moraine at the mouth of Bells Canyon. The scarp is over 30 m high across the moraine, and although the scarp is accentuated by low-angle sunlight, the main fault scarp and some secondary scarps can be mapped using parallax, whereas in a single photograph they are not as apparent

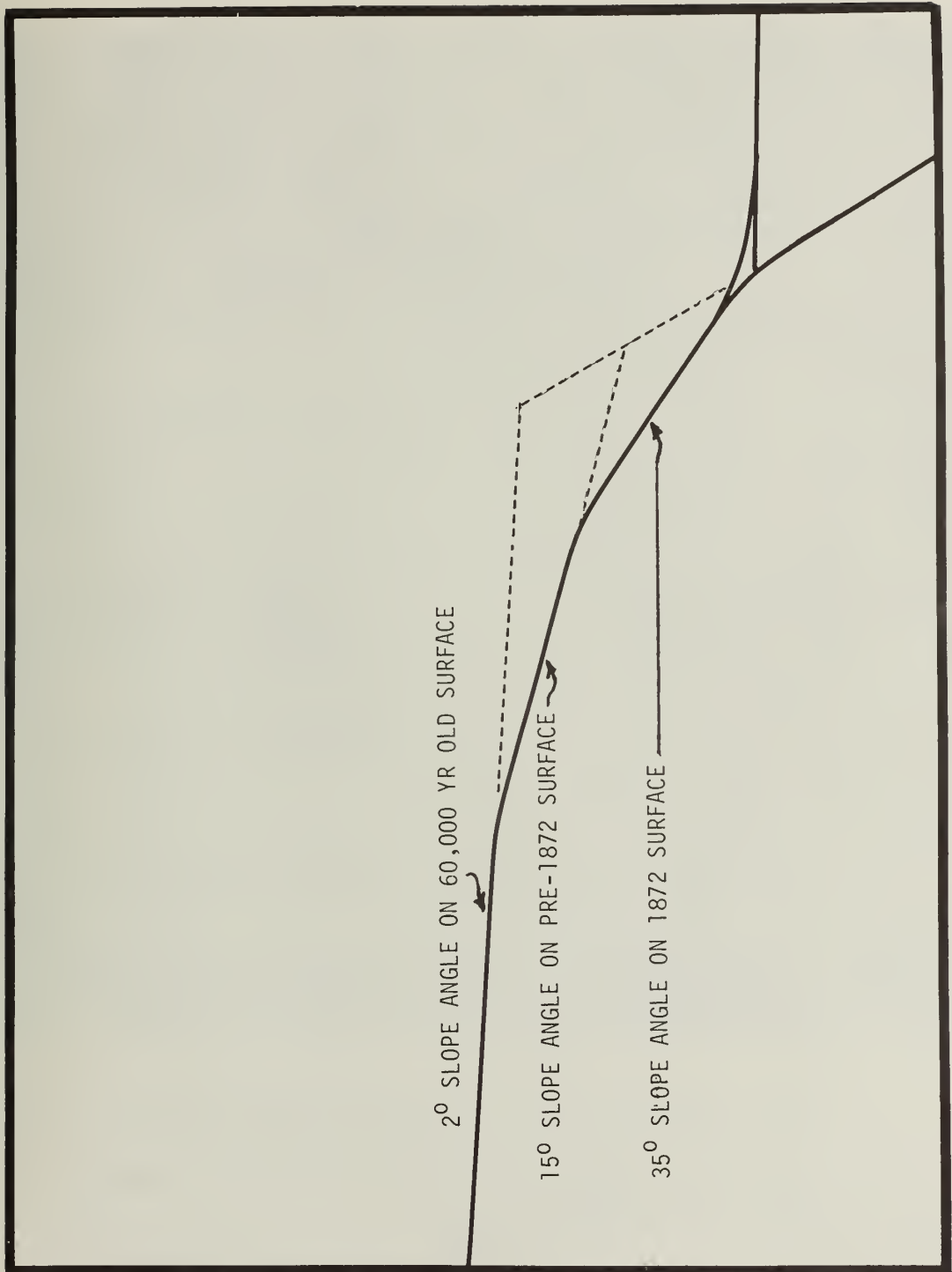


Figure 19. Cross section of bevelled fault scarp developed from three or more surface faulting events. Use of various low angles of sunlight from left can give variable shading of scarp

- a. Stereoscopic parallax.
- b. Low irradiation angle.\*
- c. High spatial resolution.
- d. Thermal differences caused by shadows and highlights.

25. Low-sun angle enhancement of scarps. The single most effective method of detecting and delineating fault scarps is to conduct aerial reconnaissance and remote sensing using low-irradiation angles to produce shadows (Figure 20) or highlights (Figure 21) on scarps having slopes steeper than the irradiation angle of the sun. Many special studies for major engineering structures have been conducted during the past ten years and have shown the importance of this method in revealing the detailed fracture patterns associated with active faults that are difficult or impossible to observe on the ground (Figure 22).<sup>1,10</sup>

26. Scarps having different strikes and dips can be selectively enhanced using low-sun angle irradiation by photographing at the ideal time of day and year for their strike and slope angle (Figure 23). At 40° north or south latitude, the sun azimuth at sunrise, or at sunset varies by over 60° between winter and summer solstice. The sunrise on June 21 is at N 58° E (58 azimuth) and on December 21 is at 58° E (122° azimuth) as shown in Figure 23.<sup>11</sup> The contrasts in observation by time of day and season is shown for the photo sequence of the McGee Creek Moraines, California:

- a. In summer high-sun angle irradiation (Figure 24), the scarp shows weak expression, except for vegetation contrast.
- b. Figure 25 shows the same scarp with highlighting from low-sun irradiation from the northeast in early morning summer. The brightness of the highlights is partly related to scarp steepness.
- c. Figure 26 shows the scarp to be clearly visible, even with heavy snow cover, with low-sun angle back irradiation from winter late afternoon sunlight from the southwest.
- d. Figure 27 shows dramatic shading effects with low-sun angle back irradiation.

---

\* See Appendix A for a discussion of the use of the term irradiation rather than illumination in this report.



Figure 20. Low oblique view of the 1954 fault scarp in northern Dixie Valley, Nevada, viewed to the west with early morning highlighting sun-light providing bright irradiation of the south-facing main scarp. Minor graben along the fault scarp shows some shadows. The right-lateral offset along the far end of the near branch fault shows an en echelon branching or ramping structure that is diagnostic of the right-slip branching



Figure 21. Low oblique view of the 1954 fault scarp in northern Dixie Valley shown in previous photograph. The late afternoon sunlight provides shadows along the main scarp. The en echelon ramps of the middle distance indicate the right-slip displacement along the fault. Note the irregular nature of the fault scarp along the bedrock-alluvium contact



Figure 22. Low oblique view of 1954 Dixie Valley earthquake fault scarp (distance) and swarm of fissures (foreground). Low-sun angle photography revealed 90 percent more fissures and minor scarps than were observed in the field or with conventional photography

DEPARTMENT OF THE INTERIOR  
UNITED STATES GEOLOGICAL SURVEY

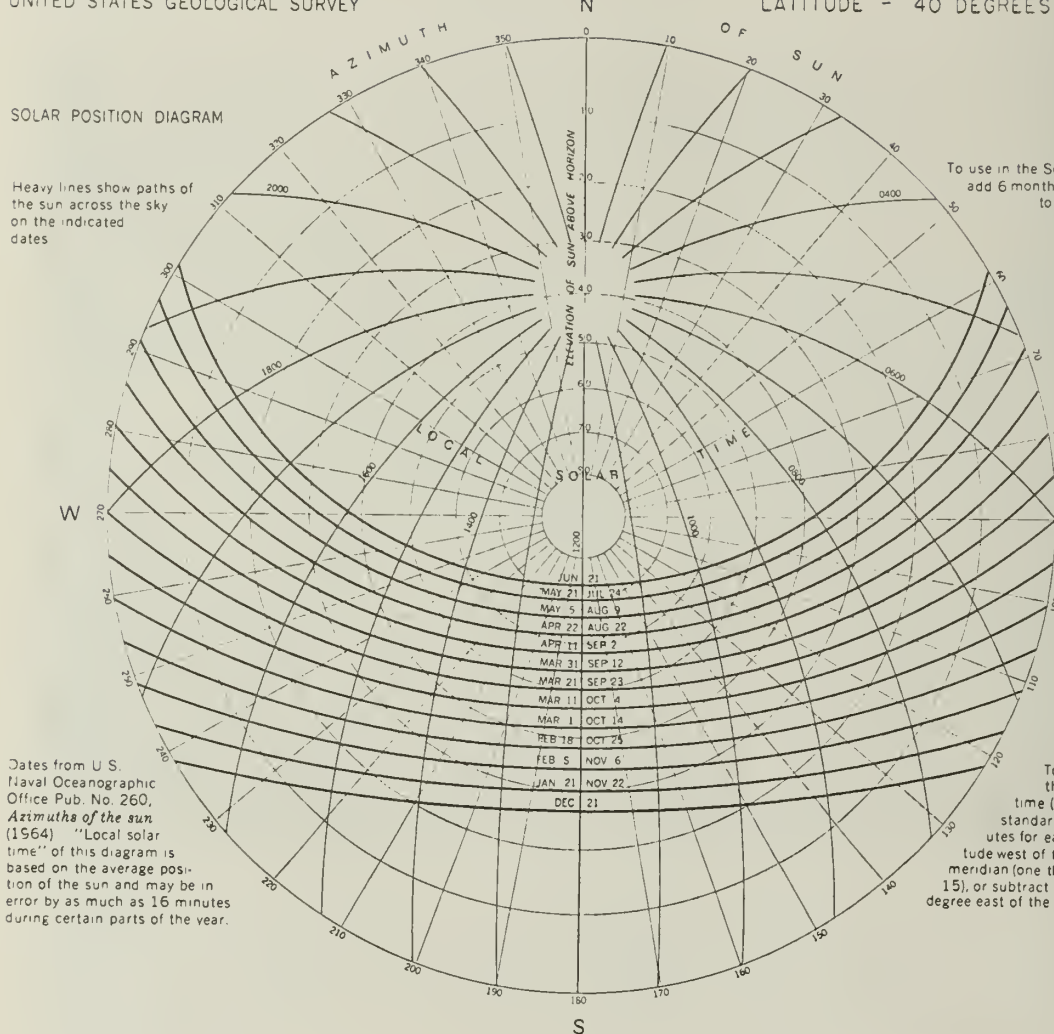


Figure 23. Diagram for use in determining optimum time of day and day of year for low-sun angle imaging



Figure 24. High oblique photograph of McGee Creek, California. This was taken at midday in the summer looking south toward the moraines at the mouth of McGee Canyon. Notice the subtle expression of the fault scarps under the high irradiation angle. The main scarp is marked by vegetation



Figure 25. Low oblique photograph of McGee Creek, California. Early morning irradiation of the north-facing fault scarps to show the greater detail obtained by highlighting (compare Figure 24). The steeper slopes of the scarp have higher intensity with the high incidence angle on the scarp



Figure 26. High oblique photograph of McGee Creek, California. Even after heavy winter snows the fault scarp is visible using late afternoon photography.

Sun irradiation is from the southwest



Figure 27. Low oblique photograph of McGee Creek, California. Fault detail is greatly enhanced using low irradiation angles provided by late afternoon photography in early fall. Compare fault detail above with Figure 24

27. Special enhancement of even greater contrast can be obtained by using light snow cover to supplement the sun-irradiation effect. Figure 28 shows effect of snow cover and sparse vegetation. Figure 29 shows the combined effect of fault shading and partial melting of snow cover. This combination enhances detection of strike-slip offset.

28. By planning photographic missions of specific faults according to the azimuth and scarp slope angle, it is possible to obtain images which are far superior to conventional imagery. The writers have done this for many specific faults, or for areas or regions of suspected faults. They prefer to accompany the aerial photography aircraft to verify from the air the ideal time to conduct the photography. Scarps across relatively flat terrain (floodplains, undissected alluvial fans, river terraces, plateau surfaces, etc.) should be imaged under very low irradiation angles to enhance subtle features. Generally, sun angles between  $10^{\circ}$  and  $25^{\circ}$  are optimum for this type of terrain. Below a sun angle of  $10^{\circ}$  (5:30 a.m. in the summer and 8:30 a.m. in the winter for a latitude of  $40^{\circ}$ , Figure 23) the shadows are too long for obtaining adequate detail and the light is too dim for obtaining sharp photographs. Beyond a sun angle of  $25^{\circ}$  the sunlight is grazing or irradiating older scarps which may have slopes between  $20^{\circ}$  and  $25^{\circ}$ . Scarps in hilly terrain (dissected plateaus, foothills, and dissected pediments) require higher illumination angles between  $20^{\circ}$  and  $35^{\circ}$ , and in mountainous or forested regions, sun angles greater than  $35^{\circ}$  may be needed. Solar position curves, available from the U. S. Geological Survey (USGS) (Figure 23), portray the sun angle and azimuth for various times of the day and year. Curves such as these are important for planning and reconnaissance stages of remote sensing investigations. During interpretation phases of a remote sensing investigation, the curves are useful in determining approximate slope angles. For example, on most aerial photographs and on Landsat imagery, the time and date of exposure is recorded on the image. By noting the time and date, approximate slope angles can be determined for scarps by noting the degree of shadowing present on the free face of the scarp. Grazing incidence angles occur



Figure 28. Low oblique photograph of two faults crossing alluvial fans with snow cover and enhancement



Figure 29. Low oblique view of 1954 Gold King fault on eastern edge of Dixie Valley, Nevada. The lack of snow on the south side of small ridges and the shading effect combine to make the scarp especially conspicuous and enhance the right-slip offset of the ridge crests and ravines on the right side of the photograph

on slopes with angles equal to the sun angle at the time the photograph was taken, steeper slopes cast a darker shadow, etc. This method is quick, but where accurate measurements are desired, a parallax bar or similar instrument should be used.

29. Active remote sensing systems such as radar (Part III) are widely used for the structural and topographic enhancement they provided through low irradiation angles.

30. Fault scarp enhancement by stream erosion. Faults which result in vertical offsets promote accelerated stream erosion of the upthrown block. This erosion results in flattening of the scarp crest and incision of stream channels on the upthrown block which stop abruptly at the scarp (Figure 30). In some cases, this erosion forms the main recognition features for scarp detection (Figures 31 and 32).

31. Stream erosion along scarps and the disruption of streamflow by faulting also provide clues to the presence of faults (Figures 33 and 34), although stream patterns are strongly influenced by other geologic



Figure 30. Vertical aerial photograph of Dixie Valley, Nevada. Accelerated erosion of the upthrown fault block in Dixie Valley provides a striking contrast in texture and pattern on different sides of the fault. The light-toned stripe extending from the upper left to lower center is a dirt road



Figure 31. Vertical aerial photograph of Owens Valley, California. The graben located just below the road (arrow) can be delineated by the incised stream erosion on the upthrown sides. The irradiation direction is parallel to the scarps but perpendicular to the streams making the change in erosion characteristics stand out



Figure 32. This vertical aerial photograph shows that preferential erosion of the upthrown block makes the fault at upper right stand out more than along the parallel faults to the lower left (USGS photograph)



Figure 33. Low oblique photograph of the San Andreas fault, California. Stream incision along the scarps within the San Andreas fault zone accentuate the scarps and the dextral slip characteristic of the fault  
(USGS photograph courtesy of R. E. Wallace)



Figure 34. Low oblique photograph of fault near Walla Walla, Washington. Disruption and funneling of the streams are caused by a fault which extends from left to right across the center of the photograph. Though there is no scarp, the fault can be traced on imagery for several kilometres because of its effect on drainages

structure as well and the mere presence of a linear stream channel should not be interpreted as a fault without additional information (Figure 35).

#### Truncation of geologic features

32. Repeated displacements along faults occasionally terminate or alter other geologic structures abnormally. These truncations, although not as obvious as some of the previously mentioned features, provide evidence for faulting (Figures 36 and 37). In many instances these features are manifest on small scale imagery such as Landsat more efficiently than on larger scale imagery. Grant and Cluff<sup>2</sup> discuss the effects of even relatively minor joints in controlling the development of conjugate sets of lineaments. They describe types of evidence for faults, including long linearity, alignments of drainage, offsets of linear features or patterns, and topographic relief. Since radar imagery is largely relief or topographic dependent with less tonal



Figure 35. High oblique photograph of a linear stream channel structurally controlled but not fault controlled. The stream flows along the axis of a syncline south of Ellensburg, Washington



Figure 36. Vertical aerial photograph showing arcuately shaped strand lines that have been truncated by the fault in the upper left corner and displaced by branching secondary scarps (center) (Soil Conservation Service (SCS) photograph)

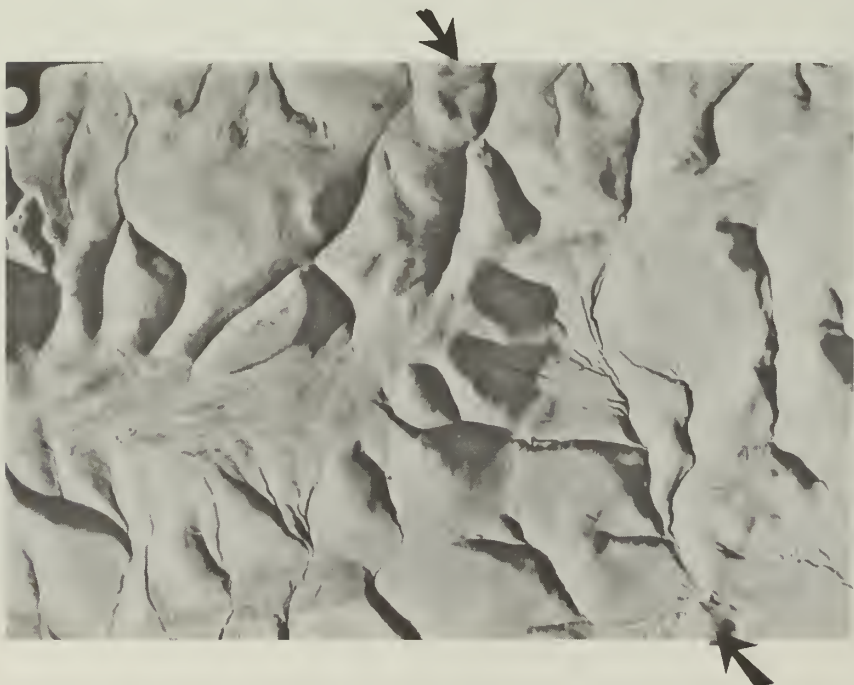


Figure 37. Vertical aerial photograph of the anti-clinal structure that has been distorted and truncated by drag along a fault extending from the lower right-hand side of the photograph to the upper center

expression than photography, the benefits are similar to those obtained by low irradiation angle photographs.

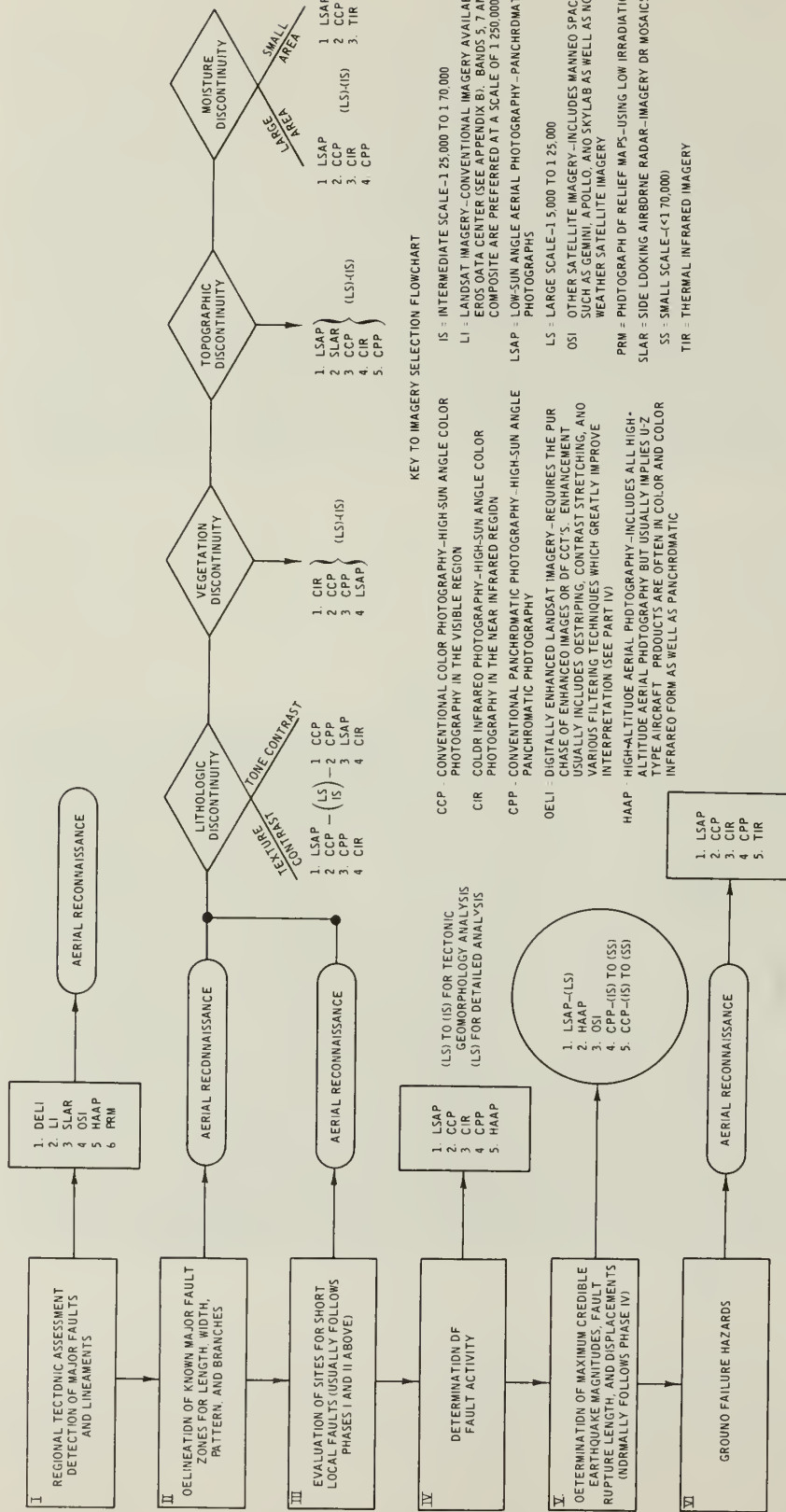
33. A general summary of important parameters for detection of active faults on imagery should include the following:

- a. Differences in surface reflectance.
- b. Stereoscopic parallax.
- c. Low irradiation angle.
- d. Spatial resolution.
- e. Thermal differences.
- f. Vegetation patterns.

34. The initial phase of work is to identify or detect the major faults and lineaments of the region. This phase of work generally has not been conducted for most parts of the country, even those that have well-known and thoroughly studied geology. This first phase of work generally embodies the kinds of remote sensing priorities of analysis that are listed for the Type I kind of evaluation of Table 1A. Following the identification of major structures, there is generally a need to conduct several kinds of fault studies by remote sensing and ground verification methods: Type II, detailed work on major fault zones; Type III, evaluation of more local faults near specific sites; or Type IV, determination of whether or not a specific fault is active. Each of these types of studies will call for a set of priorities for kinds of imagery to be used. A generalized listing for each of the above types of study is given in Table 1A, but the specific region being evaluated, the budget available for the study, the importance of the engineering structure, and the availability of imagery may require modification of the listing recommended in Table 1A. The terminology for activity or nonactivity and capability or noncapability is discussed by Slemmons and McKinney;<sup>8</sup> and Slemmons<sup>3</sup> has summarized the criteria for recognition and classification of active faults and their activity based on available data in his Tables 7 and 8. His Table 1 summarizes engineering design parameters (earthquake magnitude, intensity, acceleration, velocity, displacement, and duration) which can be determined from a complete fault evaluation. Studies of this type generally require

Table 1A

## Flow Diagram for Selection of Imagery



extensive literature and field evaluation, including low-sun angle aerial reconnaissance, detailed mapping of the main faults that have evidence for activity, exploratory trenching, possible geochronological studies to obtain recurrence rates or intervals, and review or collection of geophysical data.<sup>12,13</sup> The use of various types of small-scale imagery (Landsat, high-altitude or small-scale photography, and side-looking airborne radar (SLAR) is important to the earlier stages of regional work to provide the synoptic view to focus study on the major geologic structures. During the later stages of an earthquake hazard assessment, one should consider higher resolution, larger scale imagery, and the use of special enhancement techniques to improve resolution of the imagery. These trends form the basis of the priorities given in Table 1A.

Assessment of fault activity from imagery

35. Detailed studies of many active faults in the western United States demonstrate that it is possible with imagery evaluations coupled with geological, geophysical, and geochronological data to determine the activity and recurrence interval (time between fault events) to be expected along many fault zones. The imagery analysis generally is used as the first step to guide the more detailed ground studies. Repeated displacements along faults produce offsets in datable geologic features (formations or landforms), scarp erosion, and adjustments in fluvial systems across the fault to provide both the landforms and lithologic contrasts that are sensed by the remote sensing imagery and the ground data for estimating the amount of prehistoric fault displacements, rupture lengths, associate earthquake magnitudes, and recurrence intervals.

36. Offset of geologic features. Remote sensing imagery at various scales may be used effectively to assess the total amount of offset of geologic features along a fault. The ability of the sensing system to permit a unique identification of the datable geologic feature is the most important requirement of such an analysis. Since many geologic features are distributed over relatively large areas (as opposed to a scarp), several of the image enhancement techniques discussed in

Part IV can be used to make interpretation easier (specifically contrast stretching, density slicing, image addition or subtraction, or multi-spectral ratios). The offset of the geologic feature may be scaled from the imagery and divided by the most likely single-event displacement indicated from field relationships or by assumption to yield the approximate number of events which have occurred since the formation of the unit. The estimation of the most likely or average single-event displacement is generally determined after a ground verification program of evaluating geomorphic features and exploratory trenching data. The age of the feature (obtained by one or more of the many available age dating methods summarized by Packer et al.<sup>14</sup>) may then be divided by the number of events to obtain an approximate recurrence interval.

37. Erosional differences across and along scarps provide an additional means of assessing recurrence, if the lithologies are uniform and rates of weathering are constant, though the dating of the erosion sequences are generally not as easily accomplished as dating of geologic units.

38. Scarp erosion. The principal characteristics of young scarps are steep free face, debris slope, and a sharp break in slope at the crest of the scarp.<sup>15</sup> Scarps associated with older displacements tend to exhibit lower slopes resulting in a broader expression on imagery. Along faults which have had repeated displacements, scarps exhibit a composite or multiple-slope form (Figure 19) that displays a steplike tonal variation (Figure 38), on images recorded under low-sun angle conditions. The tones progress from narrow, dark tones associated with young scarps to broad, lighter tones associated with older, gentler slopes. Scarp angles can be approximated using the sun angle azimuth charts discussed previously (Figure 23). Follow-up detailed field studies using fault recurrence techniques developed by Slemmons, Cluff, Sherard, Wallace, and Clark<sup>1,3,9,10,13,15,16</sup> should be a basic ingredient in all fault recurrence evaluations.

39. Adjustments in fluvial systems. Records of repeated fault activity over long periods of time indicate that many faults do not have uniform rates of activity but show periods of accelerated activity,



Figure 38. Vertical aerial photograph showing fault swarm in Quaternary alluvium, about 10 miles south of Reno, Nevada. The photograph is taken with a sun angle azimuth of N77°E and 25° inclination. Scarps steeper than 25° cast deep shadows, if west-facing, and have bright highlighting where east-facing. More gentle west-facing slopes have lighter grays on less bright highlighting, respectively

followed by periods of quiescence. These intermittent periods of activity may be distinguished on imagery by variations in the amount of erosion which has taken place along the scarp. An excellent example of periodic activity of an active fault can be seen along the Watsatch fault near Springville, Utah (Figure 39). The fault in this area appears to represent at least three periods of activity, as shown by the sets of triangular facets, followed by periods when the fault scarp was eroded by streams. The size of the youngest facets at the base of the range relative to the older facets suggests that currently the fault is experiencing an active period, and future displacements along the fault can be expected.

40. Wallace\* discusses the migration of stream erosion of the upthrown block as a potential dating technique. He found that channel regrading at the crest of a scarp (knickpoint) may be preserved for hundreds of years depending on climate and size of the channel. At places in Pleasant Valley, Wallace documented the presence of multiple knickpoints which provide evidence of multiple displacements on the scarp, some of which do not show evidence of bevelling.

41. Geomorphic evidence of late Pleistocene and Holocene movements along faults include fault ruptures of: (a) alluvial fans, (b) strath terraces, (c) playas, and (d) rock falls from fault scarps onto Pleistocene or Holocene surfaces.\*\* In areas where scarps are not present, Bull<sup>17</sup> has developed a fault classification system based on the adjustments that tectonic activity causes to fluvial systems crossing the fault. His classifications are as follows:

- a. Class 1 (tectonically active). Terrains generally characterized by mountain-front sinuosities (see Bull<sup>17</sup> for definition) from 1.0 to 1.6, unentrenched alluvial fans, elongate drainage basins having narrow valley floors and steep hill slopes. Class 1 terrains are characteristic of areas exhibiting active faulting or folding during the Pleistocene and Holocene (Figure 40).
- b. Class 2 (moderate to slightly active). Terrains generally characterized by mountain-front sinuosities from

---

\* R. E. Wallace, unpublished paper on the 1915 Pleasant Valley Earthquake.

\*\* W. B. Bull, personal communication.



Figure 39. Low oblique photograph of the Wasatch fault near Springville, Utah. Triangular facets are common indicators of normal faulting. Here at least three sets of facets indicate a pulsating type of activity along the fault with periods of intense activity separated by periods of quiescence. The lack of significant erosion of the youngest facets may indicate that this portion of the fault is in an active period. The V-shaped gullies, lack of sinuosity of the mountain front, and active deposition of alluvial fans indicate its activity



Figure 40. Vertical aerial photograph (Stovepipe Wells, California) of the edge of the Grapevine Mountains (upper right) exemplifying an active tectonic area. Note the straight mountain front, narrow "V" shaped stream canyons, unentrenched alluvial fans. This range corresponds to a Class 1 tectonic terrain after Bull 17 (USGS photograph prepared by the University of Illinois Committee on Aerial Photography)

1.4 to 3, permanent entrenchment of alluvial fans, large drainage basins which are more circular than Class 1, steep hill slopes, and valley floors which are wider than the floodplain. Class 2 terrains are characteristic of areas which were active in the Pleistocene but not in the Holocene (Figure 41).

- c. Class 3 (tectonically inactive). Terrain generally characterized by mountain-front sinuosities from 2 to greater than 7, pedimented mountain fronts and embayments, and few large integrated stream channels in mountains which have steep slopes associated only with very resistant rocks (Figure 42).

42. In all of the dating techniques above, both synoptic and detailed imagery scales are useful and several of the spectral regions and enhancement techniques can often be applied to aid in the analysis.

#### Types of active faults

43. Once an assessment has been made regarding the age and activity of the faults in the vicinity of a project, the total length and type of faulting associated with active faults in the site region should be investigated. The relative movement on a fault may be vertical, horizontal, or oblique<sup>18</sup> and will strongly affect the character of ground motion at a site. Most of the documented fault displacements fall into one of the following three main categories: normal-slip, reverse-slip, or strike-slip. The surface fracturing associated with movement along these faults is diagnostic of fault type and generally can be evaluated on large-scale imagery which accentuates topographic features.

44. Normal-slip faults. Normal faults are characterized by a combination of vertical and extensional displacements. Due to the extensional component, normal faults tend to have complex fracture patterns (Figure 43) consisting of a wide zone of scarps, fissures, and graben. The dip of the fault plane is generally steep (approximately 60°) yielding an irregular surface expression over hilly terrain (see Slemmons,<sup>3</sup> Figures A-14, A-15, A-17, A-18). Major active normal faults are characterized by steep, faceted fault blocks (Figure 44), which may show several periods of activity and quiescence. Other major landforms apparent on images include features listed in Table 1B.

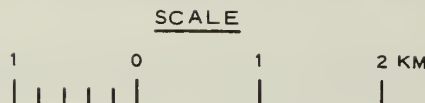


Figure 41. Vertical aerial photograph of Mojave Desert, California, illustrating a Class 2 tectonic terrain.<sup>17</sup> It shows an embayed mountain front, permanent entrenchment of alluvial fans, circular drainage basins, and flatter valley floors than Class 1 terrains

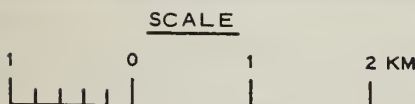


Figure 42. Vertical aerial photograph of Mojave Desert, California, showing an area equivalent to a Class 3 tectonic terrain.<sup>17</sup> This deeply embayed, pedimented range front and slopes associated with resistant rocks are typical of a tectonically inactive range



Figure 43. Vertical aerial photograph of the Wasatch fault, Utah. The complex shattered zone along the Wasatch fault is due to a combination of vertical and extensional movement. Both front-facing (light) and back-facing scarps (shadow) can be seen as well as scarps within the graben. The pond at the lower center of the photograph has been dammed to serve as a water supply



Figure 44. Low oblique photograph of the Wasatch fault near Springville, Utah. A closer view than Figure 39, this photograph exemplifies the irregular character of the most recent fault scarp

Table 1B  
Common Geomorphic Features of Normal-Slip Faults

Geomorphic Feature	Ability of Imagery to Resolve Feature*			Example of Geomorphic Feature
	Synoptic Scale (Landsat)**	Intermediate Scale**	Detailed Large Scale**	
1. Scarps				
a. Simple scarps	+ (for larger scarps)	+	+	Figures 27, 28, 44
b. Fissure scarps or fissure traces	0	0	+	Figure 22
c. Trench-trace scarps or graben-trace scarps	Only if scarp is high, vegetation is sparse, and sun angle is low	+ if large feature (>1 m)	+	Figure 43
d. Longitudinal-trace scarps or step-trace scarps	Only if scarp is high, vegetation is sparse, and sun angle is low.	+ if large feature (>1 m)	+	Figures 20, 21
e. Subsidence-trace scarp	0	0	+	
f. En echelon scarps	0	+	+	Figures 20, 21
g. Beveled scarps	0	0	+	Figure 38
2. Triangular facets, faceted spurs, or battered facets	+	+	+	Figures 39, 44
3. Zigzag faults on orthogonal fracture systems	+	+	+	Figure 14
4. Arcuate scarps, especially at terminations or in deep, poorly consolidated sediments	0	0	+	
5. Rejuvenated valley or ravine floors with terraces upstream from scarps	0	+	+	Figure 40
6. Wine glass canyons	+	+	+	Figure 40
7. Alluvial aprons, fans, breached fans	0	+ if large (>1 m)	+	Figure 40
8. Ramps (oblique slip)	0	0	+	
9. Groundwater effect: Linear spring alignments, differential water tables, hot or warm springs	+	+	+	Figures 11, 17
10. Volcanic centers	+	+	+	

\* + indicates that the feature is generally resolvable on imagery. 0 indicates that the feature is not generally resolvable on imagery.

\*\* For the purpose of this paper the terms synoptic or large scale apply to imagery of <ca 1:75,000, intermediate scale of ca 1:25,000 to 1:75,000, and detailed on large scale of ca 1:5,000 to 1:25,000.

45. Reverse-slip faults. Reverse faults are characterized by combined vertical and compressional displacements. Reverse faults typically have a wide range of dip angle. Low-dipping faults tend to exhibit a very sinuous surface expression over hilly to flat terrain (Figure 45) (see Krinitzsky,<sup>6</sup> Meckering Fault Figure 14). Reverse fault scarps are difficult to locate precisely due to widespread landslides which commonly cover the fault trace (see Slemmons,<sup>3</sup> Figure A-22). Surface fracturing is characterized by folding or distortion and displacements along subsidiary faults and fractures within the upthrown block (Figure 46). The fracturing on the upthrown block of a reverse fault is commonly spread over a wider area (tens of miles) than is common with normal-slip and strike-slip faults. The main geomorphic features are listed in Table 2. Reverse-slip faults commonly have their main trace near the base of mountains.

46. Strike-slip faults. These faults are characterized by horizontal movement with little or no vertical movement. The fault planes



Figure 45. View of major fault zone, New Zealand. The fault is a high-angle reverse-oblique fault zone with right-oblique slip. The main fault trace is at the break in slope along the central part of the photograph. The high angle of dip into the mountain is indicated by the trace of the fault zone at the far right side of the photograph



Figure 46. Mole-track, or bull-dozed appearance along a trace of the 1971 San Fernando surface fault traces. The fault plane dips into the far side of the fault zone at a moderate angle (photograph courtesy of Clarence Allen)

Table 2  
Common Geomorphic Features of Reverse-Slip Faults

Geomorphic Feature	Ability of Imagery to Resolve Feature*			Example of Geomorphic Feature
	Synoptic Scale (Landsat)**	Intermediate Scale**	Detailed Large Scale**	
1. Fault scarps	+ if large 10's of m	+	+	Figures 45, 46
2. Blunted or oversteepened base of hills at fault	+	+	+	Figure 45
3. Talus and landslide alignments	0	+	+	Slemmons <sup>3</sup> (Figure A-22)
4. Mole-track or bulldozed traces	0	+	+	Figure 45
5. Graben or fissure swarms on up-thrown block	0	+ if large (>1 m)	+	Slemmons <sup>3</sup> (Figure A-23)
6. Upstream terraces	0	+	+	
7. Drag warping of downfaulted block fans, terraces, or sediments	0	0	+	Slemmons <sup>3</sup> (Figure A-23)
8. Sinuous traces on planar surfaces	+ if on scale of km	+	+	
9. Single traces or multiple, widely separated (short cut) traces	0	+ if large (>1 m)	+	

\* + indicates that the feature is generally resolvable on imagery. 0 indicates that the feature is not resolvable on imagery.

\*\* For the purpose of this paper, the terms synoptic or large scale apply to imagery of ca 1:75,000, intermediate scale of ca 1:25,000 to 1:75,000, and detailed on large scale of ca 1:5,000 to 1:25,000.

generally have a nearly vertical dip and exhibit linear or gently curved fault traces on flat to hilly terrain. Fault breaks tend to be relatively simple with some branching or secondary scarps along the main break. En echelon and Riedel patterns are common. Typical geomorphic features are listed in Table 3. The most important elements needed to detect, delineate, and characterize active faults by imagery analysis are:

- a. High spatial resolution.
- b. Stereoscopic parallax.
- c. Low irradiation angle.
- d. Synoptic coverage.

The effect of image scale and sun angle is important to the interpretation of fault scarp type and activity as is demonstrated on Figures 47a through 47c.

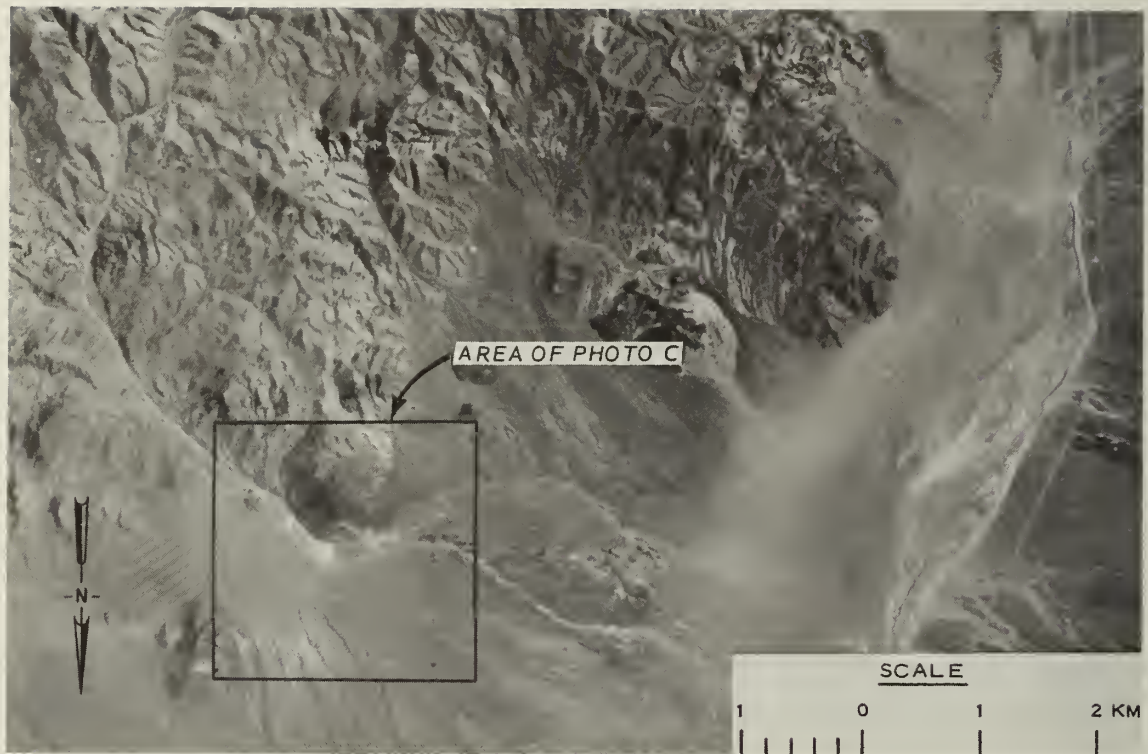
Amount and length of potential fault displacements

47. The most productive method of predicting the amount and length of faulting to be expected during a single event along an active fault involves mapping the amount and length of faulting which occurred during past events. Individual fault breaks during a single earthquake have ranged in length from less than a kilometre to several hundred kilometres, and ranged in displacement from a few millimetres to greater than 10 m.<sup>3,9</sup> The maximum length of fault break occurring during a single event is usually only a fraction of the length of the fault, ranging from approximately 20 to 30 percent for strike-slip faults to as high as 50 percent and greater for reverse faults. One example of surface faulting over the entire length is reported by Matsuda<sup>19</sup> and Allen<sup>20</sup> for the magnitude 8 earthquake of 1891 in Mino-Owari, Japan. Detailed descriptions of methods for determining the full fault length and for determining the maximum credible earthquake or maximum earthquake is given by Slemmons.<sup>3</sup> High resolution imagery possessing parallax and oblique irradiation, coupled with detailed geological and geo-physical studies, is necessary for determining the total fault length and the amount of potential fault displacements.

Table 3  
Common Geomorphic Features of Strike-Slip Faults

Geomorphic Feature	Ability of Imagery to Resolve Feature*			Example of Geomorphic Feature
	Synoptic Scale (Landsat)**	Intermediate Scale**	Detailed Large Scale**	
1. Scarp, eroded or battered scarp	+	+	+	
2. Bench	+ if >10 m	+	+	
3. Linear canyon, gully, swale, trench, trough, stream, or valley	+	+	+	
4. Pond, depression, swampy depression, playa, sag pond, swampy trench	+ if ~100 m and filled with water or vegetation	+	+	
5. Lateral stream or drainage channel offset	+ if >100's m	+	+	Figure 33
6. Fault gap, notch, or saddle	+ if >100 m	+	+	
7. Trench, wedge		+	+	Figure 33
8. Offset ridgeline or hill		+	+	
9. Linear or elongated ridge		+	+	Figure 33
10. Trough		+	+	Figure 33
11. Ponded alluvium		+	+	Figure 11
12. Shutter ridge		+	+	
13. Scarplet	0	+ if >1 m	+	
14. Swale	0	0	+	
15. Aligned vegetation or linear boundary	+	+	+	
16. Side hill trench or trough	0	+	+	
17. Fault valley	+	+	+	
18. Fault trace	0	+	+	

\* + indicates that the feature is resolvable on imagery. 0 indicates that the feature is not resolvable on imagery.  
 \*\* Synoptic (small) scales for this chart are scales of ca 1:75,000 to 1:1,000,000, intermediate (conventional mapping) scales of ca 1:25,000 to 1:75,000, and detailed (large) scales of ca 1:5,000 to 1:25,000.



a. This photograph was taken by the USGS with high-sun angle irradiation. The high irradiation angle is optimum for recording subtle tone contrasts between different geologic units; however, the structure and topography appear subdued and the scale is too small for detailed fault studies

Figure 47. Vertical aerial photographs of the Louderback Mountains, east side of Dixie Valley, Nevada (sheet 1 of 3)



b. Same area and same scale as (a) but with a lower sun irradiation angle. Notice that the lower irradiation angle results in an accentuation of topography and structure and more detail regarding stream patterns is presented. However, the subtle tonal variations visible in (a) are not reproduced well on this image

Figure 47 (sheet 2 of 3)



c. Enclosed area shown of (a) and (b). The larger scale and low irradiation angle make it possible to distinguish the scarp crossing the fan on the lower right-hand corner of the photograph which was not possible on (a) and (b). However, the lithologic interpretation on this photograph is poorer than (a)

Figure 47 (sheet 3 of 3)

### Crustal Tilting or Distortion

48. Large fault breaks and major earthquakes are accompanied by deformation of the surrounding ground surface.<sup>21</sup> This deformed area may correspond to relatively narrow, elongate areas along strike-slip faults, or to large areas extending as far as several hundred kilometres from the low-dipping reverse fault of the 1964 Alaskan earthquake.<sup>22,23</sup> Image of localized distortion and tilting may be recorded using the parameters listed under topographic variations. Large areal deformations require a more synoptic coverage and the use of multiday imagery (Figure 48). Localized evidence of crustal tilting, such as raised, lowered, or folded ocean or lake shorelines, stream terraces, or deformed alluvial plains, requires a combination of large-scale, high resolution imagery and synoptic, lower resolution imagery. In most cases, adequate topographic control or geodetic leveling is necessary for detailed analyses.

### Ground Failure

49. The analysis of ground failure can generally be considered in two parts: landslides or rockslides, and liquefaction.

#### Landslides and rockslides

50. The magnitude 6.4 San Fernando earthquake of 1971 initiated or reactivated over 1000 landslides and rockfalls (Figure 49).<sup>24</sup> Larger earthquakes are capable of generating even greater numbers of landslides, sometimes at distances exceeding 600 km from the fault.

51. One of the most important indications of potential landslide problems is the existence of areas having over-steepened slopes, formations characterized by unstable materials, and particularly areas having geomorphic expressions of previous failures. Thus, recognizing the presence of landslide debris or landslide scars is the most effective way of assessing areal landslide risk.

52. Landslide debris is generally characterized by an irregular and disrupted topographic expression (Figure 50). The topography tends



Figure 48. National Oceanic and Atmospheric Administration (NOAA) weather satellite image of the State of Washington. The east-west trending Yakima anticlines (lower right quadrant) are not as apparent on this image as they are in Figure 14 due to the lower spatial resolution and early morning sunlight. In this image the deformation of the Columbia Plateau appears to be dominated by ramplike upwarps and broad folds. The deformation appears to decrease from west to east suggesting that the plateau has responded to the general uplift of the Cascades and not to specific structural features within the Cascades. (Image processed at Battelle Northwest Laboratory and provided through the courtesy of Mr. David D. Tillson, Washington Public Power Supply System)

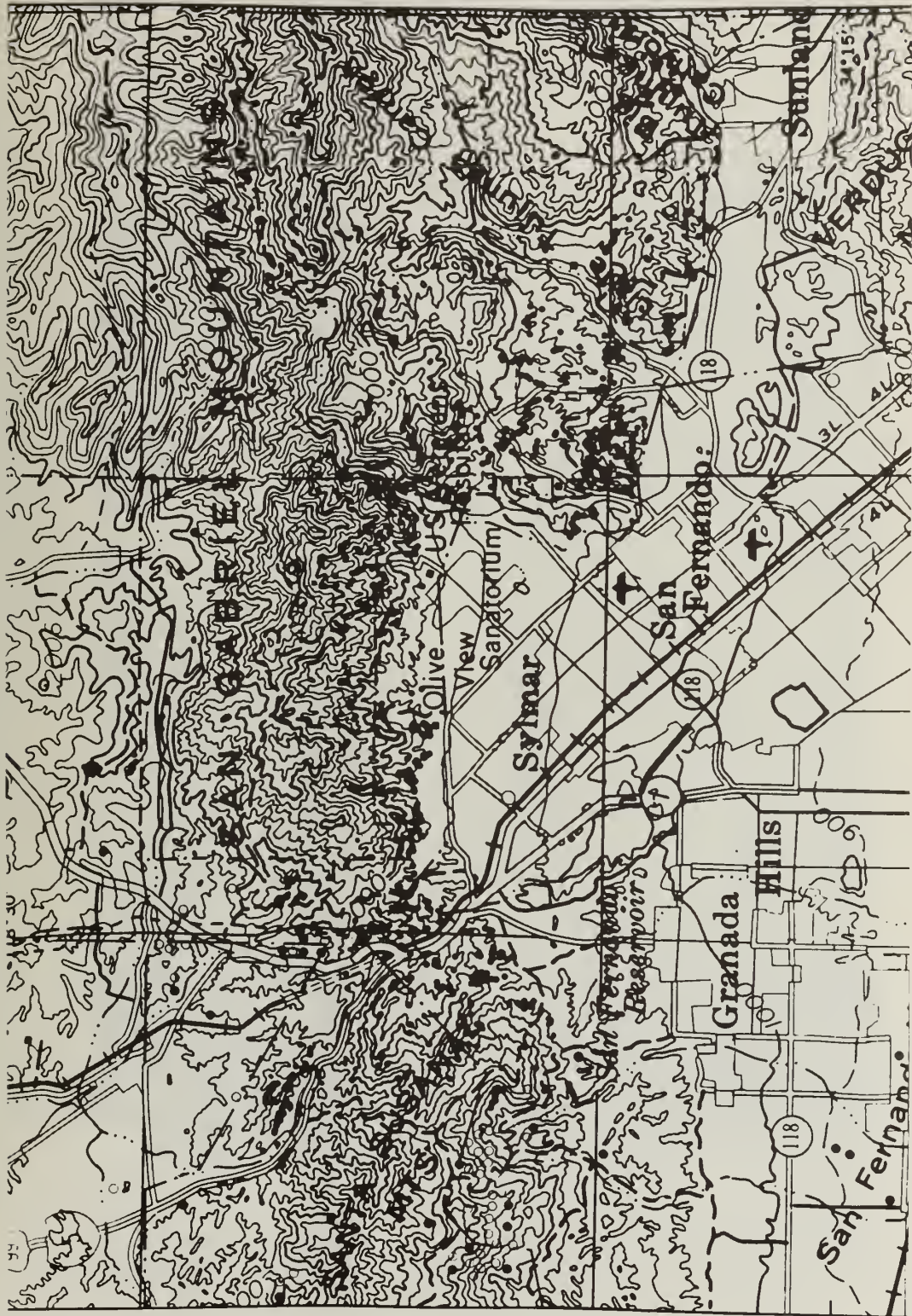


Figure 49. Plot of landslides triggered by the San Fernando, California, earthquake, 1971 24



Figure 50. Vertical aerial photograph of the Gros Ventre landslide, Wyoming. This slide typifies the highly irregular and disrupted topographic expression of landslide debris. This landslide is historical, but the characteristic features will persist for hundreds or thousands of years

to be hummocky and the edges of the slide tend to be globular or lobate (Figures 51 and 52). Slide scars are commonly arcurate in shape, or more rarely are angular where structurally controlled and often form graben at the head of the slide (Figures 53 and 54). Figure 55 classifies the types of landslides that may result from earthquakes.

53. Commonly landslide debris forms many enclosed basins, and in humid climates water is ponded on the slide mass and the debris is very moist. Older slides will develop preferential vegetation assemblages which correspond to local variations in moisture content within the slide mass. The slide scar will be characterized by vegetation of a younger age than surrounding areas or by a lack of vegetation.

54. For landslide identification on imagery, advantage should be taken of the topographical features, reflectance differences of vegetation, and the cooling effect of moisture. The following are the most important characteristics for detection of landslides or rockslides on imagery:



Figure 51. Vertical aerial photograph of a large landslide near Corfu, Washington. The disrupted surface topography of the slide debris is characteristic of a relatively fluid slide mass. Note the hummocky texture of the slide mass in the lobate edges at the lower portion of the photograph



Figure 52. Vertical photograph of a landslide near Corfu, Washington, showing different ages of landslides. The largest slide mass is old enough to have a well-developed drainage pattern on the slide debris. Near the lower edge of the image, a younger, smaller slide has occurred exhibiting a fresher morphology. This helps to point out the continued unstable nature of landslides even after hundreds or thousands of years

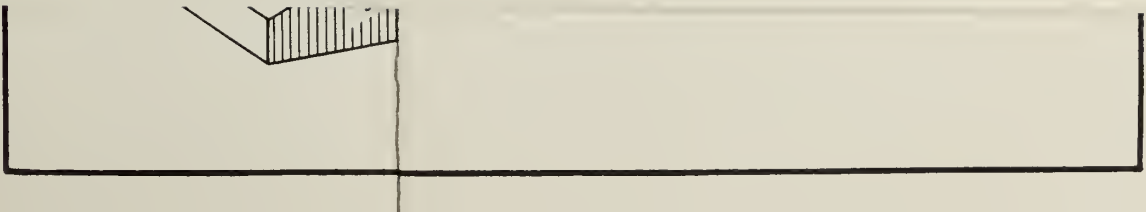


Figure 53. Vertical aerial photograph of a landslide in New Mexico. The arcuate slide scar and hummocky terrain typify landslide hazards



Figure 54. Low oblique photograph of graben formation at the head of this slide near Cirfu, Washington. The graben is much more extensive than usual. The slide is old and probably stable under present conditions





**I FALLS**  
Mass in motion travels most of the distance through the air. Includes free fall movement by leaps and bounds; and rolling of fragments of bedrock or soil.

**II TOPPLES**  
Movement due to forces that cause an overturning moment about a pivot point below the center of gravity of the unit. If unchecked, will result in a fall or slide.

**III SLIDES**  
Movement involves shear displacement along one or more surfaces or within a relatively thin zone which are visible or may reasonably be inferred.

**A ROTATIONAL**  
Movement due to forces that cause a turning moment about a point above the center of gravity of the unit. Surface of rupture concave upward.

**B TRANSLATIONAL**  
Movement predominantly along more or less planar or gently undulating surfaces. Movement is usually controlled by surfaces of weakness such as faults, joints, bedding planes, variations in shear strength between layers of bedded deposits, or by the contact between firm bedrock and overlying detritus.

**IV LATERAL SPREADS**  
Distributed lateral extension movements in a fractured mass.

A. Without a well defined controlling basal shear surface or zone of plastic flow (predominantly in bedrock).  
B. In which extension of rock or soils results from liquefaction or plastic flow of subjacent material.

**V FLOWS**

**A IN BEDROCK**  
Includes specially continuous deformation and vertical as well as deep creep. Involves extremely slow and generally noncohesive differential movements strong relatively intact units. Movements may:  
1. Be along many shear surfaces that are apparently not connected, or  
2. Result in folding, bending, or buckling.  
3. Roughly simulate thinnings of viscous fluids in distribution of velocities.

**B IN SOIL**  
Movement within displaced mass such that the form taken by moving material or the apparent distribution of velocities and displacements resembles those of viscous fluids. Slip surfaces within moving material are usually vertical or are short lived. Boundary between moving mass and material generally has a sharp surface of differential movement or a zone of distributed shear. Movement ranges from extremely rapid to extremely slow.

**VI COMPLEX**  
Movement is by a combination of one or more of the five principal types of movement described above. Many landslides are complex, although one type of movement generally dominates over the others at certain times within a slide or at a particular time.

**EXAMPLES**

**Figures and Labels:**

- Fig 21-a-1**: ROCK FALL - DEBRIS FLOW - ROCK-FALL AVALANCHE - Extremely rapid. After Heim (2-58) from Switzerland, 1981.
- Fig 21-a-2**: SLUMP AND TOPPLE - Zaruba (2-192).
- Fig 21-a-3**: ROCK SLIDE - ROCK FALL - Namok, Pakse, River (2-76).
- Fig 21-a-4**: CAMBERING AND VALLEY BULGING.
- Fig 21-a-5**: SLIDE - EARTH FLOW - Earth flow.
- Fig 21-b-1**: ROCK FALL - Extremely rapid. Fig 21-b-2: DEBRIS FLOW - Very rapid. Fig 21-b-3: DEBRIS TOPPLE - Fig 21-b-4: DEBRIS SLUMP - Fig 21-b-5: EARTH SLUMP - Fig 21-b-6: EARTH TOPPLE.
- Fig 21-c-1**: DEBRIS FLOW - Fig 21-c-2: SOIL CREEP - Fig 21-c-3: DEBRIS AVALANCHE - Fig 21-c-4: SOIL CREEP - Extremely slow.
- Fig 21-d-1**: ROCK TOPPLE - Daffy and Warren (2-27).
- Fig 21-d-2**: ROCK SLIDE - Fig 21-d-3: ROCK SLIDE - Nemcek (2-181) after Beck (2-5).
- Fig 21-e-1**: DEBRIS TOPPLE - Fig 21-e-2: DEBRIS SLUMP - Fig 21-e-3: EARTH SLUMP - Fig 21-e-4: EARTH TOPPLE.
- Fig 21-f-1**: EARTH FLOW - Fig 21-f-2: RAPID EARTH FLOW - LOUD, CLOUDY - Fig 21-f-3: EARTH FLOW - Zara and Manci (2-78) - Fig 21-f-4: DRY SAND FLOW - Rapid to very rapid. After Heim (2-58) from Switzerland, 1981.
- Fig 21-g-1**: DEBRIS FLOW - Fig 21-g-2: SOIL CREEP - Fig 21-g-3: DEBRIS AVALANCHE - Fig 21-g-4: SOIL CREEP - Extremely slow.
- Fig 21-h-1**: DEBRIS SLUMP - Fig 21-h-2: EARTH SLUMP - Fig 21-h-3: EARTH TOPPLE.
- Fig 21-i-1**: EARTH BLOCK SLIDE - Hanssen (2-27).
- Fig 21-j-1**: DEBRIS FLOW - Fig 21-j-2: SOIL CREEP - Fig 21-j-3: DEBRIS AVALANCHE - Fig 21-j-4: SOIL CREEP - Extremely slow.
- Fig 21-k-1**: DEBRIS SLUMP - Fig 21-k-2: EARTH SLUMP - Fig 21-k-3: EARTH TOPPLE.
- Fig 21-l-1**: EARTH BLOCK SLIDE - Hanssen (2-27).
- Fig 21-m-1**: JAHN (2-73) - Fig 21-m-2: ZARUBA and MANDI (2-152) - Fig 21-m-3: OSTAFITZU (2-77).
- Fig 21-n-1**: DEBRIS FLOW - Fig 21-n-2: SOIL CREEP - Fig 21-n-3: DEBRIS AVALANCHE - Fig 21-n-4: SOIL CREEP - Extremely slow.
- Fig 21-o-1**: WET SAND or SILT FLOW - Fig 21-o-2: RAPID EARTH FLOW - LOUD, CLOUDY - Fig 21-o-3: EARTH FLOW - Zara and Manci (2-78) - Fig 21-o-4: DRY SAND FLOW - Rapid to very rapid. After Heim (2-58) from Switzerland, 1981.
- Fig 21-p-1**: NAMOK, Pakse and River (2-116) - Fig 21-p-2: ZACHINSKY (2-34) - Fig 21-p-3: ZACHINSKY (2-34) - Fig 21-p-4: RAYON and DODR (2-37).
- Fig 21-q-1**: DEBRIS FLOW - Fig 21-q-2: SOIL CREEP - Fig 21-q-3: DEBRIS AVALANCHE - Fig 21-q-4: SOIL CREEP - Extremely slow.
- Fig 21-r-1**: EARTH FLOW - Fig 21-r-2: RAPID EARTH FLOW - LOUD, CLOUDY - Fig 21-r-3: EARTH FLOW - Zara and Manci (2-78) - Fig 21-r-4: DRY SAND FLOW - Rapid to very rapid. After Heim (2-58) from Switzerland, 1981.
- Fig 21-s-1**: DEBRIS FLOW - Fig 21-s-2: SOIL CREEP - Fig 21-s-3: DEBRIS AVALANCHE - Fig 21-s-4: SOIL CREEP - Extremely slow.
- Fig 21-t-1**: EARTH FLOW - Fig 21-t-2: RAPID EARTH FLOW - LOUD, CLOUDY - Fig 21-t-3: EARTH FLOW - Zara and Manci (2-78) - Fig 21-t-4: DRY SAND FLOW - Rapid to very rapid. After Heim (2-58) from Switzerland, 1981.
- Fig 21-u-1**: EARTH FLOW - Fig 21-u-2: RAPID EARTH FLOW - LOUD, CLOUDY - Fig 21-u-3: EARTH FLOW - Zara and Manci (2-78) - Fig 21-u-4: DRY SAND FLOW - Rapid to very rapid. After Heim (2-58) from Switzerland, 1981.
- Fig 21-v-1**: EARTH FLOW - Fig 21-v-2: RAPID EARTH FLOW - LOUD, CLOUDY - Fig 21-v-3: EARTH FLOW - Zara and Manci (2-78) - Fig 21-v-4: DRY SAND FLOW - Rapid to very rapid. After Heim (2-58) from Switzerland, 1981.
- Fig 21-w-1**: EARTH FLOW - Fig 21-w-2: RAPID EARTH FLOW - LOUD, CLOUDY - Fig 21-w-3: EARTH FLOW - Zara and Manci (2-78) - Fig 21-w-4: DRY SAND FLOW - Rapid to very rapid. After Heim (2-58) from Switzerland, 1981.
- Fig 21-x-1**: EARTH FLOW - Fig 21-x-2: RAPID EARTH FLOW - LOUD, CLOUDY - Fig 21-x-3: EARTH FLOW - Zara and Manci (2-78) - Fig 21-x-4: DRY SAND FLOW - Rapid to very rapid. After Heim (2-58) from Switzerland, 1981.
- Fig 21-y-1**: EARTH FLOW - Fig 21-y-2: RAPID EARTH FLOW - LOUD, CLOUDY - Fig 21-y-3: EARTH FLOW - Zara and Manci (2-78) - Fig 21-y-4: DRY SAND FLOW - Rapid to very rapid. After Heim (2-58) from Switzerland, 1981.
- Fig 21-z-1**: EARTH FLOW - Fig 21-z-2: RAPID EARTH FLOW - LOUD, CLOUDY - Fig 21-z-3: EARTH FLOW - Zara and Manci (2-78) - Fig 21-z-4: DRY SAND FLOW - Rapid to very rapid. After Heim (2-58) from Switzerland, 1981.

**NOMENCLATURE OF THE PARTS OF A SLUMP EARTH FLOW**  
(See drawing at left)

**MAIN SCARP**—A steep surface on the undisplaced ground around the periphery of the slide, caused by the movement of slide material away from undisturbed ground. The projection of the scarp surface under the displaced material becomes the surface of rupture.

**MINOR SCARP**—A steep surface on the displaced material produced by differential movement within the sliding mass.

**HEAD**—The upper part of the slide material along the contact between the displaced material and the main scarp.

**TOP**—The highest point of contact between the displaced material and the main scarp.

**TOE OF SURFACE OF RUPTURE**—The intersection (sometimes buried) between the lower part of the surface of rupture and the original ground surface.

**TOE**—The margin of displaced material most distant from the main scarp.

**TIP**—The point on the toe most distant from the top of the slide.

**FOOT**—That portion of the displaced material that lies downvalley of the toe of the surface of rupture.

**MAIN BODY**—That part of the displaced material that overlies the surface of rupture between the main scarp and toe of the surface of rupture.

**FLANK**—The side of the landslide.

**GROWTH**—The material that is still in place, physically undisplaced and adjacent to the highest parts of the main scarp.

**ORIGINAL GROUND SURFACE**—The slope that existed before the movement which is being considered took place. If it is the surface of an older landslide, that fact should be stated.

**LEFT AND RIGHT**—Compass directions are preferable in describing a slide, but if they are used they refer to the slide as viewed from the crown.

**SURFACE OF SEPARATION**—The surface separating displaced material from stable material but not known to have been a surface on which failure occurred.

**DISPLACED MATERIAL**—The material that has moved away from its original position on the slope. It may be in a deformed or undeformed state.

**ZONE OF SEPARATION**—The area within which the displaced material lies below the original ground surface.

**ZONE OF ACCUMULATION**—The area within which the displaced materials above the original ground surface.

The rate of material movement is denoted according to its rate prior to initial movement or if the type of movement changes according to its rate at the time of the change in movement. Thus, the first slide began as a rock slide and rock fall in bedrock, but at the same time a flowing type of movement started that material was an unconsolidated mass of extremely rapidly moving debris.

Approximate ranges of rates of movement are according to the scale below:

1 sec	Extremely rapid
10 sec	Very rapid
1 min	Fast
1 hr	Slow
1 day	Extremely slow
1 month	Very slow
1 year	Slow
10 years	Extremely slow

Figure 55. Classification of landslides

- a. Low irradiation angles
- b. Spatial resolution.
- c. Stereoscopic parallax.
- d. Reflectance variations in vegetation and soil.
- e. Temperature changes due to moisture.

#### Liquefaction

55. Liquefaction frequently accompanies strong earthquake shaking of saturated cohesionless soils and may accompany even minor shocks.<sup>25</sup> Studies have shown that liquefaction does little to compact a soil and sites which have exhibited liquefaction in the past are likely candidates for future liquefaction failure during earthquakes.

56. Liquefaction of surface or near face soils generally produces sand boils and flows which are readily discernable on large scale aerial photographs (Saucier,<sup>26</sup> Figures 8 and 9). Where deeper deposits exist and where slopes provide an avenue for liquified soils to move downslope, graben, tilted blocks, and fissures often mark the location of potential liquefaction hazards even though erosional forces may have subdued them (Figure 56). The weathering and erosion processes are generally slow, and the geomorphic and textural evidence for liquefaction features persists from hundreds to tens of thousands of years. Thus it is possible to identify areas of potential liquefaction by using imagery having the following attributes:

- a. Low irradiation angle.
- b. Stereoscopic parallax.
- c. High spatial resolution (fraction of a metre).
- d. Reflectance changes in vegetation.

#### Tsunamis

57. Tsunamis are caused by an impulse source within a body of water. Evidence of previous tsunamis generally consists of stripped vegetation and soil along coastal areas (Figure 57). The tsunami hazard of an area is basically a function of two things: tectonic setting at the source, and coastal geometry of the site area. Tsunami source



Figure 56. Vertical aerial photograph of Owens Valley, California. Graben, titled land surface, and fissuring due to liquefaction of sands during the 1872 Owens Valley earthquake



Figure 57. High oblique photograph showing stripped vegetation along the shores of Lituya Bay, Alaska. This is the path of a devastating landslide-generated wave. Similar features may provide clues to tsunami hazard in coastal areas

parameters are not within the scope of remote sensing, but some features of a site's coastal geometry may be assessed. Both the coastal geometry with respect to the source of a tsunami and the offshore water depth and slope of the shelf area are important. Qualitative information may be obtained using remote sensing. In dealing with hazards of this type, it is often possible that a large local landslide may create a wave potentially more disastrous than a tsunami. Historical records and imagery are effective methods for assessing these problems. Parameters which imagery should possess are:

- a. Synoptic coverage.
- b. High spatial resolution.
- c. Steroscopic parallax.
- d. Reflectance variation--water and vegetation.
- e. Low irradiation angle.
- f. Water-land contrast.

PART III: RESPONSE OF EARTH MATERIALS TO  
ELECTROMAGNETIC RADIATION

58. Once specific earthquake hazards have been realistically defined, the optimum image acquisition methods can be selected. This selection process depends primarily on the response of the earthquake hazard to electromagnetic radiation.

59. Electromagnetic radiation comprises a continuous spectrum of energy extending from long, very low frequency radio waves to short, very high frequency gamma and cosmic waves. The electromagnetic spectrum and the regions commonly associated with remote sensing are displayed in Figure 58. The spectrum is normally divided into the following regions: gamma ray, x-ray, ultraviolet, visible, infrared, microwave (radar), and radio. None of these regions have exact boundaries; therefore, there is some overlap between them.

60. Early remote sensing utilized primarily the narrow visible portion of the spectrum (Figure 58); however, with the advent of modern

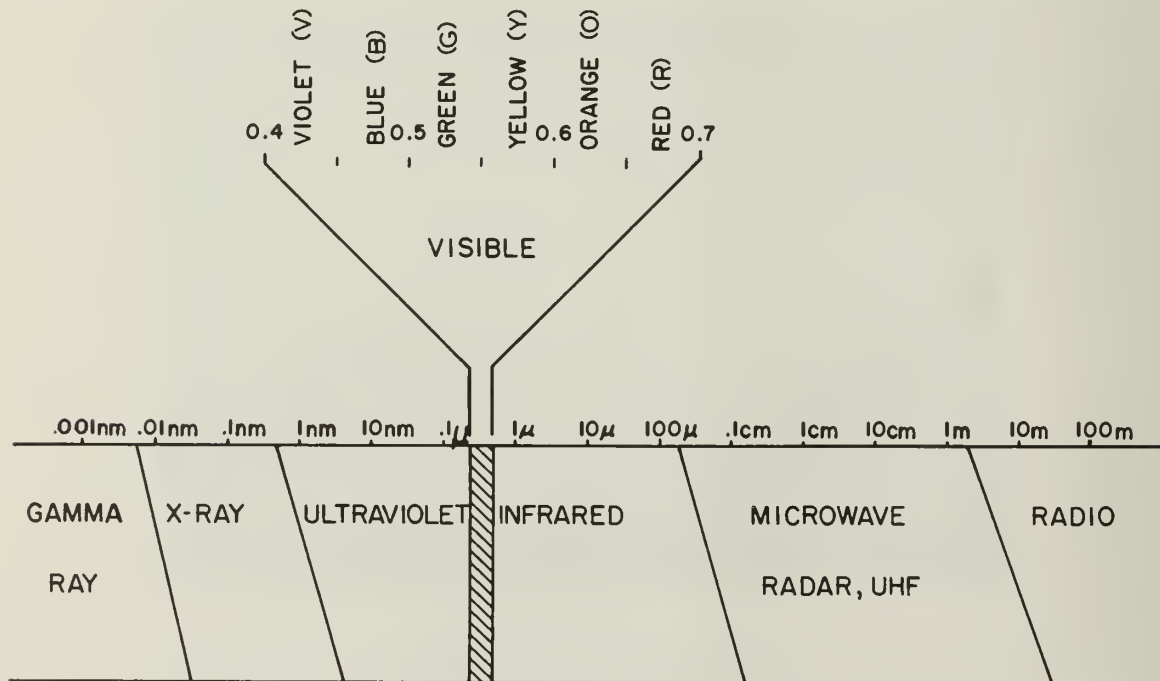


Figure 58. Electromagnetic spectrum (note letter abbreviations for color)

sensors, an increasingly larger portion of the spectrum has become available for use. Today the potential for simultaneously sensing target response to electromagnetic radiation in several spectral regions has lead to development of multispectral remote sensing.

#### Process of Response

61. Although images recorded during a remote sensing project are the end result of a number of factors which are unique to the specific project, all of the energy detected by a remote sensing system undergoes the same basic process:

- a. It is radiated by a source, either natural (passive) or artificially induced (active).
- b. It is propagated through the atmosphere and to some extent attenuated by it.
- c. It interacts in some way with a target.
- d. It is reemitted from the target.
- e. It is propagated back through the atmosphere.
- f. It is detected by a sensor.

62. Exceptions to this process occur when targets act as their own source. Sources which exhibit this behavior may do so as a result of radioactive decay, heat generated by friction or chemical processes, or heat conducted to a target from the interior of the earth.

#### Sources of electromagnetic radiation

63. All bodies having temperatures above absolute zero emit electromagnetic radiation. A convenient way to characterize this phenomenon is by considering a blackbody which is a conceptual body characterized by perfect absorption and emission of energy. Figure 59 shows curves of the radiant exitance for blackbodies at different temperatures. As the temperature of the blackbody increases, the radiant exitance of the blackbody peaks at progressively shorter wavelengths (Figure 59); thus, the maximum spectral response of systems sensitive to longer wavelengths is dominated by energy emitted from cooler bodies. Of primary concern to passive remote sensing for

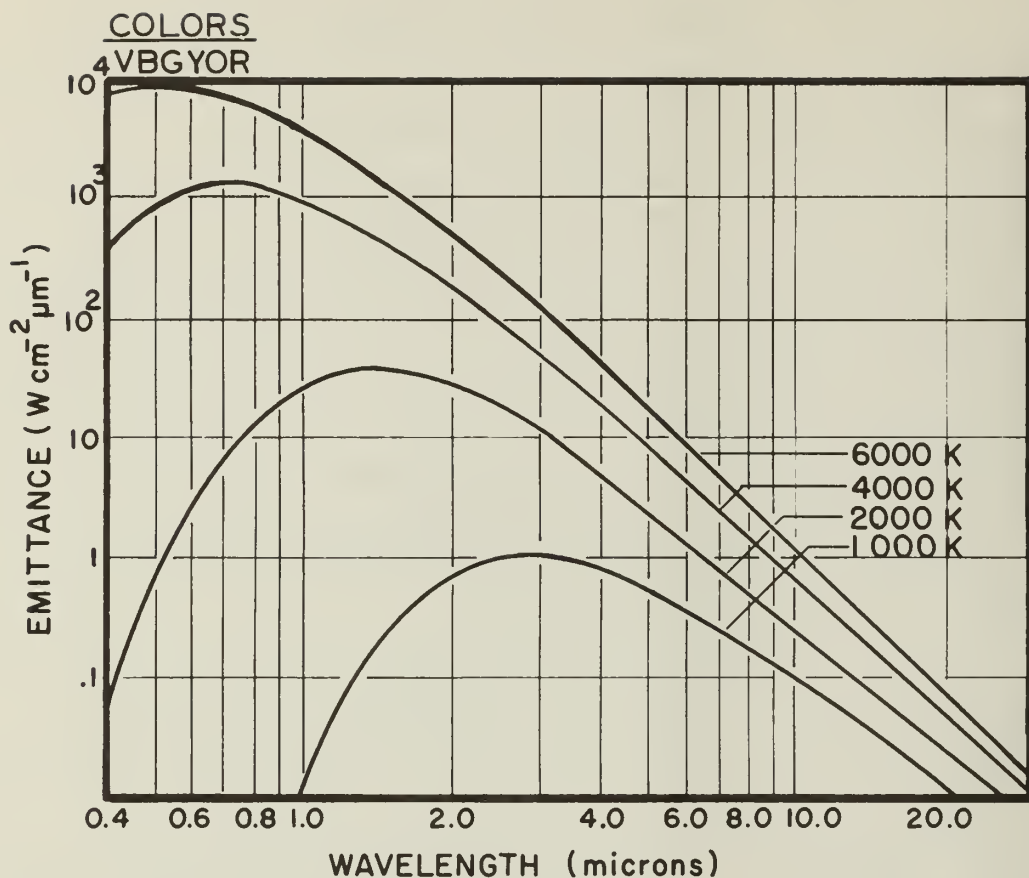


Figure 59. Blackbody curves for temperature from 1000 K to 6000 K. Notice that warmer bodies emit more energy and that the energy peaks at progressively shorter and shorter wavelengths. The sun, which can be represented by a 6000-K blackbody, has a spectral peak at 0.55  $\mu\text{m}$ . The earth (300 K) has a spectral peak at 9.6  $\mu\text{m}$ .

earthquake engineering purposes is the effect of two sources, the sun and the earth. The sun, for example, may be represented by a blackbody having a temperature of 6000 K, and the earth may be represented by a 300 K blackbody. The amount of electromagnetic radiation at the earth's surface (as a function of wavelength) due to these two sources may be calculated using Planck's law.

64. This radiation (spectral irradiance) is plotted in Figure 60. This figure indicates that the solar spectral irradiance at the earth's surface reaches a peak at a wavelength of 0.55  $\mu\text{m}$  in the green portion of the visible spectrum. The earth's spectral exitance peaks at 9.66  $\mu\text{m}$

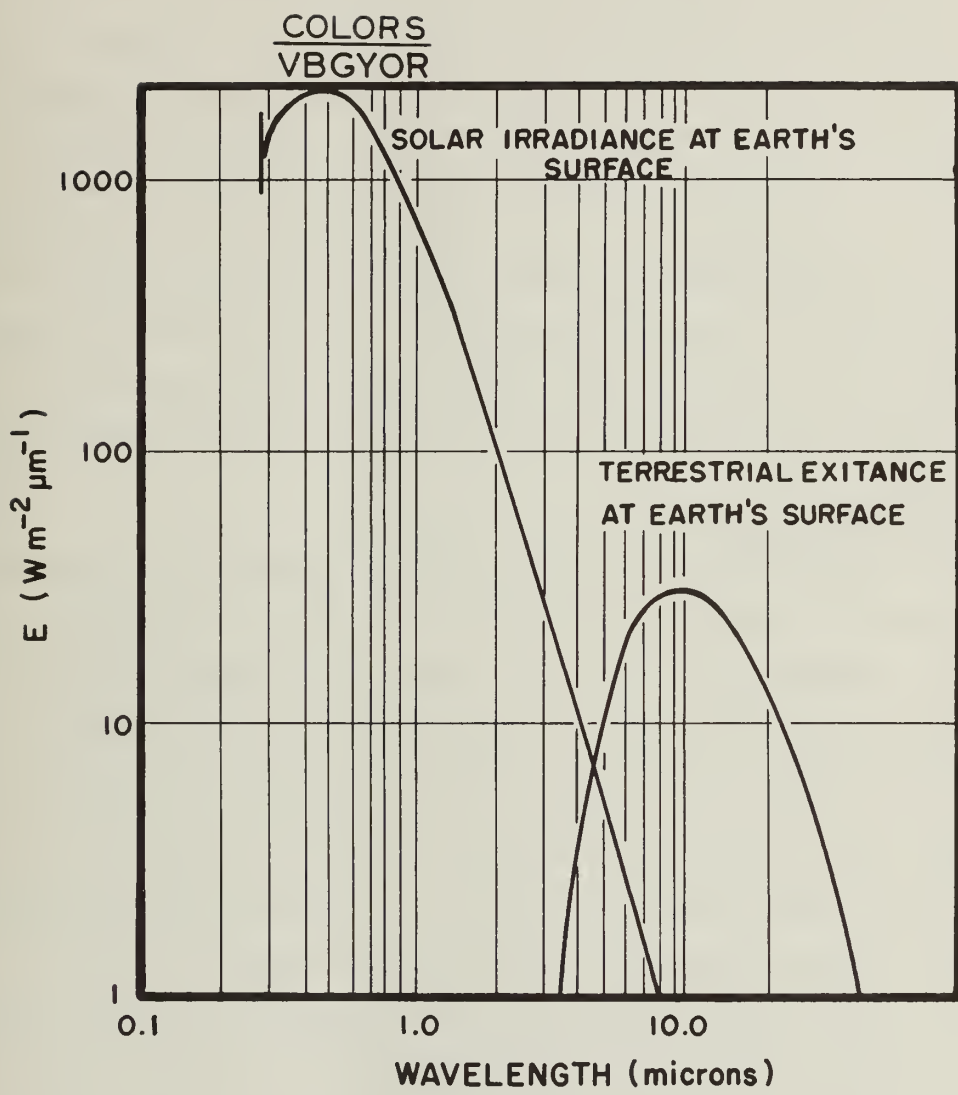


Figure 60. Solar spectral irradiance and terrestrial exitance at the earth's surface. Below approximately  $4.5 \mu\text{m}$  the sun provides the major source of energy. Beyond  $4.5 \mu\text{m}$  the earth, along with absorbed and reemitted solar energy, contributes the major energy

in the thermal infrared region. The solar spectral irradiance at the earth's surface and earth's exitance are equal at approximately 4.5  $\mu\text{m}$ . Thus, below approximately 4.5  $\mu\text{m}$  the sun contributes the majority of the energy measured by remote sensing systems. Below approximately 2.5  $\mu\text{m}$  remote sensing systems effectively measure only reflected solar energy. Beyond 4.5  $\mu\text{m}$  the earth's spectral exitance contributes the majority of the electromagnetic energy, and beyond about 6  $\mu\text{m}$  remote sensing systems effectively measure only that energy generated by earth materials as a result of their temperature. Accordingly, passive systems sensitive to radiation in the near infrared region through the visible region sense only reflected solar energy, while passive systems sensitive to radiation within the thermal infrared region and microwave region sense only energy generated by earth materials as a result of their temperature.

#### Propagation through the atmosphere

65. Once electromagnetic radiation is emitted by a source it must travel through the earth's atmosphere before it may be recorded. Although the atmosphere has a profound effect on spectral signatures (to the point that the upwelling radiance from the atmosphere often constitutes a larger component than that from the surface feature of interest at the sensor), simple and reliable methods by which to correct these effects have not yet been developed. Although several atmospheric models exist, only in a relatively few cases have they been used to correct spectral signatures for atmospheric effects.

66. The atmosphere may affect electromagnetic radiation through three basic mechanisms: scattering, absorption, and refraction. The atmosphere thus alters its speed of propagation, its frequency, its spectral distribution, and its direction.<sup>27</sup>

67. Scattering. One of the most serious atmospheric effects is scattering. Scattering alters the direction of radiation propagation in an unpredictable manner and occurs in four basic forms: Rayleigh scatter, Raman scatter, Mie scatter, and Nonselective scatter.

68. Rayleigh scatter is largely due to molecules and small particles which are many times smaller than the wavelength of the radiation

being propagated through the atmosphere. Rayleigh scatter occurs as a result of the absorption of radiation by atmospheric atoms or molecules and reemission of radiation in an unpredictable direction. The amount of scatter is inversely proportional to the radiation wavelength raised to the fourth power. Thus, ultraviolet light, which is approximately 1/2 the wavelength of red light, is scattered 16 times as much as red light by Rayleigh scatter. The bulk of Rayleigh scattering occurs below an elevation of 10,000 m and accounts for the predominance of blue in unfiltered color aerial photographs.

69. Raman scatter occurs less often than Rayleigh scatter and is the result of partly elastic collisions of photons with atoms. As a result of this collision, photons lose or gain energy with an attendant alteration in the radiation wavelength proportional to the energy exchanged.

70. Mie scatter is caused by atmospheric particles with diameters approximately dimensionally equivalent to the radiation wavelength. For radiation in the visible range, water vapor, dust, and other particles ranging from a few tenths of a micrometre to several micrometres in diameter contribute to this type of scatter. Mie scatter is generally greater than Rayleigh scatter and affects longer wavelength energy. The bulk of Mie scatter occurs below an elevation of 5000 m.

71. Nonselective scatter occurs due to particles in the atmosphere having diameters several times the wavelength of the radiation being transmitted. This type of scatter is nonselective with respect to wavelengths smaller than the particles. For this reason, water droplets scatter all wavelengths of visible light equally well, causing clouds to appear white. Because of the increased scattering of smaller wavelength energy, remote sensing in the infrared region and beyond is generally free of all but the most severe atmospheric scattering (Figures 61 and 62). Microwave radiation with wavelengths on the order of several centimetres is unaffected by scatter and yields imagery free of atmospheric effects. Accordingly, radar imagery is effective even under poor weather conditions.

72. Absorption. Some wavelengths of energy are affected more by



Figure 61. This scene was extracted from a Landsat image (band 4, 0.5 to 0.6  $\mu\text{m}$ , green). The area is near Globe, Arizona, and shows the extensive mining activity currently taking place in the area (upper left corner). Near the left edge of the scene (arrow) ground features are obscured by smoke or dust making interpretation in this area impossible

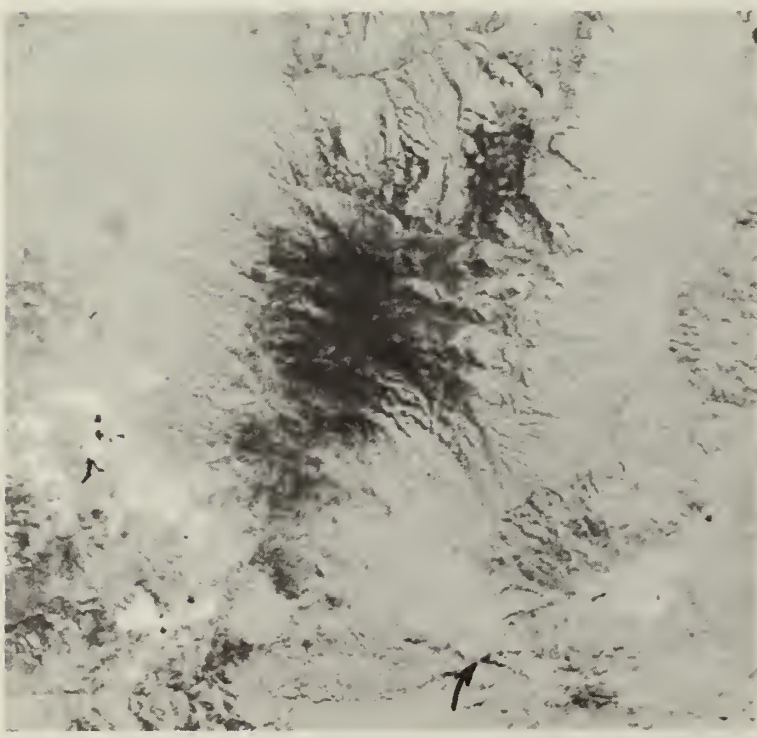


Figure 62. This scene and the scene in Figure 61 were recorded simultaneously. However, the spectral band represented by this scene is the near infrared (Landsat band 7, 0.8 to 1.1  $\mu\text{m}$ ). The area obscured by dust or smoke in Figure 61 is clearly visible on this scene (arrow) demonstrating that the longer wavelength energy comprising the near infrared is free of atmospheric effects which may render imagery in other, shorter wavelength spectral bands useless

absorption than by scattering (infrared and ultraviolet radiation are examples). Absorption occurs when radiation, with a frequency matching the resonant frequency of an atom or molecule, strikes the atom or molecule producing an excited state. The energy is generally transformed into heat and is reemitted at a longer wavelength.

73. The absorption and scattering phenomena are generally combined into an "extinction coefficient" to account for atmospheric effects. The transmission of radiation through the atmosphere is inversely related to the product of the extinction coefficient and the thickness of the atmospheric layer. The effect of atmospheric thickness on radiation transmission is shown in Figure 63.

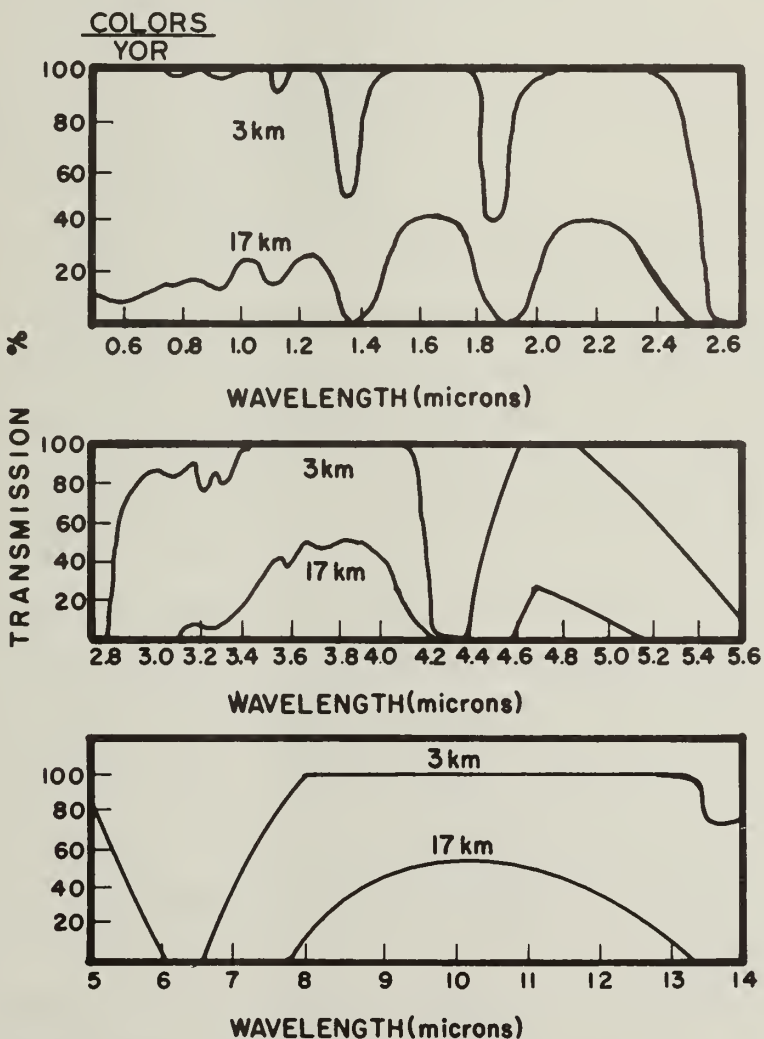


Figure 63. Atmospheric transmission of electromagnetic radiation<sup>28</sup>

74. Atmospheric absorption effectively blocks solar radiation below 0.28  $\mu\text{m}$  in the ultraviolet region. Several additional absorption bands occur in other portions of the spectrum severely limiting the wavelengths which can be used for remote sensing applications. Some of these bands are outlined in Table 4.

Table 4  
Absorption Bands Which Limit Usable Wavelengths

Spectral Region $\mu\text{m}$	Cause of Absorption
0.7 to 3.0	Several water absorption bands
2.8	Carbon dioxide absorption band
5.0 to 8.0	Strong water absorption band
9.0 to 10.0	Strong ozone absorption band
15 to 100	Not used due to strong carbon dioxide absorption and poor detector capabilities

75. Refraction. Electromagnetic radiation bends as it passes from one medium to another medium possessing different optical properties. This may result in predictable errors in target location for low angles of radiation incidence; however, if the atmosphere is turbulent, random turbulent motions may bend the radiation in unpredictable directions.

76. These atmospheric effects are responsible for the upward scattered radiant flux which contributes to the energy at the sensor. This "sky radiation" often exceeds the signal from a target and significantly reduces image contrast. For example, possible contrasts between an asphalt road through a snow field may exceed 100:1;<sup>29</sup> however, due to sky radiation the maximum attainable contrast for high-altitude photographs seldom exceeds 10:1 and for satellite imagery seldom exceeds 5:1.

#### Target interactions

77. The energy which reaches a target and the resultant interaction which takes place is of direct importance to sensing the target. Physically, the incident electromagnetic radiation induces an oscillatory

motion of the free and bound charges on the target surface. These oscillations radiate a secondary field either back into the atmosphere or forward into the target medium. If a target is opaque to the incident energy, the energy is reflected back into the atmosphere, or absorbed and reemitted at a longer wavelength. This reflection or absorption allows perception of the target. If the target is transparent to the incident energy, the wave is transmitted through the target and out the opposite side. The relationship between absorptance, transmittance, and reflectance is:

$$\alpha(\lambda) + \rho(\lambda) + \tau(\lambda) = 1 \quad (1)$$

where

$\alpha(\lambda)$  = spectral absorptance

$\rho(\lambda)$  = spectral reflectance

$\tau(\lambda)$  = spectral transmittance

Thus, good absorbers tend to be poor reflectors and vice versa.

78. Absorptance, transmittance, and reflectance vary with wavelength and are functions of the natural resonance frequencies of the atoms, molecules, lattice vibrations, and free electrons which make up the target. Targets may behave differently when exposed to radiation of different wavelengths. Glass, for example, is transparent to electromagnetic radiation in the visible region while being essentially opaque to radiation in the ultraviolet region.

79. The reflectivity of a target is dependent upon a number of parameters. The most important of these are radiation incident angle, polarization, electrical properties of the surface, and surface roughness. The roughness of a surface plays a dominant role in determining the type of reflection (specular or diffuse) which occurs and thus the appearance of the surface on imagery. Whether a surface appears rough or smooth on an image depends upon the surface irregularities as well as the wavelength of the reflected radiation. For this reason, a surface which appears rough when exposed to radiation in the visible region may appear smooth when exposed to radiation in the microwave region.

80. Specular reflection (mirrorlike) occurs when a surface is radiometrically smooth, that is, surface irregularities are smaller than the incident radiation wavelength. Under these conditions, reflection follows Snell's Law with the majority of the reflected energy being confined to a small angular region about the angle of reflection.

81. Surfaces having irregularities that are large relative to the wavelength of incident energy will reflect energy at angles other than the specular. This is termed diffuse or scattered reflection. The Rayleigh criterion expresses the relationship between surface roughness and incident radiation wavelength required for diffuse reflection. According to this criterion, a surface is radiometrically smooth if

$$h \leq \frac{\lambda}{8 \sin \beta} \quad (2)$$

where

$h$  = height of surface irregularities

$\lambda$  = wavelength of incident radiation

$\beta$  = slant angle, angle that the incident ray makes with horizontal

82. Thus, at an incident angle of  $45^\circ$  a surface with irregularities equal to 10 mm would appear smooth on Landsat-band radar imagery ( $\lambda = 24$  cm) but rough on a standard aerial photograph ( $\lambda = 0.4$  to  $0.7$   $\mu\text{m}$ ). The different ways by which surfaces reflect energy determine the tonal variations on an image. Materials with different reflectivities produce tone contrasts and an opportunity for geologic interpretations. Finally, energy which is reflected or otherwise emitted by a target must be propagated back through the atmosphere to the remote sensor before it can be sensed and recorded.

#### Response of Earth Materials to Ultraviolet Radiation

83. The first discovery of ultraviolet radiation is credited to James Ritter who, in 1801, showed that certain chemical reactions are initiated by energy in the "dark" portion of the electromagnetic spectrum adjacent to the blue hues of the visible region.<sup>30</sup> Ritter studied

this region (ultraviolet) by observing that silver chloride decomposed more rapidly in the ultraviolet region than in the visible.

84. The ultraviolet region extends arbitrarily from 4 to 400 nm, thus bridging the gap between the longest X-ray wavelengths and the shortest visible wavelengths. The ultraviolet portion of the spectrum is divided into the near ultraviolet (0.300 to 0.400  $\mu\text{m}$ ), the far ultraviolet (0.200 to 0.300  $\mu\text{m}$ ), and the extreme ultraviolet (4 to 200 nm). Of the three regions, the near ultraviolet is the most important for remote sensing applications since solar energy below approximately 0.28  $\mu\text{m}$  cannot be detected at the earth's surface due to atmospheric absorption.

85. Sources of ultraviolet radiation may be divided into natural (passive imagery) and man-made (active imagery). The only natural source of significance is the sun, and less than 5 percent of solar radiation lies in the ultraviolet region. Terrestrial incandescent bodies, a second natural source, are weak and inefficient sources of ultraviolet radiation. This poor emission of ultraviolet by terrestrial sources, combined with atmospheric absorption of ultraviolet energy, requires that natural ultraviolet radiation measured on a remote sensing scale be derived from primarily two sources: reflection of solar ultraviolet energy from earth materials, and luminescence of earth or organic material.

#### Reflection of ultraviolet radiation

86. Many substances that are good reflectors of visible light are poor reflectors of ultraviolet energy. For example, most metals are very good reflectors of ultraviolet over a large range of wavelengths provided that the surface is clean. For this reason, unpainted metal roofs tend to show strongly on ultraviolet imagery. Water is generally a good transmitter of ultraviolet, but the presence of dissolved salts and organic matter profoundly affects the transmission properties and provides a promising opportunity for remote location and monitoring of pollution in water bodies.

87. Carbonates, phosphates, and evaporites generally have higher reflectances in the ultraviolet than other lithologic materials while

acidic rocks, such as granite, show little reflectance in the ultraviolet but strong reflectance in the visible. Basic rocks, such as basalt, show little reflectance in either the ultraviolet or the visible.

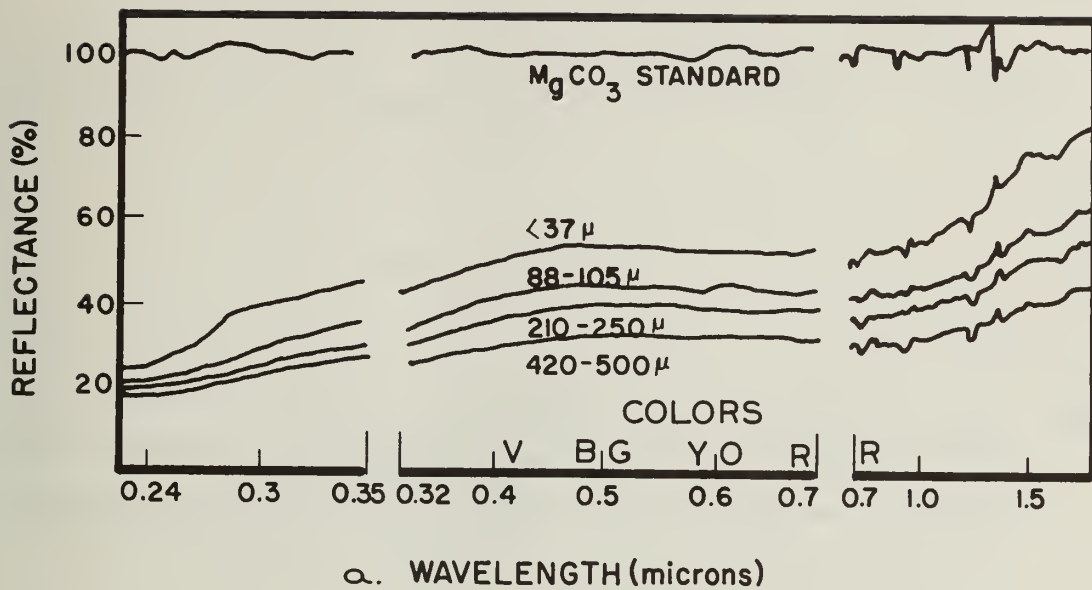
88. Hemphill et al.<sup>31,32</sup> have shown that at 0.250  $\mu\text{m}$ , limestone is 2.5 times more reflective than rhyolite. Reflectance spectra for granite, obsidian, basalt, and calcite are plotted in Figure 64. These plots show that there are no distinct spectral peaks for the samples within the range from 0.240 to 1.800  $\mu\text{m}$ . The reflectance for all samples falls off in the ultraviolet reaching 15 to 30 percent of maximum, with the calcite slightly higher. These curves indicate that discrimination of carbonate rocks may be feasible by use of the ultraviolet region alone, although the addition of other spectral bands further improves interpretation. For example, if one were to divide the reflectance of the four rock types in Figure 64 at 0.500  $\mu\text{m}$  (green) by their reflectances at 0.240  $\mu\text{m}$  (ultraviolet) the following ratios would result:

- a. Granite = 2.3.
- b. Obsidian = 3.6.
- c. Basalt = 2.0.
- d. Calcite = 1.17.

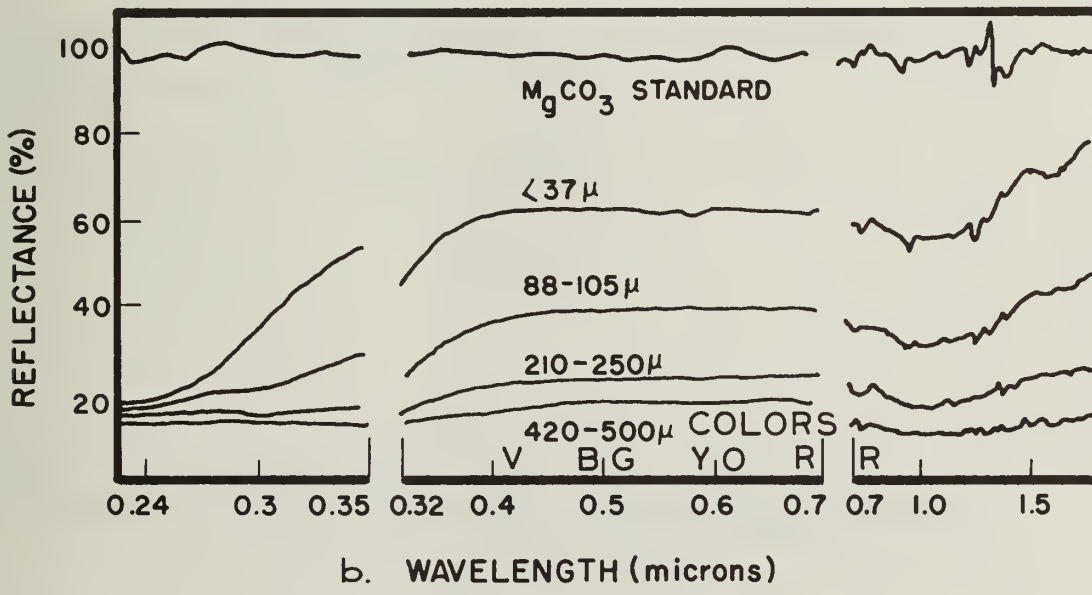
89. Thus, by using only two spectral bands ( $\lambda = 0.24 \mu\text{m}$  and  $\lambda = 0.5 \mu\text{m}$ ), one could separate the carbonate from the other rock types in the ultraviolet, the granite and obsidian from the basalt in the visible, and the granite from the obsidian by computing the ratio of the two bands.

#### Luminescence of earth materials

90. Vegetation, soils, and rocks absorb solar radiation and reemit this energy at longer wavelengths, often within the visible spectrum (luminescence). One technique to measure luminescence of earth materials is through the use of the Fraunhofer Line-Depth method. The sun's center emits a continuous spectrum of energy given by Planck's equation. However, gases at the outer part of the sun are cooler than its center and effectively absorb solar energy within specific wavelength bands. These "Fraunhofer Bands" hold promise as a remote sensing



a. WAVELENGTH (microns)



b. WAVELENGTH (microns)

Figure 64. Spectral reflectance curves<sup>33</sup>  
(sheet 1 of 2)

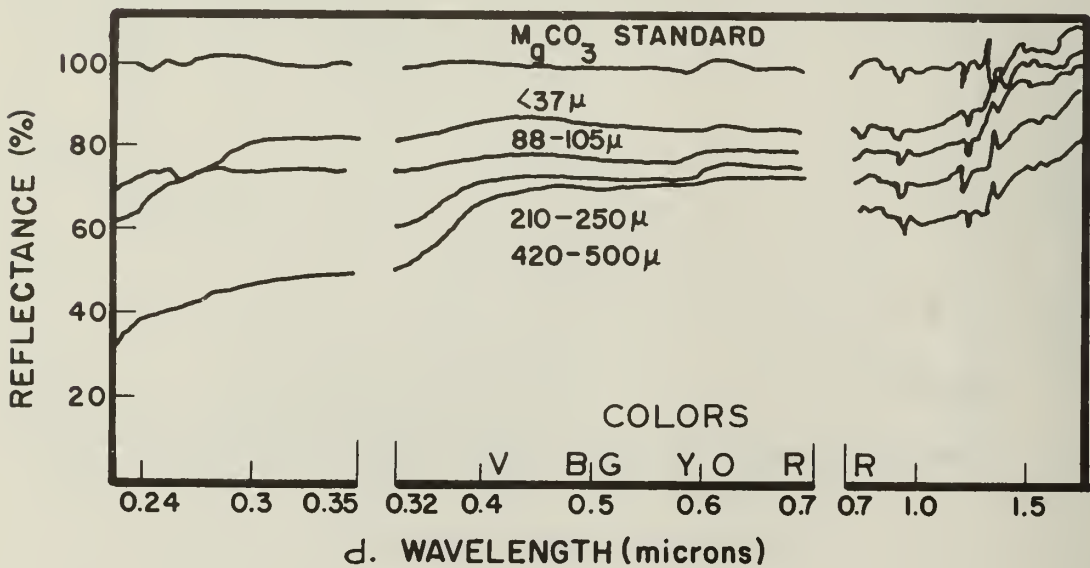
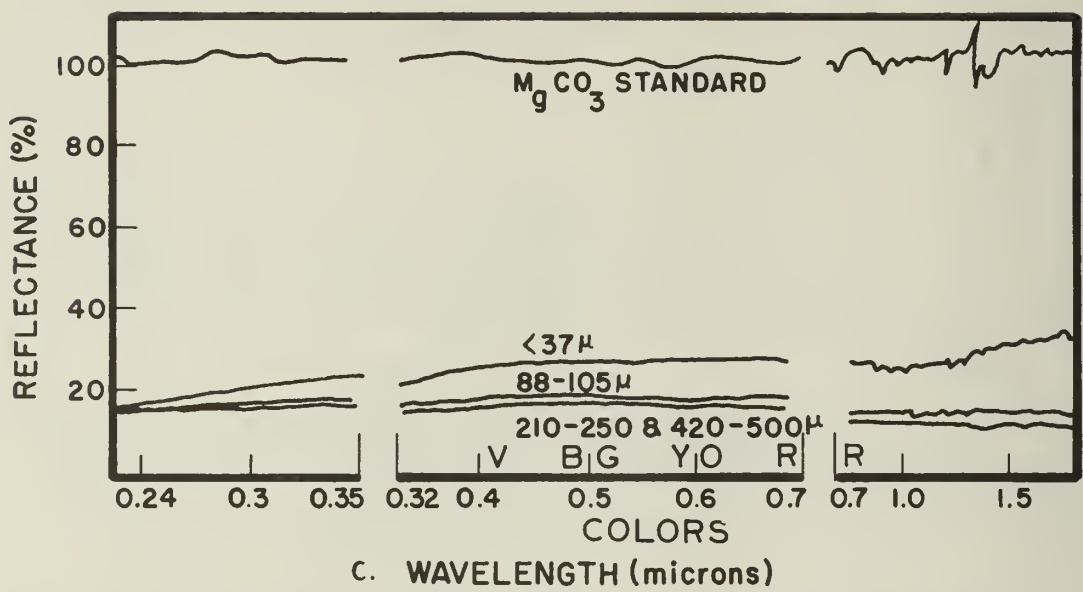
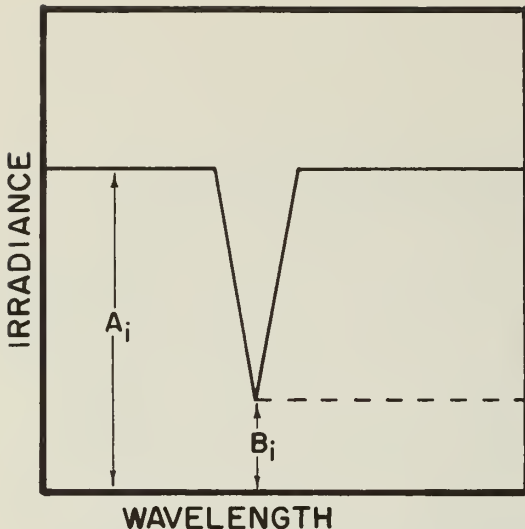


Figure 64 (sheet 2 of 2)

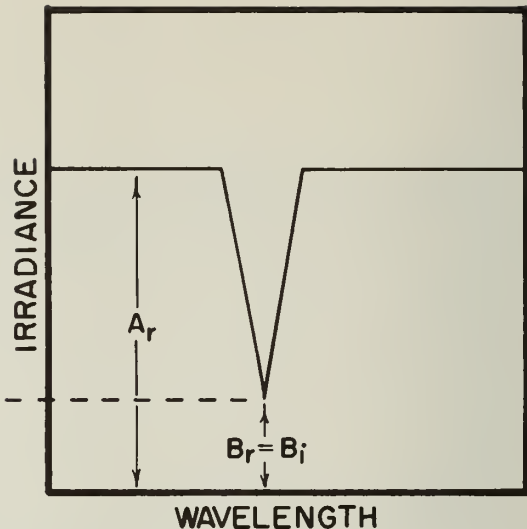
technique since energy sensed at the earth's surface within these bands must be the result of luminescence, not reflected solar energy. There are Fraunhofer lines at 0.396  $\mu\text{m}$ , 0.393  $\mu\text{m}$ , and an optimum line for most materials at 0.486  $\mu\text{m}$  which can be remotely sensed with the proper equipment. The equipment (Fraunhofer Line Discriminator, FLD) consists basically of two sensors; one pointed skyward to measure the amount of incident radiation, and the other pointed downward to measure the amount of reflected or reemitted radiation within a narrow spectral band. The Fraunhofer line may be depicted as illustrated in Figure 65a. The FLD measures the ratio of the energy within the Fraunhofer line (B) to the energy within the adjacent continuous spectrum (A) (Figure 65a) for both the incident and reflected energy. A luminescence coefficient equal to the difference between (B/A) reflected and (B/A) incident can then be computed. For a perfectly reflecting surface this difference is zero (Figure 65b), but for materials which luminesce the difference is measurable (Figure 65c). This technique has been used successfully by the USGS for applications including: monitoring location and concentration of pollution in water bodies,<sup>32</sup> detection of phosphate and gypsum deposits, detection of manganese halos above petroleum reservoirs, and detection of geochemically stressed vegetation associated with ore bodies. By computing the ratio between the luminescence coefficient in selected Fraunhofer lines, some rock discrimination has been possible and future applications look promising. However, only three FLD's exist, and all three are experimental models operated by the USGS. Applications of the Fraunhofer line depth method are still experimental and are currently of limited value for earthquake engineering purposes. However, if commercial systems having adequate resolution become available, the ability of the technique to record plant stress more accurately than near infrared photography may prove useful for fault investigations under special circumstances.

91. In summary, the use of ultraviolet energy for geological remote sensing is limited because of the relatively weak sources of natural ultraviolet radiation, severe atmospheric absorption, and scattering which reduces resolution. These factors seem to preclude



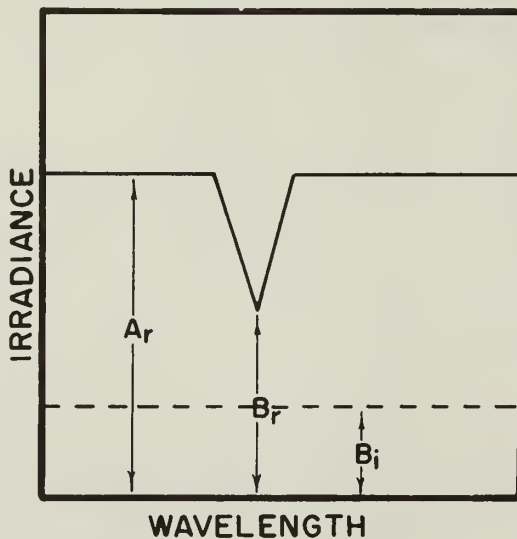
WAVELENGTH

- a. The incident solar radiation is measured by sensor pointed skyward. This radiation is represented by a continuous intensity (denoted by  $A_i$ ) in the neighborhood of the Fraunhofer line. The depth of the Fraunhofer line is denoted  $B_i$



WAVELENGTH

- b. The energy from the earth's surface is measured by a downward directed sensor. If the surface does not luminesce, the reflected intensity and line depth equal the incident energy as in B



- c. If the surface luminesces, there will be energy within the Fraunhofer line which was not available in the incident energy, and the difference between the ratios  $B_r/A_r$  and  $B_i/A_i$  represents a luminescence quantity or coefficient

Figure 65. Fraunhofer line depth technique for measuring luminescence of earth materials

all but low altitude recording systems. The main source of recorded energy is direct reflection of solar ultraviolet from earth materials. Even though carbonates, phosphates, and evaporites appear to be the only effective reflectors, the use of ultraviolet imagery in combination with imagery derived from other spectral bands (multispectral) may provide a useful discrimination tool. It is unfortunate that very little data exist regarding the response of earth materials in the ultraviolet region and current investigations appear to be directed toward areas such as pollution monitoring to the exclusion of geological applications. The development of active multispectral systems will undoubtedly improve the usefulness of the ultraviolet region as a remote sensing tool in the future. At present, however, the ultraviolet should be considered a low-priority spectral region for remote sensing involving earthquake engineering.

#### Response of Earth Materials to Radiation in the Visible Region

92. Most historical studies of imagery have been in the visible region of the electromagnetic spectrum because of the high sensitivity of film emulsions to radiation within this wavelength range. Panchromatic film, for example, has a sensitivity which ranges from 0.360 to 0.720  $\mu\text{m}$ . Even though most earth materials have flat spectral characteristics in the visible range, imagery in the visible region will undoubtedly receive emphasis in the future due to the advantages of low cost, high resolution, numerous commercial products available, and the multispectral capabilities provided by the use of various filter combinations. Since panchromatic films are sensitive to the same general spectral range as the human eye, the shades of gray recorded on a positive photo are comparable to the intensity (spectral reflectance) or an object's color response as perceived by the human brain. This is one of the fundamental reasons why panchromatic film has been, and will continue to be, so successful for image interpretation.

93. Since many rock-forming minerals do not display compositionally diagnostic spectral signatures in the visible region, the spectrum

of a rock composed predominantly of minerals lacking distinctive spectral characteristics may be dominated by the spectral features of a minor constituent or of alteration products only indirectly related to primary mineralogy.<sup>34</sup> Additionally, many rocks contain opaque minerals which tend to mask the spectral features of other mineral combinations and reduce reflectance. In terrestrial applications, furthermore, some of the most diagnostic spectral features such as carbonate bands tend to be obscured by atmospheric absorption.<sup>34</sup> For these reasons, it has not been possible to uniquely identify lithologies by remote sensing in the visible range. Imagery in the visible range will continue to provide a powerful tool for geologic interpretation, however, since the overall contrasts in rock reflectance generally provide important interpretative keys. Thus, one may accurately map different geologic units from color or black and white imagery without necessarily knowing the mineralogic composition of the units. Since the mineralogy may be important to fault studies, subsequent or prior ground studies should always be employed to provide detailed mineralogic information to further refine interpretations.

#### Reflectance of rocks

94. Examples of spectral reflectance in the visible region for igneous rocks are provided in Figure 66 (Reference 34). The pure minerals of acidic (silica-rich) or salic (silica-alumina-rich) rocks tend to be spectrally featureless in the visible region. The high transparency of these minerals produces a high average reflectance (due to specular returns) which increases the intensity of energy at the sensor, producing a light tone. The increase in iron content, especially the magnetite content of intermediate and basic rocks, tends to decrease the reflectance and the contrast of any spectral features which may be present. However, the presence of iron in basic rocks tends to produce a spectral characteristic more diagnostic of rock type than in the silica and alumina-rich (salic) rocks. Phonolite, for example, exhibits a weak ferric band near 0.7  $\mu\text{m}$  due to the presence of minor pyroxene and olivine. The ultrabasic rocks in Figure 66 contain less magnetite than the diorite and diabase; thus, their spectral

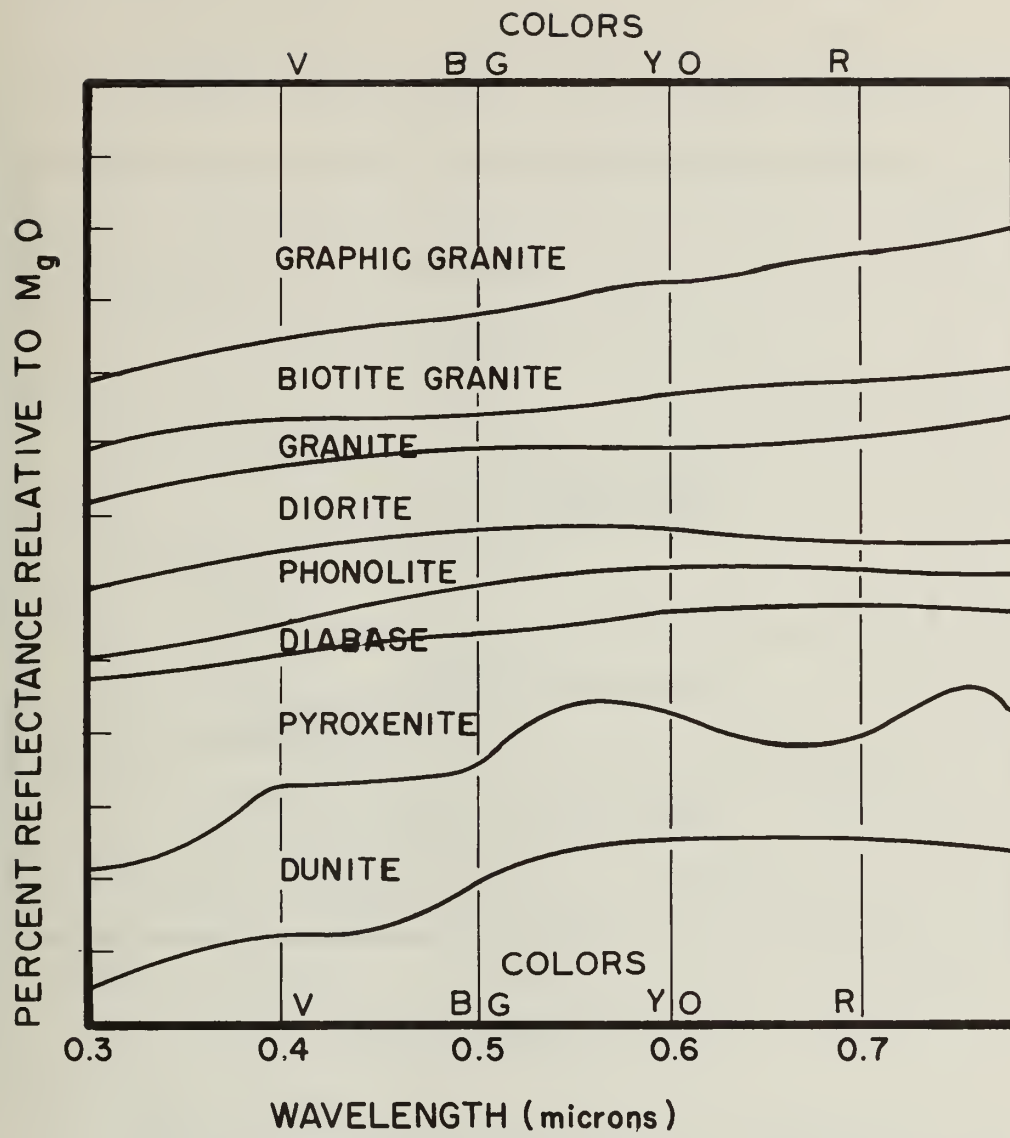


Figure 66. Spectral reflectance of igneous rocks in the visible region of the electromagnetic spectrum<sup>34</sup>

characteristics are more easily sensed. The most obvious characteristic of the spectral curves for igneous rocks is the large change in overall reflectance represented by the vertical scale in Figure 66 for varying silica content that varies from high (graphic granite) to low (dunite). This variation in reflectance results in tone variations and provides dependable recognition keys for the igneous rocks in both panchromatic and color applications.

95. Spectral characteristics for some common sedimentary rocks are shown in Figure 67. The limestones are relatively flat and featureless throughout the visible range exhibiting a rapid falloff toward the

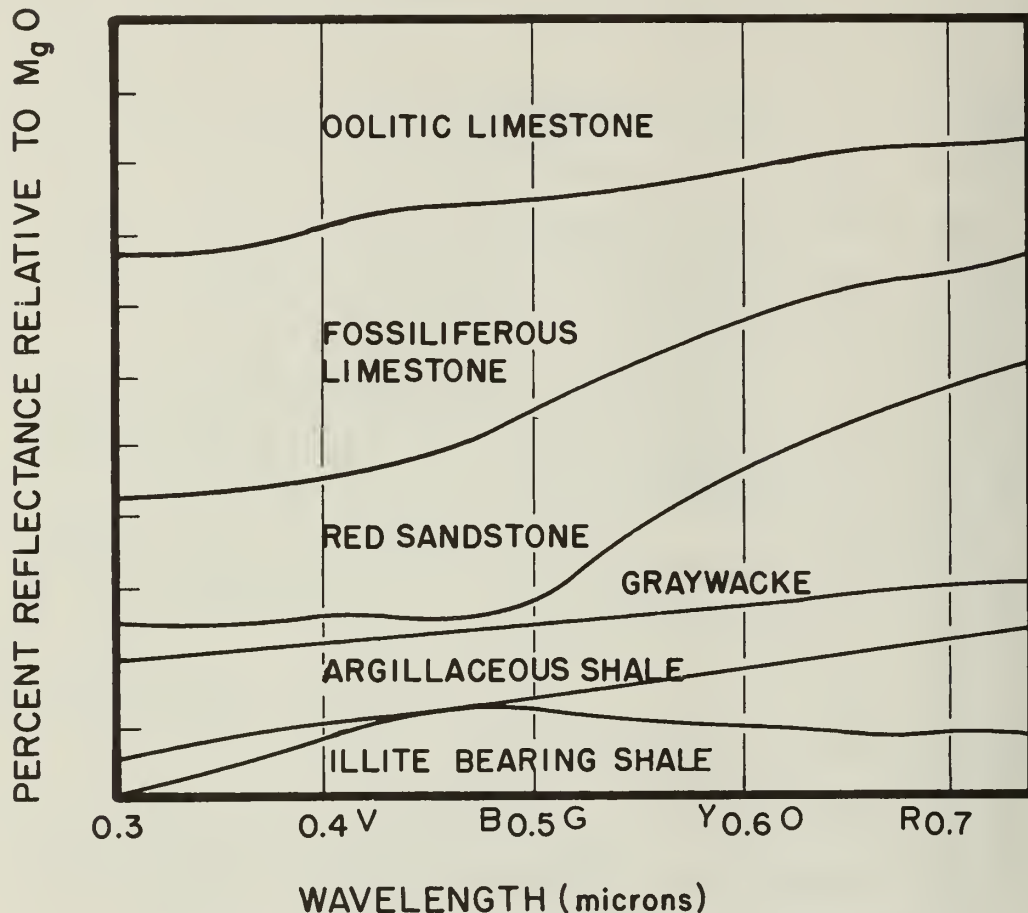


Figure 67. Spectral reflectance of sedimentary rocks in the visible region of the electromagnetic spectrum<sup>34</sup>

blue. Sandstones typically display the spectral features of the ferric oxide stain typically found on the sand grains. A pure quartz sandstone with a silicious cement would appear spectrally featureless. Shales generally contain sufficient carbonaceous material to significantly reduce or obliterate the intensity of all bands, yielding a featureless spectrum sloping upward toward the red. This explains the commonly observed dark tones of shales on panchromatic film. Presence of iron may produce a broad peak between 0.5 and 0.6  $\mu m$ . Generally, as with the igneous rocks, the changes in overall reflectance and erosion qualities

of sedimentary rocks is more important for geologic interpretation in the visible region than their spectral features.

96. Spectral curves for some common metamorphic rocks are provided in Figure 68. Metamorphic rocks display some of the most distinctive rock spectra, probably due to their crystalline nature. The green quartzite and serpentine marble show interesting features at  $0.625 \mu\text{m}$  and  $0.425 \mu\text{m}$ , respectively. The marble shows a gradual falloff to about  $0.400 \mu\text{m}$  followed by an abrupt decline toward the ultraviolet. The red quartzites, pink marbles, and red slates show distinctive ferric oxide features at approximately  $0.550 \mu\text{m}$  and a strong response at approximately  $0.800 \mu\text{m}$ . These features, while disclosing nothing about the composition of the material, are eminently detectable in a remote sensing application using color imagery.<sup>34</sup>

#### Reflectance of soils

97. The spectral characteristics of soils in the visible region are not unlike those of rock with the exception of the effect of moisture. In the laboratory, a decrease in grain size generally results in an increase in reflectivity due to heavier light scattering, lower extinction of light passing through the particles, and the smaller area covered by shadows. In the field, however, the water content, the presence of organic matter, or a combination of both tends to make the reflectivity lower for fine-grained soils than for coarse-grained soils. Thus, fine-grained soils tend to appear dark on aerial imagery in the visible region.

98. The moisture content of soils above the hygroscopic limit causes a marked decrease in reflectivity. The magnitude of this reflectivity fluctuation depends upon the soil type with dark soils tending to show a larger fluctuation with water content than light soils, providing a potential recognition key for discontinuities in moisture across a fault within a single soil unit (Figure 17).

99. The shape of the spectral signature of soils does not change with added moisture. The controlling factor for spectral shape appears to be the ratio of humus to iron oxide in the soil. Low ratios tend to cause a spectral peak in the red wavelengths ( $0.700 \mu\text{m}$ ), while high ratios

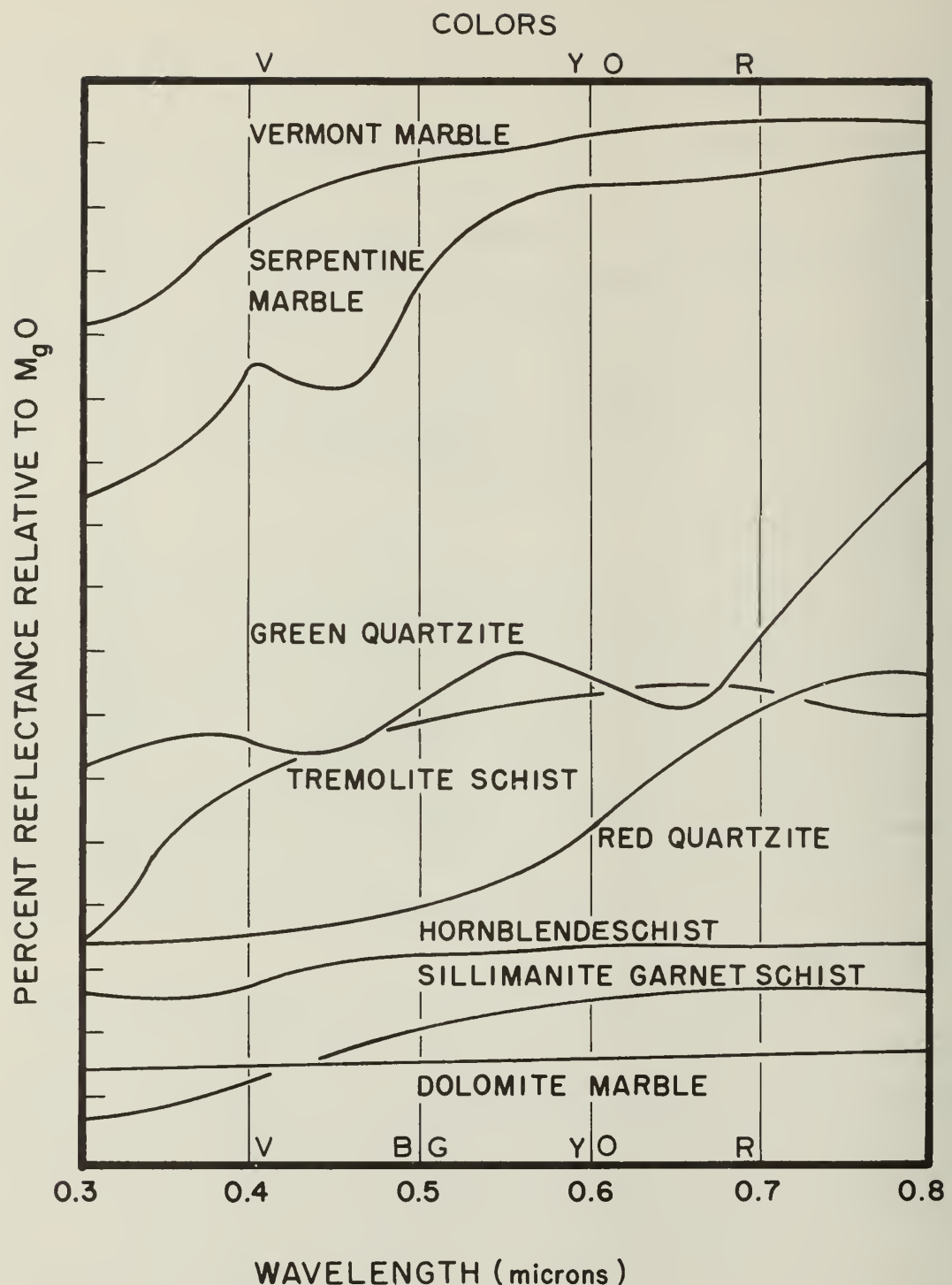
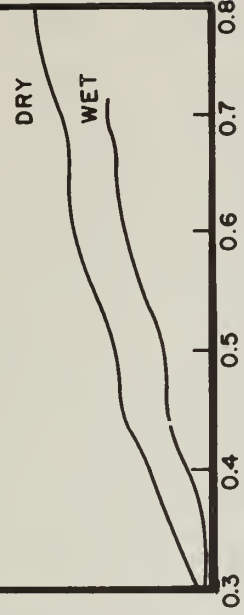


Figure 68. Spectral reflectance of metamorphic rocks in the visible region of the electromagnetic spectrum<sup>34</sup>



a. Category I soils rich in humus and carbonates typical of chernozem soils

REFLECTANCE



b. Category II soils rich in alumina and iron typical of pedalferr soils from humid regions

REFLECTANCE



c. Category III soils consisting of laterites, and red quartz and calcite sands

Figure 69. Spectral reflectance of American soils 35

tend to lower the intensity and level out the spectral curve. Surface structure does not appreciably affect the spectral shape of soils.

100. Condit<sup>35</sup> studied reflectance of 258 soil samples from 36 states and found that the spectral characteristics could be broadly classified into three categories. Category I soils correspond to black soils rich in humus and carbonates typical of the chernozem type. Spectral curves for Category I soils are typified by a slow increase in slope or constant slope throughout the visible spectrum (Figure 69a). All Category I soils have low reflectances. Category II soils are generally from humid regions rich in alumina and iron typical of pedalfer type soils. The spectra of this type of soil is characterized by a fairly rapid increase in reflectance from 0.320 to 0.450  $\mu\text{m}$ , followed by a slight dip in slope to about 0.480  $\mu\text{m}$  where the slope rises again. Another dip in slope occurs from 0.600 to 0.700  $\mu\text{m}$  with very little change beyond 0.700  $\mu\text{m}$  (Figure 69b).

101. Category III soils consist of laterites, and red quartz and calcite sands. This group is characterized by a moderate increase in reflectance from 0.320 to 0.530  $\mu\text{m}$ , followed by a rapid rise to approximately 0.58  $\mu\text{m}$ . The slope decreases between 0.620 and 0.740  $\mu\text{m}$  to a moderate slope (Figure 69c).

102. A characteristic vector analysis of the soil data<sup>35</sup> indicated that reflectance measurements made at only five wavelengths could be used to predict the reflectance values at the other 30 wavelengths. These critical wavelengths were 0.400, 0.540, 0.640, 0.740, 0.920  $\mu\text{m}$ .

103. The above studies of rock and soil reflectance indicate the presence of minor differences in the spectral characteristics of different rock types in the visible range. Because these differences are subtle, utilizing them in an effort to determine the compositional nature of rocks and soils would not be fruitful. However, rock and soil units do exhibit rather significant variations in overall reflectance in the visible region, providing powerful interpretive keys if different units are brought into juxtaposition by a fault. In addition, most spectra display an increase in reflectance toward the red wavelengths, making it possible to discriminate between geologic units by selecting

specific filter combinations. For example, discrimination between an argillaceous shale and an illite-bearing shale is more effective if the units are recorded using only the red region (filtered panchromatic print) than when the entire spectrum is used (standard panchromatic print) (Figure 67). Similarly, distinguishing between fossiliferous limestone and oölitic limestone may be more successful only in the blue or green region. The red region appears to be the best for interpretation and mapping of soils because the reflectance contrasts are at a maximum due to changes in the ratio of humus to iron oxide (Figure 69a, b, and c).

#### Color versus black-and-white imagery

104. As a general rule, color imagery is superior to black-and-white imagery for all interpretation tasks, particularly since new color emulsions are rapidly approaching panchromatic films in terms of image resolution and cost. According to Evans,<sup>36</sup> the human eye can distinguish more than 100 times more color combinations (hues, values, chromas) than shades of gray. Image interpreters consistently detect more targets on conventional color imagery than on conventional black-and-white imagery.<sup>29</sup> Most, or many, photo interpreters prefer to use black-and-white photography in conjunction with color, as color can mask subtle tones that are well expressed in the black-and-white printing of some of the spectral bands. Thus, slight differences in the spectral characteristics and reflectivity of a material will be more discernable on color imagery.

105. The use of color imagery also facilitates the interpretation of plant assemblages as keys to geologic structure, lithology, and local water content. Slight changes in the reflectance characteristics of plants are much more discernable on color imagery than on black-and-white. Advantages of color imagery decrease with lower irradiation angles, since the films are of high contrast and the sensitivity of currently used films is marginal for low-sun angle applications.

Several recent applications of low-sun angle irradiation with color and false color IR films have given spectacular results, but others have given results of marginal use. The acquisition of both high-sun angle

color and low-sun angle panchromatic imagery is recommended. Low-sun angle imagery is essential for most fault studies to enhance even subtle topographic variations associated with earthquake hazards.

Response of Earth Materials to Radiation  
in the Near Infrared Region

106. The properties of the infrared region, which includes wavelengths from 0.7 to 2.5  $\mu\text{m}$ , were first discovered by Sir Frederick William Herschel in 1800. Remote sensing in this region has become extremely popular for earth sciences applications since film emulsions have been developed which make infrared photography routine.

107. Atmospheric absorption of infrared radiation restricts the wavelengths which may be sensed. There are several water absorption bands between 0.700 and 3.000  $\mu\text{m}$  with a strong carbon dioxide band at 2.800  $\mu\text{m}$ . A large window exists in the mid-infrared region from 3.200 to 4.200  $\mu\text{m}$ , followed by strong water absorption between 5.000 and 8.000  $\mu\text{m}$ .

108. Salsbury and Hunt<sup>34</sup> studied the spectra of more than 200 minerals and 150 rock samples in the near infrared region. They found that the vast majority of the discernable features in igneous, sedimentary, and metamorphic rocks occur as a result of the presence of two substances, iron and water. The only exception was the carbonates which display strong vibrational features due to the  $\text{CO}_3$  ion; however, the carbonate and water characteristics tend to be obscured by atmospheric absorption.

109. Figure 70 displays the spectral curves for igneous rock measured by Salsbury and Hunt. Most of the igneous rocks display spectral features near 1.4, 1.9, and between 2.2 and 2.3  $\mu\text{m}$ , with the feature at 1.9  $\mu\text{m}$  being more intense. These features are caused in part by water in fluid inclusions, which are common in such rocks. The graphic granite, which was formed during a late stage of differentiation when the melt was rich in water, has abundant water present in microscopic fluid inclusions within the quartz and feldspar. The "dryer" granite shows fewer features in the infrared region.

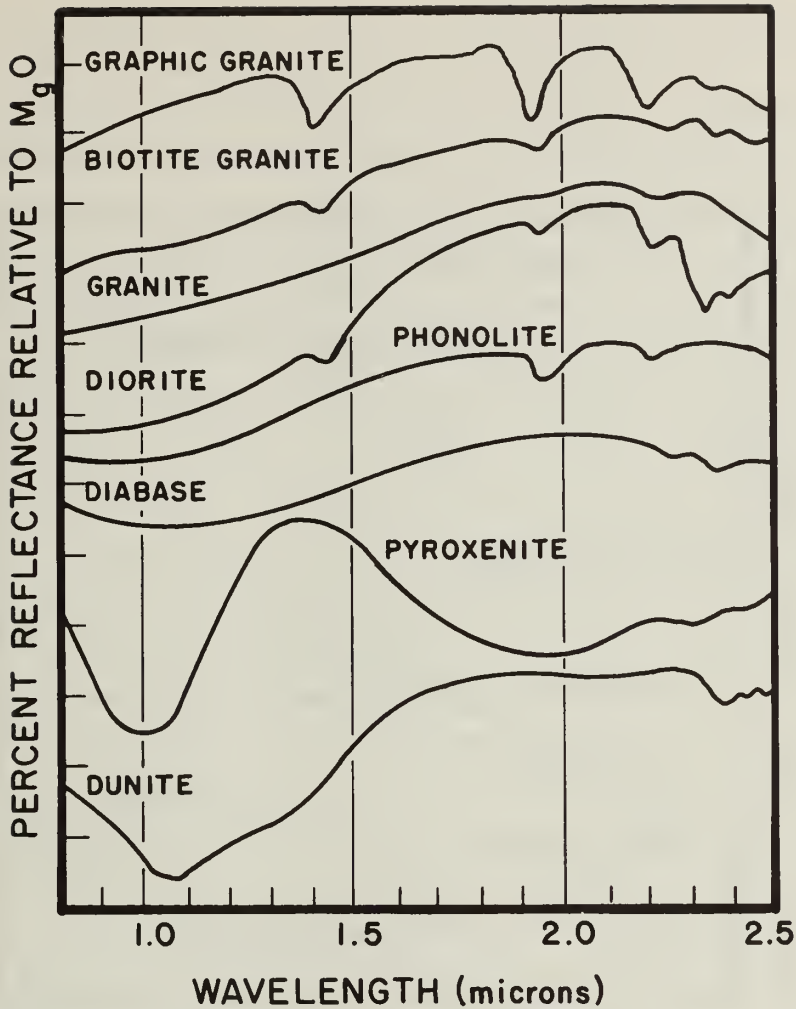


Figure 70. Spectral reflectance of igneous rocks in the near infrared region of the electromagnetic spectrum<sup>34</sup>

110. The intermediate igneous rocks in Figure 70 show a progressive reduction in the magnitude in these bands. As noticed in the visible range (Figure 66), the higher magnetite content tends to obscure spectral features. The intermediate rocks, however, possess weak ferrous bands at  $1.1 \mu\text{m}$ . In addition, alteration of plagioclase yields a well-defined water band near  $1.9 \mu\text{m}$ . The diabase spectrum is typical of basic rocks exhibiting subdued features due to the high magnetite content. Basalts, the end results of extremely abundant magnetite, yield a flat featureless spectra. As in the visible region, the ultra basic

rocks show strong ferrous bands ( $1.0$  and  $2.0 \mu\text{m}$ ) making it possible to distinguish them by using multispectral techniques.

III. Spectra for several sedimentary rock types are provided in Figure 71. The sedimentary rocks tend to display characteristic

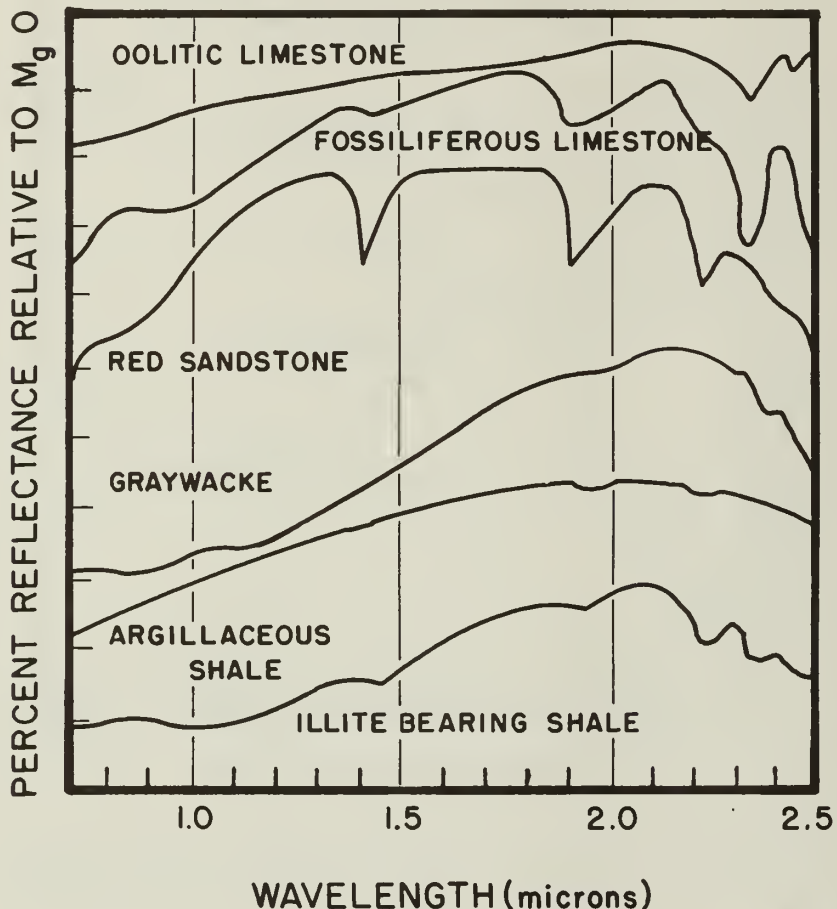


Figure 71. Spectral reflectance of sedimentary rocks in the near infrared region of the electromagnetic spectrum<sup>34</sup>

features due to vibration of the carbonate radical. For this reason, the limestones display diagnostic features between  $1.9$  and  $2.5 \mu\text{m}$ . Unfortunately, these features lie in a region characterized by high atmospheric absorption, which makes their detection difficult. Most limestones show features at  $1.4$  and  $1.9 \mu\text{m}$  due to ferrous iron, and all show a rapid falloff in the blue. When argillaceous or carbonaceous materials are present, the contrasts of the above features and the overall reflectivity are reduced in a manner similar to the reduction of

reflectivity in igneous rocks due to increases in magnetite content.

112. Sandstones show strong H<sub>2</sub>O and OH bands at 1.4, 1.9, and 2.20  $\mu\text{m}$ , due to water in the fluid inclusions within the quartz grains. Sandstones with a calcerous cement will commonly exhibit a carbonate feature at 2.30  $\mu\text{m}$ . Shales generally contain enough carbonaceous material to significantly reduce all spectral detail.

113. Spectra for several metamorphic rocks are shown in Figure 72. These rocks are spectrally more variable than the other major rock classes. Marble is spectrally very similar to pure calcite (Figure 64d), showing distinctive features at 1.88, 2.0, 2.16, and 2.35  $\mu\text{m}$  due to carbonate bands. Even impure marbles show the 2.35- $\mu\text{m}$  carbonate feature. These carbonate bands coupled with the high reflectivity in the near infrared make the marbles a distinctive group.

114. The Condit<sup>35</sup> study of American soils included the near infrared region as far as 1.0  $\mu\text{m}$  (Figure 69a, b, and c). Although the Category I and Category II soils show very little spectral variance in this region, the Category III soils show a flattening of slope between 0.760 and 0.800  $\mu\text{m}$  with some soils decreasing in reflectivity in this region. The reflectance for the Category III soils increases in the wavelength interval 0.88 to 1.0  $\mu\text{m}$ .

115. With the exception of the iron bands, most of the spectral features exhibited by rocks in the near infrared region are obscured by atmospheric absorption. Thus, the overall reflectance contrasts between rock types is presently the most promising feature for rock discrimination in this region. The reflectance contrast between pyroxenite and dunite is higher in the near infrared as is the reflectance contrast between the illite-bearing shale and argillaceous shale. However, unless ground studies indicate significant advantages in reflectance contrast in the near infrared, imagery in the visible region is adequate for interpretation of rock types and soils.

116. The most intense spectral responses in the near infrared region are due to reflectance of vegetation. Plant reflectance in the visible region is dominated by pigments (primarily chlorophylls a and b, carotines, and xanthophylls). The strong reflectance in the near

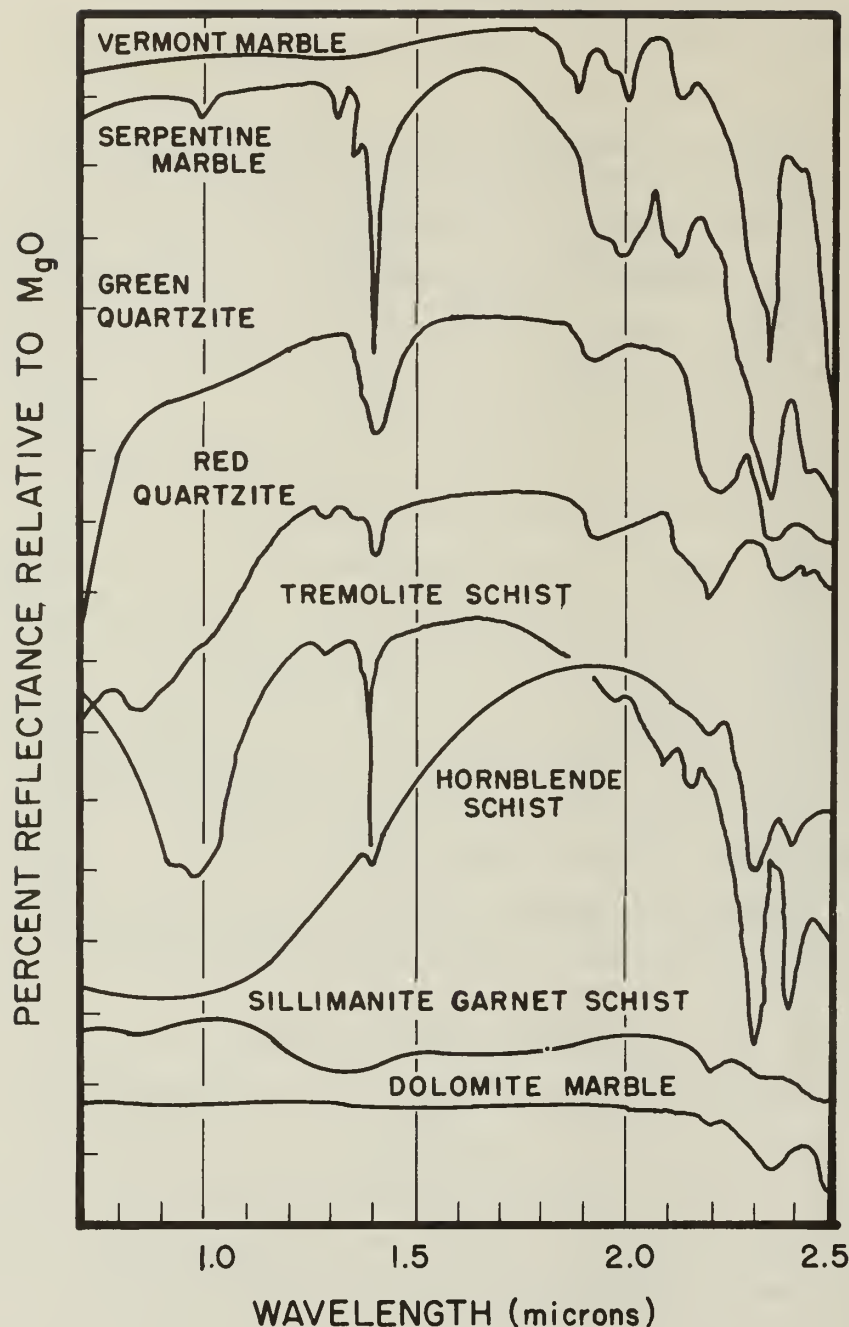


Figure 72. Spectral reflectance of metamorphic rocks in the near infrared region of the electromagnetic spectrum.<sup>34</sup>

infrared is caused to a considerable degree by the internal structure of leaves and water concentration in the plant tissues (Figure 73).



Figure 73. Low oblique photograph of a citrus orchard re-planted due to nematode infestation. Older trees have been removed and the soil treated. The blue color to trees at the left edge of the image and left top indicate some trees still under stress. (Photograph by G. G. Norman, Florida Department of Agriculture, Division of Plant Industry; from Applied Infrared Photography, A Kodak Technical Publication M-28, 1968.)

117. The location and amplitude of spectral peaks in the near infrared region appear to be controlled by a number of parameters, including: (a) leaf maturation, (b) leaf structure, (c) leaf water content, (d) leaf pigments, (e) leaf damage, (f) leaf pubescence, (g) leaf senescence, and (h) leaf salinity. Thus, subtle differences in vegetation may provide clues to rock and soil type or stress in vegetation along a fault, which are readily distinguishable on aerial imagery in the near infrared region.

Response of Earth Materials to Radiation  
in the Thermal Infrared Region

118. The thermal infrared region includes radiation with wavelengths ranging from approximately 4 to 14  $\mu\text{m}$ . Two atmospheric windows

are available for sensing: from 3.5 to 5.5  $\mu\text{m}$  and 8 to 14  $\mu\text{m}$ . The 8-to-14- $\mu\text{m}$  window is the most commonly used in remote sensing. Since the earth's spectral exitance peaks at approximately 9.66  $\mu\text{m}$  (Figure 60), the earth dominates this spectral region with its temperature (300 K). Thermal energy is also generated through absorption of solar energy by the atmosphere and the earth and reemittance at thermal wavelengths. This contributes significant diurnal variations to thermal imagery.

119. Imagery in the thermal infrared region is collected using scanning systems similar to the multispectral scanner on Landsat. Ordinary photographic film is not sensitive to wavelengths in the thermal infrared region. Although it would be technically possible to coat a film with a material sensitive to this energy, the thermal energy generated by the camera would cause the film to fog, necessitating a cooling system capable of cooling the camera to approximately absolute zero. To circumvent this problem, optical mechanical scanners are used which consist of a detector coated with an infrared-sensitive material at the end of an electric wire. This detector is usually the size of a pinhead which can be cooled even in airborne systems.

120. Mathematical models can be used to provide frames of reference in which the thermal behavior of geologic materials can be understood and predicted. Models developed by Watson<sup>37,38</sup> utilize the parameters of rock and soil properties (thermal inertia and reflectance), atmospheric effects (transmission and effective air temperature), site location (latitude), and season (sun's declination). Some general results of the model behavior using representative values are shown in Figures 74-77. Generally, the model results indicate that those rocks with the highest thermal inertia have the lowest diurnal temperature change (reflectance being equal (Figures 74 and 75)) and, therefore, appear cooler during the day and warmer during the night than rocks with low thermal inertia. Materials with equal thermal inertias but differing reflectances show the greatest temperature contrast during the day and the lowest contrast at dawn. Since the effects of thermal inertia are maximized and the effects of reflectance are minimized, the optimum time to observe thermal contrasts due to variations in the thermal

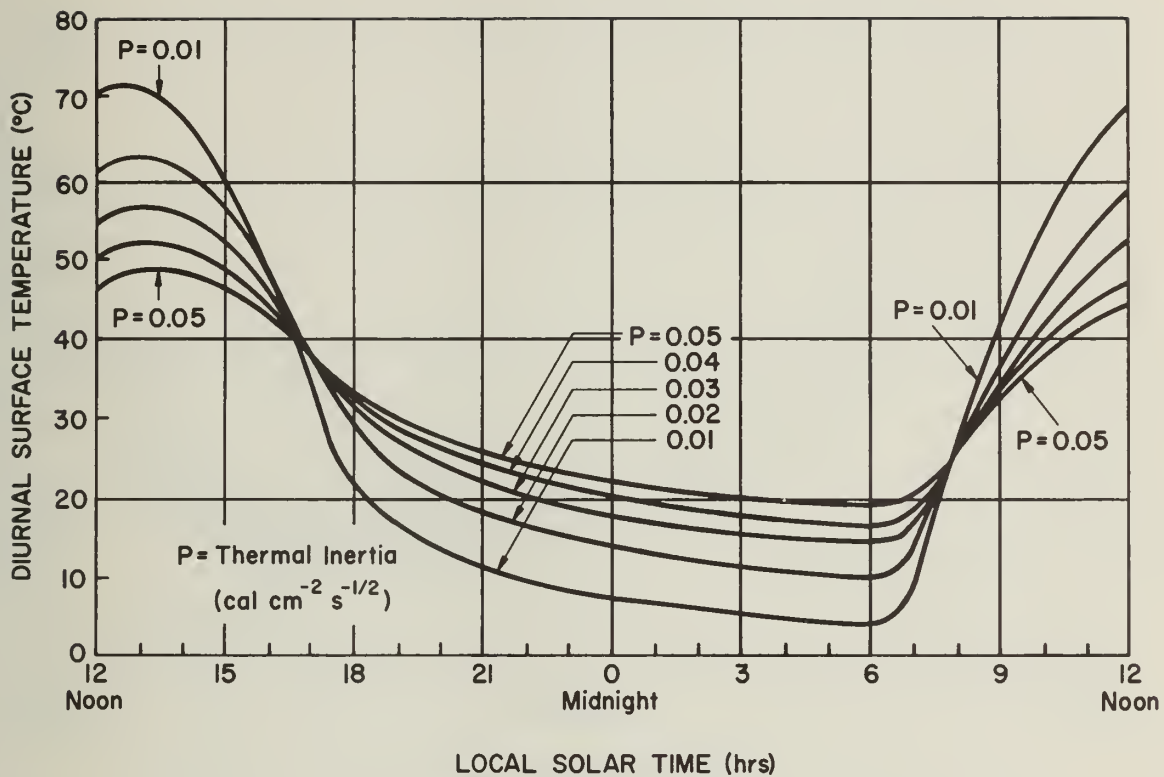


Figure 74. Diurnal variation of thermal inertia for rocks calculated from model of Watson.<sup>37</sup> The rocks having lower thermal inertias (0.1) are warmer during the day and cooler at night than rocks having higher inertias even though the reflectances (Figure 75) may be equal

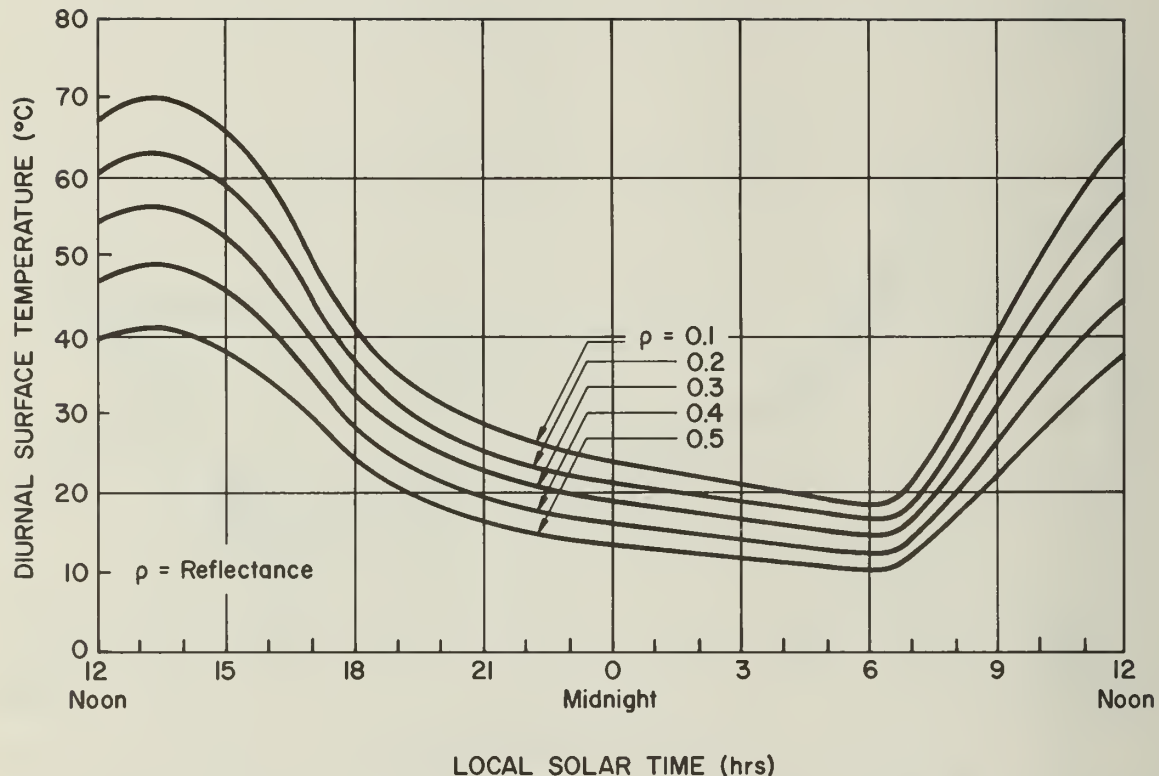


Figure 75. Diurnal variation of reflectance for rocks calculated from the model of Watson.<sup>37</sup> Compare with Figure 74; two rock units having a reflectance of 0.1 and 0.2 may not be distinguishable on conventional imagery; however, if one unit had a thermal inertia of 0.01 and the second an inertia of 0.05, they could be distinguished on thermal imagery

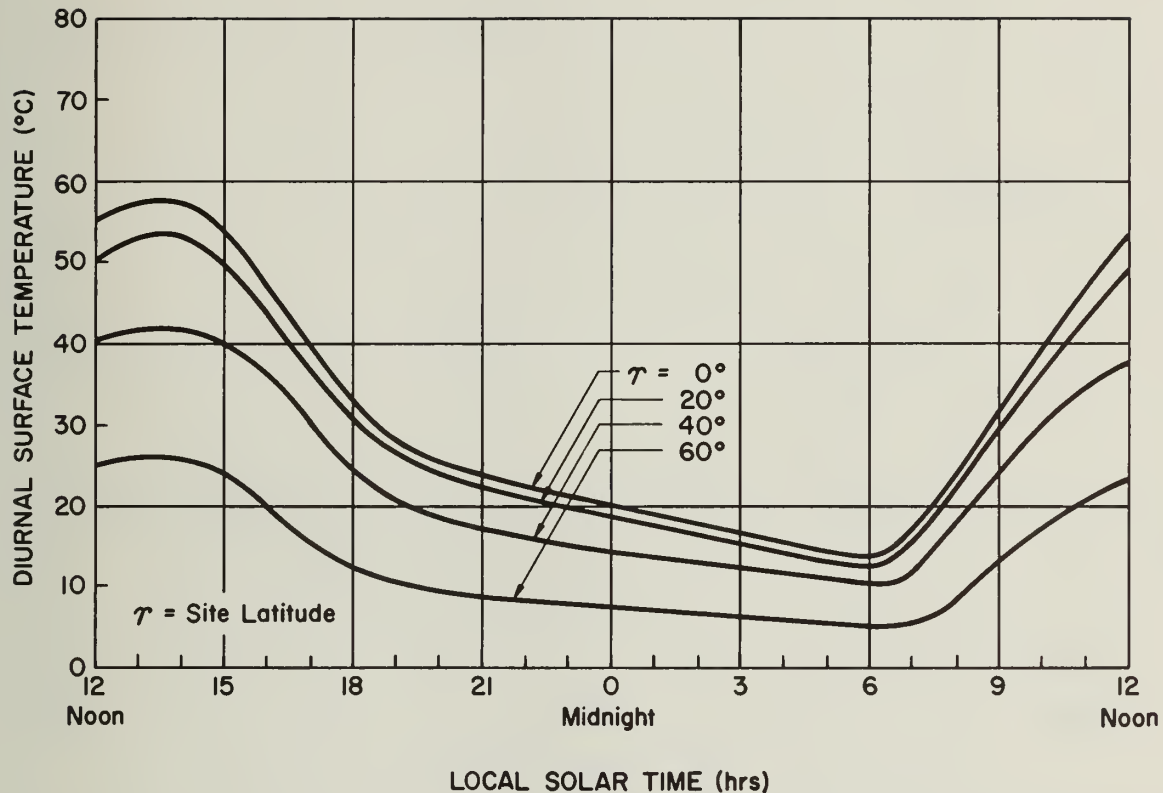


Figure 76. Diurnal variation of rock surface radiometric temperature as a function of latitude of a site.<sup>37</sup> Northern latitudes ( $60^\circ$ ) show less variation than lower latitudes. Compare with Figure 23 for a site at latitude  $40^\circ$

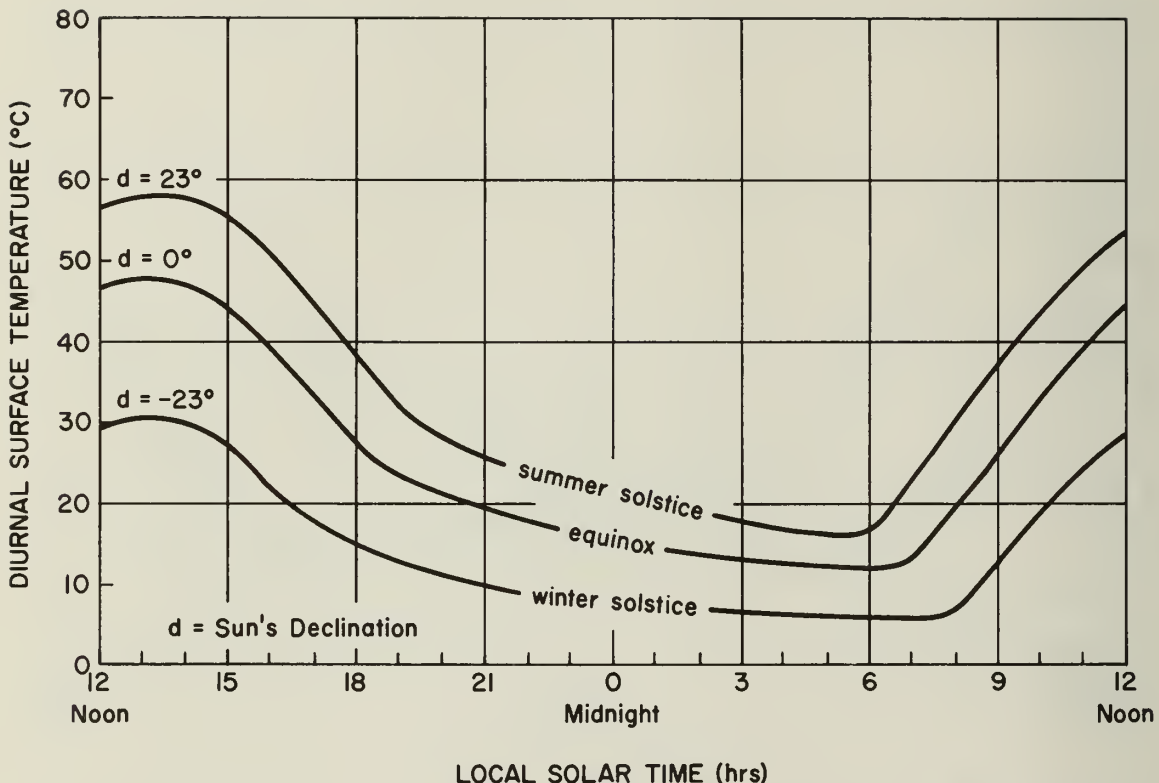


Figure 77. Diurnal variation of rock surface radiometric temperature at different times of the year.<sup>37</sup> For temperature variations, the summer solstice is optimum for thermal differentiation of rocks

properties of earth materials is at dawn. Because energy in this region is not due to solar reflection, flights can be made a short time after sunrise and still preserve the dawn thermal contrasts.

121. Surface coatings or degradations due to weathering, chemical contamination, or lichen cover affect a rock's thermal properties in three ways: (a) they produce changes in the reflection characteristics, (b) they modify the spectral emissivity of the surface, and (c) they reduce the average thermal properties.

122. Models by Watson<sup>37,38</sup> incorporating an insulating layer over a conducting half-space indicate that the insulation provided by a 1-mm-thick cover of lichen or soil is negligible, but as the layer thickness approaches 1 cm for lichen and 10 cm for soil, the thermal properties approach those of an infinitely thick soil layer. Thus, good geologic exposure similar to those provided by arid to semiarid regions are prerequisites for geologic interpretations of rock types using thermal imagery.

123. A tradeoff must be made between spatial resolution and thermal resolution with the size of the sensor aperture determining both. A large aperture system is more effective for applications where high spatial resolution is not as important as the measurement of small temperature variations (high signal resolution). Small aperture systems are more effective when accurate location of anomalies is more important than measuring the absolute thermal magnitude of the anomaly.

124. In the spectral range from approximately 4 to 6  $\mu\text{m}$ , the increase in emitted energy is approximately the 10th power of the temperature for earth ambient temperature; thus, imagery in this region is sensitive to minute changes in temperature. However, reflection of solar radiation is still significant in this range. Although the energy emitted by the earth in the wavelength range between 8 and 13  $\mu\text{m}$  is a maximum, the energy increases linearly with temperature resulting in lower image contrasts but better quantification of temperatures.

125. In soils, the temperature is a significant variable. The soil moisture and soil-air humidity are the most important factors influencing the thermal characteristics of soils. Thermal imagery of

soils has the unique characteristic of being influenced by subsurface changes in moisture content within the top few centimetres. Caution should be used in choosing the season for image recording since the presence of vegetation affects the soil temperature. A grass cover does not greatly alter mean daily soil temperatures, but the temperature control mechanism of most plants effectively masks the measurable soil moisture characteristics. Haugen et al.<sup>39</sup> reported that:

although much detail on land-use patterns is portrayed in thermal imagery, its application in a mapping program should be limited to a few specialized areas....For general mapping efforts the low resolution, narrow field of coverage, lack of geometric control and expense preclude the use of thermal imagery.

The authors agree with this assessment for general mapping purposes; however, the thermal region may provide valuable information in specific areas where thermal discontinuities aid in earthquake hazard assessment (Figures 78 and 79).

#### Response of Earth Materials to Radiation in the Microwave Region

126. Electromagnetic radiation in the microwave region is generally separated into two types for remote sensing applications. These are passive microwave and active microwave. Passive microwave radiometers measure naturally emitted microwave energy from earth materials, while active microwave systems generate a signal and measure its intensity and travel time upon reflection from earth materials.

##### Passive microwave radiation

127. Passive microwave remote sensing consists of measurements of electromagnetic radiation in the range from approximately 1 mm to 1 m. This type of imagery holds promise as an all-weather image acquisition technique and as a sensor of near-surface temperature variations. Long wavelength (1 m) sensors provide a means for subsurface analysis through the broad variation in dielectric properties of surface materials and subsurface moisture content.

128. Most currently available passive microwave radiometers



Figure 78. Vertical aerial photograph of the San Andreas fault, California. The fault extends across the center of the image. The fault is marked by a topographic discontinuity, erosional variations, and offset streams. Several subparallel faults can be seen to the east of the main fault. Note the orthogonal pattern of roads and fences



Figure 79. Thermal infrared image of the San Andreas fault, California. This image of the same area as Figure 78 shows the main scarp of the San Andreas fault as a sharp contrast in tone. The darker areas correspond to cooler areas, and the tone contrast is due to near-surface moisture on the east side of the fault and a relatively warmer ridge on the west. The subparallel branches (Figure 78) are not visible on the thermal scan and the orthogonal road system has been transformed into a curvilinear system due to the scanner. Significant geometrical corrections and field checks are required before accurate mapping may proceed.

operate in the range from approximately 8 mm to 0.7 m with experimental instruments being developed in the following wavelength ranges: 5, 3.3, 2, and 1.3 mm.<sup>40</sup> Below approximately 20 mm, the atmosphere attenuates electromagnetic radiation exponentially down to approximately 1 mm where little propagation is possible. The angular resolution of passive microwave systems is currently two or three orders of magnitude poorer than infrared radiometers so that the gain in weather penetration and subsurface sensing is accompanied by a loss in spatial resolution. In general, the parameters that affect the microwave radiation of earth materials are soil moisture, surface roughness, particle size, density, reflectance, and mineralogy. Materials with large dielectric constants, such as water, and materials with high conductivity, such as metal, appear cool on microwave imagery. Surfaces appear warmer as the conductivity, dielectric constants, and moisture content go down and the surface roughness increases (Figure 80).

129. The dielectric constant of soils changes significantly as the moisture content increases. Thus, increasing the soil moisture increases its reflectance and decreases its emissivity, causing the radiation of dry soils to be dominated by their emissivity and of wet soils by their reflectance. Measurements of the radiometric temperature of various soils as a function of incidence angle are given in Figure 81 for radiation having a wavelength of 8 mm. These curves indicate that as soil moisture content increases, the response approaches a response characteristic of water (the inundated mud). The totally saturated mud is substantially warmer than the inundated mud, and there is a large difference between the temperature of the mud and the dryer soils (water content = 10 percent and less). The temperature difference is greater at small angles of incidence with the playa and mud (possessing essentially the same composition and grain size) differing by 94°K at an incident angle of 10°. This temperature change corresponds to 0.8°K per percent change in moisture content. With radiometers capable of achieving accuracies of 0.5°K, one could conceivably measure changes in moisture content as small as 1 percent. The effect of polarization also increases as moisture content increases. Curves for horizontally polarized

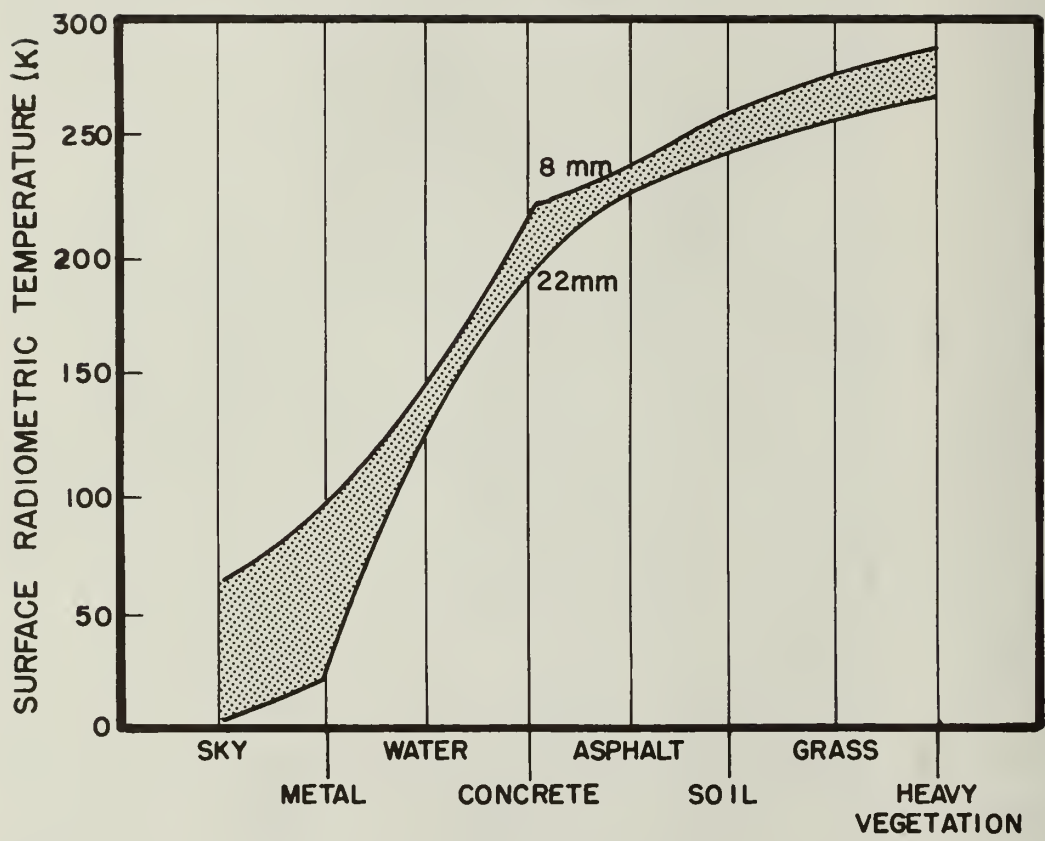


Figure 80. Surface radiometric temperature for various materials<sup>40</sup>

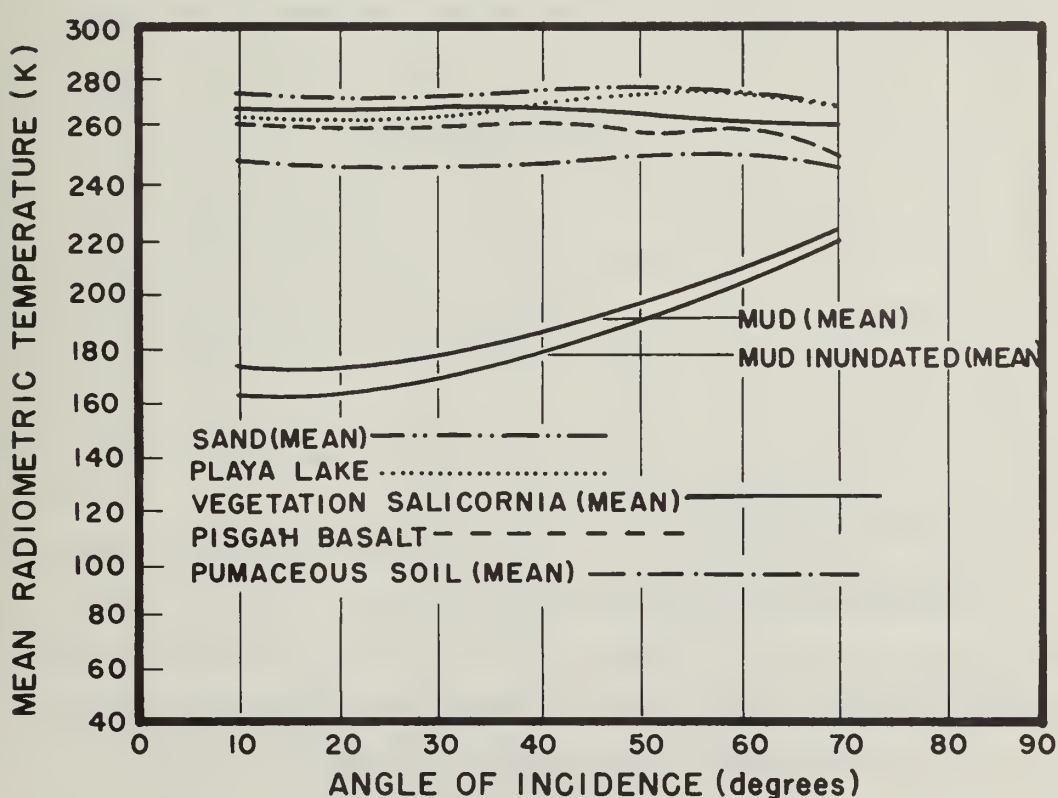
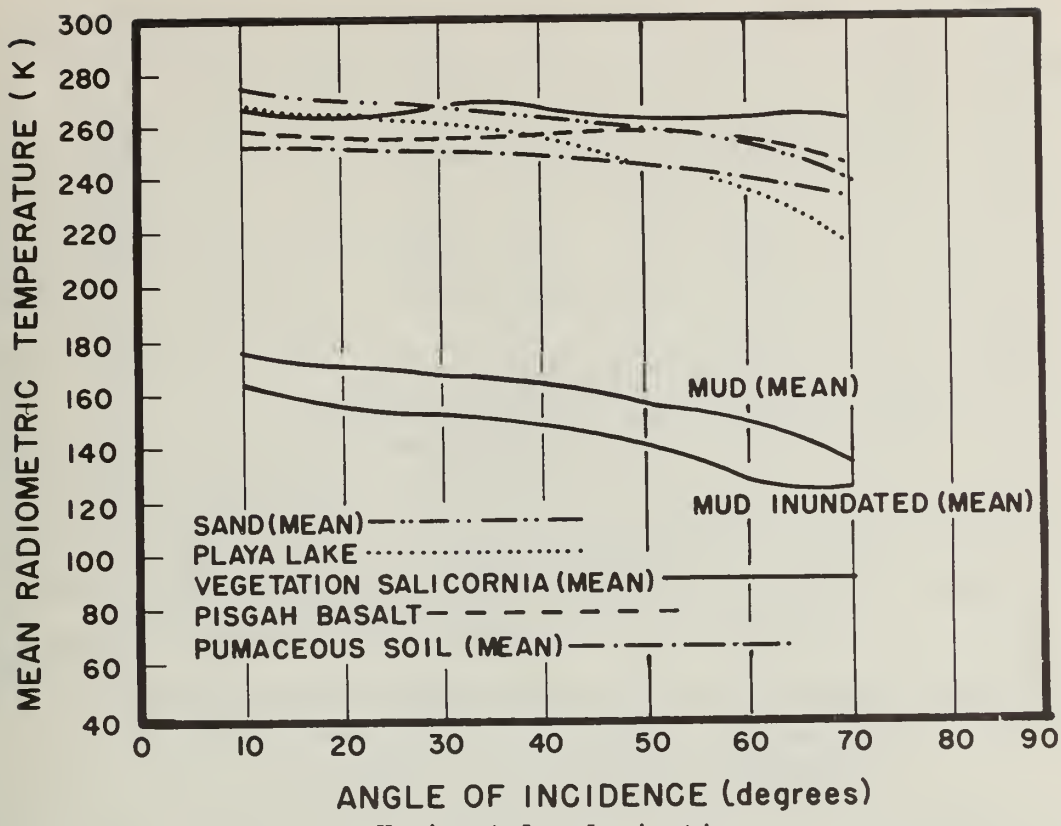


Figure 81. Mean radiometric (8mm) temperature for various soils as a function of radiation incidence angle<sup>40</sup>

microwave energy show larger temperature variations than for vertically polarized energy.

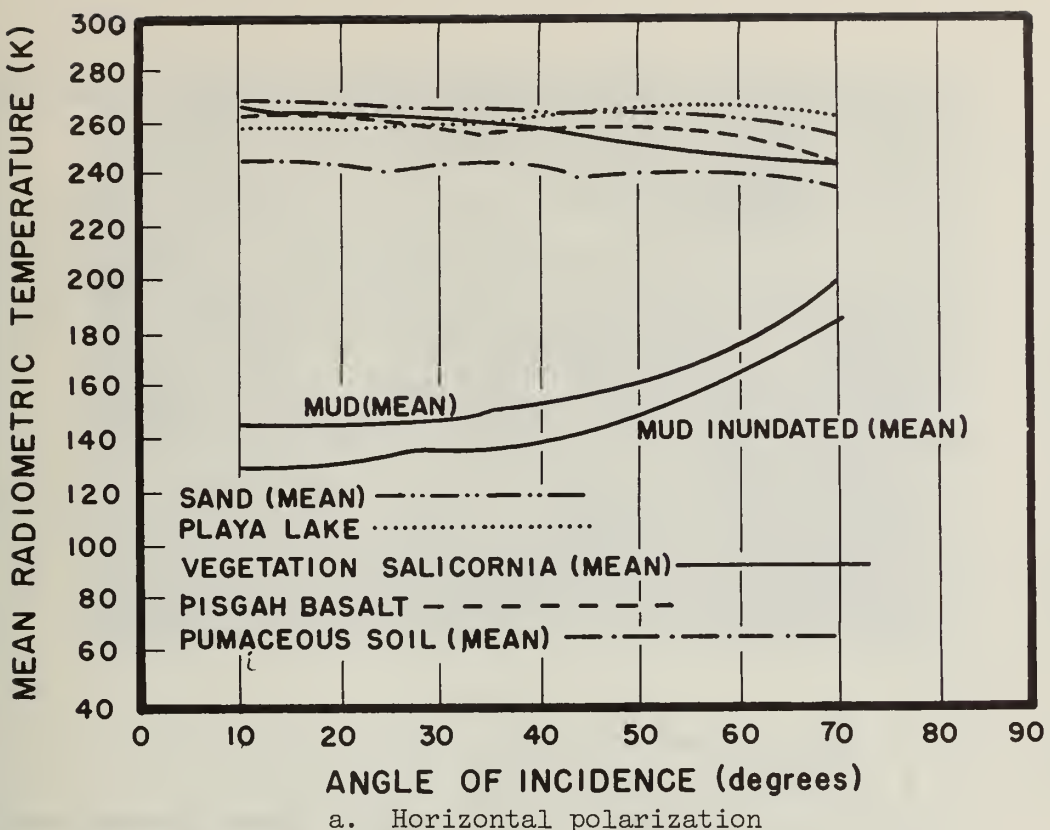
130. Similar measurements at a wavelength of 22 mm result in more evident moisture content effects due to the greater surface penetration of the longer wavelength energy. The temperature difference between the mud and playa sediments in this wavelength band (Figure 82) is 112°K. The longer wavelengths are more sensitive to changes in moisture content and less sensitive to surface roughness.

131. Measurements for a single material taken at different moisture contents show similar results (Figure 83). The temperatures decrease significantly as the moisture content increases. Additionally, the parameter  $\Delta T = T_v - T_h$  changes significantly with water content. The temperature changes are not linearly related to moisture content, suggesting the existence of a complex relationship between the moisture content and the dielectric constants for soil and water.<sup>40</sup>

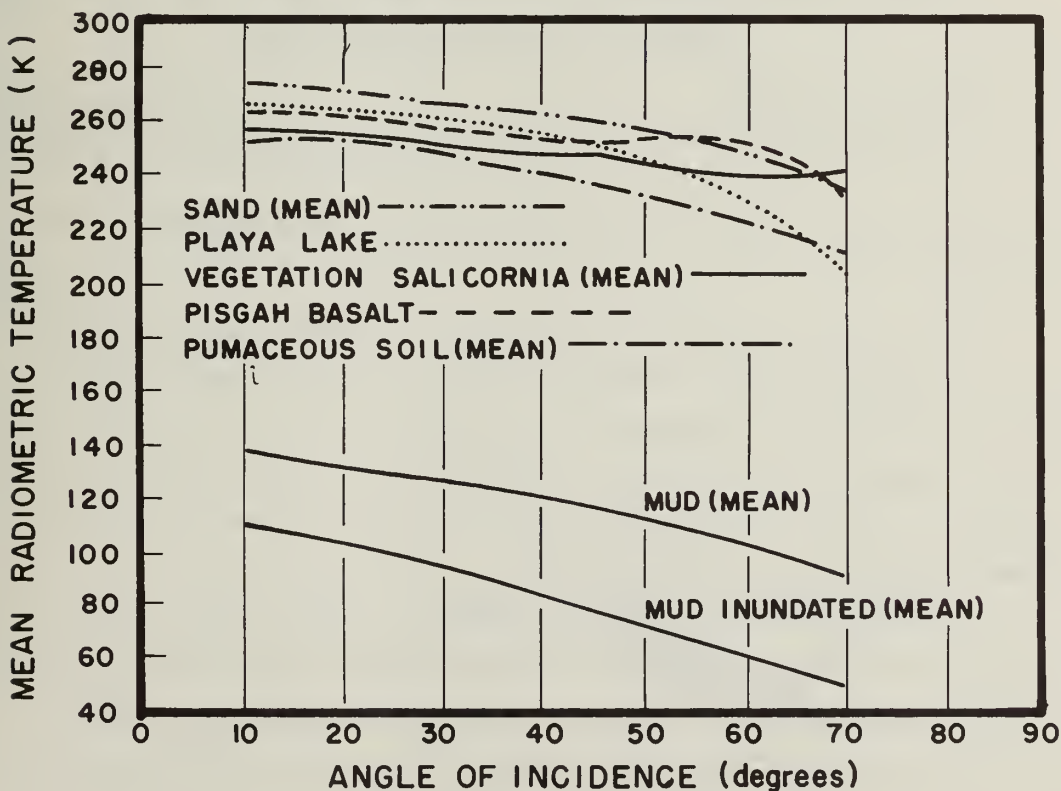
132. Interpretation of passive microwave imagery depends upon an understanding of the relative contributions of reflectance (atmospheric sources), emittance (upper soil or rock), and transmittance (through the surface layer from deeper layers). Also, some objects exhibit a temporal change in radiometric temperature due to fluctuations in actual object temperature, changes in atmosphere temperature, or changes in the reflection and emittance properties of the object. A major limitation to passive microwave remote sensing is the poor spatial resolution currently available. The ground resolution of the NASA PMIS system results in pixels 140 m long and 56 m wide when imaged at a flight altitude of 1300 m.<sup>39</sup> This results in a poorer resolution at 1300 m than can be obtained by the Landsat 2 multispectral scanner at 817 km.

#### Active microwave systems

133. Early development of active microwave systems dealt primarily with Radio Detection and Ranging (RADAR). The term radar has become a generic name for a broad class of active electromagnetic sensing systems, operating in the microwave region and at longer wavelengths, which have capabilities that far surpass the original concepts. These systems are termed active because they supply their own irradiation.



a. Horizontal polarization



b. Vertical polarization

Figure 82. Mean radiometric (22 mm) temperature for various soils as a function of radiation incidence angle<sup>40</sup>

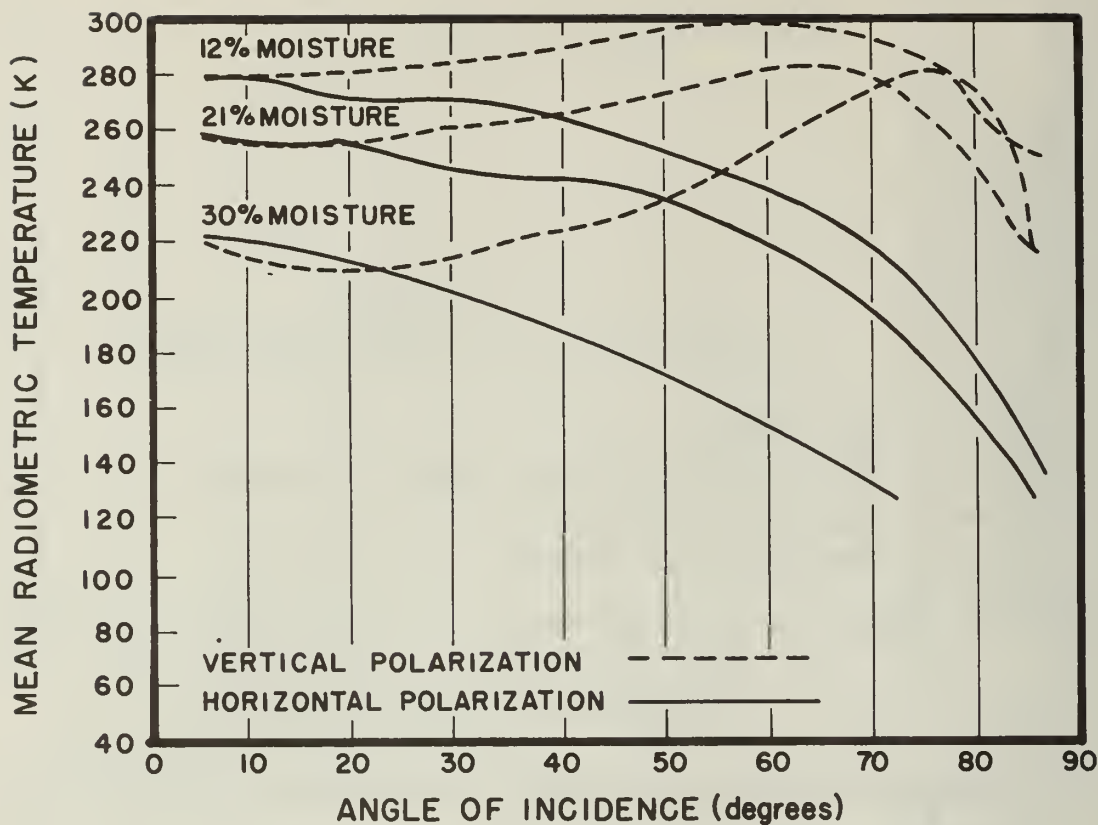


Figure 83. Radiometric (22 mm) temperature of a playa deposit as a function of incidence angle for samples having different moisture contents and polarity<sup>40</sup>

The low irradiation angle results in enhancement of topographic features (Figure 84).

134. There are basically two types of radar systems available for remote sensing use: one provides an image of the surface (imaging radar), and the other measures the proportion of transmitted electromagnetic radiation returned as a function of  $\beta$  angle (scatterometer). The imaging radar is the most popular type and will be the only type treated in the present discussion.

135. The microwave region is characterized by very little emitted energy from the sun or the earth, yet microwave energy may be man-made at high intensities. As a result, several parameters are under the control of the operator, including timing, strength, phase, and polarization. Radar is unidirectional compared with solar and sky radiation,



Figure 84. Radar image of Managua, Nicaragua. The low irradiation angle accentuates topographic features. The dark interiors of volcanic cones show strikingly against the strong return from urban Managua

which is scattered by atmospheric particles. Consequently, radar irradiates and receives energy reflected from only those surfaces on a line of sight from the antenna (Figure 85).

136. Imaging radar returns appear very similar to standard aerial

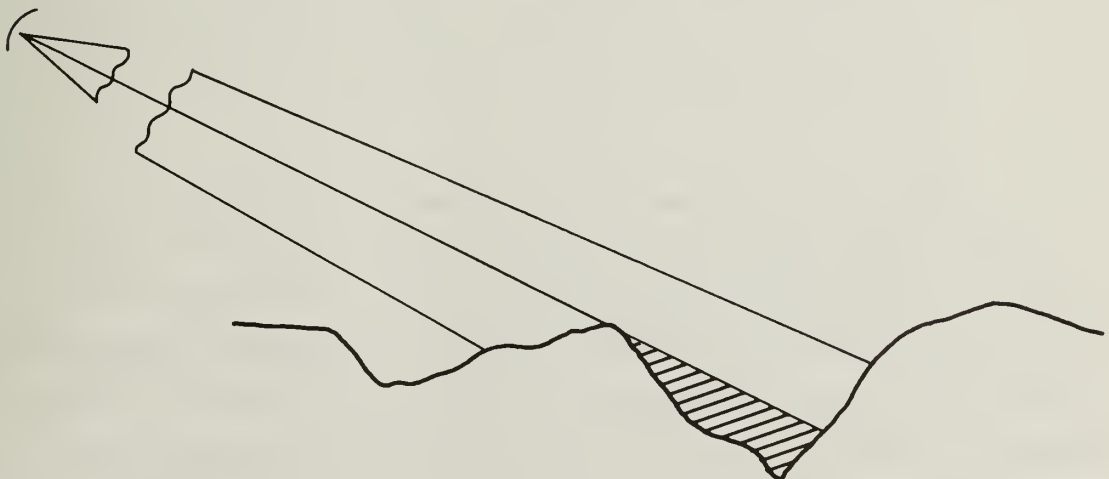


Figure 85. Unidirectional geometry of a radar system

photography, but the similarities are more apparent than real. Radar does not sense earth materials in the same manner as aerial photography, and since people have a tendency to relate images to familiar references such as aerial photographs, errors in interpretation may result. Once the wavelength ( $\lambda$ ), transmitter power, gain, and polarization of the radar system are fixed, variations in gray tones on the resulting image are due to variations in the polarization and look angle, the complex dielectric constant, the wavelength, and the surface roughness, not to variations in color as is the case with panchromatic photography.

137. Polarization and look angle. Imaging radars usually transmit a horizontal electric field vector and receive either horizontal or vertical return signals or both. Since radar images from like-polarized returns look different from images from cross-polarized (or depolarized) returns, differentiation of some geologic units is possible. Like-polarized returns generally arise from quasi-specular reflection and scattering. There tends to be a strong return near  $0^\circ$  incident angle. Since most imaging radars transmit at moderate to large incident angles, the scattering process plays a dominant role in like-polarized returns.

138. Cross-polarized returns can generally be attributed to the following four causes:<sup>40</sup>

- a. Quasi-specular reflection due to the difference between the Fresnel reflection coefficients for a homogeneous, undulating two-dimensional smooth surface.
- b. Multiple scattering due to target surface roughness.
- c. Volume scatter due to nonhomogeneities within or on the surface.
- d. Anisotropic properties of the target.

Only the first three are commonly encountered in practice.

139. Complex dielectric constant. The electrical properties of a surface, as expressed by the material's complex dielectric constant, significantly affect radar return. Since the dielectric constant varies almost linearly with the moisture content per unit volume,<sup>29</sup> the radar return is strongly a function of this variable. Thus, the penetration is greatest and reflection least in materials with low moisture content. In addition, good conductors such as metals scatter radar waves more strongly.

140. Wavelength effects. The depth of penetration of radar waves depends upon the wavelength and complex dielectric constant of the surface. For example, penetration depth for wavelengths of 1 cm is negligible, but for wavelengths of 1 m the depth of penetration may range from 0.3 m for wet soil to 1 m or more for dry soil. Wavelength ranges for radar remote systems are summarized in Table 5.

Table 5  
Commercial Radar Systems

P-band - $\lambda =$	77.0	-	136.0 cm
L-band - $\lambda =$	15.0	-	77.0 cm
S-band - $\lambda =$	7.5	-	15.0 cm
C-band - $\lambda =$	3.8	-	7.5 cm
X-band - $\lambda =$	2.5	-	3.8 cm
K <sub>l</sub> -band - $\lambda =$	2.0	-	2.5 cm
Ku-band - $\lambda =$	1.67	-	2.0 cm
K-band - $\lambda =$	1.13	-	1.67 cm
Ka-band - $\lambda =$	0.75	-	1.13 cm
V-band - $\lambda =$	0.4	-	0.75 cm
F-band - $\lambda =$	0.23	-	0.4 cm
G-band - $\lambda =$	0.1	-	0.23 cm

141. Surface roughness. The dominant factor in determining radar return is surface roughness and topography. The roughness of a surface is given by the Rayleigh criterion (Equation 2) and results in either specular or diffuse reflection. Specular reflection yields the most intense contrasts on a radar scene resulting in either a strong return or no return. Three ways in which a radar antenna may receive a specular return are: (a) angle of incidence equal to  $0^\circ$ , (b) dihedral reflector oriented at  $90^\circ$  to radar beam, and (c) trihedral reflection.

142. Trihedral reflectors can be man-made and serve as ground control, or as reported by Rydstrom,<sup>41</sup> they can be formed by orthogonal jointing, as in basalts. In populated areas, the large numbers of corners and vertical walls result in strong radar returns (Figure 84). Due to the unidirectional nature of radar imagery, topographic features produce shadows (areas of no return). The criteria for the occurrence of shadows is the relationship between the radar depression angle ( $\beta$ )

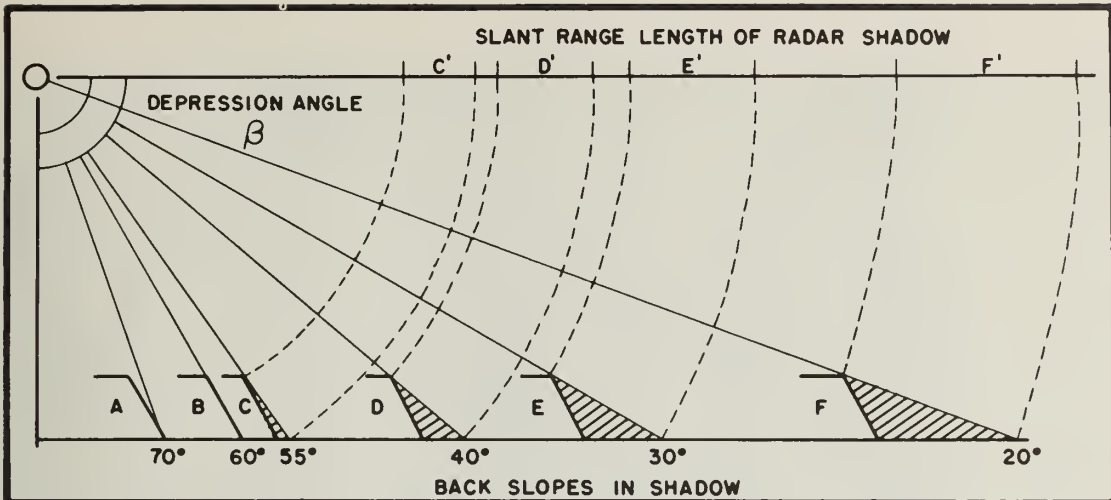
and the angle that the terrain feature's backslope (slope facing away from the radar beam) makes with the horizontal ( $\alpha_b$ ) (Figure 86a).

143. Assuming diffuse reflection, if  $\alpha_b$  is less than  $\beta$ , then the backslope is irradiated and no shadow is formed. At  $\alpha_b$  equal to  $\beta$ , the backslope is grazed by the radar beam, and for  $\alpha_b$  greater than  $\beta$ , the backslope is obscured and no return is received. This condition for shadowing ( $\alpha_b > \beta$ ) is valid only for the case where the flight line and the strike of the topographic feature are parallel. As the angle between the flight line and the feature ( $\alpha$ ) changes, the condition for shadowing changes as shown on Figure 86b. Once a shadow is formed, its length in slant range ( $S_s$ ) is directly related to the height of the terrain feature and to the total slant range ( $S_r$ ) and is inversely related to aircraft height  $H$  (Figure 86a). The relation is:

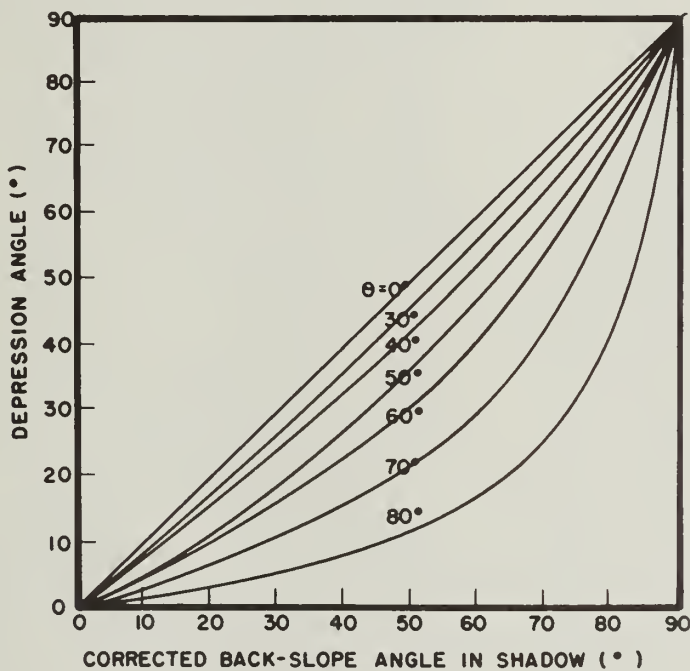
$$S_s = \frac{hS_r}{H} = \frac{h}{\sin \beta} \quad (3)$$

144. The length of a slope on radar imagery is determined by the length of time a slope is illuminated. Consequently, slopes appear shortened on radar imagery except in cases of grazing illumination. The radar length  $L_f = L \sin \phi$ , and the percentage of foreshortening  $F_p = (1 - \sin \phi) \times 100\%$  (Table 6).

145. In summary, radar return may be due to a number of rock or mineral constituents such as dielectric constant, moisture content, and surface roughness. For most presently commercially available radar systems, the image tone is primarily due to reflection from vegetation. This vegetation forms the predominant surface to radiation masking or overriding the contributions due to earth materials. Consequently, radar is advantageous in four circumstances: (a) where earthquake hazards are characterized by significantly different vegetation, (b) where there are significant topographic features, (c) where a region is characterized by sparse vegetation, or (d) where all-weather capabilities are important. Though present side-looking radar systems cannot match the geometric fidelity obtainable from stereoscopic aerial photographs, such imagery is valuable in areas of low vegetation or areas of



- a. Criteria for shadow formation in the case where the imaging aircraft flies parallel to structure (adapted from Janza<sup>40</sup>)



- b. Criteria for shadow formation in the case where the imaging aircraft does not fly parallel to structure (from Janza<sup>40</sup>). This curve can be used to correct backslope angles on radar imagery. If the slope at depression angle ( $\beta$ , Figure 86a) of 30° is shadow when the angle between the flight line and structure ( $\theta$ ) vary by 60°, the true backslope angle, from the curve, must be greater than approximately 48°. If the imagery is of recent scarps, this curve can be used to roughly evaluate youthfulness of the scarps

Figure 86. Shadow criteria for imaging radar

Table 6  
Foreshortening for Various Incident Angles

<u><math>\phi</math></u>	<u><math>\frac{F}{p}</math></u>
10	82.6
20	65.8
30	50.0
40	35.7
50	23.4
60	13.4
70	6.0
80	1.5
90	0.0

high degree of cloud cover. Rydstrom<sup>41</sup> suggests using extremely low-altitude radar imagery to reveal very subtle relief in arid regions in a similar fashion to low-sun angle aerial photography. In addition to the advantages mentioned above, radar can utilize opposing or orthogonal flight lines to alter the look angle, and preferential shadow enhancement of geologic structures (Figures 87 and 88).



Figure 87. Radar mosaic of western Montana. This mosaic was compiled from a series of flight lines trending horizontally across the figure. The look direction is toward the bottom of the figure (as opposed to Figure 88). The water appears black due to specular reflection and the topographic expression of a fault (arrows) is enhanced.



Figure 88. Radar mosaic of same area as Figure 87. In this mosaic, the look angle is toward the top of the figure (as opposed to Figure 87). Details along the strike of the fault are not shown in as much detail as in Figure 87. Note the strong return from the populated area in the valley in the upper left quadrant of the figure

PART IV: USES AND LIMITATIONS OF MULTISPECTRAL  
IMAGE ANALYSIS

Image Enhancement Techniques

146. Image enhancement:

refers to operations performed on an image in order to modify it in some useful way or to extract information on image properties for further analysis<sup>42</sup>

Image enhancement operations are generally used to improve the interpretability of an image and may achieve this goal at the expense of the aesthetic qualities of the original image. An example is edge enhancement which accentuates the sharp edges in a scene to the exclusion of the smoother, more gradual tonal contrasts. For the purpose of processing, which in most cases is essentially a mathematically derived procedure, an image or scene may be considered as a two-dimensional distribution of light intensity or hue, chroma, and saturation.

147. Upon digitizing a scene, each value of emulsion density on the image is assigned an integer to represent that density. Digitization allows scenes to be processed by digital computers and for these applications the image may be considered as a discrete array of numbers (a matrix). The elements of these matrices are called picture elements (pixels) and can be represented in statistical terms. The statistical character of the light intensity distribution in typical scenes is important to the application of enhancement techniques. For example, data derived from typical remotely sensed images tend to be characterized by low spatial frequencies.<sup>43</sup> These low frequencies dominate the scene and contribute to the macro-structure of the image. High spatial frequencies, though weak in absolute magnitude, contribute to the fine detail of the image and are often of more importance in geological interpretation. As one proceeds from one image element to another, the probability that the radiance values of each new point are equal is substantially greater than zero and increases as the points get closer together.<sup>43</sup> Two of the most significant statistical measures used for

image enhancement are the marginal probability density function and the joint probability density function.

#### Marginal probability density function

148. The marginal probability density function is defined<sup>42</sup> as the relative frequency of occurrence of scene radiance values (a histogram of gray scales). Generally the relative frequency of occurrence of low radiance values (dark) in a scene are higher than the relative frequency of occurrence of high scene radiance values. This causes a skewness of the marginal probability density function toward low values of scene radiance or to low values of object reflectivity (Figure 89).

#### Joint probability density function

149. The joint probability density function is defined<sup>42</sup> as the relative frequency of occurrence of pairs of radiance values at two points in a scene separated by a specific distance. Generally, as the distance between two points increases, the likelihood of the two points being of equal radiance decreases. Since there is a high probability that neighboring pixels possess the same radiance values, many enhancement techniques can be optimized by using every fifth or every tenth pixel in the enhancement algorithm rather than every pixel.

150. The statistical properties of a scene exert an influence on the choice of enhancement techniques to be applied to earthquake hazard studies.

151. Once the statistical properties of a scene (represented by the marginal and joint probability functions) have been assessed, enhancement techniques may be selectively applied based upon the statistical characteristics of the scene. Enhancement techniques can be separated into two classes: point operations and local operations.

#### Point operations

152. Point operations are also termed zero memory operations since each point of the image is operated on without reference to values of neighboring points. These techniques require a minimum of storage on a computer and can generally be accomplished using a look-up table algorithm. Point operation techniques are constrained to analyzing only

BAND 4 HISTOGRAM  
10000 PIXELS USED, TAKEN AT AN INTERVAL OF 5 PIXELS FROM IMAGE

MEAN = 37  
STANDARD DEVIATION = 6.9  
HISTOGRAM AND PERCENT HISTOGRAM FOLLOWS

0	0	0.00	16	.23	.00	3.2	707	.07
1	2	0.00	17	.46	.01	3.3	6.63	.07
2	3	0.00	18	.61	.01	3.4	7.00	.06
3	4	0.00	19	.81	.01	3.5	7.60	.06
4	5	0.00	20	.91	.01	3.6	7.97	.06
5	6	0.00	21	1.01	.01	3.7	8.00	.04
6	7	0.00	22	1.21	.02	3.8	8.00	.04
7	8	0.00	23	1.49	.02	3.9	8.15	.03
8	9	0.00	24	2.04	.03	4.0	8.25	.02
9	10	0.00	25	2.71	.03	4.1	8.41	.02
10	11	0.00	26	2.93	.03	4.2	8.46	.02
11	12	0.00	27	4.63	.05	4.3	8.68	.01
12	13	0.00	28	4.68	.05	4.4	8.70	.01
13	14	0.00	29	4.94	.05	4.5	8.72	.01
14	15	0.00	30	3.62	.04	4.6	8.77	.01
			19	.00		4.7	8.87	



Figure 89. Typical histogram (a portion of a Landsat scene (band 4)) of gray scales from a remotely sensed image. The predominance of dark tones is typical of most scenes that the authors have dealt with.

the value of the image point under consideration. Regardless of this constraint, several operations can be performed which may aid in interpretation of the image.

Level slicing or density  
slicing (equidensitometry)

153. In this technique, the density range (gray tones) is subdivided into a number of discrete intervals, and a discrete gray tone (or hue) is assigned to each. A possible algorithm for this operation is

```
if:           ( $0 \leq S(i,j) \leq a$ )       $S'(i,j) = 0$ 
if:           ( $a < S(i,j) \leq b$ )       $S'(i,j) = a$ 
            :
if:           ( $n-1 < S(i,j) \leq n$ )     $S'(i,j) = n - 1$           (4)
```

where

$S(i,j)$  = the original image value of point  $(i,j)$

$S'(i,j)$  = the new modified value at that point

154. The total number of levels ( $n$ ) may be any number less than the number of gray levels present in the raw data. Often  $n$  is set equal to  $a$ , which leads to a binary image containing only 1's and 0's. The steps between the levels need not be uniform (Figures 90, 91, and 92). Density slicing is a popular enhancement technique due to its simplicity, especially on a digital computer. However, the technique can be performed optically without expensive or special hardware.

155. One method of optical density slicing consists of partially developing a negative, thus producing a single gray level corresponding to an original density on the film. The negative is then reexposed to diffuse light for a short period of time increasing the density of the undeveloped portions of the negative. Further development extracts the next gray tone and so forth. The amount of density levels depends upon the developing and exposure times. One drawback is that the original image is changed. Agfacontour film is a commercially available film for this purpose.  
<sup>44</sup>

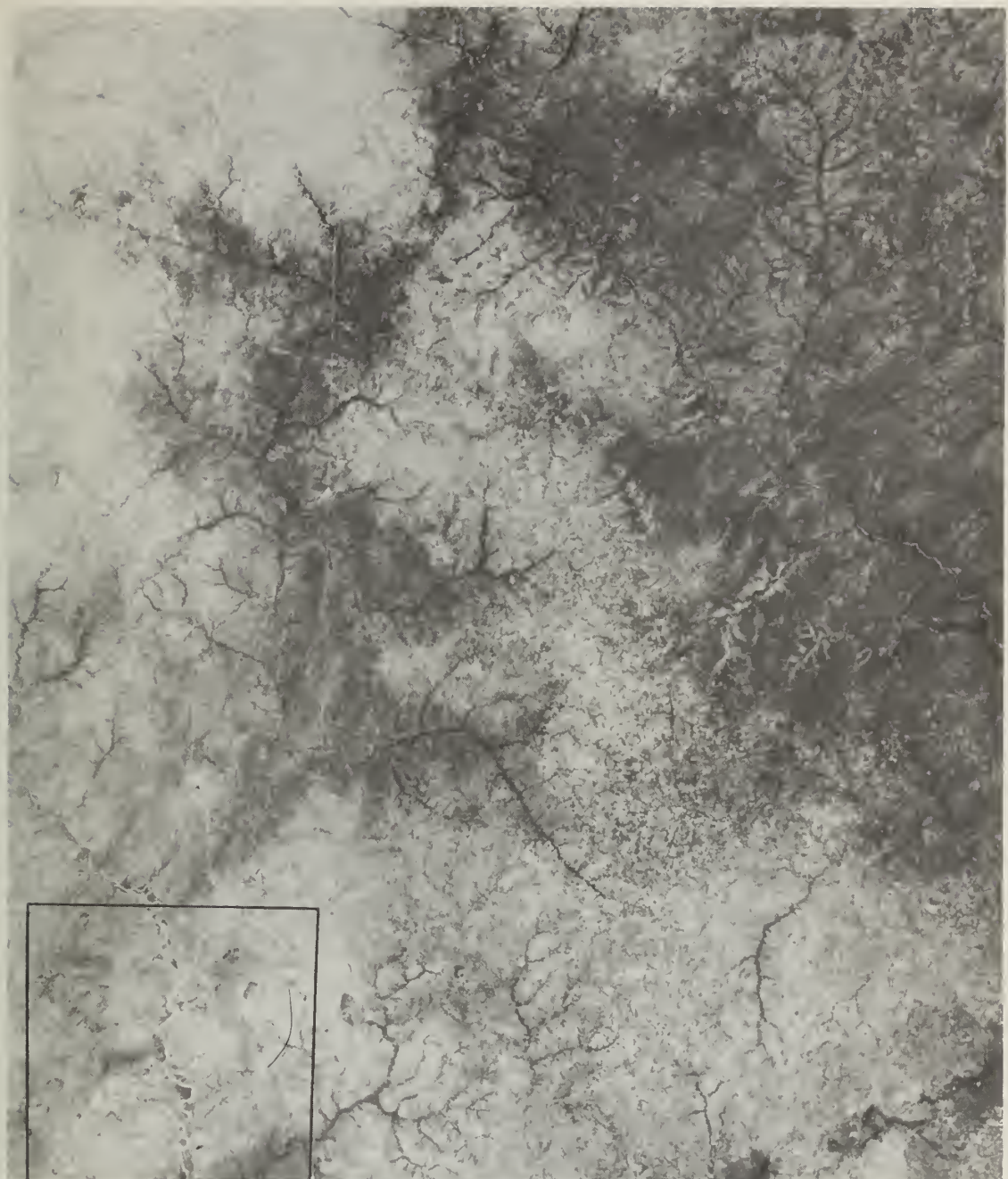


Figure 90. Landsat image of Ghana. This band 4 image was produced from a computer compatible tape (CCT) at the University of Arizona. The image has been destriped and an area (lower left corner) extracted to demonstrate several enhancement techniques



Figure 91. Band 7 image corresponding to the area denoted in Figure 90. This image has had no enhancement applied with the exception of destripping and geometric corrections



Figure 92. Density slice of Figure 91. The density range of Figure 91 has been separated into five levels and a specific tone (gray level) associated with each. This image makes features having larger areal extents easier to interpret and the water bodies stand out with respect to land areas

156. A more elaborate technique, but one which preserves the original image, has been reported by Nony and Cazabat.<sup>45</sup> In this method, the original photograph is copied onto extremely high contrast film, resulting in a binary mask. By changing the exposure, the light-dark boundary can be shifted on the density scale and a set of different masks produced. Contact copies of these are then produced to show the light/dark pattern in reverse. It is then possible to extract and enhance various density levels by combining the masks and counter masks and exposing color film (Figures 93, 94, 95, and 96), or by using a color additive viewer. It is the authors' experience that these photographic techniques require a significant amount of time and experience in dark room techniques before useful results can be acquired. There are numerous optical density slicing machines commercially available, however, which make optical density slicing routine. This equipment generally assigns a hue to each density level and displays the result on a screen for easy interpretation. The authors recommend this equipment over the cumbersome photographic techniques. Density slicing is useful for relatively large areal subjects. For investigation of active faults, boundaries (edges) and lineaments (lines) are more important than the zones between them, and density slicing for lineaments and fault evaluation may be of limited value. Density slicing has not been thoroughly tested for other earthquake hazards.

#### Contrast modification

157. This technique, also called contrast enhancement and contrast stretching, corresponds to accentuating intensity ratios between elements of the image. Some typical algorithms for this technique are

$$\begin{aligned} \text{linear modification; } & y = ax + b \\ \text{logarithmic modification; } & y = b \log(ax) + c \\ \text{exponential modification; } & y = b \exp(ax) + c \\ \text{general nonlinear modification; } & y = f(x) \end{aligned} \tag{5}$$

where

$x$  = original image element

$y$  = final enhanced image element

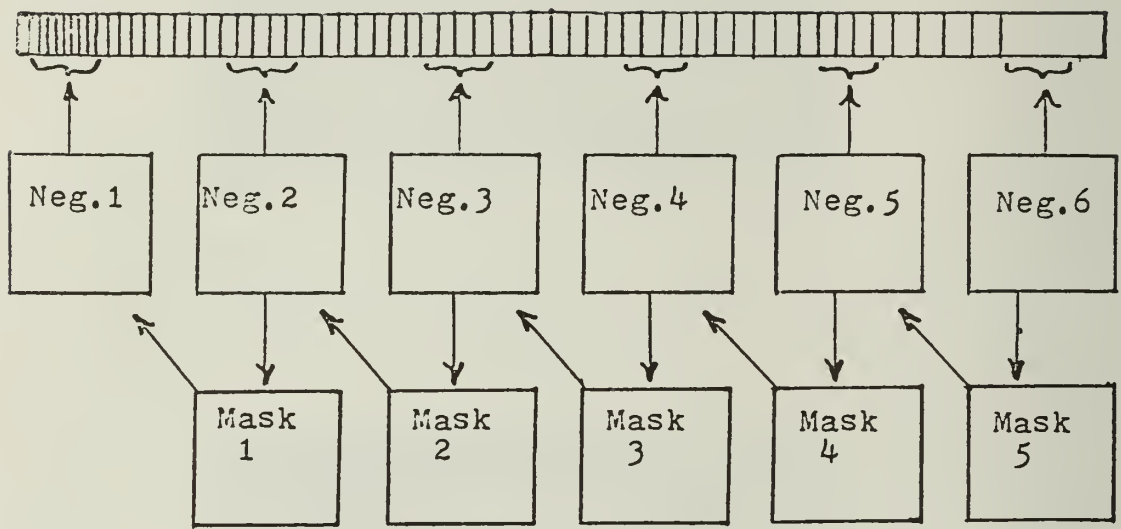


Figure 93. Negative and positive mask relationships in the gray scale density slicing<sup>46</sup>



Figure 94. Original thermogram of part of Tucson, Arizona (provided by the Applied Remote Sensing Laboratory of the Office of Arid Lands Studies, University of Arizona)

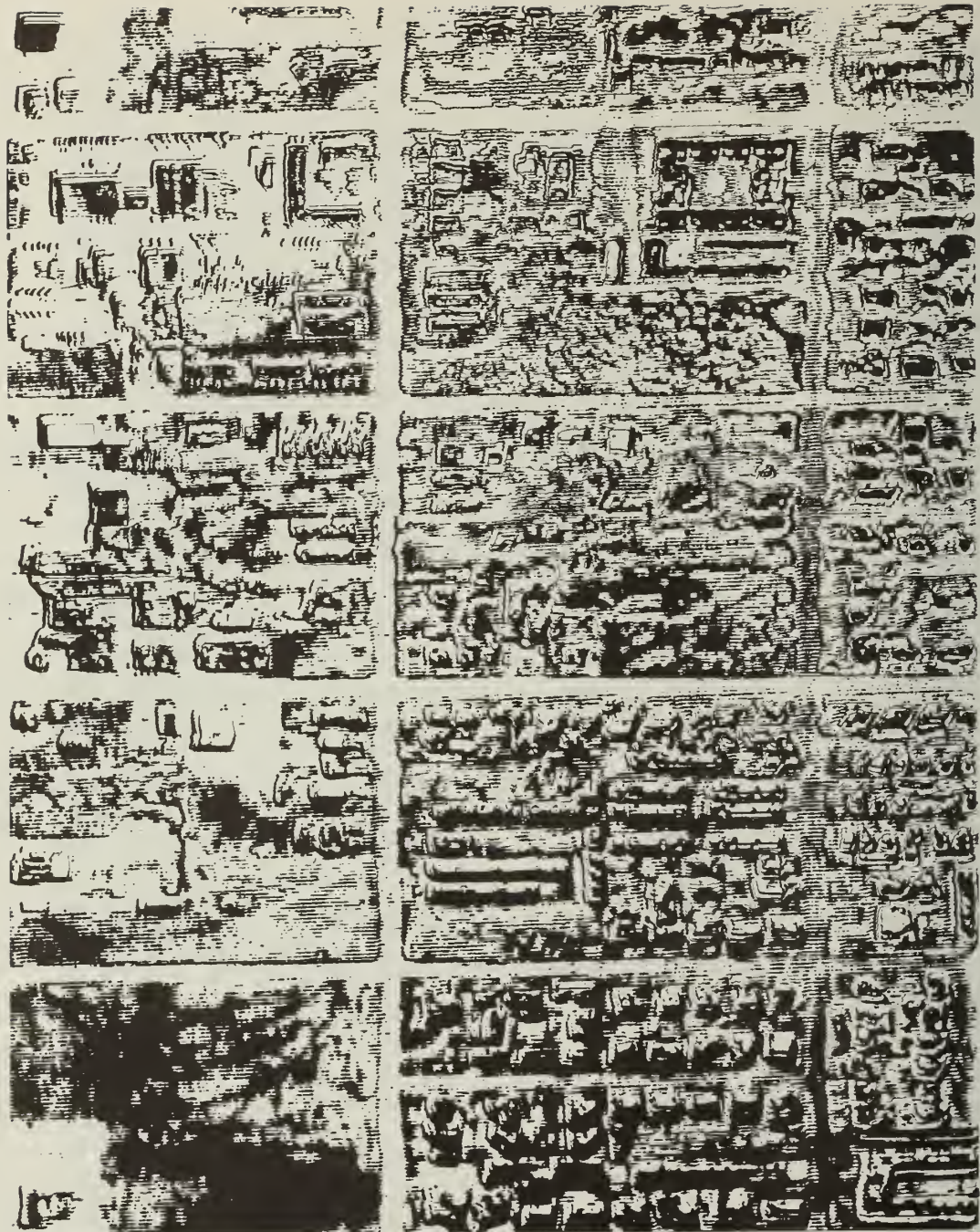


Figure 95. Interpositive print of original thermograph (Figure 94) from Parton.<sup>46</sup> The original thermograph was photographed using Kodak Ortho Film, Type 3. High contrast negatives were produced using different exposure times. From the negatives, positive masks were produced. In order to extract the sliced gray values, each negative was registered with the positive mask produced from the negative of higher density (Figure 93), producing the interpositive prints above

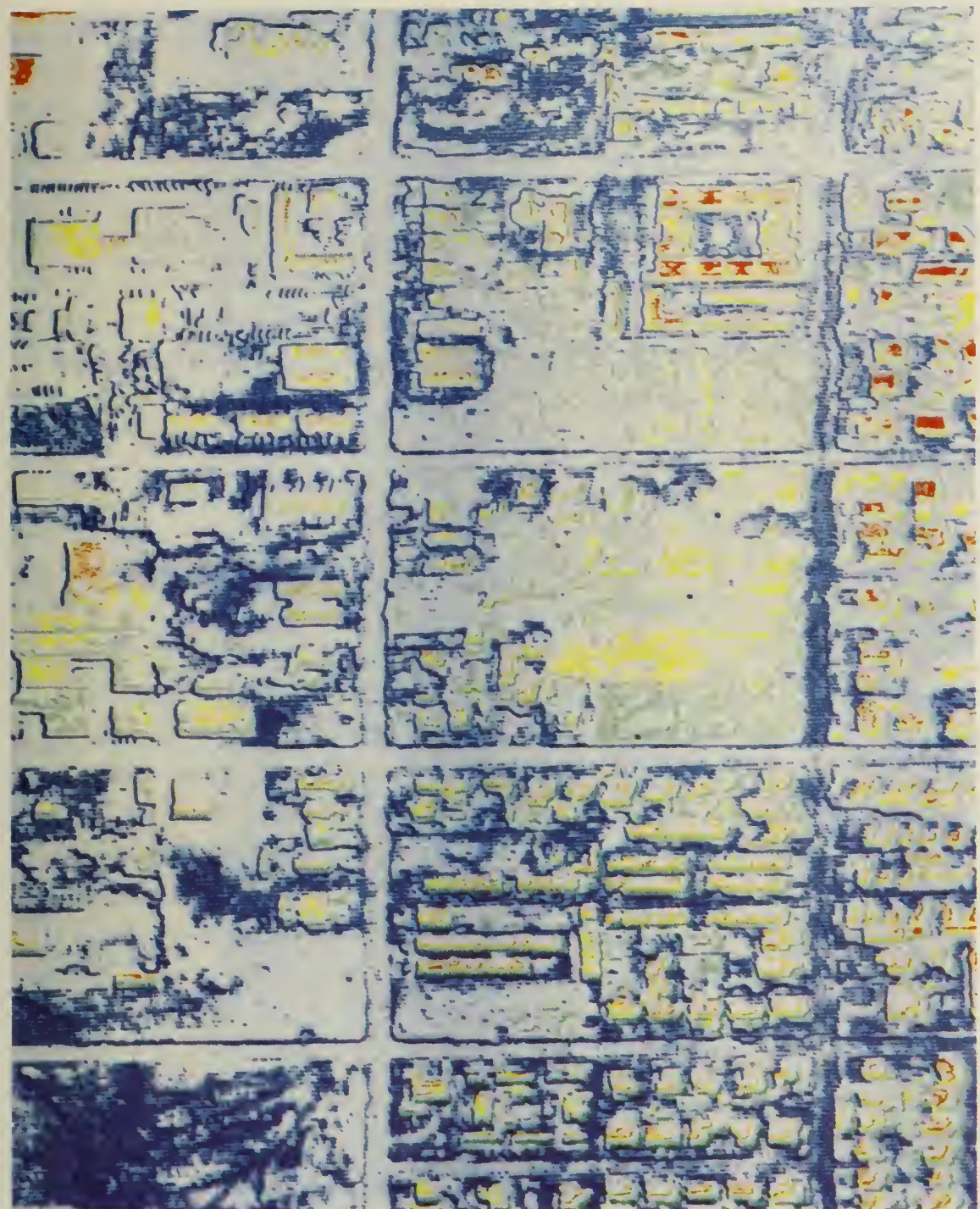


Figure 96. Color positive sandwich of Figure 94 (from Parton<sup>46</sup>). To aid in the analysis of the density sliced image, the interpositives (Figure 95) were printed onto Diazochrome Positive Color-Key film.

158. Contrast modification is often combined with density slicing by expanding each discrete level to the full range of gray tones.<sup>47,48</sup> For example, simple contrast modification may be accomplished by linearly stretching the levels of points between 11 and 64 on Figure 97 to full scale. In this figure, the scene was sliced into 100 discrete gray tones, and the tones between 11 and 64 were stretched linearly to the full range of gray tones. The output shows that input image levels from zero to 11 are assigned a zero-level output (black) and from 64 to 100 are assigned a 100-level output (white). Input levels between 11 and 64 range from white to black (Figure 98a and b). An expansion of this concept is to divide the original input into several intervals and stretch each interval simultaneously (Figure 99a). This multicycle contrast modification results in the creation of a substantial amount of artifact, and caution should be exercised in the interpretation of images enhanced using this technique. Most successful applications of this technique stretch tones associated with low spatial frequencies (gradual tone changes), such as those present on images of water bodies.<sup>49</sup> In these studies, the gradual density variations within a lake were stretched and significantly enhanced, but the cyclic stretching process on high spatial frequencies resulted in a nearly random noise appearance over cultivated land. The cyclic stretching technique is most efficient in enhancing features such as subtle, low-frequency alteration zones, or subtle moisture variations.

159. Several variations on the above contrast stretching can be applied. For example, the dark region or light region could be selectively stretched (Figures 100, 101, and 102). Another approach includes use of the probability density function (Figure 97a). For a digitized scene, the probability density function is essentially a histogram describing the number of occurrences for each gray level. Once a scene histogram is generated (Figures 89 and 97a), the cumulative distribution may be computed (Figure 103a). The scene can then be stretched using the cumulative distribution as the transformation or mapping function (Figure 103b). Contrast modification of this type (histogram equalization) expands the contrast modified output,

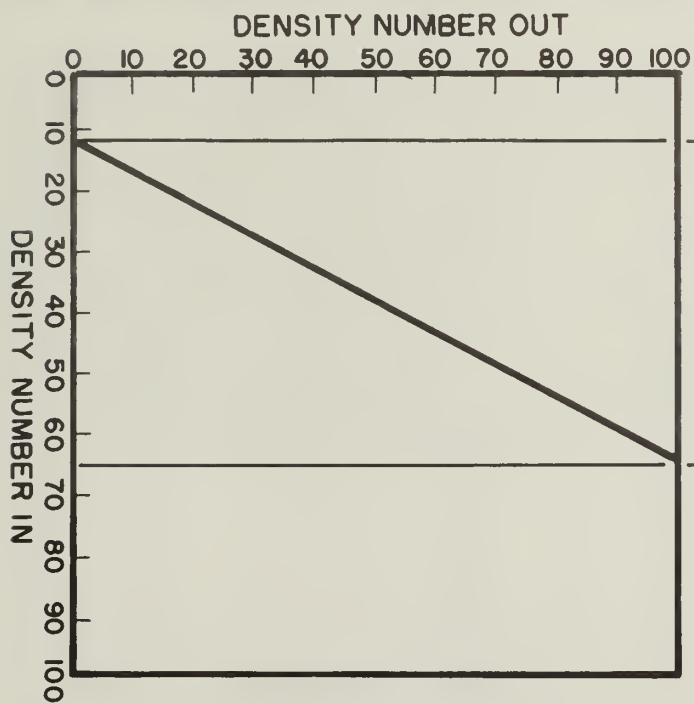
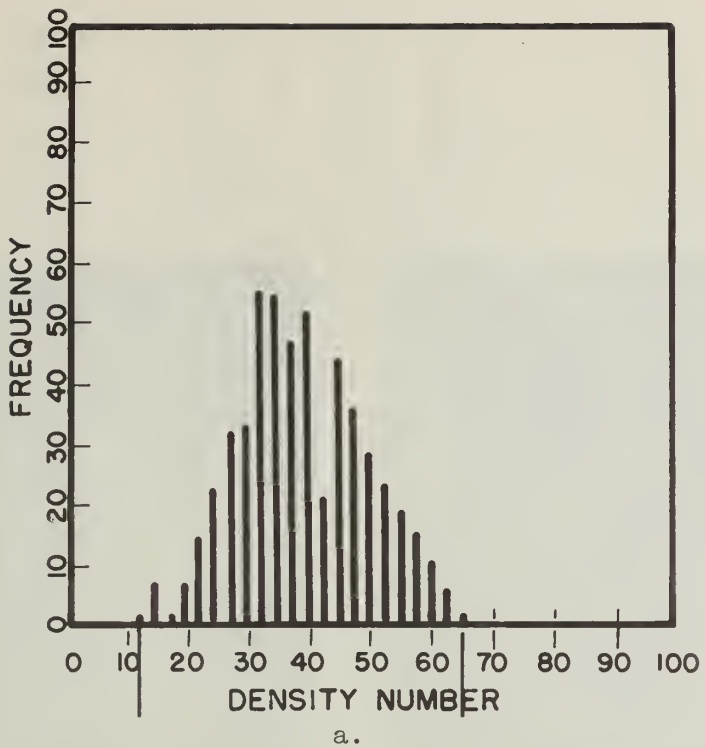


Figure 97. Contrast modification using a histogram of gray levels (marginal probability density function). The histogram is used to assign limits (here 11 and 64) to use the full gray scale capacity of a film or display device. In effect, the operation performed by b would linearly spread out the histogram in a to cover the entire range 0-100

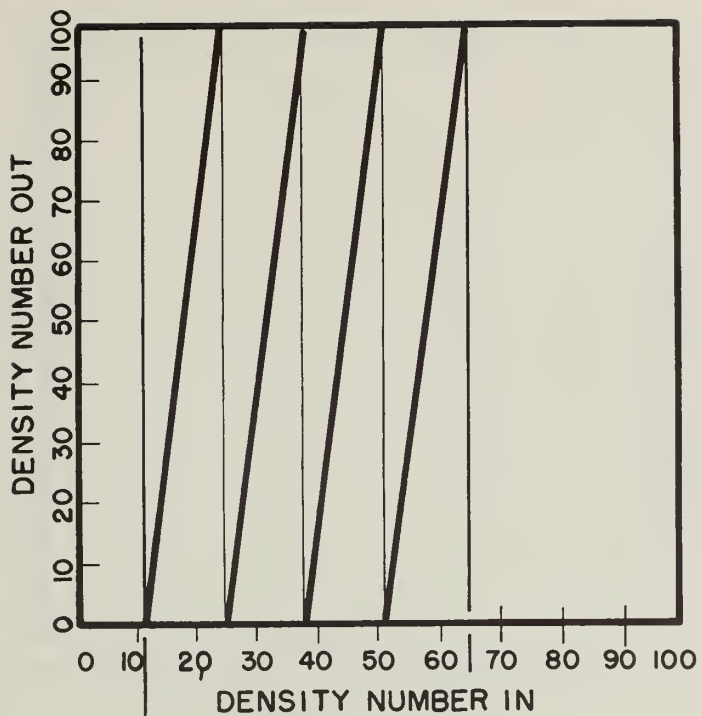


a.

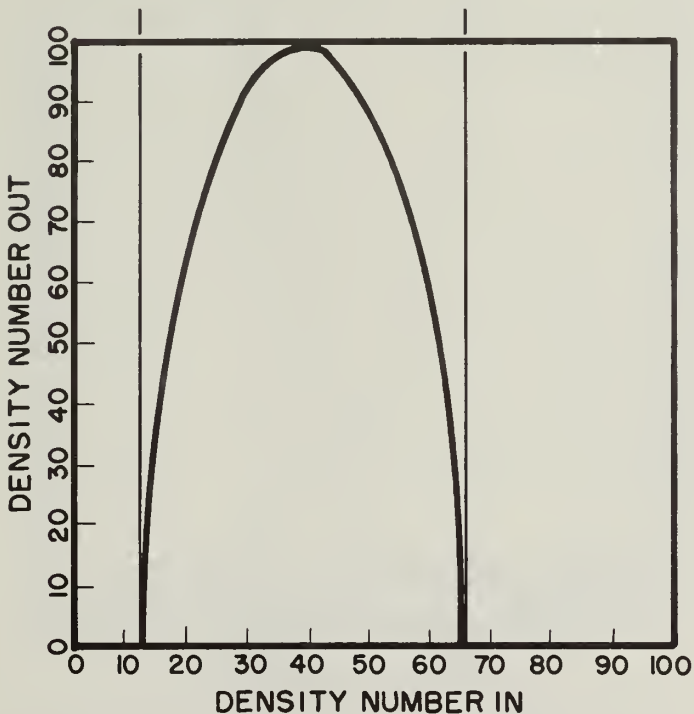


b.

Figure 98. Linear contrast stretch (Figure 97) of Figure 91. The band 7 Landsat image has a mixture of 64 gray levels (6 bit). However, the output device at the University of Arizona can accommodate 128 gray levels (7 bit). A histogram of Figure 91 indicates that the image is composed primarily of gray tones between 13 and 34. In a the image has been stretched so that the entire range of the band 7 image (0-64) will use the maximum number of gray scales available on the output device. Thus, the limits of the stretch are 0 and 64 (compare with 11 and 64 in Figure 97). In b the limits of the contrast stretch were set at 13 and 34 (compare with Figure 91). Stretches such as these increase the "effective" resolution of an image by increasing tone contrasts without sacrificing image aesthetics

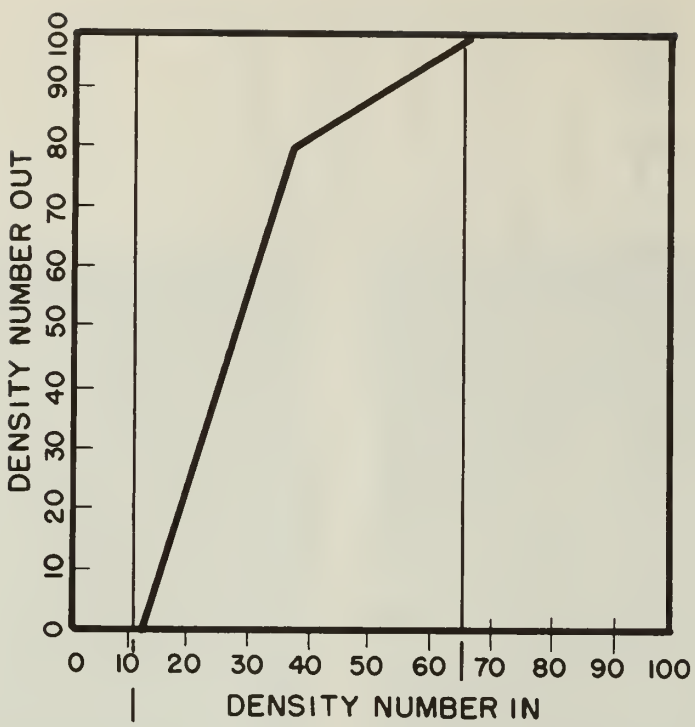


a. Multicycle stretch (limits correspond to those in Figure 97)

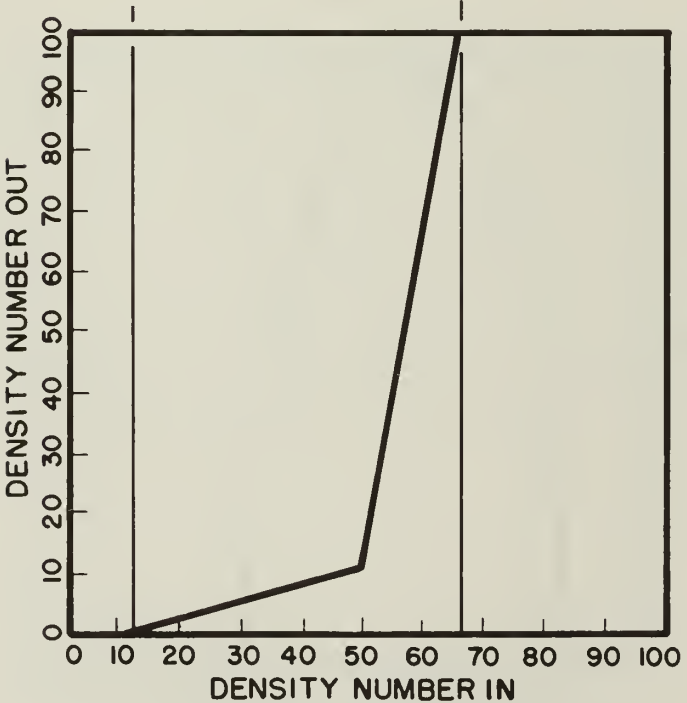


b. Sine stretch. The middle tones are stretched and the lighter tones converted to dark

Figure 99. Nonlinear contrast modification

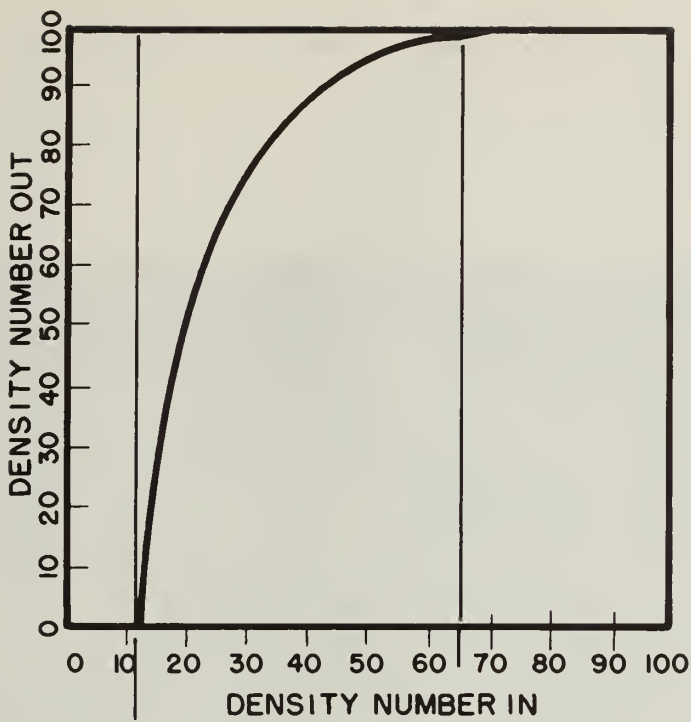


a. Dark region preferential stretch

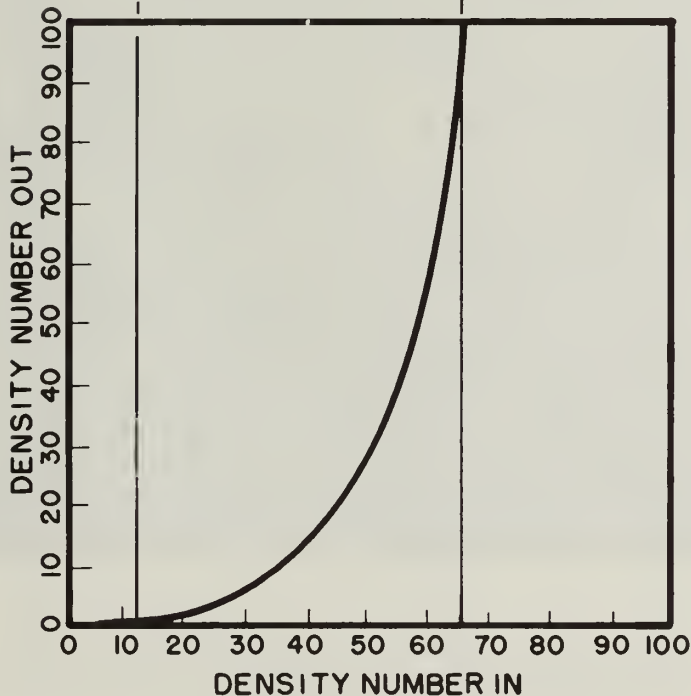


b. Light region preferential stretch

Figure 100. Bilinear contrast stretch,  
limits correspond to those in Figure 97



a. Logarithmic contrast stretch



b. Exponential contrast stretch

Figure 101. Logarithmic and exponential contrast modification. These stretches perform essentially the same operations as Figure 100a  
b only smoother

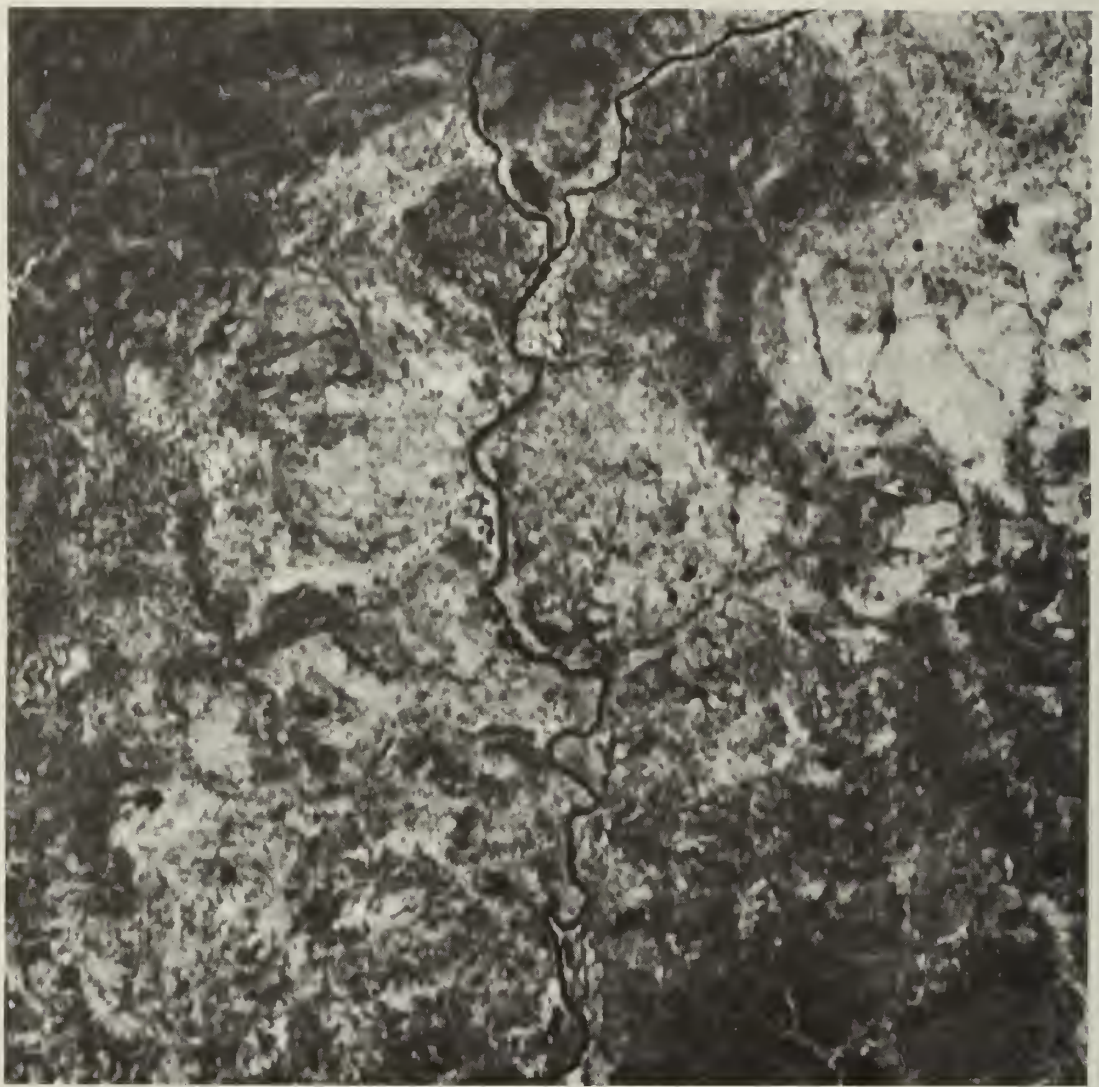
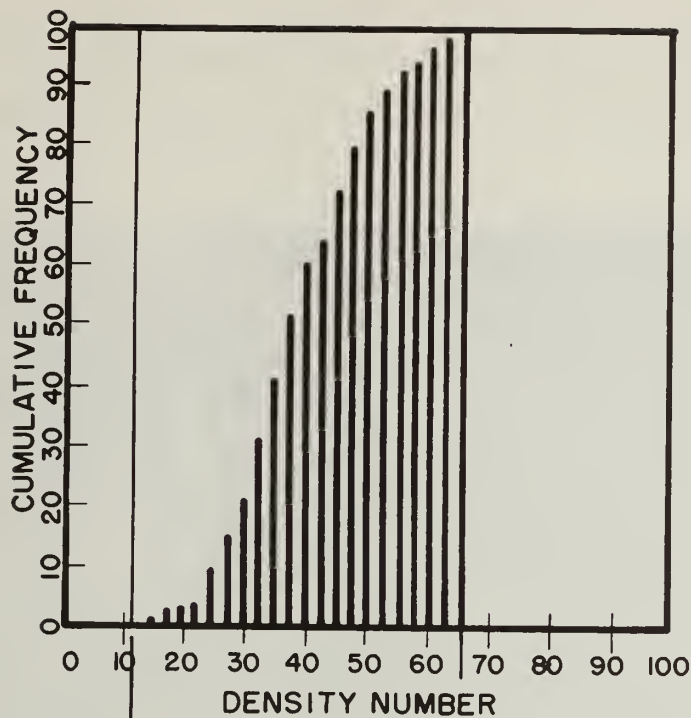
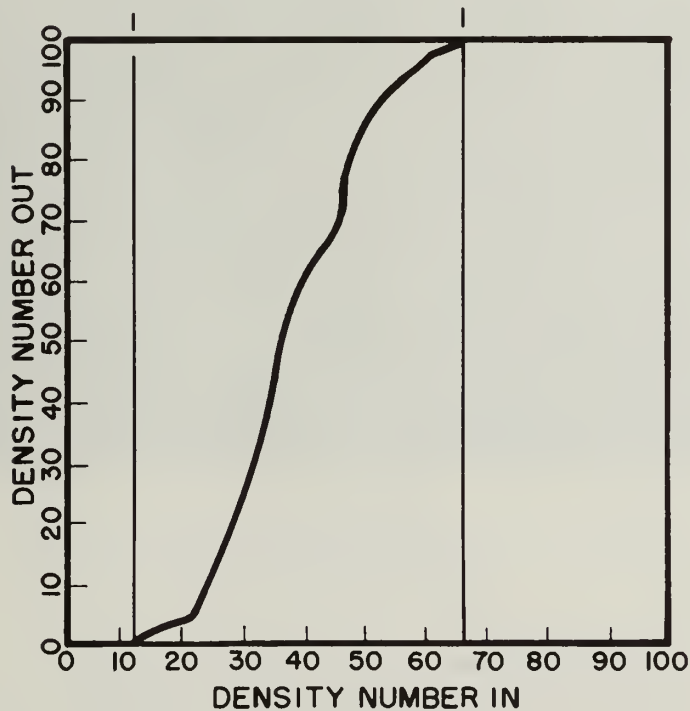


Figure 102. Logarithmic contrast stretch of Figure 101. Darker tones have been stretched more relative to lighter tones. Thus, the darker areas show more contrast and the lighter areas show less contrast than Figure 98a and b



a. Cumulative probability density function



b. Transfer curve used to stretch scene.  
Limits are those given in Figure 97

Figure 103. Histogram equalization contrast modification

according to the intensity levels which occur most frequently on the original scene. A light, washed-out print, for example, would have its light grey levels stretched toward the dark region to produce higher contrast (Figure 104).

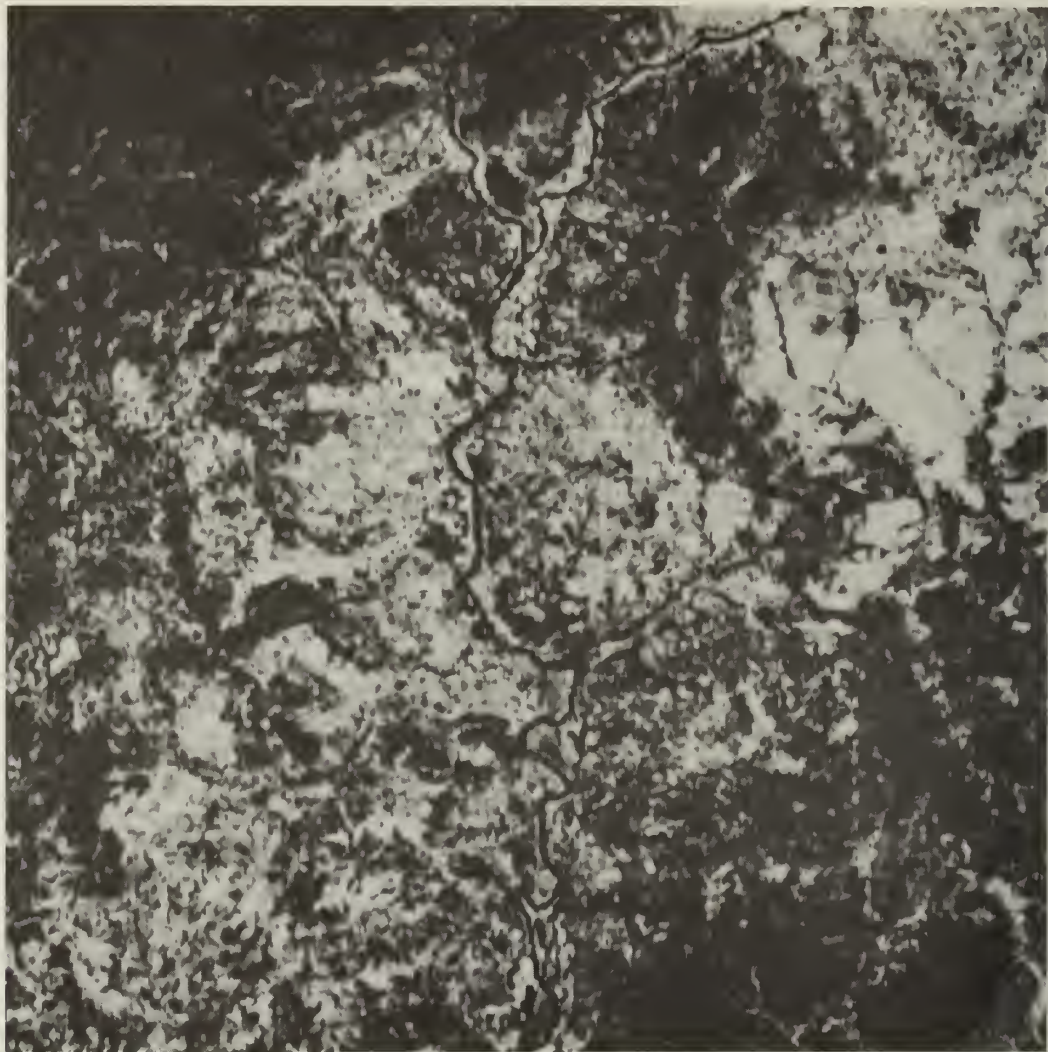


Figure 104. Histogram equalization contrast stretch of Figure 91

#### Image addition and subtraction

160. This technique is usually done in connection with color enhancement. Multispectral, multitemporal, or density sliced images are registered and then added or subtracted point by point to yield an

arbitrary color composite. Equipment for optical addition consists of a combination of standard slide projectors or of a specially designed enhancement viewer (Figures 14 and 15).

#### Local operations

161. Local operations, also termed nonzero memory operations, consider the value of neighboring scene elements in the enhancement operation, requiring computer storage. These techniques have considerably more power and versatility than point operations but require a greater amount of computation.

#### Image filtering

162. The general objective of image enhancement is to make selected features easier to see. This task might require suppression of useless data such as random noise and background shading or perhaps amplification of fine detail. The relative amplitude response of two imaging systems considering the response as a function of frequency is shown in Figure 105. System B produces equal or less attenuation of signal at all frequencies; thus, system B will tend to reproduce fine detail better than system A, since small features with sharp edges will

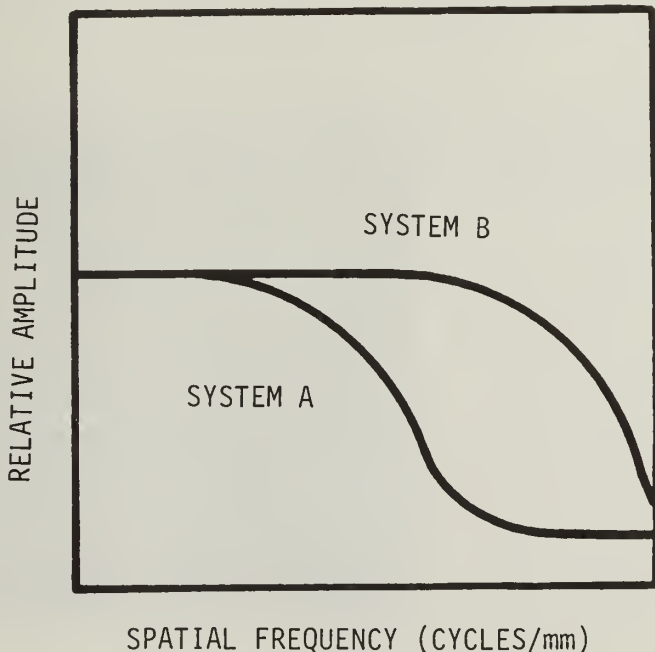


Figure 105. Comparison of two imaging systems

usually result in an input signal whose spectrum has a greater proportion of its energy at high frequencies. System B would not necessarily prove to be the best system to use, however. For example, if one were looking for a low contrast, diffuse zone characterizing a hydrothermally altered area within a scene where background noise was high due to topographic features, a system such as system A might prove superior since it rejects these high frequencies (Figure 48). An alternative to this system selection problem would be provided if one could record with system B, then remove those spatial frequencies which are undesirable from the subsequent image. One of the most important image enhancement techniques which accomplishes this goal is filtering. Digital filtering is basically a process by which discrete output values are produced by weighting image values. This is essentially a convolution of a filter array with an image array. For example, let  $(x_0, x_1, x_2, \dots, x_n)$  be a sequence of numbers derived by digitizing a continuous signal such as the optical density along a line of film. A simple three-point filter would replace each  $x_i$  with the average of the points  $x_{i-1}, x_i, x_{i+1}$ . Thus, if  $y_n$  is the filtered point at position  $i$ ,

$$y_i = \frac{1}{3} x_{i-1} + \frac{1}{3} x_i + \frac{1}{3} x_{i+1} \quad (6)$$

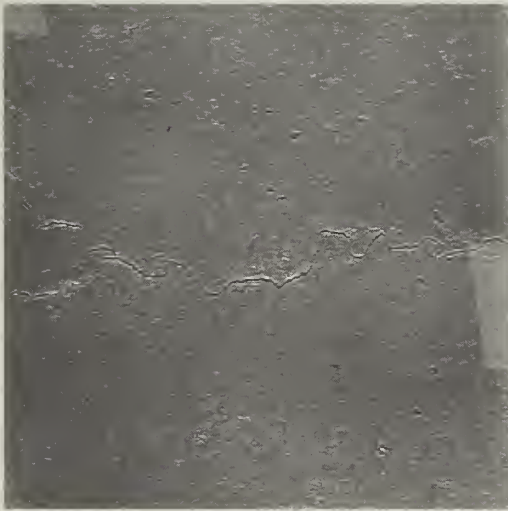
The values  $1/3$  are the filter weights which are in general not equal. The filtering relation using  $2k + 1$  weights  $g = (g_{-k}, \dots, g_{-1}, g_0, g_1, \dots, g_k)$  is

$$y_i = \sum_{j=-k}^k g_j x_{i+j} \quad (7)$$

In two dimensions, this becomes

$$y_{i,j} = \sum_{m=-k}^k \sum_{n=-\ell}^{\ell} g_{mn} x_{i+m, j+n} \quad (8)$$

This type of averaging technique results in a low-pass filtering operation since the high spatial frequencies are removed by the averaging operation (Figure 106a). This low-pass filter results in a smoothing of



- a. Low-pass filter of Figure 91. Note the blurring of the image caused by the averaging of Equation 6. The subtle tone changes are enhanced to the exclusion of the sharper tone changes (fine details)



- b. High-pass filter of Figure 91. Here the sharp tone changes are enhanced and the more gradual tone changes are deleted. This operation sacrifices image aesthetics for enhancement of edges and lines. The filter weights were calculated using Equation 9

Figure 106. Low-pass and high-pass filters of Figure 91. The filter used to produce these images was a simple three-element row filter ( $1 \times 3$  array) with weights equal to  $1/3$  (Equation 6)

the image and often causes the image to appear blurred. A high-pass filter has the opposite function removing low-frequency signals (gradual tone changes), in favor of high frequencies (abrupt tone changes) (Figure 106b). A simple algorithm for a high-pass filter is

$$Y_{i,j} = \sum_{m=-k}^k \sum_{n=-\ell}^{\ell} g'_{m,n} x_{i+m, j+n} \quad (9)$$

where

$$\begin{aligned} g' &= \delta(k) - g_k \\ g'_{m,n} &= \delta(m,n) = 1 \text{ for } m = n = 0, 0 \text{ otherwise} \\ \delta &= \text{Kroneker delta.} \end{aligned}$$

This operation may be performed by simply subtracting the low-pass filter results from the original image.

163. A high-emphasis filter (high-frequency restoration filter) passes low-frequency signals unchanged while amplifying high-frequency signals (Figure 107). A high-emphasis filter may be derived from a high-pass filter by multiplying all of the high-pass weights by a constant and adding 1 to the central term. Thus,

$$g''_{mn} = \delta(m,n)A g'_{mn} \quad (10)$$

where

$$\begin{aligned} g' &= \text{high-pass filter weight} \\ g'' &= \text{high-emphasis filter weight} \end{aligned}$$

164. Feature-selective filters operate by cross correlating the image with a matrix of weights that geometrically resembles the feature to be enhanced. For example, if vertical features are to be enhanced, the filter weights are made positive along a vertical line in the center of the matrix and negative or zero otherwise, so that the output of the filter is centered on vertical lines. The filter should be approximately as large as the feature to be enhanced. When dealing with two-dimensional filters, the expense increases significantly.

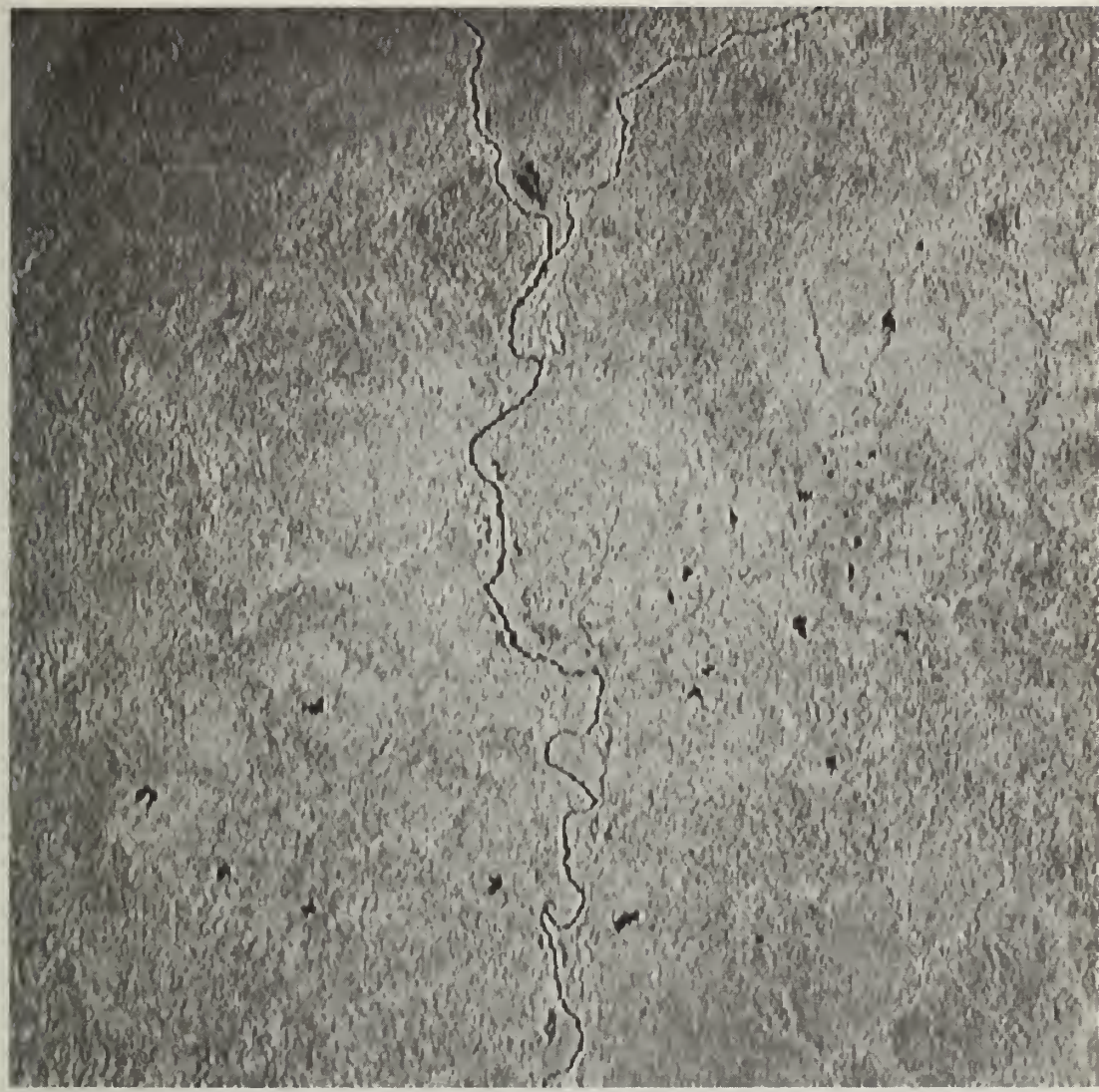


Figure 107. High-emphasis filter of Figure 91. The high-emphasis filter retains the low spatial frequencies (gradual tone changes) while boosting the high frequencies resulting in an image which is more pleasing than Figure 106b. Note that the row filter enhances vertical structures and tends to smooth horizontal structures. A column filter ( $3 \times 1$  filter array) would enhance the horizontal features. The filter weights were calculated from Equation 10 with  $A = 5$

$$\begin{bmatrix} 0 & 0 & 1/5 & 0 & 0 \\ 0 & 0 & 1/5 & 0 & 0 \\ 0 & 0 & 1 & 0 & 0 \\ 0 & 0 & 1/5 & 0 & 0 \\ 0 & 0 & 1/5 & 0 & 0 \end{bmatrix}$$

Edge enhancement

165. Edge enhancement involves determining the derivative of the scene radiances. The results are then multiplied by a constant and added to the original scene values (Figure 108). Two digital algorithms for edge enhancement are given by:

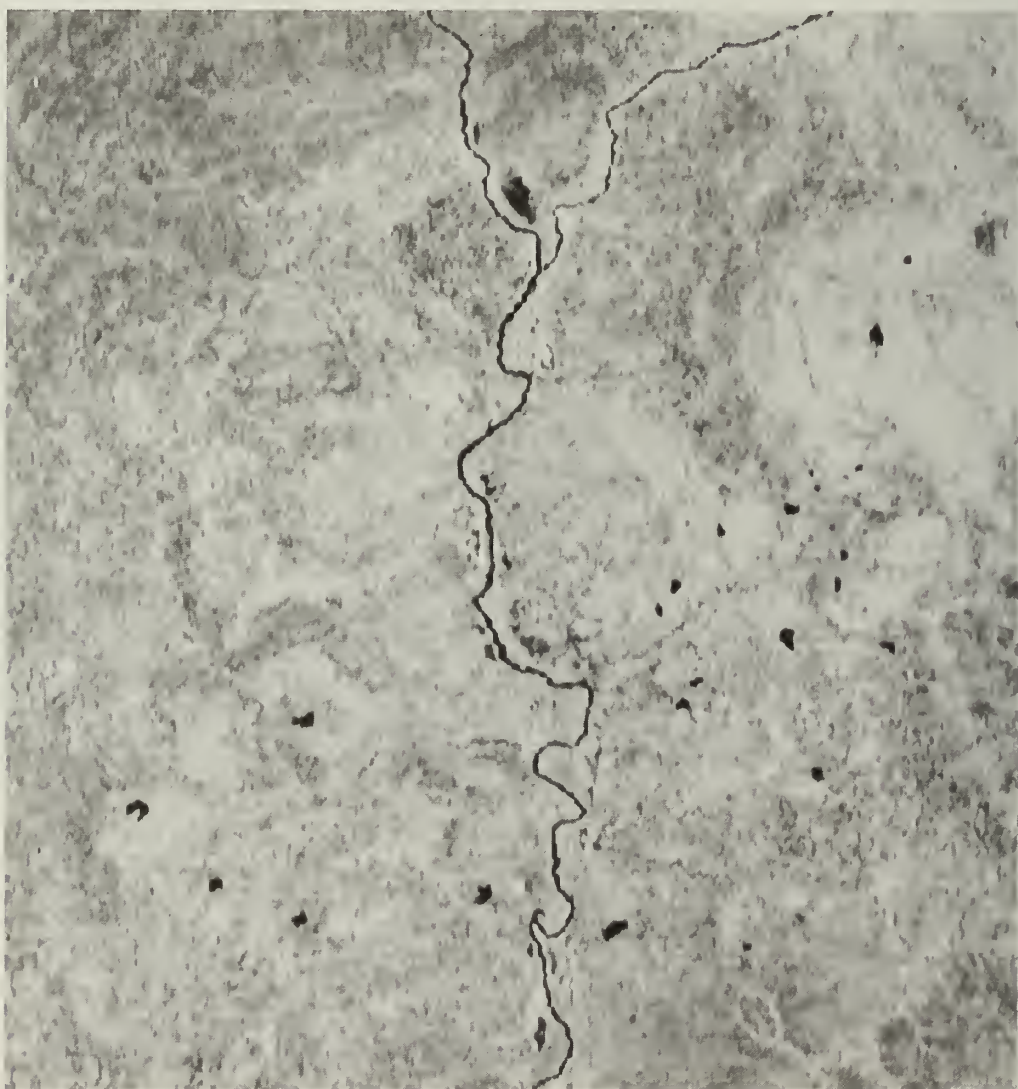


Figure 108. Edge enhancement of Figure 91

$$\Delta L_v(i,j) = 2L_v(i,j) - L_v(i-1,j) - L_v(i,j-1)$$

$$\Delta^2 L_v(i,j) = 4L_v(i,j) - L_v(i-1,j) - L_v(i+1,j)$$

$$- L_v(i,j-1) - L_v(i,j+1)$$

166. A familiar optical technique for edge enhancement is the use of "unsharp masking." In this technique, an image is copied onto film in register with a blurred negative of itself.<sup>44</sup> This produces essentially the same effect as subtracting a low-pass filtered image from an original; thus, edge enhancement is essentially equivalent to applying a high-pass filter to an image and selecting the filter weights accordingly. Edge enhancement also may be accomplished by copying through a positive-negative sandwich using nonblurred transparencies. Directionality may be obtained by slightly offsetting the transparencies. Figure 96 was inadvertently enhanced this way by slight misregistration of the positive-negative sandwich due to film shrinkage.

#### Multispectral ratios

167. Part III dealt with the way in which different earth materials respond to electromagnetic radiation. The fact that materials respond differently to radiation of varying wavelengths has led to the concept of multispectral imagery, where films or optical-mechanical sensors are used to record simultaneous images of an object in different spectral bands. This technique provides an opportunity to distinguish between materials based on their varying spectral responses. When more than two spectral bands are used, the job of comparing responses on several images becomes a burdensome one for the image analyst. Efforts to simplify this task have led to the development of color additive viewers and ratio techniques.

168. The color additive viewer, mentioned earlier, consists of registering two or more photo positive transparencies and projecting light of chosen hues through them onto a screen. For example, red for an infrared wavelength band, yellow for a red wavelength band, and blue for a green wavelength band. The resultant color composite is

called a "false color" image since hues are assigned to wavelength regions not normally associated with them. For example, since vegetation has a strong reflectance in the infrared, it appears red on a false color image instead of its characteristic green color (Figures 14 and 15).

169. Using multispectral ratio techniques, radiance-values in one spectral band are divided by radiance-values in another spectral band. Once the ratio operation is complete any of the enhancement techniques mentioned earlier may be applied to the image. Commonly the image is contrast modified or "stretched" to improve interpretability (Figures 109 and 110). In one case, the authors have found that application of a high-pass filter to a ratioed scene displayed lineaments which were not apparent on the original scene (Figure 111). Since the ratio operation enhances contrasts in the spectral reflectance of earth materials, the subsequent high-pass filter operation enhances the boundaries or edges where abrupt changes in spectral reflectance occur. Caution should guide the interpretation of images enhanced in this way since the filter operation results in artificial relief which bears no relation to the actual topography. Consider the responses of common soils (Part III). These responses are nearly identical throughout the ultra-violet and the visible, making a discrimination between them unlikely in this region. However, changes are apparent in the infrared region. If the reflectance values for the pedalfer-type soils at 0.760  $\mu\text{m}$  (Figure 69b) are divided by the reflectance values at 0.500  $\mu\text{m}$ , the resulting ratio ranges from 1.2 to 2.8 with an average of 2.0. A similar operation for laterites (Figure 69c) yields ratios ranging from 2.9 to 7.3 with an average of 4.6. Stretching these values by computing  $e^{(\text{ratio})}$ , yields an average stretched ratio of 99.4 for the laterites, and an average stretched ratio of 7.4 for the pedalfer-type soils. The maximum stretched ratio for the pedalfer-type soil is 16.4 while the minimum for the laterites is 18. If the ratios are assigned a film density, the laterites would appear light and the pedalfers dark.

170. Turner<sup>50</sup> used ratios to detect short-term changes in vegetation by dividing Landsat band 6 (near infrared, characterized by high



Figure 109. Linear contrast stretch of Landsat band 7 image of the Barcley Dam, northwestern Kentucky



Figure 110. Ratio of band 7 (near infrared) by band 4 (green) of same area as Figure 109. The ratio operation removes the shadows, thus significantly reducing image texture so important to structural interpretation. However, much more detail is available in the cultivated areas. The highway (upper right corner to damsite) is more evident in the ratio than in Figure 109, and occasionally rock discrimination is facilitated by a ratio operation



Figure 111. High-pass filter of a band 5/band 6 ratio. This scene near Flagstaff, Arizona, displays numerous northwest-southeast lineaments which are not apparent on the original band 5 and band 6 images. The diagonal feature extending from the lower left to the upper right is a highway. (Image processed by Dr. Robert A. Schowengerdt, Assistant Professor of Remote Sensing, University of Arizona)

vegetation reflectance) by Landsat band 5 (red, characterized by low vegetation reflectance). The resulting densities were then sliced by assigning ratios above 1.25 black and ratios below 1.25 white.

171. Rowan et al.<sup>51</sup> used a combination of ratios, contrast stretching, and color addition to study rock types and alteration in Nevada. In his study, reflectance values in Landsat band 4 were divided

by values in band 5, band 5 was divided by band 6, and band 6 was divided by band 7. A blue hue was projected through the band 4-band 5 ratio, a yellow hue through the band 5-band 6 ratio, and a magenta hue through the band 6-band 7 ratio. On a subsequent color composite, mafic rocks (basalt and andesite) appeared white, felsic intrusives and extrusives appeared pink, vegetation appeared orange, playas and mine waste structures were blue, and altered areas were either green to dark green or brown to red brown. Interpretation of the color composite was significantly improved by the ratio technique. Other possible ratio algorithms are commonly used.

For example, the difference in scene values between two bands can be divided by the sum

$$\frac{DN_{Band\ x} - DN_{Band\ y}}{DN_{Band\ x} + DN_{Band\ y}},$$

or scene values in each band can be divided by the average value of all

band  $\frac{DN_{Band\ x}}{\frac{1}{N} \sum_{i=1}^N DN_{Band\ i}}$ .

172. Goetz et al.<sup>52</sup> studied the usefulness of several enhancement techniques including multispectral ratios for geological interpretations. Their findings on ratios are summarized in Table 7. The current approximate cost for enhanced imagery from the EROS Data Center is \$1,000.00 (destripping, 11 × 1 array edge enhancement, and contrast stretch) per scene for an initial enhancement. Purchase of available enhanced imagery is possible and the cost ranges from \$24.00 to \$150.00 per image depending upon the product desired. Price lists and a catalogue of processed imagery is available through EROS.

173. Each scene acquired of different areas, or of a single area at different times of the year, is unique. No two images are ever alike and enhancement techniques applied to one may be less than optimum for another. For this reason, several private and governmental agencies are processing their own imagery to satisfy specific project demands rather than purchasing enhanced imagery "off the shelf." For most earthquake engineering studies, enhancement operations which enhance the relatively sharp edges or lines commonly associated with geologic structures are

Table 7

Ranking Extending from 1 to 6 of Ratio Images with  
and Without Atmospheric Correction in the  
Coconino Plateau<sup>52</sup>

<u>Category</u>	<u>Area</u>	<u>4:5</u>	<u>4:6</u>	<u>4:7</u>	<u>5:6</u>	<u>5:7</u>	<u>6:7</u>
I	Structures and limestone contacts						
	Without correction	3	2	1	5	4	6
	With correction	3	2	1	5	4	6
II	Faults in Tertiary basalts						
	Without correction	1	5	4	3	2	6
	With correction	1	5	4	3	2	6
III	Vegetation in Tertiary basalts						
	Without correction	1	6	5	3	2	4
	With correction	1	6	5	3	2	4
IV	Grand Canyon, southern rim: vegetation						
	Without correction	1	6	5	3	2	4
	With correction	6	5	4	2	1	3
V	Tertiary basalt escarpment						
	Without correction	1	3	2	5	4	6
	With correction	1	6	5	3	2	4
VI	Quaternary basalt						
	Without correction	3	2	1	5	4	6
	With correction	1	3	2	5	4	6
VII	Moenkopi Formation						
	Without correction	3	2	1	5	4	6
	With correction	3	2	1	5	4	6

preferable. Edge enhancement is good for edges and boundaries; two-dimensional high-pass or high-emphasis filters are best for lines or other high spatial frequencies, and the feature-selective filters are useful for enhancing both edges and lines in various directions. Multispectral ratios are less useful due to suppression of image texture and geologic structures. However, if subtle tone contrasts associated with rock type, vegetation, or moisture is fault related, ratio techniques may be useful. Contrast stretching is always helpful. In summary, the enhancement technique should be carefully tailored to the specific area to be interpreted.

### Image Quality

174. The relevant factors necessary for assessing the usefulness of imagery are:

- a. The informational needs of the user. For earthquake hazards, these needs are outlined in Part II and basically consist of a discontinuity or lineation involving different reflectances, temperatures, or topography.
- b. The available means of extracting desired information from the imagery. This subject is outlined in this chapter and includes optical, photographic, and computer techniques aimed at accentuating the tone differences in images.
- c. The attainable quality of the remote sensing imagery. This factor has not yet been treated although it will have a major impact on decisions involving image type for specific projects.

### Attainable quality of imagery

175. There are basically three factors which control the quality of an image. These are: (a) tone or color contrast between an object and its background, (b) resolution or sharpness of the image, and (c) the stereoscopic parallax characteristics of the image. Of the three, the first is directly related to the success of a preimagery field and literature investigation to determine the most promising spectral range within which to record images. As previously mentioned, the primary goal of a remote sensing project is to record earthquake hazards

so that the contrast between them and their background is a maximum.

Tone contrasts and image sharpness are largely a function of the type of hard-copy image available to the interpreter. The dynamic range (gray levels) of film emulsions is far greater than the dynamic range of paper prints yielding much sharper images. For this reason, back-illuminated transparencies are superior to paper prints for nearly all interpretation tasks, even if the transparencies are negatives.

176. Image resolution.

The ability of an imaging system (including lens, filter, detector, emulsion, exposure, and processing, as well as other factors) to record fine detail in a distinguishable manner is referred to as the resolution, or resolving power of the system.<sup>29</sup>

Although resolution is a valid and often quoted measure of image quality, it is difficult to assign a value which gives an interpreter a valid idea of the information content of the image. For example, resolution has been described in terms of ground resolution (the distance two objects must be separated on the ground so that they are imaged as two objects), line pairs per millimetre (the number of lines that would occupy 1 mm on a photograph when the individual lines are just barely distinguishable), acutance, or modulation transfer function. Yet, in general, the spatial resolution of imagery is not only a function of lens quality but is also proportional to the tone contrast between the object and its background, the object's aspect ratio (ratio of length to width), the regularity of object shape, the number of objects involving the pattern to be resolved, and the uniformity of the background. Also, spatial resolution is inversely proportional to the graininess of the film and the amount of atmospheric haze present.<sup>53</sup>

177. While the resolving power of an image recording system yields an indication of its ability to separate objects in a scene, and can be defined and measured accurately, image sharpness ("the abruptness with which the tone contrast appears to take place on the photograph")<sup>53</sup> is more difficult to quantify but equally as important. These edge gradients are influenced by the total photographic exposure. The steeper gradients are associated with intermediate exposures, and the

lower gradients are associated with exposure extremes.

Image interpreters are often confused by errors in assessing resolution. When telephone wires resolve on a particular photograph it does not necessarily follow that any object the thickness of a telephone wire will resolve. The wire is detectable because its length results in exposure to several silver halide grains rather than because the camera system can resolve very small images.<sup>29</sup>

178. The ground resolution on USDA photographs (scale 1:20,000) is such that circular and square objects less than 1 m across are seldom discernable.<sup>29</sup> For active fault investigations, the authors have found that images having original scales of 1:12,000 provide a ground resolution of less than 1 m and are an effective scale for detailed interpretation. These are used with small-scale photographs and other imagery to achieve a regional view. Often for complex faulting, scales of 1:6000 and 1:3000 have been used providing ground resolutions on the order of 10 cm and less.

#### Stereoscopic parallax

179. As a result of the revolutionary developments occurring over the last several years in remote sensing, stereoscopic parallax as a measure of image quality has been largely ignored, or omitted.

Colwell<sup>53</sup> states:

Stereoscopic parallax is of extreme importance in the interpretation of remote sensing imagery...

The authors have evaluated imagery of numerous active earthquake areas throughout the past 15 years and have found that more information, by a large margin, may be extracted from a stereoscopic pair of images than from a single image. Consequently, the ease with which stereoscopic parallax may be obtained with overlapping photography gives the aerial photograph an advantage over continuously scanned imagery. Stereoscopic parallax may be attained on scanner systems by designing the flight lines so that the coverage of adjacent flight lines overlaps. However, distortion must be carefully corrected and flight lines must be accurately flown to ensure thorough stereoscopic coverage. In choosing imagery, the relative benefits of these three measures of image quality

are important considerations, and a decision analysis approach, as outlined in Part VII, may prove to be the optimum way in which to make such decision.

Airborne Multispectral Imagery

180. A large number of platforms have been used for remote sensing--ranging from pigeons to spacecraft. Multispectral imagery utilizing aircraft has provided the primary source of data throughout the years. For example, the EROS Data Center currently stores approximately 4.5 million frames of National Aeronautics and Space Administration (NASA) aircraft and USGS mapping photography compared with approximately 0.85 million frames of spacecraft imagery. This situation is undoubtedly due to the relatively recent emergence of spacecraft as sensor platforms; however, spacecraft are not anticipated to completely replace aircraft as platforms in the foreseeable future since each type of platform has unique advantages.

181. There are a number of advantages to aircraft platforms which make them desirable for imaging purposes. One of the major advantages for earthquake studies lies in the ability to attain increasingly better spatial resolution with the same equipment by altering the flight altitude of the aircraft. It is often desirable to image a fault zone, for example, at more than one altitude to obtain both synoptic and detailed coverage. The authors anticipate an increase in the use of airborne multispectral scanners similar to the scanners employed on Landsats 1 and 2. These scanners will provide multispectral digital data at resolutions that far exceed those possible on satellite systems. The spatial resolution attainable using airborne systems makes these systems preferable to spacecraft imagery for most detailed earthquake engineering purposes.

182. Aircraft also enable images possessing parallax to be recorded quickly and inexpensively, particularly in the visible and near infrared regions where standard photography is possible. In addition to the two major advantages mentioned above, another important advantage is the presence of crew members on the platform. Colvocoresses et al.<sup>54</sup> points to the fact that remote-control systems are rapidly being

developed to the point that unmanned aircraft will become practical. They assert that once automated systems become available there is no real reason why remote sensing missions need a crew of more than one or two. The authors feel that there is no substitute for having a geologist, geological engineer, or someone familiar with earthquake hazards, physically present on the platform during image recording. The obvious advantage is the ability to alter flight paths, or altitude, or time for image recording to most efficiently image the earthquake hazards.

183. A major disadvantage of aircraft platforms is the instability presented to the image recording system as the aircraft plows its way through the atmosphere. These effects are most profoundly felt in scanning-type sensors. Pitch, yaw, and crab all affect the quality of images taken from aircraft platforms. An additional disadvantage is the limited field of view available on a single image.

184. Since the acquisition of imagery early in a project is important, addresses are provided in Appendix B locating sources where airborne imagery may be purchased.

#### Spacecraft Multispectral Imagery

185. Space systems introduce a new dimension to remote sensing. Platforms may now be maintained at altitudes above 150 km which are free of the turbulent effects of the atmosphere.

186. Remote sensing from spacecraft began with photographs taken from space by the Gemini and Apollo missions at an altitude of approximately 200 km, and Sky Lab at an altitude of approximately 300 km. A great new impetus to remote sensing use of space platforms started when Landsat I was launched on July 23, 1972, and was followed closely by launching of Landsat II on January 20, 1975. Landsat systems operate at an altitude of approximately 817 km, and both are equipped with three return beam vidicon (television) cameras (RBV) and a 4-channel multispectral scanner. The principal control switch failed on the RBV camera aboard Landsat I, and the camera was turned off before many images could be transmitted.<sup>55</sup> The characteristics of the Landsat image acquisition

system are given in Table 8. The output from the multispectral scanners are digitized on the satellites, and the output from the RBV cameras remain in analog form. This data is either transmitted directly to receiving stations on the ground or is stored on onboard tape recorders and transmitted during the satellite's next nighttime pass.<sup>55</sup> This data is stored in both digital (MSS) and analog (RBV camera) form on high density tape for subsequent conversion to image form by Goddard Space Flight Center, Greenbelt, Maryland, in the United States, and other existing or planned installations throughout the world. Appendix B describes how to order Landsat imagery.

Table 8  
Spectral Characteristics of the Landsat System

<u>Band</u>	<u>Spectral Range, <math>\mu\text{m}</math></u>
<u>Return Beam Vidicon Camera</u>	
1	0.475 to 0.575 (Blue-Green)
2	0.580 to 0.680 (Green-Yellow)
3	0.698 to 0.830 (Red-Near IR)
<u>Multispectral Scanner</u>	
4	0.5 to 0.6 (Green)
5	0.6 to 0.7 (Red)
6	0.7 to 0.8 (Near IR)
7	0.8 to 1.10 (Near IR)

187. Landsat "C" was launched in 1978 to include a sensor in the thermal infrared region; Seasat is planned for 1978 to include radar to monitor the oceans; and Landsat "D" (thematic mapper) will be launched in the 1980's and will be equipped with a seven-channel multispectral scanner.

188. The major advantages of the Landsat systems described above, not shared by aircraft systems, are:

- a. Synoptic coverage. The present Landsat imagery covers approximately 28,000 sq km per frame at scales of 1:3,000,000 for transparent chips; 1:1,000,000 for paper prints; and 1:500,000 and 1:250,000 for standard enlargements. This coverage makes mapping of major geographic structures much easier than larger scale imagery.

- b. Worldwide coverage. The availability of imagery in areas where acquisition of imagery by aircraft is politically sensitive makes the Landsat system extremely valuable.
- c. Multidate coverage. Images of an area can be acquired at 18-day intervals with Landsat I and more often using both Landsats I and II.

These advantages, combined with the convenience that digital format provides, make Landsat imagery an extremely useful tool in earthquake engineering studies.

189. There are two disadvantages to the existing and planned Landsat imagery, however, which preclude its use as an exclusive tool for earthquake engineering applications. These disadvantages deal with spatial resolution and atmospheric backscatter.

#### Spatial resolution of Landsat systems

190. Current Landsat (MSS) systems are capable of an areal coverage of 185 by 185 km. This includes a total of approximately 7,581,600 pixels, 3240 pixels along each of the 23<sup>40</sup> scan lines. Each ground resolution element corresponds to the energy within a particular wavelength band associated with an area on the ground 79 m wide (across track) by 79 m long (along track). This is the best spatial resolution possible on Landsats I and II. Landsat III RBV approaches a 30-m resolution. Purchased imagery may have poorer resolution due to image processing at Goddard or EROS. Resolution equivalent to the 80-m digital data may be maintained by purchasing the computer compatible digital Landsat tapes (CCT's) from EROS. The current price is \$200.00 and includes four bands of each scene. The CCT format requires computer cleanup and geometric rectification before digital enhancement can proceed. No enhancement, however, can improve upon the 80-m ground resolution.

191. Plans for Landsat "D" call for an optimum ground spatial resolution of 30 m, but future spacecraft probably will not improve upon this due to considerations of national sovereignty and defense, and personal privacy considerations involved with higher resolution information being available in the worldwide public domain.

192. Another perplexing problem associated with increased spatial resolution is the tremendous volume of data which will be generated by a system of higher resolution. For example, Landsat "D" will generate data at a rate of  $10^8$  bits per second, yet the most advanced data processor currently available can only process data at a rate of  $10^{11}$  bits per day; thus, the satellite will only be able to transmit for a little over 15 min per day. An increase in resolution simply could not be handled without significant advances in data-handling techniques even if the political objections mentioned above could be overcome.

#### Atmospheric backscatter

193. A second disadvantage of Landsat imagery is due to the high elevation of the sensing platform. At this altitude (817 km), a large amount of upward scattered radiant flux from the atmosphere enters the sensor. This "sky radiation" tends to reduce the quality of the image by reducing both the tone contrasts and the edge gradients on the image which determine image sharpness. Generally, the sky radiation adds a component of blue to the image. This effect is most pronounced in band 4 with bands 6 and 7 essentially free of all but the most severe atmospheric problems (Figures 61 and 62). Unlike the spatial resolution which cannot be improved, the effects of atmospheric backscatter may be partially reduced by suitable enhancement techniques or EROS Data Center level adjustment. Similar problems occur in high-altitude aircraft imagery, but not to the same degree.

PART VI: EVALUATION AND SELECTION OF MOST APPROPRIATE  
TYPES OF IMAGERY FOR SPECIFIC TYPES OF STUDY AREAS

194. The basic objective of an image acquisition program in earthquake engineering is to acquire imagery which possesses the maximum contrasts between rock types, vegetation, etc. This contrast may not be possible to achieve on a single type of imagery and some optimum combination may be required. The decision regarding the optimum combination may be difficult, incorporating several conflicting objectives. The most effective way to make such decisions is to follow a general decision analysis algorithm. The present discussion attempts to formulate such an algorithm for a general selection process.

Determination of Specific Information Desired

195. The first step should be to conduct a thorough literature review of the area under study. Information relating to rock types in the area and their descriptions, including mineralogy, grain size, reflectance, color, and density, is extremely useful. Information on vegetation type and density, general topography, and surface and groundwater character of the area is also useful. Lee et al.<sup>56</sup> suggest organizing this data into a matrix of rock unit properties and rock type (Table 9). A matrix of this type helps to organize important rock properties and serves as preliminary image interpretation keys.

196. The thorough literature review provides a basis for assessing features which indicate earthquake hazards. For example, in the Basin and Range area normal faults predominate; on the west coast strike-slip and thrust faults predominate; in Alaska megathrusts are dominant, with thrust, normal, and strike-slip faults present to the north of the ocean trench. In central and eastern United States, crustal lineaments, density and stress contrasts at igneous centers, warps, and some fault zones are believed to control earthquake hazards. The literature review should incorporate meetings with professionals familiar with the study area. Proper use of available expertise is fundamental to the decision process.

Table 9  
Qualitative Descriptor Matrix<sup>56</sup>

<u>Property</u>	<u>Morrison Formation</u>	<u>Dakota Formation</u>	<u>Benton Formation</u>	<u>Niobrara Formation</u>
Lithology	Shale	Qtz-SS	Shale	Shale
Grain size	Very fine	Medium	Very fine	Very fine
Reflectivity	Low	Moderate	Low	Moderate
Color	Green	Tan	Gray	Gray-tan
Density	Low	Moderate	Low	Low
Topography	Gentle	Rugged	Gentle	Gentle

197. Immediately following the literature review, a preliminary field reconnaissance study and data collection program should be undertaken. This program should be directed toward satisfying the major objective by quantifying the physical or chemical differences within the study area. During this phase, the reflectance of the rock units should, if possible, be quantified. This can be accomplished by a spectroradiometer, which measures the spectral flux quantities of a surface, or more simply by a color chart (visible region) or a light meter. An aerial reconnaissance during this phase is important since the human eye is an efficient, if qualitative, spectroradiometer in the visible region and the advantages of oblique irradiation may be assessed by an early morning or late afternoon reconnaissance flight. In some Corps of Engineers projects, multispectral photography is acquired using hand-held cameras to aid in image selection. This field program should also include a measurement of the thermometric and, if possible, the 8- to 14- $\mu\text{m}$  radiometric temperature of major rock and soil units in addition to acquisition of available imagery of the study area.

198. At the end of these two phases, it should be possible to determine the scale and resolution required to accurately map features of interest. The matrix (Table 9) developed in the literature review can be expanded and used as an aid to selecting appropriate spectral regions for imaging. Out of 32 rock and soil properties, Lee et al.<sup>56</sup> found four to be important to remote sensing in geological applications: (a) topographic landform, (b) color, (c) reflectivity, and (d) surface

temperature. Though the relative importance of these four parameters may vary from project to project, the authors agree that these are the overriding parameters in imagery selection.

Determination of most useful spectral band(s)

199. Once the site has been properly characterized, the most appropriate spectral band or bands may be chosen for image recording. Table 10 was originally compiled by Lee et al<sup>56</sup> and expanded by the authors as an aid in this selection process. Table 10 indicates that ground reconnaissance before, during, and after imaging is extremely important. A combination of bands for ratioing or a combination of sensors such as panchromatic for low-sun angle and color infrared for vegetation changes may also be advantageous. The specific combination may be selected with the aid of Table 10, the discussions in Parts III and IV, and the decision analysis approach discussed at the end of this chapter.

Determination of optimum platform for sensing

200. Platform selection determines the scale, format, availability, and cost of the sensing project.

201. Imagery scale. The optimum scale of the imagery will vary from project to project and from hazard to hazard (Part II). However, the authors have found that a progression from small scale, for synoptic interpretation, to large scale, for detailed interpretation, is preferable. The most commonly available small-scale imagery is Landsat (1:1,000,000) and AMS (1:62,500). The authors recommend a scale of 1:10,000 to 1:12,000, and larger for specific, complex areas when seeking large-scale imagery on active fault and earthquake engineering projects.

202. Imagery format. The imagery format, photographic or scanned, is more a function of spectral region than platform type. It is more common to use photographs for the near infrared, visible, and ultra-violet regions and scanned imagery for the thermal infrared and microwave regions. The major advantage of scanner imagery is its digital

Table 10  
Site Characterization Criteria

Spectral Region	Sensor Type	Without Ground Control	With Ground Control	Cost	
		Derived Information	Ground Information		
Ultra-violet	Black and white photography	Topographic variations, landforms, minor lithologic discrimination of carbonates, and some evaporites	1. Elevations and locations 2. Geologic geomorphic reconnaissance 3. Geologic reconnaissance 4. Geologic reconnaissance	1. Topography 2. Geomorphology 3. Mapping of some units 4. Structural mapping	\$10/Exposure Not commercially available
	FLD discriminator	Plant stress			
Visible	Black and white photography	1. Topographic variations-- particularly using low-sun angle irradiation 2. Landforms 3. Lithologic distribution-- through not unique mineralogy 4. Surface structures Detailed fracture and topographic analysis when oblique irradiation is utilized. 5. General surface reflectivity variations	1. Elevations and locations 2. Geomorphic reconnaissance 3. Geologic reconnaissance 4. Geologic reconnaissance 5. Geologic reconnaissance	1. Topography Quantitative stratigraphy Engineering geology 2. Geomorphology Fault type and age Landslide and liquefaction hazard 3. Map of geologic units 4. a. Structural geologic maps b. Fracture and fissure patterns to determine type of fault--depending on scale c. Tilting and folding 5. a. Density changes in vegetation b. Alteration and weathering	\$10/Exposure
	Color photography	1. All of the above 2. Subtle variations in lithology 3. Color anomalies 4. Qualitative water depth	1. All of the above 2. Geologic reconnaissance 3. Spectral reflectance 4. Measurement of depths	1. All of the above 2. Detailed geologic mapping	\$15-\$20/ Exposure
Near infrared	Black and white photography	1. All of visible black and white 2. Minor variations in vegetation	1. All of visible black and white 2. a. Vegetation type b. Vegetation size c. Lithology selective vegetation d. Moisture selective vegetation	1. All of visible black and white 2. a. Vegetation species mapping b. Vegetation density mapping c. Differentiation of geology d. Geologic structures controlling ground water	\$10-\$15/ Exposure
	Color photography	1. All of the infrared black and white 2. Subtle variations in vegetation 3. Vegetation reflectance anomalies	1. All of the infrared black and white 2. Same as 2a, b, c, and d above 3. Phenology	1. All of the infrared black and white 2. Detailed mapping of 2a, b, c, and d above 3. Vegetation vigor; stress due to moisture deficiency, salinity, or disease	\$20-\$25/ Exposure
Thermal infrared	Scanner imagery	1. Radiometric temperature variations associated with moisture, thermal properties of rocks, vegetation, and shadowing and atmospheric conditions 2. Tonal lineaments 3. Thermal anomalies	1. a. Radiometric temperatures b. Spectral emissivity c. Thermal diffusivity d. Geologic reconnaissance 2. a. Moisture sampling b. Vegetation observations c. Topography d. Surficial geology 3. Geologic reconnaissance	1. a. Isoradiance maps b. Isothermal maps c. Gross lithology d. Mapping of some geologic units 2. a. Fractures controlling ground water b. Fractures controlling vegetation c. Fractures controlling topography d. Fractures controlling geologic deposits 3. a. Bedrock/alluvium contacts b. Disturbed ground c. Cultural features d. Hot springs and hot ground e. Subsurface openings	Average \$16 per line mile, less for more miles
Passive microwave	Scanner imagery	1. Relative radiometric temperatures	1. a. Moisture sampling b. Density and particle size c. Surface and subsurface thermometric temperature	1. a. Relative moisture content b. Changes in density and porosity c. Microwave emissivity and penetration depth	Approximate same list as TIR
Active microwave	Scanner imagery SLAR	1. Topographic variations and landforms* 2. Lineaments* 3. Textural variations*	1. Geomorphic reconnaissance 2. Geologic reconnaissance 3. Geologic reconnaissance surface roughness particle size	1. Geomorphology 2. Faults and fracture mapping 3. Gross lithologies	Approximate same list as TIR

\* For areas having sparse vegetation. In areas having dense vegetation the vegetation canopy provides the primary reflector for radiation.

format, and because of this advantage scanners sensitive to wavelengths below 4  $\mu\text{m}$  (such as Landsat) will probably be widely used in airborne systems in the future. A disadvantage of scanned imagery is that parallax must be acquired through sidelapping strips which may result in areas of no stereoscopic coverage. Acquiring imagery with parallax is easier and more efficient with photography. At the present time, the authors would choose photography over scanned imagery within the spectral range where the two systems overlap.

#### Formulating a Decision Analysis

203. Once all available data and expertise are accumulated, a decision can be made regarding the optimum sensor or combination of sensors to be used on a particular project. In attempting to make such a choice, the researcher will be faced with two major problems:

- a. There are generally a number of conflicting objectives such as synoptic coverage versus spatial resolution, contrasts in rock reflectance, contrasts in temperature, and balancing the economics of the remote sensing phase with overall project costs.
- b. There will always be uncertainties as to whether these objectives will be attainable; for example, actual reflectance contrasts cannot be predicted with absolute certainty, weather conditions affect the temperature responses of rock, etc.

204. The decision dilemma becomes one of balancing these considerations, all of which are important to selecting the best alternatives concerning a remote sensing project. The problem involved in doing this informally in one's mind is that the large number of factors and interactions often associated with remote sensing projects makes it difficult to think through and rationally balance the objectives. For most projects, a table such as Table 10 or Table 1A is adequate to use in aiding the decision. However, as the current explosion in available data increases from remote sensing as well as other geophysical areas, a more structured decision process will be needed. A rational decision analysis technique can greatly simplify the dilemma and may be considered in four steps.<sup>57</sup>

## Step I: structuring the decision problem

205. This step involves a precise definition of the decision problem, and generally includes the following:

- a. Identification of all useful alternatives. In remote sensing applications, these alternatives will generally include the type of imaging system; for example, ultra-violet, visible, near infrared, thermal infrared, micro-wave, digital output, photographic output, space platform, or airborne platform.
- b. Generation of an appropriate set of objectives and measures of effectiveness to indicate the degree to which these objectives may be achieved by the various alternatives.

The stated objective is clear, to image the earthquake hazard at maximum contrast with its background. However, this is too general for a formal analysis at this stage of the remote sensing project. Table 11 gives an example of some specific objectives along with some measures of effectiveness or attributes associated with them.

Table 11  
Some Examples of Objectives, Subobjectives, and Attributes  
for a Typical Remote Sensing Project

Objective	Subobjective	Measure of Effectiveness (Attributes)
Minimize cost	Savings realized Synoptic coverage	Dollars/frame Dollars/region
Maximize contrast between earthquake hazard and background	Contrast in rock reflectance Contrast in vegetation reflectance Contrast in temperature Contrast in topography Parallax Spatial resolution Digital format	Pixel ratio Pixel ratio Pixel ratio Dip angle of slope Overlap (percent) Metres Yes-no

Step II: description of possible results of alternatives in terms of attributes

206. In this step, the uncertainty associated with each attribute is identified. Assume that there are  $n$  attributes given by  $\underline{x} = (x_1, x_2, x_3, \dots, x_n)$ . Associated with each attribute is a number  $x_i = (x_{i1}, x_{i2}, \dots, x_{in})$ . For example, if  $x_1$  corresponds to "Savings realized,"  $x_{11}$  would correspond to a dollar per frame value, say \$40.00. Each  $x_{ij}$  would correspond to a unique value for each alternative. The results  $\underline{x} = (x_1, x_2, \dots, x_n)$  of implementing a particular alternative may be described by the levels of  $x_{ij}$  for each alternative. These results can seldom be predicted with certainty, however, and in order to represent this uncertainty rationally in the decision, a probability distribution function  $p_j(x)$  associated with each alternative ( $j$ ) and the results  $(x) = (x_1, x_2, \dots, x_n)$  is needed. By implementing this probability function it is possible to assess the decision maker's degree of belief in the likelihood that certain results will occur.

207. If statistical independence of the results  $(x_i)$  is valid, then the probability distribution function for all results may be represented by

$$p_j(x) = p_j(x_1, x_2, \dots, x_n) = [p_j(x_1)][p_j(x_2)] \dots [p_j(x_n)]$$

and can be determined by assessing the decision maker's belief in the likelihood of occurrence of each result independently.

208. Step II is an extremely important step since it incorporates the experience of professionals with prior experience gained through experimental studies, fieldwork, or similar projects into the decision analysis. For example, a geologist familiar with a particular region may consider that the likelihood of observing high contrasts in rock reflectance are lower than the likelihood of observing high contrasts in temperature. Such experience is valuable and should be used in the decision process.

Step III: prescription  
of the relative prefer-  
ences for the possible results

209. In this step, the trade-offs among conflicting objectives which the decision-maker is willing to accept are identified. In order for a rational decision to be made, the decision-maker's subjective preferences must be quantified. For example, are the set of results  $x' = (x'_1, x'_2, \dots, x'_n)$  preferred over the results  $x'' = (x''_1, x''_2, \dots, x''_n)$ ? Are the set of results  $x''$  preferred to the results  $x'$ ? Or is the decision-maker indifferent to both? In order to quantify these preferences, a preference function is needed which assigns some number  $u$  to each of the possible results. This preference function has two attractive properties:<sup>57</sup>

- a.  $u(x'_1, x'_2, \dots, x'_n) > u(x''_1, x''_2, \dots, x''_n)$  if and only if  $\underline{x}$  is preferred to  $\underline{x}''$ .
- b. In situations of uncertainty, the expected value of  $u$  is an appropriate guide to make decisions. Furthermore, for each alternative  $j$ , the probability distribution  $p_j$  and the preference function  $u_j$  are necessary and sufficient to calculate the expected value of  $u_j$ . The alternatives are then ranked with the most promising alternative having the highest expected value.

Step IV: synthesize the in-  
formation of steps I through  
III and rank the alternatives

210. This step involves the actual ranking and selection of the most promising system or combination of systems for the remote sensing project. At this time, a sensitivity analysis may be performed to assess the effect that alterations in the preferences and probabilities may have on the final selection.

Example problem

211. As an example of the decision process, assume that there are only four alternatives ( $j = 4$ ) available to a specific project and these are: (a) panchromatic photography, (b) color photography in the visible spectral range, (c) color photography in the near infrared range, and (d) Landsat multispectral imagery.

212. The first step in the decision analysis is to define the

possible alternatives (a) through (d) above), generate an appropriate set of project objectives, and finally generate an appropriate set of levels of effectiveness (attributes) by which to measure the success in accomplishing the stated project goals. Since most remote sensing projects are not blessed by infinitely large budgets, one of the objectives should be to keep the project within some specified budget. The remaining objectives will be kept to a minimum for simplicity and will be chosen to represent imagery quality (Table 12).

Table 12  
Objectives and Attributes for Example Project

<u>Objectives</u>	<u>Attributes</u>
Budget constraints-- small-scale imagery	Dollars
Contrast in rock · reflectance	Pixel ratio (1-128)
Contrast in vegeta- tion reflectance	Pixel ratio (1-128)
Spatial resolution	Metres

213. In order for the highest expected value of  $u$  to correspond to the most attractive alternatives, the results ( $x$ ) must be consistent and increasing in value from poorest to best. Thus, the economics will be expressed in terms of dollars spent under the budgeted amount (dollars saved), and the spatial resolution will be expressed in terms of the ratio of the spatial resolution available for Landsat imagery (80 m) to the spatial resolution available for each alternative ( $j$ ).

214. Step II involves assigning probabilities to the likelihood of achieving the specified objectives for each alternative. For this example, assume that preimagery literature and field studies in addition to consulting geologists' opinions have established the probabilities in Table 13. The savings and resolution, for this example, are assumed to be absolutely determined; the savings by the price of the imagery, and the resolution by the type of system chosen. The resolution is actually a function of several system properties (Part IV) and should be

considered as an uncertainty with an appropriate probability assigned. Table 13 shows that prior studies and experience indicate a higher likelihood of recording a contrast in vegetation in the study area than a contrast in rock type. Implicit in both of these probabilities is the likelihood that the possible contrasts are directly or indirectly related to features of interest. In addition, there is a direct conflict between the objective of acquiring small-scale imagery to increase savings and the objective of acquiring large-scale imagery to improve spatial resolution.

Table 13  
Established Probabilities for Example Project

Objectives	Alternatives (j)			
	1	2	3	4
Savings	1.0	1.0	1.0	1.0
Rock reflectance	0.58	0.65	0.75	0.45
Vegetation reflectance	0.6	0.69	0.8	0.8
Resolution	1.0	1.0	1.0	1.0
$P_j(\underline{x})$	0.35	0.45	0.6	0.36

215. Once the probabilities have been established, the trade-offs between conflicting objectives and results may be specified (step III). This step involves the generation of a preference function  $u(x_1, x_2, \dots, x_n)$  to quantify the preferences of the decision-maker. In order to derive this function, it would be convenient to consider the preference for each result independently. This was done in deriving the probability distribution function; thus,

$$u(x_1, x_2, \dots, x_n) = f[u_1(x_1), u_2(x_2), \dots, u_n(x_n)]$$

Specifically, it would be convenient if the preference function was of an additive form.

$$u(x_1, x_2, \dots, x_n) = \sum_{i=1}^n k_i u_i(x_i)$$

or a multiplicative form,

$$1 + ku(x_1, x_2, \dots, x_n) = \prod_{i=1}^n [1 + k u_i(x_i)]$$

In either of these forms, it would be relatively simple to derive the preference function simply by considering preferences for each result independently. In order for such a formulation to be valid, however, two measures of independence must hold.<sup>57</sup> Assuming that both preferential and utility independence hold, one may assume a preference function of the form

$$u(x_1, x_2, x_3, x_4) = \sum_{i=1}^4 k_i u_i(x_i) \quad (lla)$$

the constants  $k_i$  are constrained so that  $\sum k_i = 1$  (llb)

and the  $u$ 's range as follows:  $0 \leq u \leq 1$  (llc)

216. By evaluating the  $k$ 's and  $u$ 's in Equation lla, the preference function  $u(x_1, x_2, x_3, x_4)$  may be evaluated. The procedure for structuring the preference function can be done in two steps by (a) assessing the preference function over individual attributes, and (b) assessing the trade-offs between attributes.

217. Assess the preference function over individual attributes. In this step, the preferences for each individual attribute are established by considering them individually. Let  $x_1$  correspond to savings,  $x_2$  correspond to rock reflectance contrast,  $x_3$  to vegetation reflectance contrast, and  $x_4$  to spatial resolution. Beginning with  $x_1$ , assume that the possibilities range from a saving of nothing to \$5000. Thus,  $0 \leq x_1 \leq 5000$ . Since  $u$  is constrained to range from 0 to 1,

$$u_1(0) = 0 \text{ least attractive}$$

$$u_1(5000) = 1 \quad \text{most attractive}$$

The decision-maker now is asked to choose between two options: one, a lottery where savings will either be \$5000 or zero, each of which has a 0.5 chance of occurring and the other where savings will surely be \$2500. The question is whether the decision-maker would prefer accepting a 50 percent chance of getting good results at a savings of \$5000 or a 100 percent chance of getting good results but only saving \$2500. Suppose that, due to costs in other phases of the project, the lottery is preferred to the \$2500 savings. Then, the expected value of the lottery  $0.5u_1(5000) + 0.5u_1(0) = 0.5(1) = 0.5$  must be greater than the expected value of  $u_1(2500)$ ; thus,  $u_1(2500) < 0.5$ . Now the lottery is compared with a 100 percent chance of getting good results at a savings of \$3000. Suppose that this is preferred to the lottery, then  $u_1(3000) > 0.5$ . Next, the decision-maker is asked to choose between the lottery and a sure savings of \$2700; and suppose that he is indifferent to the choice, then  $u_1(2700) = 0.5$  and there is a third point on the  $u_1$  preference function (Figure 112).

218. The process is repeated using a lottery with a 50 percent chance of success at a savings of 0 or \$2700 and sure success at, say \$1000. In this way, the remaining points are constructed in Figure 112. Similar procedures are used to develop preference functions for  $x_2, x_3$ , and  $x_4$  (Figures 113, 114, and 115).

219. Assessing trade-offs among attributes. During this step, the conflicts between objectives are considered by assessing the values of the constants ( $k_i$ ) in Equations 11a and 11b. The attributes were structured in increasing order from worst to best; thus,

$$x_1^0 \leq x_1 \leq x_1^*$$

$$x_2^0 \leq x_2 \leq x_2^*$$

$$x_3^0 \leq x_3 \leq x_3^*$$

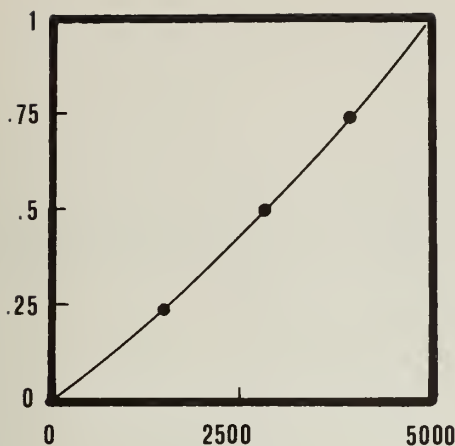


Figure 112. Preference function for savings

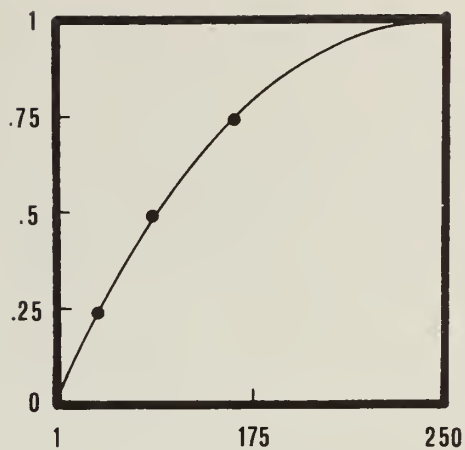


Figure 113. Preference function for rock reflectance contrast

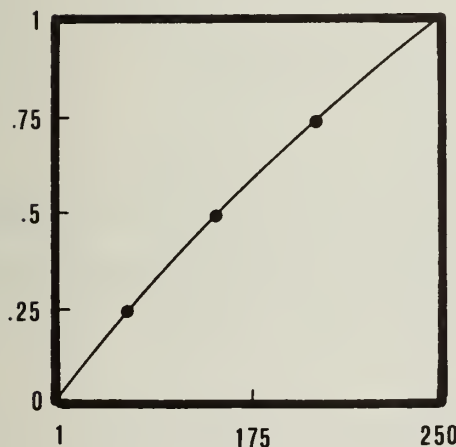


Figure 114. Preference function for vegetation reflectance contrast

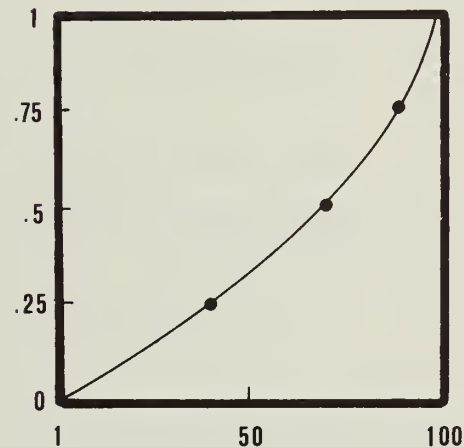


Figure 115. Preference function for spatial resolution

$$x_4^0 \leq x_4 \leq x_4^*$$

where

$x^0$  = worst and  $x^*$  = best

220. In addition, the  $u$ 's were assigned values from 0 to 1 with a preference value of zero given to the least attractive result and a preference value of one to the most attractive. Thus,

$$u_1(x_1^0) = 0 \quad \text{and} \quad u_1(x_1^*) = 1$$

$$u_2(x_2^0) = 0 \quad \text{and} \quad u_2(x_2^*) = 1$$

$$u_3(x_3^0) = 0 \quad \text{and} \quad u_3(x_3^*) = 1$$

$$u_4(x_4^0) = 0 \quad \text{and} \quad u_4(x_4^*) = 1$$

From Equations 11a and 11b

$$u(x_1^0, x_2^0, x_3^0, x_4^0) = 0 \quad \text{and} \quad u(x_1^*, x_2^*, x_3^*, x_4^*) = 1$$

221. The decision-maker is now asked to rank, in order, the attributes based on the one he would prefer to move from worst to best holding others constant. Suppose, based on the preliminary studies of the area, that it is preferable to first increase the spatial resolution; then,

preference No. 1, move  $x_4$  from  $x_4^0$  to  $x_4^*$ , next

preference No. 2, move  $x_3$  from  $x_3^0$  to  $x_3^*$ , next

preference No. 3, move  $x_2$  from  $x_2^0$  to  $x_2^*$ , and finally

preference No. 4, move  $x_1$  from  $x_1^0$  to  $x_1^*$

and thus  $k_4 > k_3 > k_2 > k_1$ .

222. At this point, the trade-off issue is directly faced by choosing between a move of  $x_4$  from  $x_4^0$  to some intermediate value, say  $x_4'$ , and a move of  $x_1$  from  $x_1^0$  to  $x_1^*$ . Suppose that an increase in resolution from  $x_4$  to  $x_4'$  remains preferable to a savings increase from 0 to \$5000, but that if the resolution is increased only to  $x_4''$ , the decision-maker is indifferent to the choice. Then,

$$u(x_1^0, x_2^0, x_3^0, x_4'') = u(x_1^*, x_2^0, x_3^0, x_4^0)$$

and then from Equation 11a

$$k_4 u_4(x_4'') = k_1 \quad (12)$$

In a similar fashion, a point of indifference is reached in a preference for moving  $x_4$  from  $x_4^0$  to  $x_4'''$ , or  $x_2$  from  $x_2^0$  to  $x_2^*$ . Thus,

$$u(x_1^0, x_2^0, x_3^0, x_4''') = u(x_1^0, x_2^*, x_3^0, x_4^0)$$

then

$$k_4 u_4(x_4''') = k_2 \quad (13)$$

Similarly, a choice between spatial resolution and vegetation reflectance contrast is made yielding

$$k_4 u_4(x_4''') = k_3 \quad (14)$$

Since  $u_4$  has been independently assessed (Figures 112-115), Equations 11, 12, 13, and 14 yield four equations for the four unknown values of  $k$ , and the constants may be evaluated. For the present example,

$$\text{if } \begin{cases} x_4'' = 40 \\ x_4''' = 60 \\ x_4'''' = 80 \end{cases} \text{ then } \begin{cases} u_4 = 0.25 \\ u_4 = 0.4 \\ u_4 = 0.6 \end{cases} \text{ from Figure 115}$$

Solving the four equations for  $k_i$  yields the following values,

$$k_1 = 0.111$$

$$k_2 = 0.178$$

$$k_3 = 0.267$$

$$k_4 = 0.444$$

223. Finally, the expected preference value for each alternative may be calculated. The values of  $x_i$  for the example are shown in Table 14 in addition to the corresponding preferences ( $u_i$ ) from Figures 112 through 115 and the probability distribution ( $p_j$ ) from Table 13. Using the values for the preferences from Table 14 and the computed values for  $k_i$ , the preference function  $u(x_1, x_2, x_3, x_4)$  can be calculated for each alternative using Equation 11a yielding,

$$u(x_1, x_2, x_3, x_4) = 0.473 \quad \text{for } j = 1$$

$$u(x_1, x_2, x_3, x_4) = 0.467 \quad \text{for } j = 2$$

$$u(x_1, x_2, x_3, x_4) = 0.548 \quad \text{for } j = 3$$

$$u(x_1, x_2, x_3, x_4) = 0.150 \quad \text{for } j = 4$$

The corresponding expected preference value may be calculated from

$$p_j(x_1, x_2, x_3, x_4) u_j(x_1, x_2, x_3, x_4) \text{ and yields}$$

0.165 for panchromatic prints ( $j = 1$ )

0.210 for color photography ( $j = 2$ )

0.328 for color infrared photography ( $j = 3$ )

0.054 for Landsat multispectral scanner ( $j = 4$ )

224. For the hypothetical project used here, the color infrared photography appears to be the optimum imaging system, followed in descending order of preference by color photography, panchromatic photography, and Landsat imagery. In an actual project, many more attributes

Table 14

Example Values for Calculation of Expected Value

<u>j</u>	<u>Alternative</u>	<u>Assumed Values</u>			<u>Corresponding Preferences, Figures 112-115</u>			<u>Probability <math>p_j</math></u>		
		<u><math>x_1</math></u>	<u><math>x_2</math></u>	<u><math>x_3</math></u>	<u><math>x_4</math></u>	<u><math>u_1</math></u>	<u><math>u_2</math></u>			
1	Panchromatic prints	3000	50	50	80	0.55	0.4	0.28	0.6	0.35
2	Color visible, photograph	2000	60	80	70	0.5	0.5	0.44	0.5	0.45
3	Color IR, photograph	1000	100	150	70	0.7	0.7	0.68	0.5	0.6
4	Landsat MSS	5000	10	10	1	0.1	0.1	0.08	0	0.36

and alternatives may be present, and a computer may be required to efficiently handle the system of equations. However, the decision structure could remain essentially unchanged. At this point, a sensitivity analysis can be conducted to determine whether the optimum system would change due to reasonable variations in the preferences and probabilities. Several iterations of the decision algorithm can be made by establishing ranges for the attributes and probability distributions, rather than the absolute values assumed for the example above.

225. A decision framework such as the one described above may not be appropriate for all remote sensing projects, particularly projects of limited scope. The point at which a formal decision analysis becomes more efficient than an intuitive analysis is not well defined. With the rapid advancements currently taking place in the quality of camera systems, scanning systems, and image processing, enhancement, and display, such analyses are becoming more and more useful. The statement by Keeney and Nair<sup>57</sup> in the conclusion to their paper seems appropriate here, and the authors concur.

... A formal analysis, which has its limitations, is to be preferred over an informal, intuitive analysis which also has limitations. Such a formal analysis will focus discussion on substantive issues and provide the basis for developing a compromise between conflicting points of view.

PART VII: CASE HISTORIES OF REMOTE SENSING USED IN  
EARTHQUAKE HAZARD ASSESSMENT

General Comments

226. This section provides examples of remote sensing studies in support of earthquake hazard assessments in a variety of areas ranging from regions of high seismicity and numerous active faults to regions having low seismicity and no known active faults. The case studies provide examples of approach, sequence of steps, and ground truth tests for a range of projects from comprehensive studies to studies having limited scope, budget, duration, or staff.

227. Each of these cases include the following topics: (a) statement of the problem, (b) approach, (c) results of remote sensing study, (d) supporting studies, and (e) conclusions.

Case History One: Wasatch Fault Zone, Utah

Statement of the problem

228. Growth of population and industry in Utah exceeds the national average. Approximately 80 percent of Utah's population and the bulk of its industry lie within a few kilometres of the Wasatch fault, which is a major, tectonically active, boundary fault between the Basin and Range Province and the Rocky Mountain-Colorado Plateau region. Nearly all of the state's vital lifelines such as water, electrical power transmission lines, gas and oil pipelines, communication lines, railway lines, and highways cross the fault zone. No detailed maps were previously available outlining the location, width, and complex character of this fault zone. The geologic map of Utah<sup>58</sup> shows the fault as an intermittent and imprecisely located structure (Figure 116).

229. Beginning in 1969, the Utah Geological and Mineralogical Survey and the U. S. Geological Survey awarded contracts to Woodward-Clyde Consultants<sup>59,60</sup> to undertake remote sensing studies of the fault zone. With limited field verification, Woodward-Clyde was to assess

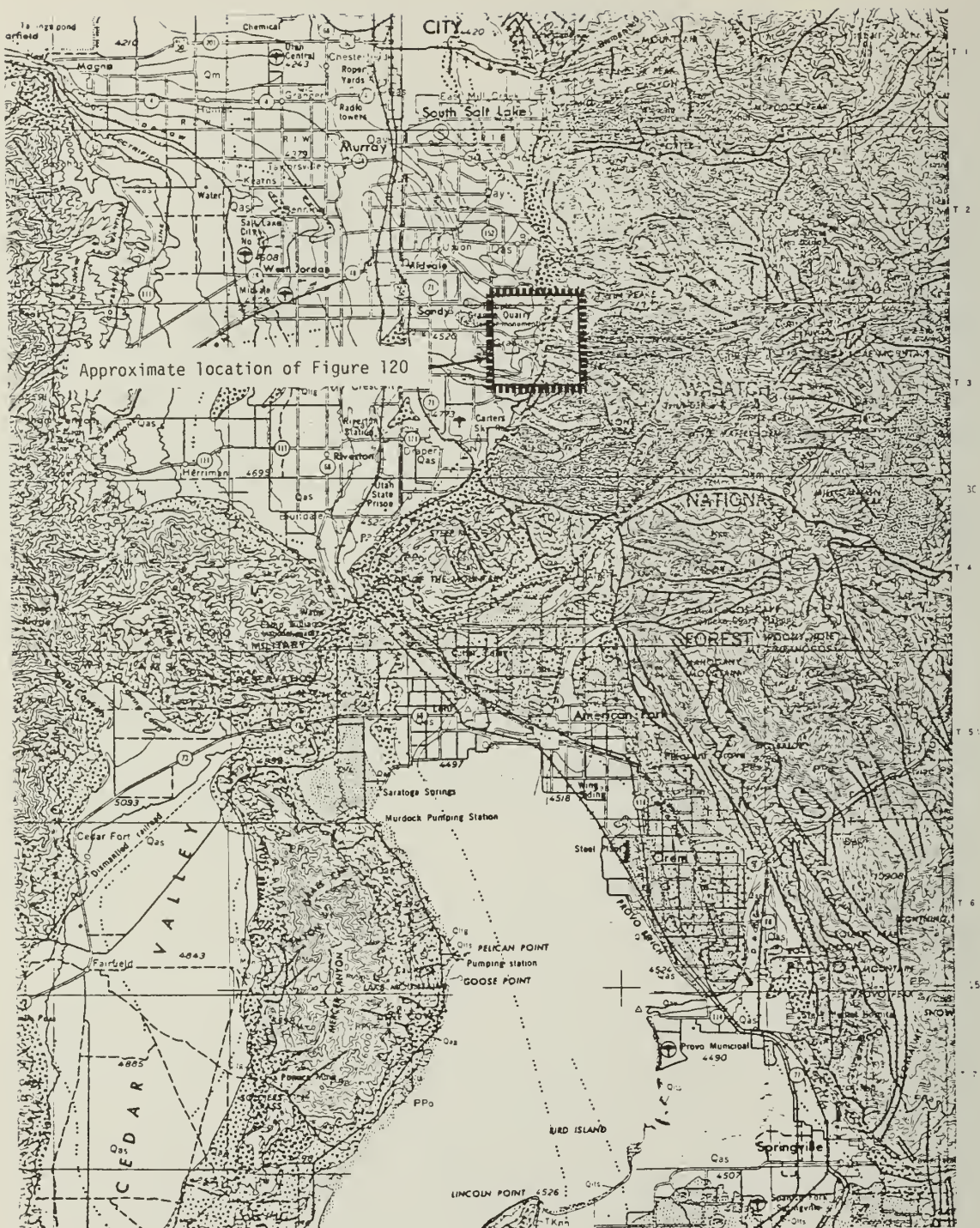


Figure 116. Geologic map of central Utah. The Wasatch fault is mapped as an intermittent fault along the base of the Wasatch range and dotted through Salt Lake City

the precise location of earthquake hazards and the expected location and extent of future ground rupture.

#### Approach

230. The remote sensing imagery analysis of the Wasatch fault zone included acquisition and interpretation of Landsat imagery, Skylab, and Gemini photography. Conventional panchromatic high-sun angle photography produced by the U. S. Forest Service at 1:10,000 scale was also used. Aerial reconnaissance of the entire fault zone, using both morning and afternoon low-sun irradiation indicated that the Wasatch fault is characterized by west-facing fault scarps in a semiarid environment. Some vegetation alignments were observed, but these could not unequivocably be related to faulting. Due to the morphology of the fault, low-sun angle aerial photography was selected as the most promising imagery technique for enhancement of fault features. Photographs were taken during morning and evening summer irradiation to selectively enhance the main fault scarps, graben, and secondary faults. Conventional panchromatic (10- x 10-in. format) photographs at a scale of 1:12,000 were used for the low-sun angle photography.

#### Results of the remote sensing study

231. The enhancement provided by the low irradiation angle permitted detailed mapping of features which had been missed during previous studies (Figures 43, 117, and 118). The low-sun angle photography made it possible to map the main scarp through the eastern one third of Salt Lake City (Figure 119) even though urban development has obscured secondary fault structures which once undoubtedly formed a zone similar in width and complexity to the one shown in Figure 43.

232. A photographic scale of 1:12,000 was used with selected photography produced at a scale of 1:6,000 for detailed mapping of complex areas. Examples of the fault maps produced using this technique are given in Figure 120.

#### Supporting studies

233. The remote sensing study provided a preliminary detailed map of the Wasatch fault zone. The limited field and extensive aerial



Figure 117. Vertical photograph of Wasatch fault, Utah, taken in 1969. It shows several recent scarps (arrows) of the Wasatch fault north of Little Cottonwood Canyon (dotted on Figure 116). The shatter zone extends to beyond the water filtration plant (lower right corner). The fresh nature of the scarps, the sharp "V" shaped canyons, active fan deposition, and lack of sinuosity of the Wasatch range front indicate a tectonically very active area. Development along and within the fault zone is exemplified by the new subdivision area.

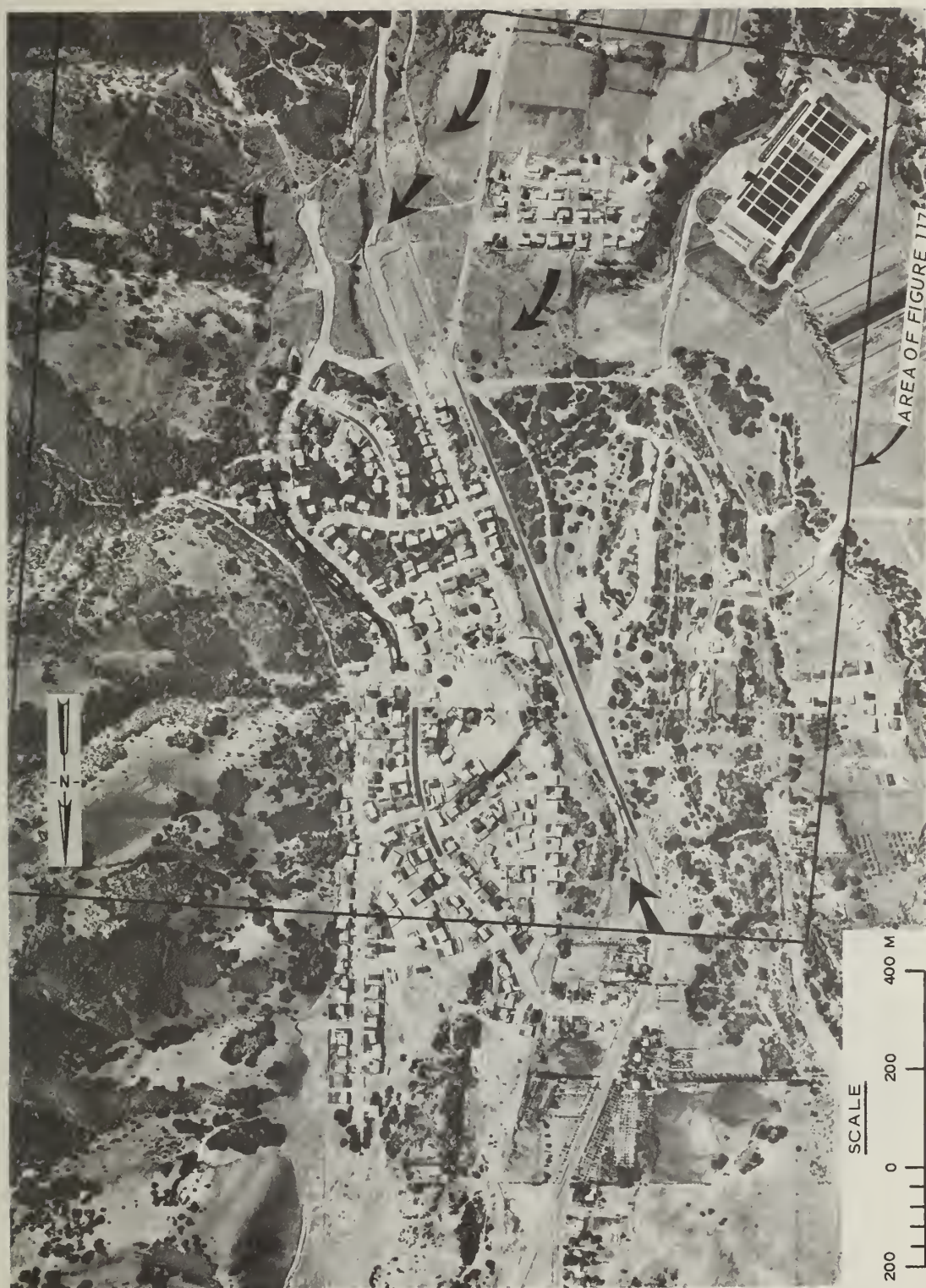


Figure 118. Vertical photograph of Wasatch fault, Utah, taken of the same area as Figure 117 in 1974. The scarps are still visible, but they are rapidly being obscured by suburban development. Note the growth since 1969 and excavation of subdivision expansion to the south across the remaining scarps.

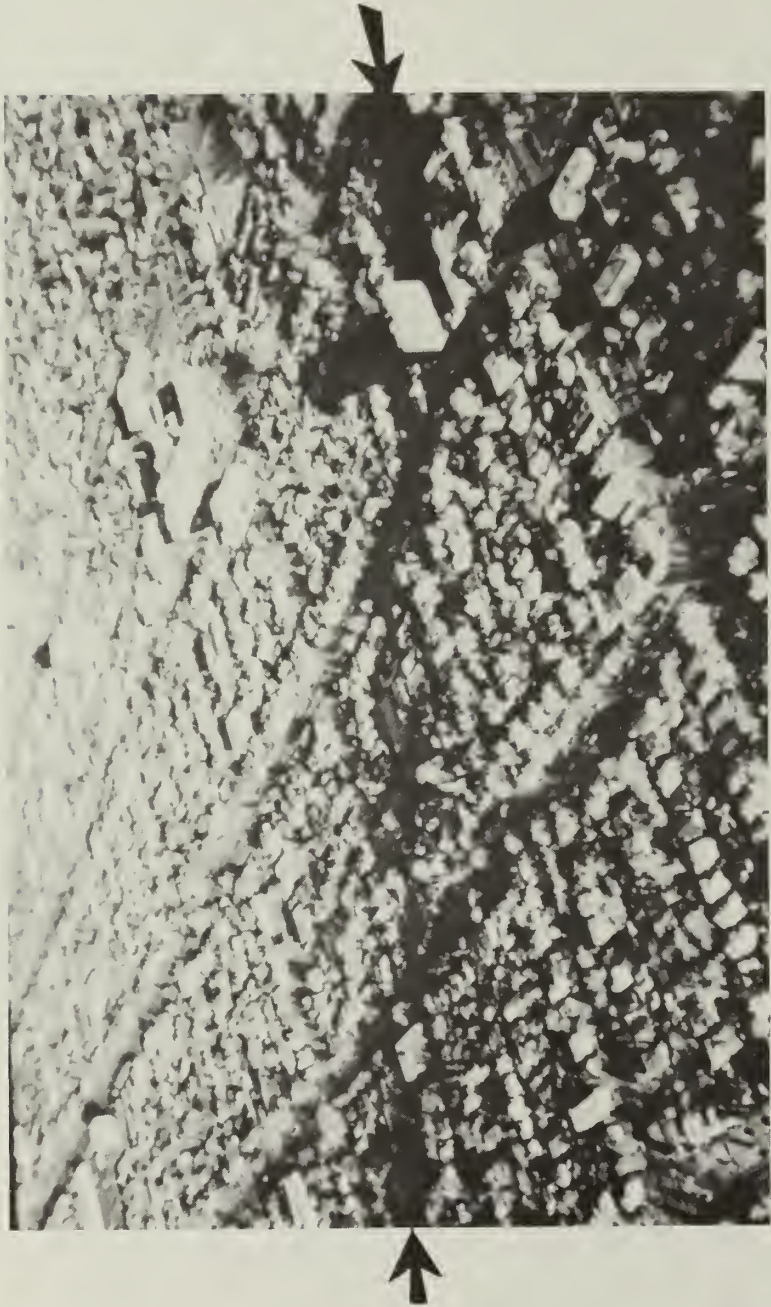
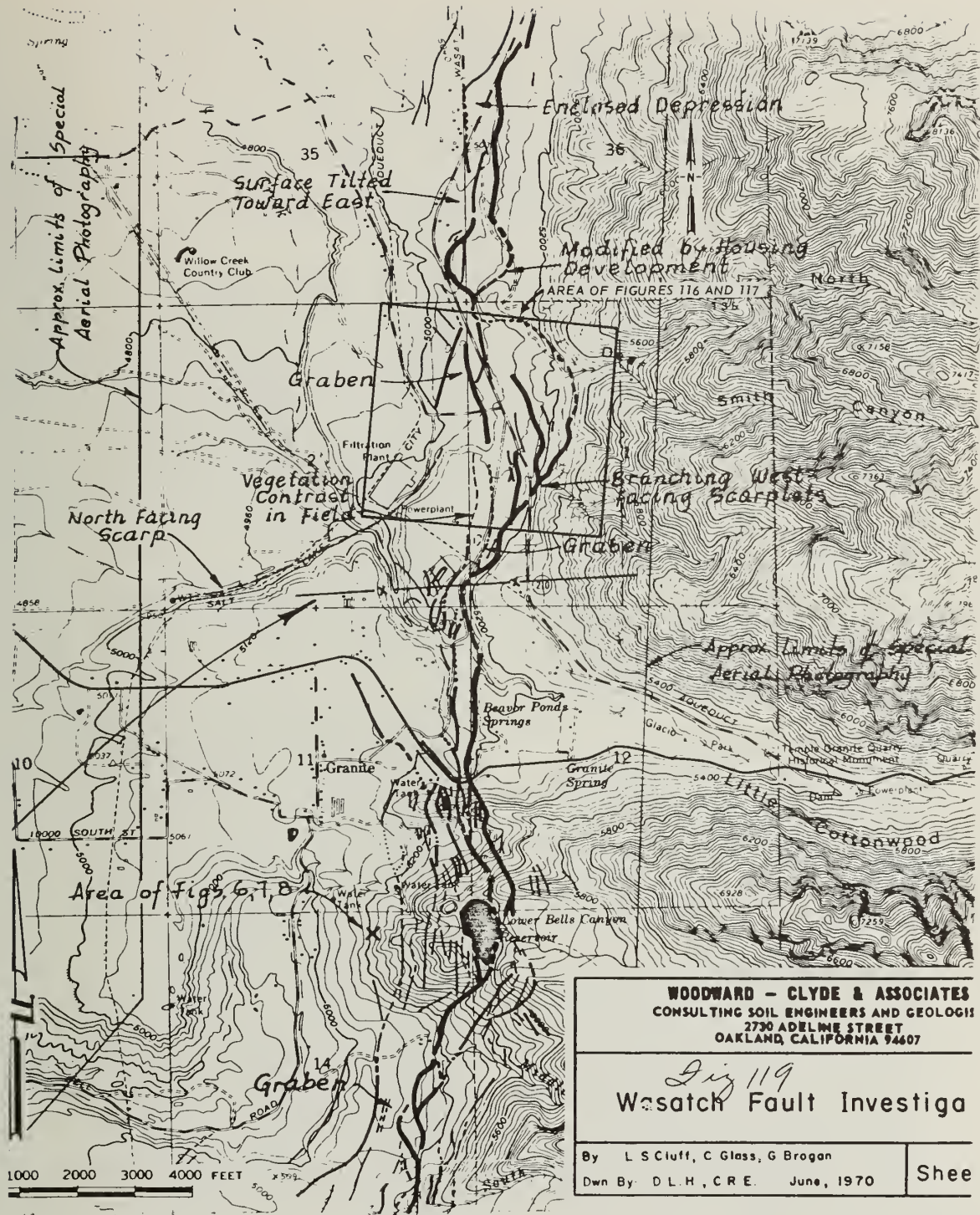


Figure 119. Early morning oblique photograph of Wasatch fault, Salt Lake City, Utah. The main scarp (arrows) traverses the eastern one third of Salt Lake City and, even though urban development has obscured secondary fissuring and graben, this image indicates a major hazard



a. Fault map of the Wasatch fault south of Salt Lake City

Figure 120. Wasatch fault map, Utah <sup>60</sup> (sheet 1 of 2)

### MAP LEGEND

- CLASS I - Prominent or Obvious Fault
- CLASS II - Probable Fault or Rupture
- CLASS III - Possible Fault or Rupture
-  LANDSLIDE - Arrow shows direction of movement
- DASHED LINES are approximate
- DOTTED LINES are concealed or inferred

All lineaments were mapped using special low sun-angle illumination aerial photographs taken especially for this project. The basic scale of the photographs is 1:12,000 (1 inch = 1,000 feet), although scales of 1:5,000 and 1:6,000 were flown for detailed investigation of specific areas. Fault-related features were optically transferred from photographs to 7-1/2 minute topographic base maps using a vertical sketchmaster and were checked by inspection and scale dividers.

#### ACCURACY

Fault-related features plotted on the map generally have a lateral accuracy of  $\pm$  100 feet. In areas of high relief or where cultural development such as roads, fence lines, and other similar features are lacking, the accuracy may be no better than  $\pm$  200 feet. In urbanized areas the fault features have been modified and obscured by city development. In these areas only the most obvious scarps are plotted and more detailed studies are needed to locate the less prominent secondary faults.

#### PURPOSE OF MAP

The purpose of these maps is an aid for general regional land-use planning. The information presented is intended to provide a framework for more detailed investigation and evaluations. We are confident that the features plotted as Class I faults are the locations of the most recent surface fault ruptures. The Class I features have significant vertical relief or extend from surface ruptures having significant vertical relief.

It is our belief that all the Class I lineaments are well defined topographic features that mark the most recent surface fault ruptures. They are believed to have been mostly produced by rapid fault displacements associated with strong earthquakes. Most Class I ruptures are undoubtedly the result of repeated fault displacements that are concentrated along previously established planes of weakness. Therefore, the Class I faults are the most likely candidates for significant future movements. Some fault movement along the Wasatch fault may be by slow tectonic creep as has been documented along other active faults.

The Class II features are probably surface faults. They have little vertical relief and may be secondary fault-

related features associated with ground failure or graben development.

The Class III features are possible surface faults. They have little or no vertical relief. Most of them appear to be related to the Class I and II fault features; however, some Class III features may represent erosional fault-line features or shore-line features and this should be taken into consideration in more detailed investigations. The Class III features are shown because we feel they are possibly fault-related and are important enough to be considered for further investigation and evaluation. Our confidence level decreases from Class I to Class III.

It is important to understand that some minor fault breaks may not have been identified or recognized, or they may be confused with shore-line features again emphasizing the need for more detailed surface mapping and subsurface investigations.

The most recent movements on the Wasatch fault are predominantly vertical, with the mountain block being displaced relatively upward in respect to the valley block. Because of the vertical movement and the geometry of the fault plane, past movements along the Wasatch fault have produced grabens and tilted blocks adjacent to the main fault break. Future movements are expected to also produce tilted blocks and this should be given serious consideration in locating high-rise buildings or other structures that cannot tolerate tilting or changes in lines of level. Tilting should be of prime concern in more detailed investigation and evaluations.

Landslides are common along portions of the Wasatch fault. Many of them are outlined on the prepared maps. Some are presently active and some appear to be in a state of equilibrium. The landslide debris deposits are important because, even though some appear not to be presently moving, they are potentially unstable, especially if they are altered or disturbed. Disturbances by earthquakes, fault movements, man-made cuts or heavy rainfall could re-activate the slide mass. Therefore, detailed investigations must be carried out before development is allowed near these landslides.

#### b. Map legend

Figure 120 (sheet 2 of 2)

reconnaissance program led to deletion of cultural or nontectonic lineaments from the maps. The study defined the extent and width of the fault zone. Additional supporting studies are required to determine the time of most recent offset, recurrence interval, and the number of Holocene events. Expanded remote sensing analysis is required to include the other Basin and Range faults of the region and to evaluate all branching structures. A detailed analysis of the Wasatch fault would require additional studies such as (a) trenching of the fault zone, (b) radiometric dating of Quaternary deposits, soils, and surfaces, (c) detailed geophysical studies to evaluate gaps in the fault pattern from recent sedimentation or urban development, and (d) more detailed study of the Quaternary stratigraphy and geomorphology.

#### Conclusions

234. The detailed maps and supporting text of this study resulted in a good definition of fault length, continuity, and width of the fault zone, and provides a basic source of data for preliminary urban planning, regional planning, and siting studies. The study resulted in accurate and detailed location of the many strands of the Wasatch fault zone along and near the front range of the Wasatch Mountains.

### Case History Two: Search for Active Faults in Eastern Alaska

#### Statement of the problem

235. Prior to final design and placement of the Trans-Alaska Pipeline, the U. S. Department of Interior issued an Environmental Impact Statement that recognized the essentially unknown risk of future earthquake and surface faulting activity on faults along and near the pipeline route. Stipulations expressed in the statement included a requirement that a search be made to identify, delineate, and provide design parameters for faults along the route. The study was undertaken by Lloyd S. Cluff of Woodward-Clyde Consultants and David B. Slemmons of the Mackay School of Mines, University of Nevada. The problem was to search for all active faults in the region, delineate their full extent, determine the character and activity, specify probable future surface

faulting offsets, and establish maximum probable earthquakes. This discussion is based on the published reports of Brogan et al.,<sup>61</sup> Cluff et al.,<sup>12</sup> and Slemmons.<sup>13</sup>

#### Approach

236. The approach is based on a regional rather than site-specific study and on a search for characteristic regional criteria shown by active faults (Cluff et al.,<sup>12</sup> and Tables 7 and 8 of Slemmons<sup>13</sup>). The method is based on the assumption that active faults show recurrence of activity and that long-term activity produces geomorphic features that can be detected and delineated by remote sensing methods. The evaluation included the following:

- a. Review of existing knowledge.
- b. Aerial reconnaissance of the major faults along and near the route.
- c. Acquisition and evaluation of all available aerial photography and imagery on a large regional basis and the acquisition of low-sun angle aerial photography of known or suspected active faults and major structures along the pipeline route.
- d. Detailed field review and study of all faults and lineaments indicated by the geologic literature and the imagery analysis.
- e. Preparation of the final report.

237. The regional approach evaluated the area shown in Figure 121. A regional approach to active fault studies is justified since many active faults do not show evidence of activity along their full length. Often the best areas for studying the character of specific faults are located at a distance from the affected site. In addition, the design of structures may be controlled by larger magnitude earthquakes occurring at a distance from the site, rather than local structures capable of generating only small earthquakes.

#### Results of remote sensing study

238. The evaluation of standard aerial photographs at scales of 1:40,000 to 1:60,000 led to the recognition of over 8,000 lineaments which received detailed field study during the summer of 1973. The field study which was conducted at various times of the day included

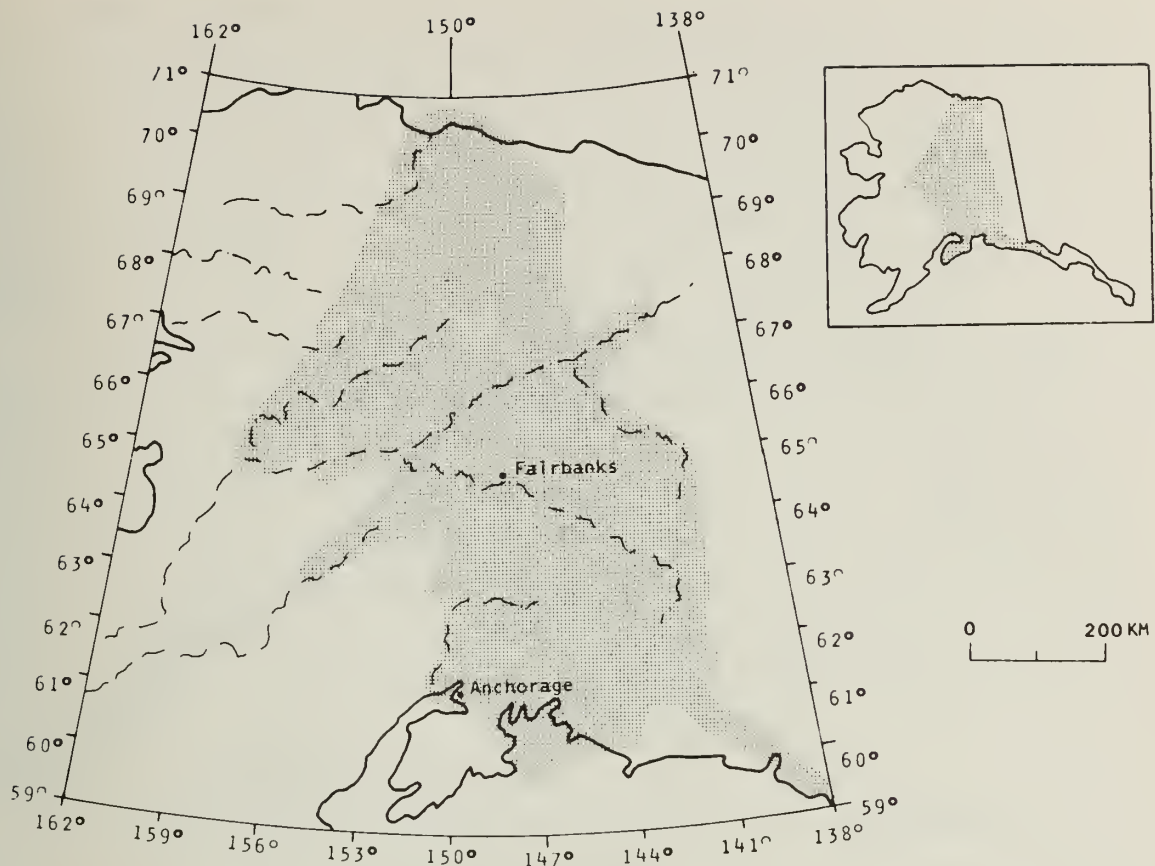


Figure 121. Map showing the area (stippled) evaluated during field studies presented in this paper

extensive aerial reconnaissance involving use of many observers and three jet helicopters. Field crews collected extensive field data on each lineament or fault. This phase of the program was conducted between May 1, 1973, and September 1, 1973, with more than 1500 hr of in-flight helicopter time and more than 800 hr of fixed-wing aircraft time.

#### Supporting studies

239. Detailed study of the major faults, intended to fully assess the activity of the faults, required performance of special surveys to assist in precise location of faults concealed by Holocene deposits.

#### Conclusions

240. The imagery analysis revealed over 8000 faults and lineaments. The field studies reduced these to 24 active faults (Figure 122),

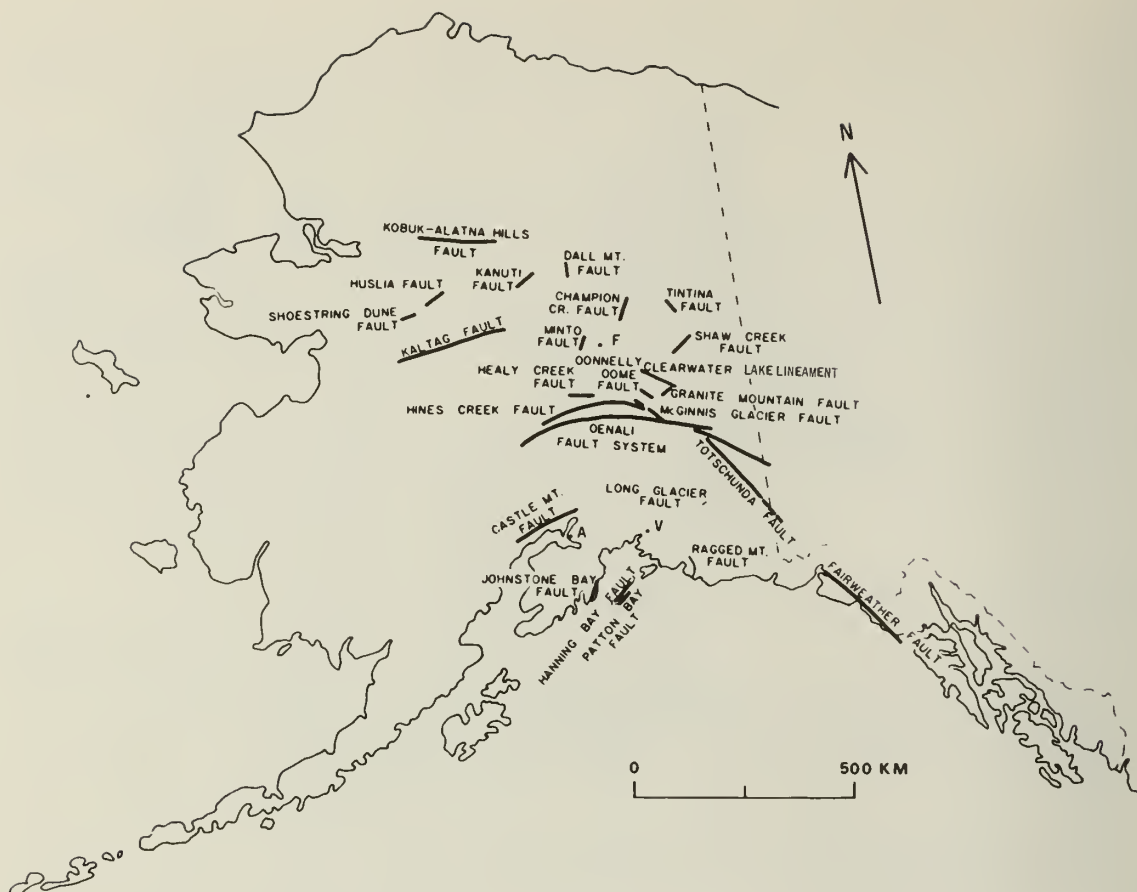


Figure 122. Map showing the locations and trends of faults discussed in this paper. All faults shown are active, except the Hines Creek fault.

A = Anchorage; F = Fairbanks; V = Valdez

of which four were not previously known. The detailed analysis provided fault characteristics of length, maximum credible magnitude, and displacement for future earthquakes.

#### Case History Three: Evaluation of the Pipe Creek Fault Zone at the Libby Reregulating Dam, Northwestern Montana

##### Statement of the problem

241. The U. S. Army Engineer District, Seattle, conducted a remote sensing program for the siting of the Libby Reregulating Dam, near Libby, Montana. Their imagery analysis included review of available Landsat special SLAR imagery. Conventional aerial photographs of an 80-km radius area were studied. These studies revealed a prominent

topographic lineament, the Pipe Creek fault. The estimated length of this fault was approximately 100 km. The special remote sensing study was to evaluate the activity, type of fault, age of last offset, possibility of renewed activity, the magnitude of potential earthquakes, and the character of other nearby faults that might be associated with damaging earthquakes.

#### Approach

242. The approach included review of existing imagery, low-sun angle aerial reconnaissance of all of the major faults of the region, within a radius of about 80 km of the dam, ground visits to critical exposures near the damsite and in areas of good exposure along the Pipe Creek fault, and the selection of three sites for exploratory trenches across the fault. The trenching sites were selected to show whether or not the Wisconsin age glacial deposits or overlying soils were cut by the fault and, if so, to determine amount and type of surface faulting events.

#### Results of remote sensing analysis

243. No evidence of postglacial faulting along major faults of the region was shown by the existing imagery. The low-sun angle aerial reconnaissance flights indicated no postglacial faulting on the Pipe Creek fault, other nearby faults, or the nearest segment of the Rocky Mountain Trench. Correlation of the fault geomorphology with the Hebgen Lake surface fault of 1959 was made to assure that the activity/nonactivity decision was based on comparison with a known active fault in a similar climatic, vegetation cover, and topographic setting. Two of the three sites selected for trenching crossed the full width of the Pipe Creek fault zone.

#### Supporting studies

244. The exploratory trenches showed the following:

- a. The trench near the damsite showed fault offset or warping of soils and glacial outwash terraces deposits of about 10,000 years age. This data was not conclusive since it was not possible to trench the full width of the fault zone.
- b. The trench located several miles north of the site

exposed poorly bedded, late Wisconsin age glacial till. There were no offsets or warping of the soil horizons and underlying till, and no fissuring or veining was present. The trench verified that there was no Holocene faulting.

- c. The Buck Creek trench site, several miles south of the damsite, exposed a late Wisconsin till and a lower till of assumed early Wisconsin glacier age. Although the till has a weak bedding that would reveal any offsets of more than a few centimetres, neither of the deposits showed any evidence of offset. The trench verified the lack of Holocene surface faulting, and strongly suggests that there has been no surface faulting since early to middle Wisconsin (100,000 to about 45,000 years B. P.).

### Conclusions

245. The study demonstrated by remote sensing studies with support from exploratory trenching that the Pipe Creek fault zone showed no geomorphic or stratigraphic evidence of activity during at least the Holocene, and probably for more than 45,000 years B. P.

246. The classification of this fault as inactive during the Holocene and probably inactive since early to mid-Wisconsin makes the fault length and earthquake magnitude method inappropriate. No maximum credible earthquake, other than a regional "floating" earthquake, is considered probable for this area.

### Case History Four: The 1872 Pacific Northwest Earthquake Fault Study

#### Statement of the problem

247. One of the greatest earthquakes in the recorded history of the Pacific Northwest was felt on December 14, 1872, in an area of about 1,300,000 sq km, with a maximum observed intensity of MM VIII.<sup>62</sup> The earthquake is estimated to have a local magnitude of about seven.<sup>63</sup> The epicenter (Figure 123) was in or near the Northern Cascades of Washington on the Coast Mountains of British Columbia. No active faults were known within this region, and the earthquake is important as a design event for many important structures. The Washington Public Power Supply System authorized a remote sensing evaluation of the region to determine whether or not active faults are present in the epicentral region.

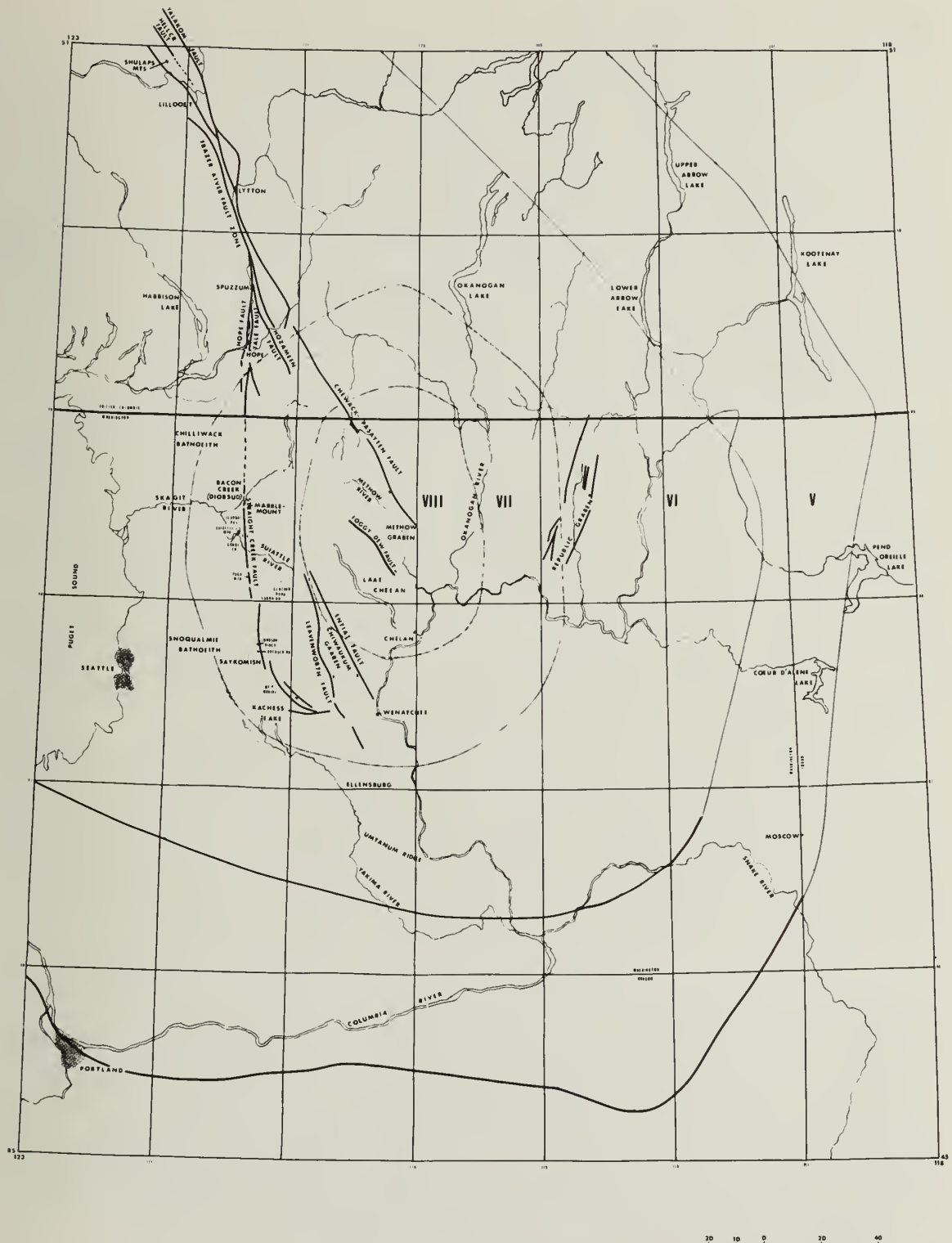


Figure 123. Isoseismal map of the 1872 Pacific Northwest earthquake<sup>62</sup> and location of the Straight Creek, Fraser River, Hell Creek, and Yalakom fault zones

### Approach

248. The approach used for the study was based on the well-established relationship between earthquake magnitude, surface rupture length, and maximum displacement on associated faults for shallow focus earthquakes.<sup>3</sup> The magnitude of 7 suggested a fault of at least some tens of kilometres in length and a surface displacement of several metres. Since most active faults have recurrent activity, active faults should have significant and diagnostic geomorphic expression. Accordingly, the study was based on a regional remote sensing and aerial reconnaissance search for active faults.

249. The method used for the study included review of Landsat, SLAR, weather satellite imagery, and black-and-white aerial photographs of the Cascade-Columbia Plateau Border zone-Fraser River area. Scales of 1:56,000 to 1:70,000 were employed. A compilation of topographic lineaments of that part of Washington between longitudes 118° and 123° west, which was based on study of 1:24,000- and 1:62,000-scale topographic maps, was also included. These investigations were focussed on detection, delineation, establishment of character, and estimation of timing of the most recent fault surface offset.

250. The study included over 200 man hours of fixed-wing aircraft and helicopter aerial reconnaissance along the major fault zones of the region. The aerial reconnaissance study was conducted at low altitudes (typically from 500 to 2500 feet above the terrain) to provide greater surface detail than is possible from imagery and air photo analysis.

251. A total of 1393 special low-sun angle aerial photographs representing scales of 1:12,000 to 1:36,000 were produced and interpreted for this project. The photo and aerial reconnaissance coverage included all of the known major fault zones in the region. During the large-scale photo analysis, each stereographic pair of photos was interpreted by three or more experienced workers. The results were then compared with available high-altitude photography, SLAR imagery, satellite imagery, and topographic and geologic maps.

### Results of the remote sensing study

252. The study led to the recognition of geomorphologically

youthful scarps along several sections of the Straight Creek fault zone in Washington (Figure 124) and along the Hell Creek faults (Figure 125), a branch of the Fraser River-Yalakom fault system. Although the remote sensing program did not specifically identify an 1872 scarp, it demonstrated the presence of active faults in the epicentral region. This suggests that the methods of fault evaluation given in Slemmons<sup>3</sup> are appropriate for earthquake hazard assessment in the Pacific Northwest region.

253. The boundary and internal faults of the Chiwaukum, Methow, and Republic grabens, and their fault extensions into Canada show no evidence of Quaternary activity and were classified as probably dead on the basis of remote sensing analysis.

#### Supporting studies

254. The fault maps prepared by Shannon and Wilson, Inc., and aeromagnetic and gravity maps prepared by Weston Geophysical Research, Inc., provided additional fault and geophysical lineaments to be evaluated. These confirmed the need to evaluate the Straight Creek and Fraser River fault zones. A trenching program conducted by Woodward-Clyde Consultants on a scarp crossing the Diobsud clearcut (Figure 125) showed an offset of the late Wisconsin age glacial till to confirm the "probably capable" classification of the Straight Creek fault zone. Their fieldwork confirmed the presence of many antislope scarps along the Straight Creek fault zone. The limited nature of the field and trenching studies, however, did not eliminate the possibility that some of the scarps may be the result of gravity failure.

#### Conclusions

255. This study of part of the Pacific Northwest and the earlier Alaska study by Brogan et al.<sup>61</sup> (1975) show that many unrecognized active or capable faults may be present, even in well-studied areas. This study demonstrates the importance of integrated programs of study using a "multi" approach to the search for active faults and for their evaluation. Studies of this type progress from a large number (over 10,000 topographic lineaments in the Washington area) obtained by remote sensing and topographic analysis to a small number of verified or partly

verified active or capable faults. Similar types of studies, if applied to other parts of United States, are likely to discover many other important active or capable faults.

256. The extensive low-sun angle aerial reconnaissance, use of "multi" methods of imagery and topography analysis, and comparison of imagery lineaments with data led to the discovery of evidence for activity on several major faults within epicentral region of the 1872 Pacific Northwest earthquake. The most conspicuous scarps are on the Hell Creek fault, a possible branch of Fraser River fault zone, in southern British Columbia. Conspicuous geomorphic evidence for postglacial surface faulting is also present at many localities along the Straight Creek fault system in the Northern Cascades of Washington. Although poorly defined, each of these fault systems appears to extend for more than 150 km. Evidence of late Quaternary surface faulting extends along this zone as a discontinuous and broad belt of scarps and antislope geomorphic features.

257. Some of the scarps along the Straight Creek fault zone are of sufficient freshness of appearance to have been generated during the 1872 earthquake.

258. Possible deep basement continuity of the Straight Creek and Fraser River fault system is shown by a relatively narrow zone of north-south trending master joints and faults within the Chilliwack intrusive complex. This possible joining of the Straight Creek and Fraser River fault zones could form a major system of faults extending for more than 250 km, from an area south of Skykomish in west-central Washington, to northwest of Lillooet in British Columbia.

259. The boundary and internal faults of the Chiwaukum and Methow grabens in the northern Cascade-Columbia Plateau Boundary region of Washington have no remotely sensed evidence of late Quaternary activity or reactivation of these faults in the late Tertiary and Quaternary. They are classified as probably dead.



Figure 124. Straight Creek fault zone on Diobsud Ridge, Bacon Creek area. The scarp in the clearcut is viewed from the south. There are two postglacial, back-facing or antislope scarps on the clearcut



Figure 125. View to south along strike of Hell Creek fault. Note dip to east (left). Fault projects southeast toward the Fraser River fault zone at Lillooet. The scarp suggests multiple scarp-forming events with a rounded upper part of gentle slope angle, about  $30^{\circ}$  to  $40^{\circ}$  slope on the main scarp, and an oversteepened base of about  $50^{\circ}$  slope. These three bevels are interpreted to represent three surface faulting events with cumulative total vertical separation of about 20 ft

## REFERENCES

1. Cluff, L. S. and Slemmons, D. B., "Wasatch Fault Zone--Features Defined by Low Sun-Angle Photography," Utah Geological Association, Publication 1, 1972, pp G1-G9.
2. Grant, T. A. and Cluff, L. S., "Radar Imagery in Defining Regional Tectonic Structure," Annual Review of Earth and Planetary Sciences, Vol 4, 1976, pp 123-145.
3. Slemmons, D. B., "Faults and Earthquake Magnitude," Miscellaneous Paper S-73-1, Report 6, 1977, U. S. Army Engineer Waterways Experiment Station, Vicksburg, Miss.
4. National Academy of Sciences, "Resource and Environmental Surveys from Space with the Thematic Mapper in the 1980's," Washington, D. C., 1976.
5. Colwell, R. N., "Introduction," Reeves, Manual of Remote Sensing, American Society of Photogrammetry, Vol 1, Chap. 1, 1975.
6. Krinitzsky, E. L., "State-of-the-Art for Assessing Earthquake Hazards in the United States: Report 2; Fault Assessment in Earthquake Engineering," Miscellaneous Paper S-73-1, 1974, U. S. Army Engineer Waterways Experiment Station, Vicksburg, Miss.
7. Krinitzsky, E. L. and Chang, F. K., "State-of-the-Art for Assessing Earthquake Hazards in the United States: Report 4; Earthquake Intensity and the Selection of Ground Motions for Seismic Design," Miscellaneous Paper S-73-1, 1975, U. S. Army Engineer Waterways Experiment Station, Vicksburg, Miss.
8. Slemmons, D. B. and McKinney, R., "Definition of 'Active Fault'," Miscellaneous Paper S-77-8, 1977, U. S. Army Engineer Waterways Experiment Station, Vicksburg, Miss.
9. Sherard, J. L., Cluff, L. S., and Allen, C. R., "Potentially Active Faults in Dam Foundations," Geotechnique, Vol 24, No. 3, 1974, pp 367-428.
10. Slemmons, D. B., "New Methods for Studying Regional Seismicity and Surface Faulting," Geoscience, Vol 10, Art. 1, 1969, pp 91-103, EOS, American Geophysical Union Transaction, Vol 50, pp 397-398.
11. Clark, M. M., "Solar Position Diagrams--Solar Altitude, Azimuth, and Time of Different Latitudes," Geological Survey Research 1971: U. S. Geological Survey Professional Paper 750-D, 1971, pp 145-148.
12. Cluff, L. S. et al., "Site Evaluation in Seismically Active Regions--An Interdisciplinary Team Approach," International Conference on Microzonation, 1972.
13. Slemmons, D. B., Microzonation for Surface Faulting," International Conference on Microzonation, 1972.

14. Packer, D., Biggar, N., and Hee, K., "Age Dating Geologic Materials--A Survey of Techniques," 1975, Woodward Clyde Consultants, Suite 200, 3 Embarcadero Center, San Francisco, Calif.
15. Wallace, R. E., "Earthquake Recurrence Intervals on the San Andreas Fault, California," Geological Society of America Bulletin, Vol 81, 1970, pp 2870-2890.
16. Clark, M. M., Grantz, A., and Rubin, M., "Holocene Activity of the Coyote Creek Fault as Recorded in Sediments of Lake Chuilla," U. S. Geological Survey Professional Paper 787, 1973, Washington, D. C.
17. Bull, W. B., "Tectonic Geomorphology North and South of the Garlock Fault, California," Geomorphology in Arid Regions, D. O. Doebring, ed., Proceedings, Volume of the Eight Annual Geomorphology Symposium, State University of New York, Binghamton, 1964, pp 115-138.
18. Bonilla, M. G., "Historic Surface Faulting in Continental United States and Adjacent Parts of Mexico," Open File Report, 1967, U. S. Geological Survey, Washington, D. C.; also Atomic Energy Commission Report TID-24124.
19. Matsuda, T., "Surface Faults Associated With the Nobi (Mino-Owari) Earthquake of 1891, Japan," (in Japanese), Special Bulletin No. 13, Earthquake Research Institute, Tokyo University, Japan, 1974, pp 85-126.
20. Allen, C. R., "Geological Criteria For Evaluating Seismicity," Geological Society of America Bulletin, Vol 86, 1975.
21. U. S. Department of Commerce, National Ocean Survey, "Reports on Geodetic Measurements of Crustal Movement, 1906-71," 1973, Government Printing Office, Washington, D. C.
22. Plafker, G., "Tectonics of the March 27, 1964 Alaska Earthquake," U. S. Geological Survey Professional Paper 543-I, 1969, Washington, D. C.
23. Hastie, L. M. and Savage, J. C., "A Dislocation Model for the Alaska Earthquake," Seismological Society of America Bulletin, Vol 60, 1970, p 1389.
24. Morton, D. M., "Seismically Triggered Landslides in the Area Above the San Fernando Valley," U. S. Geological Survey Professional Paper No. 733, 1971, pp 99-104.
25. Krinitzsky, E. L. and Bonis, S. B., "Notes on Earthquake Shaking in Soils Guatemala Earthquake of 4 February 1976," 1976, Informal Report of the Soils and Pavement Laboratory, U. S. Army Engineer Waterways Experiment Station, Vicksburg, Miss.
26. Saucier, R. T., "Effects of the New Madrid Earthquake Series in the Mississippi Alluvial Valley," Miscellaneous Paper S-77-5, 1977, Soils and Pavements Laboratory, U. S. Army Engineer Waterways Experiment Station, Vicksburg, Miss.

27. Nunnally, N. R., "Introduction to Remote Sensing: The Physics of Electromagnetic Radiation," The Surveillant Science, Remote Sensing of the Environment, Part I, Chap. 3, R. K. Holz, ed., Houghton Mifflin Co., Boston, Mass., 1973, pp 18-27.
28. Blythe, R. and Kurath, E., "Thermal Mapping," Bendix Technical Journal, The Bendix Corporation, Detroit, Mich., 1968.
29. Estes, J. E. and Simonett, D. S., "Fundamentals of Image Interpretation," Reeves, Manual of Remote Sensing, American Society of Photogrammetry, Vol II, Chap. 14, 1975.
30. Koller, L. R., Ultraviolet Radiation, Wiley, New York, 1952, 270 pp.
31. Hemphill, W. R., "Ultraviolet Absorption and Luminescence Studies, U. S. Geological Survey Progress Report, Interagency Report, NASA-100, 1968, Washington, D. C.
32. Hemphill, W. R., Stoertz, G. E., and Markle, D. A., "Remote Sensing of Luminescent Materials," Proceedings, 6th International Symposium on Remote Sensing of the Environment, Ann Arbor, Mich., 1969.
33. Cronin, J. F. et al., "Ultraviolet Radiation and the Terrestrial Surface," The Surveillant Science Remote Sensing of the Environment, R. K. Holz, ed., Part 3, Chap. 8, Houghton Mifflin Co., Boston, Mass., 1973, pp 67-77.
34. Salsbury, J. W. and Hunt, G. R., "Remote Sensing of Rock Type in the Visible and Near Infrared," Proceedings, 9th International Symposium on Remote Sensing of the Environment, Ann Arbor, Mich., 1974.
35. Condit, H. R., "Spectral Reflectance of American Soils," Photogrammetric Engineering, Vol 36, 1970, pp 955, 966.
36. Evans, R. M., An Introduction to Color, Wiley, New York, 1948, 370 pp.
37. Watson, K., "A Thermal Model for Analysis of Infrared Images," NASA Third Annual Earth Resources Aircraft Program Review, Houston, Tex., 1971.
38. \_\_\_\_\_, "Geologic Applications of Thermal Infrared Images," Proceedings, Institute of Electrical and Electronics Engineers, Special Issue on Infrared Techniques for Remote Sensing, 1975.
39. Haugen, R. K., McKim, H. L., and Marlar, T. L., "Remote Sensing of Land-Use and Water Quality Relationships - Wisconsin Shore, Lake Michigan," CRREL Report 76-30, p 15, U. S. Army Cold Region Research and Engineering Laboratory, CE, Hanover, N. H.
40. Janza, F. J., "Interaction Mechanism," Reeves, Manual of Remote Sensing, Vol 1, Chap. 4, American Society of Photogrammetry, 1975.
41. Rydstrom, H. O., "Geological Exploration with High Resolution Radar," Goodyear Aerospace Corporation Publication, GIB-9193A Code 99696, 1970.

42. Steiner, D. and Salerno, A. E., "Remote Sensor Data Systems, Processing and Management," Reeves, Manual of Remote Sensing, American Society of Photogrammetry, Vol 1, Chap. 4, 1975.
43. Scott, R. M., "The Practical Application of Modulation Transfer Functions," SPSE.
44. Ross, D. S., "Image Tone Enhancement," Proceedings, American Society of Photogrammetry, 1969, pp 301-319.
45. Nony, J. P. and Cazabat, C., "Les Équidensités Colores-- Applications à la Photo-Interprétation," Bull. Société, Francais de Photogrammétrie, Vol 43, 1971, pp 17-27.
46. Parton, M. C., "Photographic Density Slicing Project," (unpublished), Department of Mining and Geological Engineering, University of Arizona, Tucson, Ariz., 1977.
47. Selzer, R. H., "Improving Biomedical Image Quality with Computers," JPL Technical Report 32-1336, 1968.
48. Andrews, H. C., "Monochrome Digital Image Enhancement," Applied Optics, Vol 15, No. 2, 1976.
49. Blackwell, R. J. and Boland, D. A., "The Trophic Classification of Lakes Using ERTS Multispectral Scanner Data," Proceedings, American Society of Photogrammetry, 41st Annual Meeting, March 1975.
50. Turner, R. M., "Detection of Short-Term Changes in Vegetation of Southern Arizona," U. S. Geological Survey Professional Paper No. 929, Washington, D. C.
51. Rowan, L. C., Wetlaufer, P. H., and Goetz, A. F. H., "Discrimination of Rock Types and Detection of Hydrothermally Altered Areas in South-Central Nevada," U. S. Geological Survey Professional Paper No. 929, 1976, Washington, D. C.
52. Goetz, A. F. H. et al., "Application of ERTS Images and Image Processing to Regional Geologic Problems and Geologic Mapping in Northern Arizona," JPL Technical Report 32-1597, 1975.
53. Colwell, R. N., "Uses and Limitations of Multispectral Remote Sensing," Proceedings, 4th Symposium on Remote Sensing of the Environment, Michigan University, Ann Arbor, Mich., 1966, pp 71-100.
54. Colvocoresses, A. P., "Platforms for Remote Sensors," Reeves, Manual of Remote Sensing, American Society of Photogrammetry, Vol 1, Chap. 10, 1975, p 549.
55. Reeves, R. G., "Geological Interpretation of Geophysical and Remotely Sensed Data, Eastern Pershing County, Nevada," U. S. Geological Survey Professional Paper (unpublished), 1977.
56. Lee, K. et al., "Ground Investigations in Support of Remote Sensing," Reeves, Manual of Remote Sensing, American Society of Photogrammetry, Vol 1, Chap. 13, 1975.

57. Keeney, R. L. and Nair, K., "Decision Analysis for the Siting of Nuclear Power Plants--The Relevance of Multiattribute Utility Theory," Proceedings, Institute of Electrical and Electronics Engineers, Vol 63, No. 3, 1975, pp 494-501.
58. College of Mines and Mineral Industries, University of Utah, "Geologic Map of Northwestern Utah," compiled by W. L. Stokes, 1963.
59. Cluff, L. S., Brogan, G. E., and Glass, C. E., "Wasatch Fault Northern Portion--A Guide to Land-Use Planning," Utah Geological and Mineralogical Survey, Open File Report, 1970.
60. Cluff, L. S., Glass, C. E., and Brogan, G. E., "Investigation and Evaluation of the Wasatch Fault North of Brigham City and Cache Valley Faults, Utah and Idaho; A Guide to Land-Use Planning with Recommendation for Seismic Safety," Woodward-Lundgren and Associates, 1970.
61. Brogan, G. E., Cluff, L. S., Korringa, M. K., and Slemmons, D. B., "Active Faults of Alaska," Tectonophysics, Vol 29, 1975, pp 73-85.
62. Coombs, H. A., Milne, W. G., Nuttli, O. W., and Slemmons, D. B., "Report of the Review Panel on the December 14, 1872 Earthquake," 1976, "WPN-1/4 Preliminary Safety Analysis Report, Amendment 23, Subappendix 2RA," 1977, Washington Public Power Supply System.
63. Tillson, D., "The Pacific Northwest Earthquake of December 14, 1872," Earthquake Notes, Seismological Society of America, Vol 49, No. 1, Jan-Mar 1978.
64. Reeves, R. G., "Glossary," Manual of Remote Sensing, 1975, American Society of Photogrammetry, Falls Church, Va.
65. Webster's Seventh New Collegiate Dictionary, G. and C. Merriman Co., Springfield, Mass.



## APPENDIX A: GLOSSARY

absorptance--Ratio of the radiant flux absorbed by a body to the radiant flux incident upon it.<sup>64\*</sup>

absorption--The process by which radiant energy is absorbed and converted into other forms of energy.<sup>64</sup>

active systems--A remote sensing system which acts as both a source and receiver of electromagnetic radiation. Active systems are generally associated with radar; however, any area of the electromagnetic spectrum could be used.

acutance--A measure of the ability of a system to show sharp edges between contiguous edges of high and low irradiance.<sup>64</sup>

algorithm--A flow of logic, or rule of procedure for solving a mathematical problem that frequently involves repetition of an operation.<sup>65</sup>

analog--A computer or signal that operates with numbers represented by directly measurable quantities such as voltages, resistances, or rotations.<sup>65</sup>

angle of incidence--The angle that a ray incident upon a surface makes with a perpendicular to the surface at the point of incidence.<sup>65</sup>

angle of reflection--The angle between a reflected ray and the normal drawn at the point of incidence to a reflecting surface.<sup>65</sup>

angle of refraction--The angle between a refracted ray and the normal drawn at the point of incidence to the interface at which refraction occurs.<sup>65</sup>

aperture--The opening in a sensor lens system through which radiation passes.

attenuation--A process in which energy decreases with increasing distance from the energy source.<sup>64</sup>

band--A selection of wavelengths (frequencies).<sup>64</sup>

bit--An abbreviation for "binary digit." Refers to the exponent to which a binary digit is raised, i.e., 6-bit =  $2^6$ .

---

\* Raised numbers refer to similarly numbered items in "References" on pp 217-221 at end of main text.

blackbody--A conceptual body which radiates and absorbs energy at the maximum possible rate per unit area at each wavelength for any given temperature.<sup>64</sup>

chroma--The color dimension on the Munsell scale that corresponds to the intensity of light (brightness).

color composite--A color picture produced by assigning a color to a particular spectral band.<sup>64</sup>

dielectric--A substance containing few free electrons and consequently is a poor conductor of electric current.<sup>64</sup>

diffuse reflection--Reflected rays are not confined to the angle of reflection as defined by Snell's law due to surface roughness and are scattered in all directions.

emissivity--Ratio of the radiant exitance of a body ( $m$ ) to the radiant exitance of a blackbody ( $m^*$ ) at the same temperature ( $m/m^*$ ) denoted by  $\epsilon$ .

exitance--Radiant flux per unit area emitted by a body or surface ( $m$ ) =  $d\phi/dA$  where  $\phi$  = radiant flux. Unit of measure Watt-m<sup>-2</sup>.

filtering--Decomposition of a signal into its harmonic components.<sup>64</sup>

flux--Rate of flow of energy across a given surface.<sup>65</sup>

Fraunhofer line(s)--Dark line(s) in the spectrum of solar radiation due to absorption of specific wavelengths of energy by gases in the outer portions of the sun.

Fraunhofer line discriminator--A remote sensing device designed to detect and measure luminescence by measuring the depths of Fraunhofer lines.

hue--Dominant wavelength determining the color of an object.

irradiance\*--Radiant flux incident upon a surface ( $E$ ) =  $d\phi/dA$  where  $\phi$  = radiant flux and  $A$  = area of surface. Unit of measure Watt-m<sup>-2</sup>.

irradiation--The impinging of electromagnetic radiation on an object or surface.<sup>64</sup>

---

\* The terms "luminance," "illumination," etc., which, correspond only to the visible portion of the electromagnetic spectrum and which are measured in terms of lumens and photos have been avoided in this manuscript in favor of the more general radiance terms that are measured in Watts and valid for the entire spectrum.

luminescence--Light emission by a process in which energy of one wavelength is absorbed by a material and reemitted at a longer wavelength.

parallax--The apparent change in position of one object, or point with respect to another when viewed from different angles.<sup>64</sup>

radiance--Radiant flux. Unit of measure Watt.<sup>64</sup>

radiometer--An instrument for quantitatively measuring the intensity of electromagnetic radiation in various spectral bands.

reflectance--The ratio of the radiant energy reflected by a body to that incident upon it. Reflectance is a property of a particular specimen surface.<sup>64</sup>

reflection--A process by which energy is returned into a medium by a surface.

reflectivity--A fundamental property of a material having a reflecting surface. Reflectivity is an intrinsic property of a material.<sup>64</sup>

return beam vidicon (RBV)--A modified television camera tube, in which the output signal is derived from a depleted electron beam reflected from the tube target.<sup>64</sup>

sky radiation--Solar radiation reaching the earth or a sensor after having been scattered by molecules or particles in the atmosphere.<sup>64</sup>

Snell's law--Law which states that the angle of reflection equals the angle of incidence.

specular reflection--Reflection where the reflected ray is confined to a region very near the angle of reflection of Snell's Law. Characteristic of smooth surfaces.

sun angle--The angle of the sun above the horizon.

thermal inertia--A measure of the rate of heat transfer.<sup>64</sup>

tone--Distinguishable shade variations from white to black.<sup>64</sup>



## APPENDIX B: GUIDE FOR ORDERING AIRBORNE AND LANDSAT IMAGERY

No other type of imagery yields the coverage and versatility that the Landsat system does. The authors feel that Landsat imagery, either conventional or enhanced, is essential to the early phases of earthquake engineering projects and valuable throughout a project due to its synoptic multispectral coverage, and we strongly encourage its use. The following appended pages described how to order Landsat imagery. These directions are published by the EROS Data Center, and additional copies may be obtained from EROS upon letter or phone request.

Directions for purchasing airborne imagery are also included in this appendix.

Prices listed are for date of publication and are subject to change.

### U. S. Department of Agriculture

- (1) Agricultural Stabilization and Conservation Service,  
Aerial Photography Division  
(Eastern U. S.) 45 Frenchbroad Ave., Ashville,  
N. C. 28802  
(Western U. S.) 2505 Parley's Way, Salt Lake City,  
Utah 84109
- (2) Forest Service, Division of Engineering, Washington,  
D. C. 20250
- (3) Soil Conservation Service, Cartographic Division, Federal  
Center Building, Hyattsville, MD 20783

### U. S. Department of Commerce

National Ocean Survey, Washington Science Center, Rockville,  
MD 20852

### National Archives and Record Service

Cartographic Branch, Washington, D. C. 20250

### U. S. Department of Interior

- (1) U. S. Geological Survey Map Information Office,  
Washington, D. C. 20242
- (2) U. S. Geological Survey EROS Data Center, 10th and  
Dakota Avenue, Sioux Falls, S. D. 57104 (see appended  
order forms.)

Canadian Aerial Photography

National Air Photo Library, Surveys and Mapping Building,  
Room 130, 615 Booth Street, Ottawa 4, Ontario, Canada

In addition to these sources many aerial photography firms,  
universities, and state agencies have photography and imagery available.

# HOW TO REQUEST A GEOGRAPHIC SEARCH

This form is used to request a computer search for imagery over a point or area of interest.

Data from this inquiry sheet will be used to initiate a computer Geosearch. The results will be returned on a computer listing along with a decoding sheet, from which imagery can be selected and ordered.

Complete the form as follows:

- A. Enter your NAME, ADDRESS, and ZIP CODE clearly. If you have had previous contact with that facility, include your ACCOUNT number. Enter a PHONE number where you can be reached during business hours.
- B. Complete the required information for either the POINT SEARCH, or AREA RECTANGLE inquiry, which includes the geographic LATITUDE and LONGITUDE coordinates. If coordinates are not available, please supply the GEOGRAPHIC NAME AND LOCATION or a map with the area of interest identified. It is beneficial that you minimize your area of interest, thereby allowing for a faster and more critical retrieval of information.
- C. Complete all other information.
- D. Complete the APPLICATION AND INTENDED USE portion of the inquiry. e.g. Will it be used for identifying buildings or will it be framed and placed on a wall. This information will assist our technicians in determining whether the products available will satisfy your requirements.
- E. Return completed form to the FACILITY NEAREST YOU.

NOTE: If an inquiry is made for Landsat Data, and the Worldwide Reference of PATH and ROW numbers are available, please insert them in the appropriate locations. Otherwise, geographic coordinates will suffice.



# INQUIRY FORM GEOGRAPHIC COMPUTER SEARCH

U.S. DEPARTMENT OF THE INTERIOR  
GEOLOGICAL SURVEY



Return  
completed  
form to  
the facility  
nearest you.

DATE \_\_\_\_\_

NAME MR \_\_\_\_\_ MS \_\_\_\_\_ (FIRST) (MIDDLE) (LAST) ACCOUNT NO. \_\_\_\_\_

COMPANY \_\_\_\_\_ (IF BUSINESS ASSOCIATED) PHONE (Bus.) \_\_\_\_\_

ADDRESS \_\_\_\_\_ PHONE (Home) \_\_\_\_\_

CITY \_\_\_\_\_ Your Ref. No. \_\_\_\_\_  
(P.O. BOX/ACCT OR OTHER)

TO INITIATE AN INQUIRY AND COMPUTER GEOSearch COMPLETE THE FOLLOWING

<b>POINT SEARCH</b>   Imagery with any coverage over the selected point will be included	<b>POINT #1</b> Latitude _____ • <b>N or S</b> Longitude _____ • <b>E or W</b>	<b>POINT #2</b> Latitude _____ • <b>N or S</b> Longitude _____ • <b>E or W</b>	<b>POINT #3</b> Latitude _____ • <b>N or S</b> Longitude _____ • <b>E or W</b>
	Landsat Only (Worldwide Reference System) Path _____   Path _____   Path _____   Path _____   Path _____ Row _____   Row _____   Row _____   Row _____   Row _____		

<b>AREA RECTANGLE</b>   Imagery with any coverage over the selected area will be included	<b>AREA #1</b> Lat. _____ • <b>N or S to</b> Lat. _____ • <b>N or S to</b> Lat. _____ • <b>N or S</b> Lat. _____ • <b>N or S</b> Long. _____ • <b>E or W to</b> Long. _____ • <b>E or W to</b> Long. _____ • <b>E or W</b> Long. _____ • <b>E or W</b>	<b>AREA #2</b> Lat. _____ • <b>N or S to</b> Lat. _____ • <b>N or S to</b> Lat. _____ • <b>N or S</b> Lat. _____ • <b>N or S</b> Long. _____ • <b>E or W to</b> Long. _____ • <b>E or W to</b> Long. _____ • <b>E or W</b> Long. _____ • <b>E or W</b>	<b>AREA #3</b> Lat. _____ • <b>N or S to</b> Lat. _____ • <b>N or S to</b> Lat. _____ • <b>N or S</b> Lat. _____ • <b>N or S</b> Long. _____ • <b>E or W to</b> Long. _____ • <b>E or W to</b> Long. _____ • <b>E or W</b> Long. _____ • <b>E or W</b>
	If the above geographic coordinates cannot be supplied please specify area by GEOGRAPHIC NAME AND LOCATION (include a map if possible)		

<b>PREFERRED TYPE OF COVERAGE</b> Black & White <input type="checkbox"/> Color <input type="checkbox"/> <input type="checkbox"/> Landsat <input type="checkbox"/> Color Infrared <input type="checkbox"/> Skylab <input type="checkbox"/> <input type="checkbox"/> Nasa-Aircraft <input type="checkbox"/> <input type="checkbox"/> Aerial Mapping Photography (Minimum color available)	<b>PREFERRED TIME OF YEAR</b> Check maximum of three <input type="checkbox"/> JAN-MAR <input type="checkbox"/> All coverage <input type="checkbox"/> APR-JUNE <input type="checkbox"/> Latest coverage <input type="checkbox"/> JULY-SEPT <input type="checkbox"/> SPECIFIC DATES _____ <input type="checkbox"/> OCT-OEC	<b>NOTE</b> Seasonal coverage normally applies only to Landsat coverage

**MINIMUM QUALITY RATING ACCEPTABLE**

0.2 3.4 5.6 7.9

(VERY POOR) (FAIR) (GOOD)

**MAXIMUM CLOUD COVER ACCEPTABLE**

10%  30%  50%  80%  100%

NOTE Classification of percent of cloud cover is subjective and is relative to the amount of clouds appearing on the imagery and not to their location

APPLICATION AND INTENDED USE \_\_\_\_\_

**NCIC HEADQUARTERS**  
U.S. Geological Survey  
507 National Center  
Reston, VA 22092  
FTS: 928-6045  
COMM: 703-860-6045

**EROS APPLICATIONS FACILITY**  
NSTL  
U.S. Geological Survey  
Bay St. Louis, MS 39520  
FTS: 494-3541  
COMM: 688-3472

**NCIC MID-CONTINENT**  
U.S. Geological Survey  
1400 Independence Rd.  
Rolla, MO 65401  
FTS: 276-9107  
COMM: 314-364-3680

**EROS DATA CENTER**  
U.S. Geological Survey  
Sioux Falls, SD 57198  
FTS: 784-7151  
COMM: 605-594-6511

**NCIC ROCKY MOUNTAIN**  
U.S. Geological Survey  
Stop 510, Box 25046  
Denver Federal Ctr.,  
Denver, CO 80225  
FTS: 234-2326  
COMM: 303-234-2326

**NCIC WESTERN**  
U.S. Geological Survey  
345 Middlefield Rd.,  
Menlo Park, CA 94025  
FTS: 467-2427  
COMM: 415-323-8111

# HOW TO ORDER SELECTED LANDSAT COVERAGE DATA

This order form is used to order only SELECTED LANDSAT COVERAGE DATA over the Conterminous United States.

Please provide the following information in the indicated areas of the order form:

- A. List your complete NAME, ADDRESS, ZIP CODE, and name of your COMPANY if applicable.
- B. List a PHONE NUMBER where you can be contacted during business hours.
- C. If you have had previous business with THAT FACILITY, please list your ACCOUNT NUMBER if known.
- D. Enter the MAP REFERENCE NUMBER

Turn to the SELECTED LANDSAT COVERAGE MAP foldout.

Identify your area of interest on the map. It may require that you reference a road map or atlas in locating the area on the map.

Trace the small coverage outline from the lower left corner of the map onto a sheet of thin paper. This outline portrays the ground coverage of a LANDSAT image on that map.

Center the coverage trace over the numbered dot nearest your area of interest on the map, aligning the extended dashed line through the dots above and below. (See example of template in use - lower left on map) Dots should fall in sequence, i.e. if your center dot is 35 - 27 the dots to align with will be 35 - 26 and 35 - 28. You may find that a photo centered over adjoining dots will also cover your area of interest. Select the framing you most prefer.

Transcribe the PATH number from the map to the first column of the Map Reference Number. Transcribe the ROW number from the map to the second column of the Map Reference Number.

NOTE: ROW numbers are identified on every FIFTH PATH.

- E. Enter the PRODUCT CODE of the type product being ordered from the STANDARD PRODUCTS TABLE.
- F. The COMMENTS portion is completed only when a CUSTOM PRODUCT is desired and you want to specify the parameters. Refer to the current price list for custom product cost determination.
- G. Enter the number of COPIES of that product which you desire in the QUANTITY column.
- H. Enter the UNIT PRICE of the type product as reflected in the STANDARD PRODUCTS TABLE.
- I. Multiply the figure in the QUANTITY column by the UNIT PRICE and enter the result in the TOTAL PRICE column.
- J. Repeat the above for each product ordered.
- K. TOTAL the costs of all products ordered on that order form and enter the net result in BLOCK A. TOTAL ABOVE.
- L. If more than one order form is required, enter the sum of the figures in BLOCKS A in BLOCK B on the last order form
- M. Enter the SUM of BLOCK A and BLOCK B in BLOCK C. TOTAL COST.
- N. Indicate the TYPE of payment being made with a CHECK MARK. Make all drafts payable to U. S. GEOLOGICAL SURVEY. DO NOT SEND CASH.
- O. Mail ORDER FORM(S) and PAYMENT to the FACILITY NEAREST YOU. If payment has been previously forwarded, the order form(s) must be mailed to the same facility.



**ORDER FORM**  
**SELECTED LANDSAT COVERAGE**  
U.S. DEPARTMENT OF THE INTERIOR  
GEOLOGICAL SURVEY



Return  
completed  
form to  
the facility  
nearest you.

PLEASE TYPE OR PRINT PLAINLY

STANDARD PRODUCTS  
BLACK AND WHITE

IMAGE SIZE	BAND(S)	SCALE	FORMAT	PRODUCT CODE
18.5cm (7.3 in.)	5	1:1 000 000	PAPER	41
18.5cm (7.3 in.)	4 5 6 7	1:1 000 000	PAPER	45
37.1cm (14.6 in.)	5	1:500 000	PAPER	42
74.2cm (29.2 in.)	5	1:250 000	PAPER	43

TOTAL ABOVE  
TOTAL FROM  
PREVIOUS SHEETS  
TOTAL COST

A	
B	
C	

PAYMENT MADE BY:

CHECK, MONEY ORDER   
PURCHASE ORDER   
GOVT. ACCOUNT

**NOTE:** Please refer to  
current price list  
for cost determination.

**COMMENTS:**

FORM 9-1943  
(Jan. 1977)

**NCIC HEADQUARTERS**  
U.S. Geological Survey  
507 National Center  
Reston, VA 22092  
FTS: 928-6045  
COMM: 703-860-6045

**EROS APPLICATIONS  
FACILITY  
NSTL  
U.S. Geological Survey  
Bay St. Louis, MS 39520  
FTS: 494-3541  
COMM: 688-3472**

**NCIC MID-CONTINENT  
U.S. Geological Survey  
1400 Independence Rd.  
Rolla, MO 65401  
FTS: 276-9107  
COMM: 314-364-3680**

**EROS DATA CENTER  
U.S. Geological Survey  
Sioux Falls, SD 57198  
FTS: 784-7151  
COMM: 605-594-6511**

**NCIC ROCKY MOUNTAIN  
U.S. Geological Survey  
Stop 510, Box 25046  
Denver Federal Ctr.  
Denver, CO 80225  
FTS: 234-2326  
COMM: 303-234-2326**

**NCIC WESTERN  
U.S. Geological Survey  
345 Middlefield Rd.  
Menlo Park, CA 94025  
FTS: 467-2427  
COMM: 415-323-2427**



**PRICE LIST**  
**STANDARD REMOTE SENSING DATA**  
U. S. DEPARTMENT OF THE INTERIOR  
GEOLOGICAL SURVEY



JANUARY 1, 1977

**SATELLITE DATA**

STANDARD LANDSAT			BLACK and WHITE		COLOR	
IMAGE SIZE	NOMINAL SCALE	PRODUCT FORMAT	UNIT PRICE	PRODUCT CODE	UNIT PRICE	PRODUCT CODE
55.8mm (2.2 in.)	1:3360000	Film Positive	\$ 8.00	11		
55.8mm (2.2 in.)	1:3360000	Film Negative	10.00	01		
18.5cm (7.3 in.)	1:1000000	Paper	8.00	23	\$12.00	63
18.5cm (7.3 in.)	1:1000000	Film Positive	10.00	13	15.00	53
18.5cm (7.3 in.)	1:1000000	Film Negative	10.00	03		
37.1cm (14.8 in.)	1:500000	Paper	12.00	24	25.00	64
74.2cm (29.2 in.)	1:250000	Paper	20.00	26	50.00	66

COLOR COMPOSITE GENERATION					\$ 50.00	50
----------------------------	--	--	--	--	----------	----

NOTE: 1) Portrayed in false color (infrared) and not true color.  
2) Cost of product from this composite must be added to total cost.

COMPUTER COMPATIBLE TAPES (CCT)						
TRACKS	b.p.i.	FORMAT	SET PRICE	PRODUCT CODE		
7	800	Tape Set	\$ 200.00	82		
9	800	Tape Set	200.00	83		
9	1600	Tape Set	200.00	84		

SELECTED COVERAGE			BLACK and WHITE		COLOR	
IMAGE SIZE	FORMAT	BAND(S)	UNIT PRICE	PRODUCT CODE	UNIT PRICE	PRODUCT CODE
18.5cm (7.3 in.)	Paper	5	\$ 6.00	41	\$12.00	46
18.5cm (7.3 in.)	Paper	4, 5, 6, 7	32.00	48		
37.1cm (14.8 in.)	Paper	5	12.00	42	25.00	47
74.2cm (29.2 in.)	Paper	5	20.00	43	50.00	48

**MANNED SPACECRAFT DATA**

SKYLAB S190A			BLACK and WHITE		COLOR	
IMAGE SIZE	NOMINAL SCALE	PRODUCT FORMAT	UNIT PRICE	PRODUCT CODE	UNIT PRICE	PRODUCT CODE
55.8mm (2.2 in.)	1:2850000	Film Positive	\$ 8.00	11	\$10.00	51
55.8mm (2.2 in.)	1:2850000	Film Negative	10.00	01		
18.3cm (6.8 in.)	1:1000000	Paper	6.00	23	12.00	63
32.5cm (12.8 in.)	1:500000	Paper	12.00	24	25.00	64
65.0cm (25.5 in.)	1:250000	Paper	20.00	26	50.00	66

SKYLAB S190B			BLACK and WHITE		COLOR	
IMAGE SIZE	NOMINAL SCALE	PRODUCT FORMAT	UNIT PRICE	PRODUCT CODE	UNIT PRICE	PRODUCT CODE
11.4cm (4.5 in.)	1:950000	Paper	\$ 6.00	22	\$ 6.00	62
11.4cm (4.5 in.)	1:950000	Film Positive	8.00	12	12.00	52
11.4cm (4.5 in.)	1:950000	Film Negative	10.00	02		
21.6cm (8.8 in.)	1:500000	Paper	8.00	23	12.00	63
43.4cm (17.1 in.)	1:250000	Paper	12.00	24	25.00	64
88.9cm (34.2 in.)	1:125000	Paper	20.00	26	50.00	66

APOLLO/GEMINI			BLACK and WHITE		COLOR	
IMAGE SIZE	NOMINAL SCALE	PRODUCT FORMAT	UNIT PRICE	PRODUCT CODE	UNIT PRICE	PRODUCT CODE
55.8mm (2.2 in.)	Variable	Film Positive	\$ 8.00	11	\$10.00	51
55.8mm (2.2 in.)	Variable	Film Negative	10.00	01		
22.6cm (8.9 in.)	Variable	Paper	8.00	23	12.00	63
45.5cm (17.9 in.)	Variable	Paper	12.00	24	25.00	64

## AIRCRAFT DATA

AERIAL MAPPING		BLACK and WHITE		COLOR	
IMAGE SIZE	PRODUCT FORMAT	UNIT PRICE	PRODUCT CODE	UNIT PRICE	PRODUCT CODE
22.9cm (9.0 in.)	Paper	\$ 3.00	73	\$ 7.00	63
22.9cm (9.0 in.)	Film Positive	5.00	13	15.00	53
22.9cm (9.0 in.)	Film Negative	6.00	03		
45.7cm (18.0 in.)	Paper	10.00	24	25.00	64
68.6cm (27.0 in.)	Paper	15.00	25	30.00	65
91.4cm (36.0 in.)	Paper	20.00	26	50.00	66

PHOTO INDEXES		BLACK and WHITE		FILM SOURCE	
IMAGE SIZE	PRODUCT FORMAT	UNIT PRICE	PRODUCT CODE	FILM SOURCE	
25.4x30.5cm (10x12 in.)	Paper	\$ 5.00	36	B & W - Size A	
OTHER	Paper	5.00	37	B & W - Size B	

NASA RESEARCH		BLACK and WHITE		COLOR	
IMAGE SIZE	PRODUCT FORMAT	UNIT PRICE	PRODUCT CODE	UNIT PRICE	PRODUCT CODE
55.8mm (2.2 in.)	Film Positive	\$ 3.00	11	\$10.00	51
55.8mm (2.2 in.)	Film Negative	4.00	01		
11.4cm (4.5 in.)	Paper	3.00	22	7.00	62
11.4cm (4.5 in.)	Film Positive	4.00	12	12.00	52
11.4cm (4.5 in.)	Film Negative	5.00	02		
22.9cm (9.0 in.)	Paper	3.00	23	7.00	63
22.9cm (9.0 in.)	Film Positive	5.00	13	15.00	53
22.9cm (9.0 in.)	Film Negative	5.00	03		
22.9x45.7cm (9x18 in.)	Paper	20.00	13	20.00	60
22.9x45.7cm (9x18 in.)	Film Positive	10.00	14	30.00	56
22.9x45.7cm (9x18 in.)	Film Negative	12.00	04		
45.7cm (18.0 in.)	Paper	10.00	24	25.00	64
68.6cm (27.0 in.)	Paper	15.00	25	30.00	65
91.4cm (36.0 in.)	Paper	20.00	26	50.00	66

## MISCELLANEOUS

MICROFILM		BLACK and WHITE		COLOR	
FORMAT		ROLL PRICE	PRODUCT CODE	ROLL PRICE	PRODUCT CODE
16mm (30.5m/100 ft.)		\$16.00	72	\$40.00	73
35mm (30.5m/100 ft.)		20.00	72	45.00	73

KELSH PLATES		BLACK and WHITE	
FORMAT		UNIT PRICE	PRODUCT CODE
Con tact Prints on Glass Specify thickness (0.25 or 0.06 inch) and method of printing (emulsion to emulsion or through film base).		\$12.00	70

TRANSFORMED PRINTS		BLACK and WHITE	
FORMAT		UNIT PRICE	PRODUCT CODE
From convergent or transverse low oblique photographs		\$ 8.00	71

VIEWING SLIDES		BLACK and WHITE		COLOR	
FORMAT		UNIT PRICE	PRODUCT CODE	UNIT PRICE	PRODUCT CODE
35mm mounted duplicate of available printing master				\$ 1.00	50

NOTE: 35mm original will require additional \$5.00, not to include cost of mounted duplicate.

Complete roll reproduction delivered in roll format carries a 50% reduction in frame pricing.  
Custom processing of non-standard products is available at three times the standard product price. If a non-standard size is desired, the cost is three times the next larger standard product price.

Priority service with guaranteed five working days shipment is offered for standard products only, at three times the standard product price.

Extra care should be taken to insure that monies and related order forms are forwarded to the same facility.

# HOW TO ORDER AERIAL MAPPING PHOTOGRAPHY

This order form is used to order either PHOTO INDEXES or INDIVIDUAL PHOTOGRAPHS of AERIAL MAPPING PHOTOGRAPHY.

Please provide the following information in the indicated areas of the order form:

- A. List your complete NAME, ADDRESS, ZIP CODE, and name of your COMPANY if applicable.
- B. List a PHONE NUMBER where you can be contacted during business hours.
- C. If you have had previous business with THAT FACILITY, please list your ACCOUNT NUMBER, if known.
- D. Enter the complete PHOTO IDENTIFICATION NUMBER as follows:

**PHOTO INDEX:** This number can be transcribed directly from a computer listing. Format size must be ordered according to available FILM SOURCE. Size A is 10" x 12". Size B is all sizes larger than 10" x 12", with most 20" x 24".

**INDIVIDUAL PHOTOGRAPHS:** This number can be transcribed directly from a PHOTO INDEX, by selecting the PROJECT, ROLL and FRAME NO. from the respective photographs. If only one frame of photography is being ordered, the column identified as LAST FRAME can be ignored, however, if more than one consecutive frame is required, please complete both the FIRST and LAST FRAME columns.

- E. REVIEW the STANDARD PRODUCTS TABLE on the order form and determine the type of PRODUCT desired.
- F. Enter the PRODUCT CODE of the type product being ordered from the STANDARD PRODUCTS TABLE.
- G. If you are ordering MORE than one photograph from a roll, enter the TOTAL in the NO. OF FRAMES column.  
Example: FIRST FRAME - 106; LAST FRAME - 112; NO. OF FRAMES = 7.
- H. The COMMENTS portion is completed only when a CUSTOM PRODUCT is desired and you want to specify the parameters. Refer to the current price list for custom product cost determination.
- I. Enter the NUMBER of copies being ordered of that product in the QUANTITY column. When the NO. OF FRAMES column reflects more than one, it will be necessary to MULTIPLY that figure times the number of copies to derive the QUANTITY figure.
- J. Enter the UNIT PRICE of the product as reflected on the current PRICE LIST.
- K. MULTIPLY the figure in the QUANTITY column by the UNIT PRICE, and enter the result in the TOTAL PRICE column.
- L. REPEAT the above for each product ordered.
- M. TOTAL the costs of all products ordered on that form and enter the result in BLOCK A. TOTAL ABOVE.
- N. If more than one order form is required, enter the sum of the figures in BLOCKS A in BLOCK B of the last order form.
- O. Enter the SUM of BLOCK A and BLOCK B in BLOCK C, TOTAL COST.
- P. Indicate the TYPE of payment being made with a CHECK MARK. Make all drafts payable to U.S. GEOLOGICAL SURVEY. DO NOT SEND CASH.
- Q. Mail ORDER FORM(S) and PAYMENT to the FACILITY NEAREST YOU. If payment has been previously forwarded, the order form(s) must be mailed to the same facility.



**ORDER FORM**  
**AERIAL MAPPING PHOTOGRAPHY**

U.S. DEPARTMENT OF THE INTERIOR  
GEOLOGICAL SURVEY



Return completed form to the facility nearest you.

**NCIC HEADQUARTERS**  
**U.S. Geological Survey**  
**507 National Center**  
**Reston, VA 22092**  
**FTS: 928-6045**  
**COMM: 703-860-6045**

PHOTO INDEXES

PLEASE TYPE OR PRINT PLAINLY

## AERIAL MAPPING PHOTOGRAPHY

## STANDARD PRODUCTS

BLACK AND WHITE

IMAGE SIZE	FORMAT	PRODUCT CODE
29.9cm 19 cm	FILM POSITIVE	13
29.9cm 19 cm	FILM NEGATIVE	03
29.9cm 19 cm	PAPER	23
45.7cm 13 cm	PAPER	24
60.9cm 17.7 cm	PAPER	23
91.4cm 135.6cm	PAPER	26

COLOR/IR/STAREC

IMAGE SIZE	FORMAT	PRODUCT CODE
22.9cm 19cm	FILM POSITIVE	63
22.9cm 19cm	PAPER	53
45.7cm 118cm	PAPER	64
68.6cm 27cm	PAPER	65
91.4cm 136cm	PAPER	66

TOTAL ABOVE	A
TOTAL FROM PREVIOUS SHEETS	B
TOTAL COST	C

PAYMENT MADE BY:

CHECK, MONEY ORDER

**PURCHASE ORDER**

## **GOVT. ACCOUNT**

**NOTE:** Please refer to  
current price list  
for cost determination.

**NCIC ROCKY MOUNTAIN  
U.S. Geological Survey  
Stop 510, Box 25046  
Denver Federal Ctr.  
Denver, CO 80225  
FTS: 234-2326  
COMM: 303-234-2326**

**NCIC WESTERN  
U.S. Geological Survey  
345 Middlefield Rd.  
Menlo Park, CA 94025  
FTS: 467-2427  
COMM: 415-323-2427**

**COMMENTS:**



**ORDER FORM**  
**NASA AIRCRAFT PHOTOGRAPHY**

U.S. DEPARTMENT OF THE INTERIOR  
GEOLOGICAL SURVEY



Return  
completed  
form to  
the facility  
nearest you.

NAME MR  
MS (FIRST) (INITIAL) (LAST) ACCOUNT NO. (IF KNOWN)  
COMPANY (IF BUSINESS ASSOCIATED) PHONE (Bus) \_\_\_\_\_  
ADDRESS \_\_\_\_\_ PHONE (Home) \_\_\_\_\_  
CITY \_\_\_\_\_ STATE \_\_\_\_\_ ZIP \_\_\_\_\_ Your Ref. No. \_\_\_\_\_  
(P.O. GOVT ACCT OR OTHER)

PLEASE TYPE OR PRINT PLAINLY

## STANDARD PRODUCTS

BLACK & WHITE PRODUCTS		FILM SOURCE				COLOR PRODUCTS		FILM SOURCE			
		COL. 1 CODE:	COL. 2 CODE:	COL. 3 CODE:	COL. 4 CODE:			COL. 1 CODE:	COL. 2 CODE:	COL. 3 CODE:	COL. 4 CODE:
55 mm 12.2 in. FILM POSITIVE	11					55 mm 12.2 in. FILM POSITIVE	51				
55 mm 12.2 in. FILM NEGATIVE	51					55 mm 12.2 in. PAPER					
55 mm 12.2 in. PAPER						114 cm 14.5 in. PAPER	62				
114 cm 14.5 in. PAPER	22					114 cm 14.5 in. FILM POSITIVE					
114 cm 14.5 in. FILM POSITIVE	12					22 cm 2 in. PAPER	63				
114 cm 14.5 in. FILM NEGATIVE	62					22 cm 2 in. FILM POSITIVE					
22 cm 2 in. PAPER	23	23	23			22 cm 2 in. FILM POSITIVE					
22 cm 2 in. FILM POSITIVE				13		22 cm 2 in. FILM POSITIVE					
22 cm 2 in. FILM NEGATIVE	9					22 cm 2 in. FILM POSITIVE					
22 9/16 cm 28.6 in. FILM POSITIVE				11		22 cm 2 in. FILM POSITIVE					
22 9/16 cm 28.6 in. FILM POSITIVE				14		22 cm 2 in. FILM POSITIVE					
22 9/16 cm 28.6 in. FILM NEGATIVE				54		45 cm 18 in. PAPER	44	34	64		
45 cm 18 in. PAPER	26	26	26			45 cm 18 in. PAPER					
68 cm 27 in. PAPER		25	25			68 cm 27 in. PAPER	53	43			
91 cm 36 in. PAPER		26	26			91 cm 36 in. PAPER	46	36			

TOTAL ABOVE  
TOTAL FROM  
PREVIOUS SHEETS  
  
TOTAL COST

A
B
C

PAYMENT MADE BY:

**CHECK, MONEY ORDER**

**PURCHASE ORDER**

## **GOVT. ACCOUNT**

#### COMMENTS.

Please refer to current  
price list for cost determination.

**NCIC WESTERN  
U.S. Geological Survey  
345 Middlefield Rd.  
Menlo Park, CA 94025  
FTS: 467-2427  
COMM: 415-323-2427**



In accordance with letter from DAEN-RDC, DAEN-ASI dated 22 July 1977, Subject: Facsimile Catalog Cards for Laboratory Technical Publications, a facsimile catalog card in Library of Congress MARC format is reproduced below.

Glass, Charles E

State-of-the-art for assessing earthquake hazards in the United States; Report 11: Imagery in earthquake analysis / by Charles E. Glass, Department of Mining and Geological Engineering, University of Arizona, Tucson, Arizona, and David B. Slemmons, Department of Geological Sciences, MacKay School of Mines, University of Nevada, Reno, Nevada. Vicksburg, Miss. : U. S. Waterways Experiment Station ; Springfield, Va. : available from National Technical Information Service, 1978.

221, 3, 11 p. : ill. ; 27 cm. (Miscellaneous paper - U. S. Army Engineer Waterways Experiment Station ; S-73-1, Report 11)

Prepared for Office, Chief of Engineers, U. S. Army, Washington, D. C., under Purchase Order No. CW-77-M-1371.

References: p. 217-221.

1. Earthquake engineering. 2. Earthquake hazards. 3. Earthquakes. 4. Remote sensing. 5. Seismic risks. 6. State-of-the-

(Continued on next card)

Glass, Charles E

State-of-the-art for assessing earthquake hazards in the United States; Report 11: Imagery in earthquake analysis ... 1978. (Card 2)

art studies. I. Slemmons, David B., joint author. II. Arizona. University. Dept. of Mining and Geological Engineering. III. Nevada. University. MacKay School of Mines. Dept. of Geological Sciences. IV. United States. Army. Corps of Engineers. V. Series: United States. Waterways Experiment Station, Vicksburg, Miss. Miscellaneous paper ; S-73-1, Report 11.

TA7.W34m no.S-73-1 Report 11





UNIVERSITY OF ILLINOIS-URBANA



3 0112 084235321